REPORT DOCUMENTATION PAGE

Public reporting burden for this collection of information is estimated to average 1 hour per response, including the time for reviewing instructions, searching data sources, gathering and maintaining the data needed, and completing and reviewing the collection of information. Send comments regarding this burden estimate or any other aspect of this collection of information, including suggestions for reducing this burden to Washington Headquarters Service, Directorate for Information Operations and Reports, 1215 Jefferson Davis Highway, Suite 1204, Arlington, VA 22202-4302, and to the Office of Management and Budget, Paperwork Reduction Project (0704-0188) Washington, DC 20503.
PLEASE DO NOT RETURN YOUR FORM TO THE ABOVE ADDRESS.

1. REPORT DATE (DD-MM-YYYY)	2. REPORT DATE TYPE	3. DATES COVERED (From - To)
11-04-2002	FINAL TECHNICAL	JUL'97 – JUN'01

4. TITLE AND SUBTITLE

SOLID STATE HIGH AUTHORITY TELESCOPING ACTUATORS

5a. CONTRACT NUMBER

5b. GRANT NUMBER

N00014-97-1-G009

5c. PROGRAM ELEMENT NUMBER

6. AUTHOR(S)

BREI, DIANN E.
HALLOVAN, JOHN

5d. PROJECT NUMBER

5e. TASK NUMBER

5f. WORK UNIT NUMBER

7. PERFORMING ORGANIZATION NAME(S) AND ADDRESS(ES)

UNIVERSITY OF MICHIGAN
DEPARTMENT OF MECHANICAL ENGINEERING
2350 HAYWARD, 2250 GG BROWN BLDG
ANN ARBOR, MI 49109-2125

8. PERFORMING ORGANIZATION REPORT NUMBER

C035913

9. SPONSORING/MONITORING AGENCY NAME(S) AND ADDRESS(ES)

DEPARTMENT OF THE NAVY
NAVAL RESEARCH LABORATORY
4555 OVERLOOK AVENUE, SW
WASHINGTON, DC 20375-5326

10. SPONSOR/MONITOR'S ACRONYM(S)

NRL

11. SPONSORING/MONITORING AGENCY REPORT NUMBER

12. DISTRIBUTION AVAILABILITY STATEMENT

UNLIMITED

13. SUPPLEMENTARY NOTES

14. ABSTRACT

15. SUBJECT TERMS

U = Unclassified

16. SECURITY CLASSIFICATION OF:			17. LIMITATION OF ABSTRACT	18. NUMBER OF PAGES	19a. NAME OF RESPONSIBLE PERSON
a. REPORT	b. ABSTRACT	c. THIS PAGE			DIANN E. BREI
					19b. TELEPONE NUMBER (Include area code)
					734-763-6617

Solid State High Authority Telescoping Actuators

Grant # N00014-97-1-G009

University of Michigan

Dr. Diann Brei, Principal Investigator
Department of Mechanical Engineering
2350 Hayward St.
2250 G.G. Brown Bldg.
Ann Arbor, MI 48109-2125
phone: (734) 763-6617
fax: (734) 647-3170
e-mail: dibrei@engin.umich.edu
web page: www-personal.engin.umich.edu/~dibrei/smartmat/

Dr. John Halloran, Co-Investigator
Department of Materials Science and Engineering
2300 Hayward St.
3062 H.H. Dow Bldg.
Ann Arbor, MI 48109-2136
phone: (734) 763-1051
fax: (734) 763-4788
e-mail: peterjon@engin.umich.edu
web page: msewww.engin.umich.edu/research/groups/halloran/

April 11, 2002

TABLE OF CONTENTS

1. INTRODUCTION

Stacks are one of the most commonly used form of piezoelectric actuation; unfortunately, they provide small displacements and as the stroke requirement grows so does the length of the stack. For many applications with small volume sizes, stacks are not viable due to their packaging size and if too long can pose a buckling risk. Fortunately, while many of these applications require more stroke, typically factor of 2 to 15 more than a stack, the force requirement is typically less than that generated by a stack, leaving room for amplification techniques. While there are several external techniques, they experience severe losses[3,33,40,42-45] leading to a great reduction in work efficiency.[1]

The goal of this research effort was to develop a family of high authority actuators ranging in size from the submillimeter scale, for embedment in composite structures, to discrete actuators up to the centimeter scale, that could provide modest stroke amplification (2 to 15 times) in a compact package with minimal force reduction. A solid state, monolithic piezoelectric actuation architecture was developed that internally leverages the piezoelectric strain by a series of cascading shells uniquely connected by end caps such that the shells "telescope" out when activated. The tailorability of the displacement output of this actuator design permits much more efficient coupling of the actuator output into a loading profile of similar impedance and thereby much greater effective actuator output.

This research consisted of the four specific tasks: 1) Manufacturing development and process modeling, 2) Actuator performance modeling, 3) Experimental component testing and 4) Performance analysis and evaluation. In this report, the methodologies employed and the results obtained are summarized for each of these tasks, for more detailed development the reader is referred to the papers in Appendix B.

2. TELESCOPIC DESIGN AND OPERATION

Conceptually, the telescopic leveraging scheme has concentric embedded piezoelectric shells that are connected at altering ends to affect a telescoping motion in a densely packed volume, as shown in Figure 1. The shells can have any cross section, but it is assumed that the cross section remains constant throughout the actuator's length, is of a shape that can be embedded within the previous shell, and has a constant wall thickness. The telescopic actuator can be built in a monolithic configuration, or individual shells can be connected with discrete end caps. The number, length, and cross-sectional area of the cascaded shells can be varied to meet the force and deflection requirements for a given application. The telescopic actuator internal leveraging scheme can be applied to either d_{31} or d_{33} actuator configurations; however there are slight variations in layup, poling and excitation methods (Figure 2).

The d_{31} telescopic actuator is a series of concentric, radially poled piezoceramic shells connected on alternating ends. The useful force and deflection of the actuator is in the axial direction of the shells. The actuator is electroded such that each shell is driven with a radial potential opposite to the radial potential of its neighboring shells. This electroding pattern causes each shell to expand (contract) while its neighboring shells contract (expand), and the activated
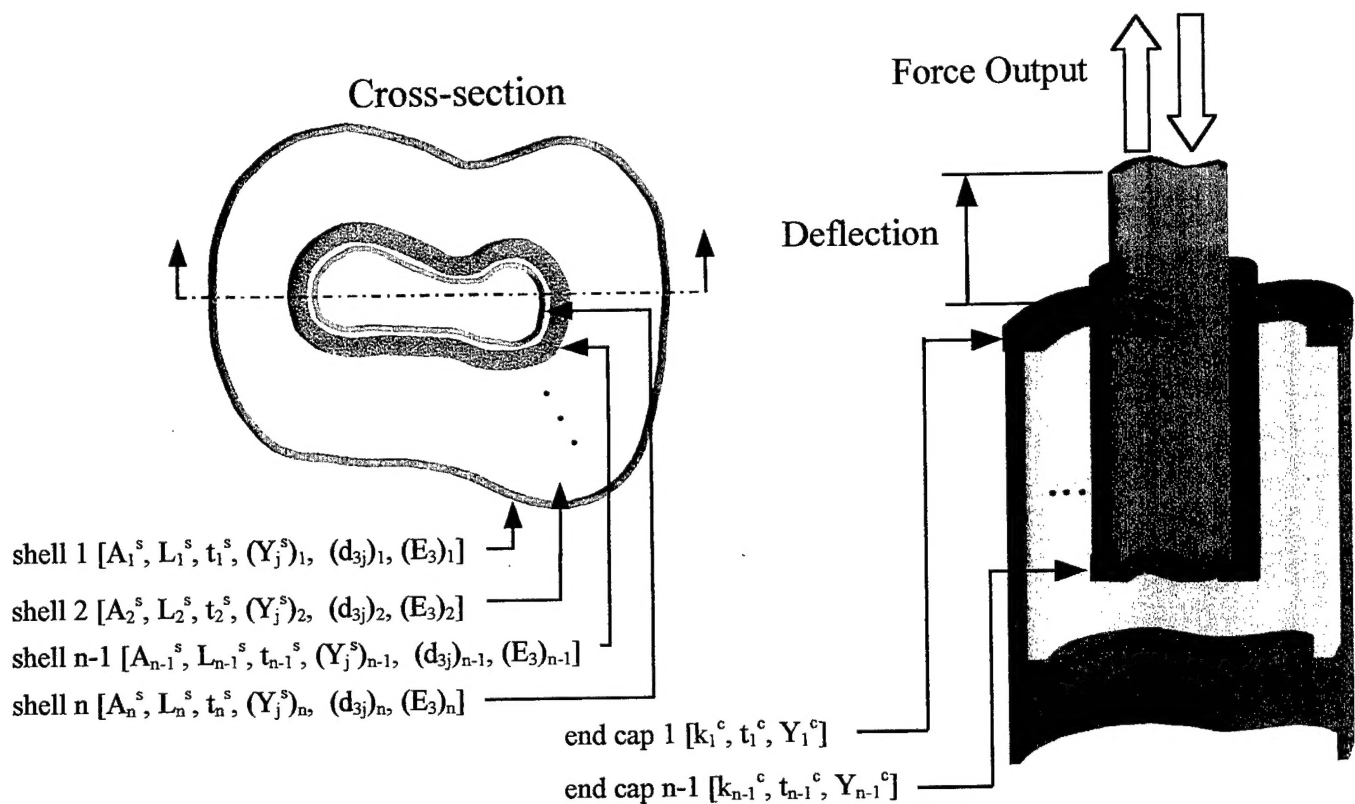

Cross-section

Force Output

Deflection

shell 1 $[A_1^s, L_1^s, t_1^s, (Y_j^s)_1, (d_{3j})_1, (E_3)_1]$

shell 2 $[A_2^s, L_2^s, t_2^s, (Y_j^s)_2, (d_{3j})_2, (E_3)_2]$

shell n-1 $[A_{n-1}^s, L_{n-1}^s, t_{n-1}^s, (Y_j^s)_{n-1}, (d_{3j})_{n-1}, (E_3)_{n-1}]$

shell n $[A_n^s, L_n^s, t_n^s, (Y_j^s)_n, (d_{3j})_n, (E_3)_n]$

end cap 1 $[k_1^c, t_1^c, Y_1^c]$

end cap n-1 $[k_{n-1}^c, t_{n-1}^c, Y_{n-1}^c]$

Figure 1: General telescopic actuation architecture

actuator "telescopes" out. The total deflection of the actuator becomes the sum of the deflections of the individual shells as depicted in Figure 3 for a three circular cylinder d_{31} telescopic actuator.

The d_{33} telescopic actuator operates in the exact same manner as the d_{31} actuator except that the shells are ring stacks axially poled and activated through their length (Figure 3b). This allows the shells in the d_{33} actuator to expand and contract in the d_{33} piezoelectric mode of actuation, where successive shells are activated oppositely, similar to the d_{31} actuator, generating
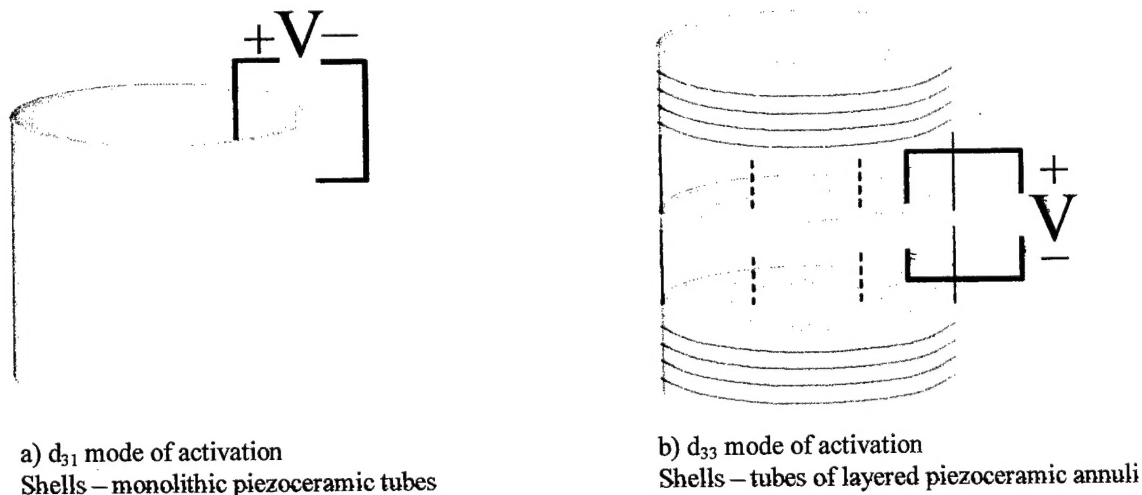
$+V-$

$+$
V
$-$

a) d_{31} mode of activation
Shells – monolithic piezoceramic tubes

b) d_{33} mode of activation
Shells – tubes of layered piezoceramic annuli

Figure 2: Telescopic architecture actuation modes

Expansion of Cylinder 1 +
Contraction of Cylinder 2 +
Expansion of Cylinder 3

Cylinder 1
Cylinder 2
Cylinder 3
End Cap 1
End Cap 2

Expansion of Cylinder 3

Contraction of Cylinder 2 +
Expansion of Cylinder 3

Section Before Activation | Section After Activation
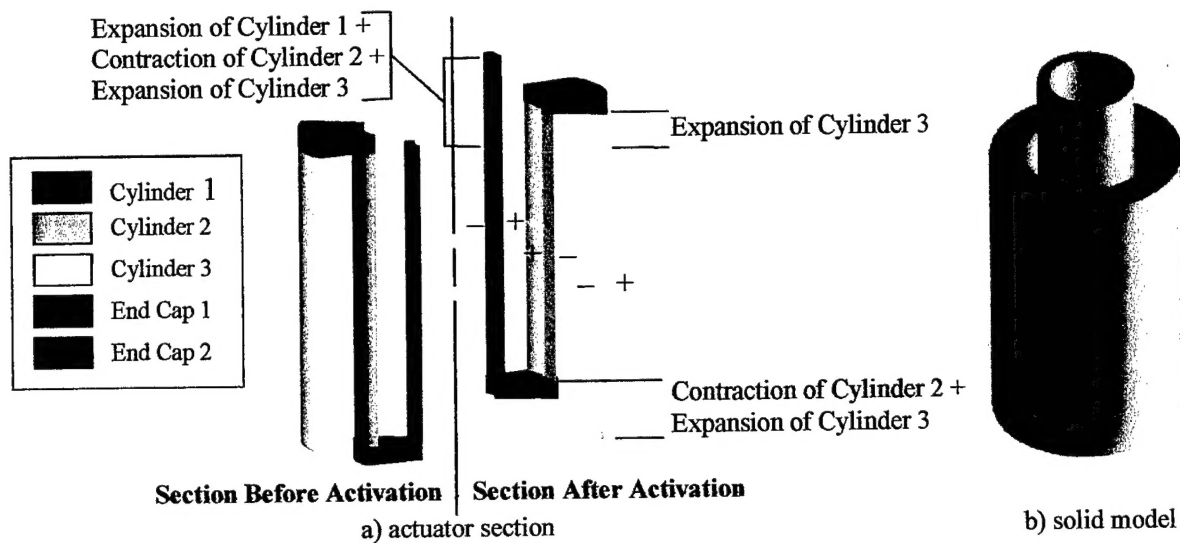
a) actuator section

b) solid model

Figure 3: Operation of a d_{31} telescopic actuator

the telescopic leveraging effect. The d_{33} mode of actuation produces approximately 2.2 times the deflection of the d_{31} mode because of the higher piezoelectric coefficient in the poling direction and enables constant field activation with variable cross-sectional area for a maximum force. The disadvantage is the manufacturing process is more complex with the introduction of more loss mechanisms. It should be noted that either amplification, d_{31} or d_{33}, does come at the sacrifice of force, but the level of force is still high, order of magnitude of a stack versus a bender. The main advantage is by nesting the shells, the length of the actuator can be decreased by the multiple of shells resulting in smaller packages with reduced buckling risks.

3. MANUFACTURING DEVELOPMENT AND PROCESS MODELING

The first task pursued in this research was development of new manufacturing processes to physically realize a generic monolithic telescopic actuator, primarily at the mesoscale (centimeters) but also at the submillimeter scale. For the mesoscale, the fabrication of piezoceramic actuators has historically depended on the assembly of simple discrete components to construct actuators capable of amplifying the limited strain produced by the material. For example, stacks are composed of multiple, thin layers of piezoceramic, each individually electroded and then bonded together. Benders are composed of two or more layers of piezoceramic bonded together or with an inactive substrate. Fortunately, piezoceramic processing technology has made great strides in the last few years. For example, stacks can now be co-fired;[2] benders can be made using rainbow[3] or thunder technology[4] or functionally gradient materials.[5-7] Very complex shapes can be fabricated using solid freeform fabrication[8] or injection molding.[9] Even micro actuators with very large aspect ratios can be fabricated using microfabrication by coextrusion.[10] These advances in processing technology open the door for actuator designers since they are no longer restricted to simple geometric shapes.

In particular, the telescopic actuation architecture has benefited from these advances. Although it is possible to construct a telescopic actuator by connecting individual tubes with discrete end-caps (as discussed later in the section *Conventional Assembly*), current processing

technologies make it feasible to construct a monolithic structure. Obviously, there are advantages to utilizing these solid-state processing techniques, such as decreased production time, reduced number of components and elimination of losses in discrete end-caps and bonding layers. Though the advantages of the telescopic architecture can be reaped in both the d_{33} and d_{31} modes of activation, all the actuators discussed in this report utilize the d_{31} mode of actuation. Through this research, two novel fabrication processes were developed for the construction of very complex ceramic telescopic structures: acrylate polymerization and injection molding. These were compared to a baseline actuator built from discrete tubes and end caps utilizing the conventional assembly method. A detailed description of the processes summarized below are provided in references.[11-14]

3.1. ACRYLATE POLYMERIZATION

Polymerization is novel technique that can be employed for fabrication of complex ceramic shapes by the casting of, or solid freeform fabrication of, a polymerized ceramic slurry.[15] Most of the research into this polymerizing procedure has been focused on aqueous polymerization where the solvent utilized is water.[16-18] Aqueous polymerization produces a green body that is relatively soft and fragile, which leads to problems removing the structure from a mold prior to the drying process. A process which uses a nonaqueous slurry was developed through this research that will produce a green ceramic body that is much more durable, thus facilitating the demolding procedure. This makes it optimal for rapid production of one of a kind, large complex ceramic structures, such as the telescopic actuator.

The proper slurry composition is crucial to this fabrication process. The slurry's main ingredient is PZT 856 powder, obtained from American Piezo Ceramics, Inc. (similar to PZT 5A) with a median particle size of 1.1 μm. This powder is mixed with the difunctional monomer propoxylated neopentyl gycol diacrylate (PNPDGA, Sartomer) and the monofunctional monomer 2-(2-ethoxyethoxy) ethyl acrylate esters (EOEOEA, Sartomer). The system solvent, decahydronaphthalene (decalin, Avocado), was also added to the mixture, as was the dispersant, 1 wt% Emcol CC-55 (Witco Corp.), which ensures the PZT powder remains in solution. The resulting slurry has a high solid load of 51 vol% PZT, but is fluid enough to easily fill a mold. Polymerization of the acrylate monomers is initiated with 0.1 wt% Benzoyl peroxide (BPO, Aldrich) and 0.025 wt% N,N-dimethyl-p-toluidine (DMPT, Aldrich) is added as a catalyst to lower the curing temperature.

This slurry remains workable for approximately ten minutes, during which time the casting process must be completed (Figure 4). In this case, the slurry was simply poured into a mold and allowed to cure at room temperature. The molds used to fabricate the telescopic actuator prototype were made from an epoxy resin utilizing a stereolithography technique. A computer designed two-piece mold was created, which produced a 75 mm tall, three tube, cylindrical telescopic actuator with 1.5 mm wall thickness. To facilitate demolding, the SLA molds were polished and lubricated prior to use. After the curing process was completed, the green ceramic actuator was carefully removed from the mold. The use of a nonaqueous slurry facilitates the removal process. The polyacrylate binder is removed by slowly heating in air. After polymer burnout, the actuator is still relatively fragile and the individual grains of the PZT must be sintered together to impart structural rigidity. The part is heated up to 1275° C where it is

sintered for 4 hours in a PbO rich atmosphere. The actuator is finished by applying silver paint for electrodes and poling it at 2000 V in a 160° C silicone oil bath.

Several very tall, between 5 and 10 cm, monolithic telescopic actuator were successfully fabricated with this process, an example shown in Figure 5. While the overall shape of the actuators produced did display variations along the length with some mild warping and micro-cracking at the ends, most of these resulted from initial trial errors in the SLA mold, all of which can be corrected upon further refinement of this new process. This fabrication procedure produced PZT of high quality. The material showed a large amount of densification, as illustrated in the micrograph of Figure 6. The density was greater than 98% of the theoretical. This compares favorably with commercially fabricated PZT whose densities are around 95-96% of theoretical. The piezoelectric properties were also higher than expected, yielding d_{33} values of 680 pm/V as opposed to the expected value of 590 pm/V for PZT856.
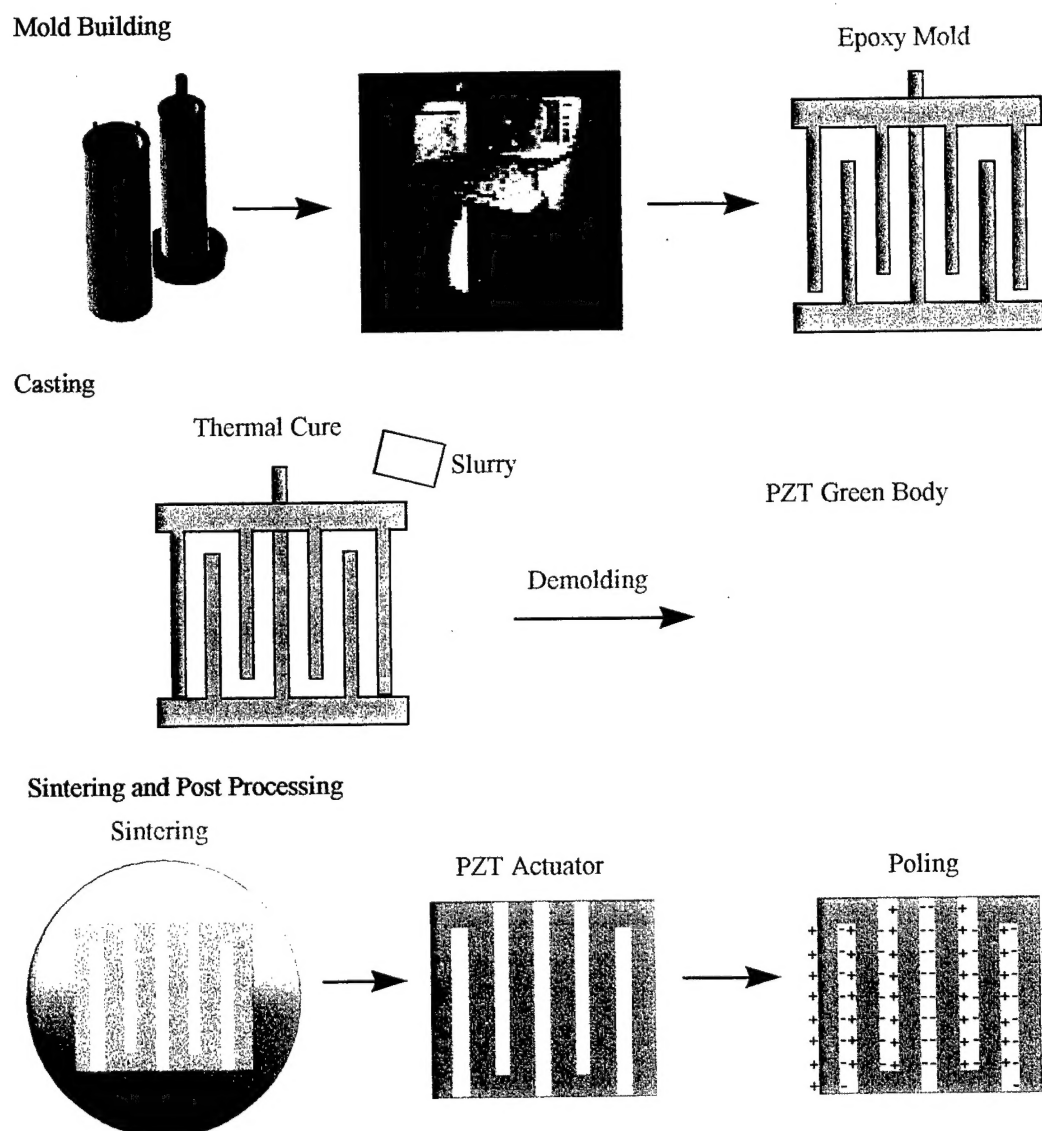
Mold Building

Epoxy Mold

Casting

Thermal Cure   Slurry

PZT Green Body

Demolding

Sintering and Post Processing

Sintering

PZT Actuator

Poling

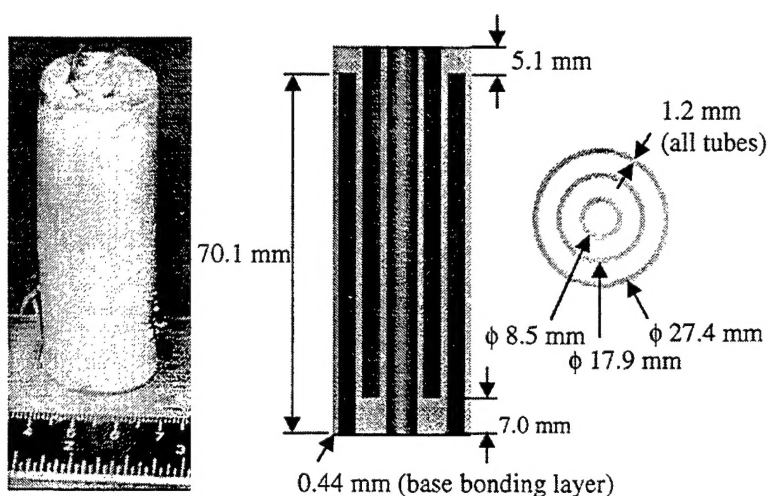**Figure 4: Schematic of acrylate polymerization process**

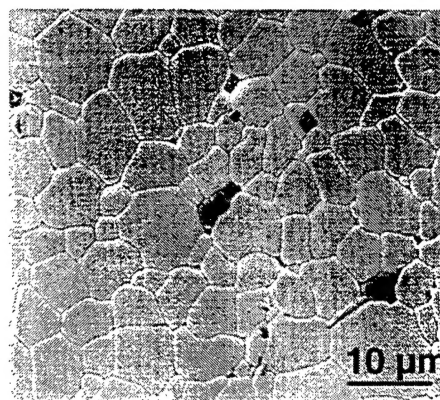Figure 5: Acrylate polymerized prototype

Figure 6: Polymerized PZT856 micrograph

3.2. INJECTION MOLDING

Injection molding is widely used in the plastics industry as a means for rapid mass production of complex shapes at low cost. It has been adapted for the fabrication of net shape piezoceramic actuators to provide several advantages over conventional fabrication techniques, including: high production rate, uniform part dimensions, uniform piezoelectric properties, and reduced fabrication and assembly costs. Ceramics injection molding was recently demonstrated as a low cost method for fabricating and simultaneously aligning thousands of identical PZT rods to produce highly repeatable, low-cost 1-3 piezocomposites for medical imaging and Navy undersea applications.[13] It has now been adapted for the fabrication of telescoping tube actuators that are difficult to produce by conventional techniques, such as isostatic pressing, machining, or slip casting.[19]

The basic injection molding process used by Materials Systems Inc. (MSI) for PZT transducer fabrication is shown schematically in Figure 7.[13] Materials Systems' injection molding process utilizes a heated thermoplastic mix of PZT powder and a wax-based binder. The binder in the mixture acts as a carrier during molding, allowing the material to be transferred as a viscous fluid when subjected to heat and pressure. The hot thermoplastic mixture of ceramic powder and organic binder is forced into a cooled mold creating a net shape green part. The molded part is subsequently heated slowly in air to remove the organic binder. The PZT shape is then sintered at 1250° C for 1 hour, under controlled atmospheric conditions to achieve the desired piezoelectric properties.

Figure 8 is an example of a telescopic actuator consisting of five nested ceramic tubes with integrated monolithic end caps. By designing the mold cavity to achieve the final actuator dimensions (18.5 mm O.D. x 25 mm overall length), no further assembly or machining is required. Each sintered part is subsequently contact poled in five steps (one tube at a time) using a field of 1.2 kV/mm through the wall thickness to achieve a positive polarity on the inner diameter of each tube. After poling, a permanent nickel electrode is applied to all surfaces except the bottom of the outer ring and wires are attached to the two resulting electrodes. This
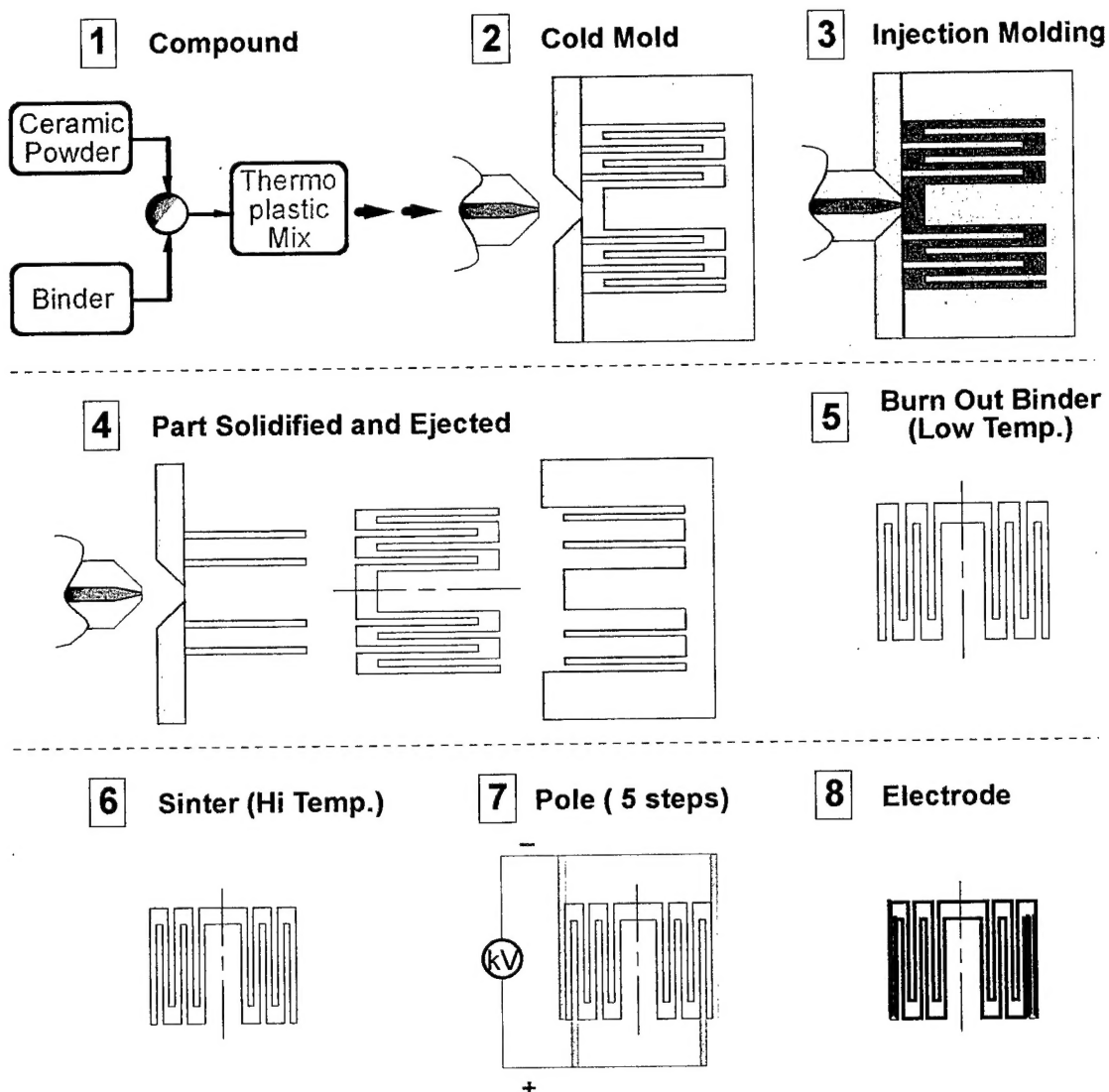
1 **Compound**   **2** **Cold Mold**   **3** **Injection Molding**

4 **Part Solidified and Ejected**   **5** **Burn Out Binder (Low Temp.)**

6 **Sinter (Hi Temp.)**   **7** **Pole (5 steps)**   **8** **Electrode**

Figure 7: Schematic of injection molding process

arrangement reverses the electric field that is applied to the second and fourth tubes, causing the structure to "telescope" during actuation.

MSI formulates its own piezoelectric compositions for enhanced piezoelectric performance, and the injection molding and proprietary sintering processes ensures a uniform and defect-free microstructure (Figure 9). Because the process utilizes a liquid feed stock injected under high pressure, the macroscopic voids often associated with traditional dry powder processing are eliminated. Furthermore, the isostatic nature of the process produces a very uniform green microstructure and green density; therefore, subsequent densification leads to uniform mechanical properties and part dimensions. PZT components routinely exceed a density of 7500 kg/m^3 (approaching the theoretical maximum density). MSI-53HD ceramic's d_{33} piezoelectric coefficient was measured to be 725 pm/V, which is similar to the MSI-53 used to fabricate the telescoping tube actuators.
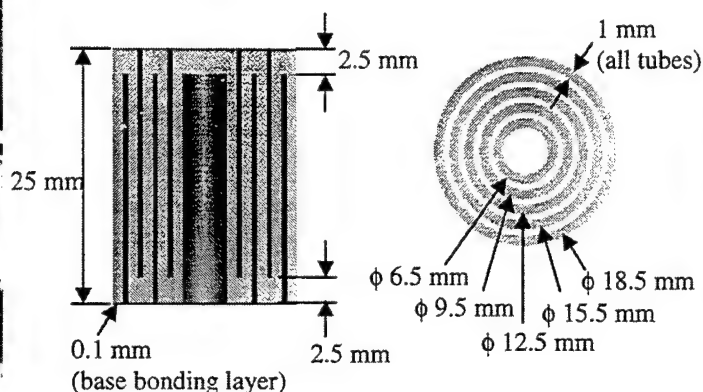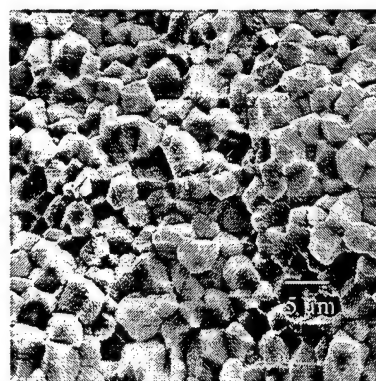
Figure 8: Injection molded prototype

Figure 9: Injection molded
MSI-53 micrograph

3.3. CONVENTIONAL ASSEMBLY

As a baseline, a third telescopic actuator prototype was constructed from off-the-shelf pre-poled piezoceramic tubes and aluminum washer end caps. The piezoceramic tubes were APC's 855 composition, similar to PZT 5H. The three tubes used to build the actuator were all of a length of 76.2 mm, a thickness of 1 mm, and outer diameters of 25.4 mm, 19.1 mm, and 12.7 mm respectively. The tubes were linked together by two aluminum end caps, each 3.18 mm thick, as shown in Figure 10. The components were bonded together using a two part epoxy from Insulcast (Insulcure 24, Insulcast 501). The actuator was completed by wiring adjacent tubes with opposite polarity.
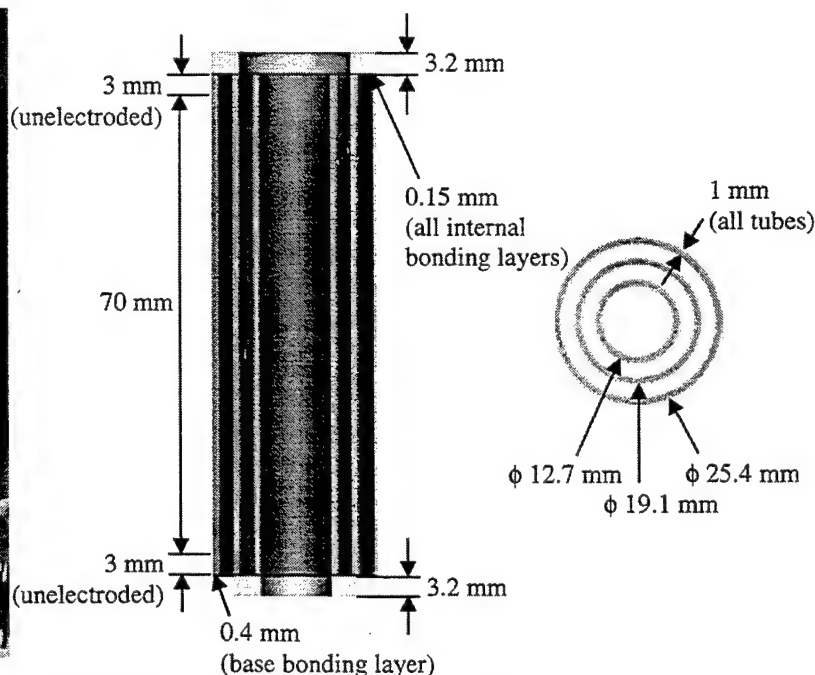

Figure 10: Conventionally assembled prototype

3.4. MICROFABRICATION BY COEXTRUSION

In addition to the development of fabrication methods at the mesoscale, attempts were made to develop telescopic actuators at the submillimeter scale using the microfabrication by coextrusion method developed at the University of Michigan by John Halloran. The MFCX process can be described as a multi-phase, or multi-material extrusion process, as depicted in Figure 11. Carbon black powder and PZT-5H (APC PZT-856) powder were each combined with thermoplastic polymers in a shear mixer (Model PL2100, CW Brabender Instruments, Inc.) at approximately 160°C at a speed of 30 rpm until the mixtures were of equal viscosity. Viscosity matching is critical because it allows the two materials to be simultaneously extruded without cross-sectional deformation. Each of the mixtures was hardened by cooling to room temperature, warm-pressed into a solid block of material, and then machined to create a feedrod of a hollow tube (Figure 11a). The cross-sectional dimensions of the feedrod were chosen so that the aspect ratio (wall thickness of the tube/ radius of the tube) matched the desired aspect ratio. During the extrusion step, the feedrod was forced through a reduction die at approximately 1200 kg on a Bradley University Research Extruder, reducing its diameter by a factor of 25, but maintaining the aspect ratio of the original feedrod. By re-bundling the extrudate and making multiple extrusion passes (Figure 11b), diameter reductions up to three orders of magnitude are possible making hollow tubular fibers. To create the hollow cross-section for these fibers, the carbon black core and the thermoplastic polymers were removed during the burnout cycle by slowly heating the fibers over 18 hours to a temperature of 600°C (HIPAN Series furnace, Micropyretics Heaters International). Finally, the fibers were sintered by heating at a rate of 180°C per hour to a two-hour dwell at 1285°C to strengthen and densify the ceramic. To prevent warping, a common problem in ceramics processing, it was necessary to burnout and sinter the fibers vertically, hanging under their own weight (Figure 11c). During the post-processing phase of fiber electroding and poling, gaining access to the fiber interior was problematic due to the hollow fiber topology and the extremely small hole in the fiber center. To address this problem,
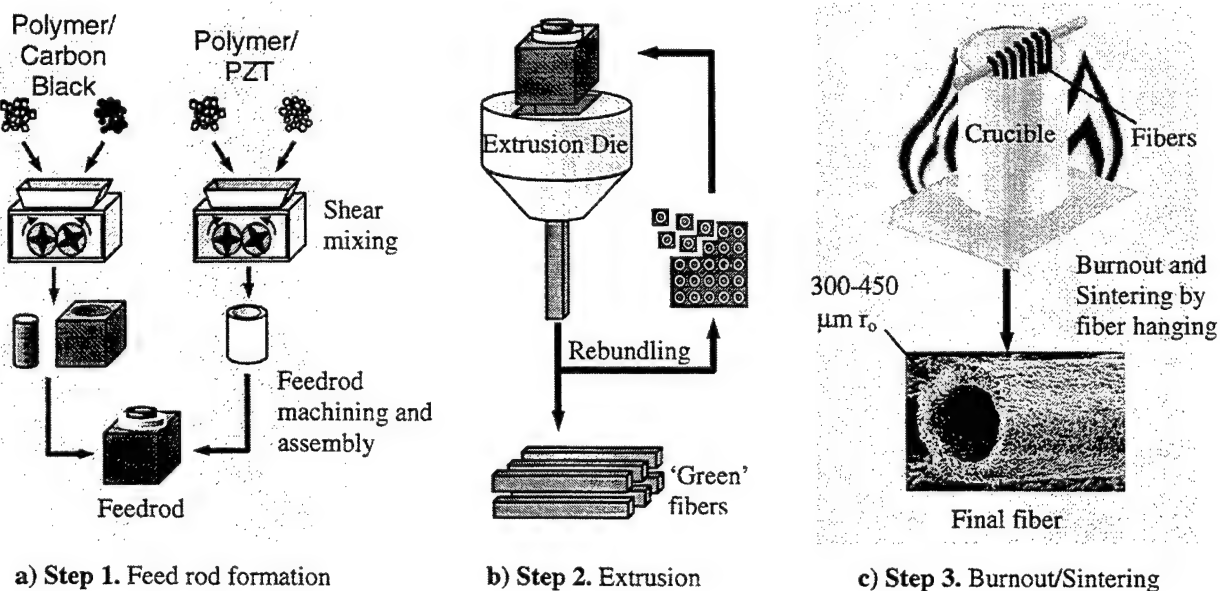

a) **Step 1.** Feed rod formation   b) **Step 2.** Extrusion   c) **Step 3.** Burnout/Sintering

Figure 11: MFCX process overview

a unique electrode pattern was introduced during this step, where the inside electrode was extended around the end of the fiber to an external patch, enabling access to both the inside and outside electrodes from the exterior of the fiber. Silver paint was used to electrode the fibers (DuPont Conductor Composition #7421), creating a large enough electrode patch so that multiple fibers could be connected through a single electrical bus. A gap (approximately 2mm) separated the inner and outer electrodes, allowing the fibers to be poled in air without arcing. Each of the fibers was poled by applying an electric field of 1200 V/mm at room temperature for approximately 30 minutes.

Many fibers were successfully fabricated, approximately 200 PZT-5H fibers of varying outside radius (300-450 μm) and aspect ratio (0.3 – 0.52); examples are shown in Figure 12. Fibers with features sizes as small as a grain size across were also successfully fabricated, but they were very fragile. While this process is very good at making long fibers with small features, it is not capable of joining the fibers out of the plane of extrusion as required for the telescopic actuator. However, the entire motivation for this submillimeter fabrication study was the development of piezoelectric actuation fibers for active fiber composites (AFC) that would improve upon the current state of art. The most common form of AFC that can generate high levels of strain (as high as 1700 microstrain) is based on embedded solid piezoelectric fibers activated by an external interdigitated electrode pattern.[20] This type of AFC has been employed in a twist configuration for control of a rotorcraft blade, where twist angles of several degrees have been achieved.[21] The major drawback to this approach is the requirement of the electric field to pass through the composite matrix. Due to the placement of the electrode on the matrix surface, electric field losses are significant requiring high voltages (on the order of 1 kV) for actuation.[22] Furthermore, this approach limits the matrix to electrically nonconductive materials, which is particularly a problem in large structure and air vehicle applications where metals and carbon fiber composites are almost exclusively utilized in construction.

An alternative approach to solid fiber AFC's is based upon hollow piezoelectric fibers (Figure 13) developed in this research. These fibers, individually electroded on both the inside and outside surfaces, are activated by an electric field applied directly across the walls of the fiber, generating longitudinal strain due to the piezoelectric d_{31} mode. Even though the longitudinal strain is decreased by approximately half by using d_{31} versus the d_{33} mode used in solid fiber AFCs, the required voltage can be decreased by a factor of ten or more since the electric field is applied only across the wall of the fiber instead of through the matrix, thereby eliminating field losses. An additional benefit to the hollow topology is the isolation of the inner electrode from the matrix, enabling the fiber to be embedded in electrically conductive matrices.[23-25] In addition to the demonstration of these improvements, a reliability study was
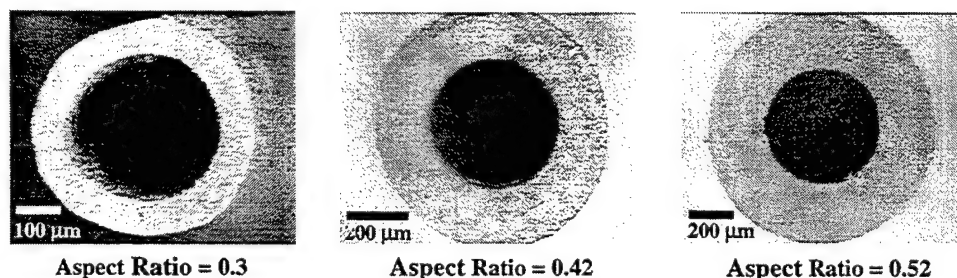

| Aspect Ratio = 0.3 | Aspect Ratio = 0.42 | Aspect Ratio = 0.52 |

Figure 12: Hollow fiber prototype cross-sections
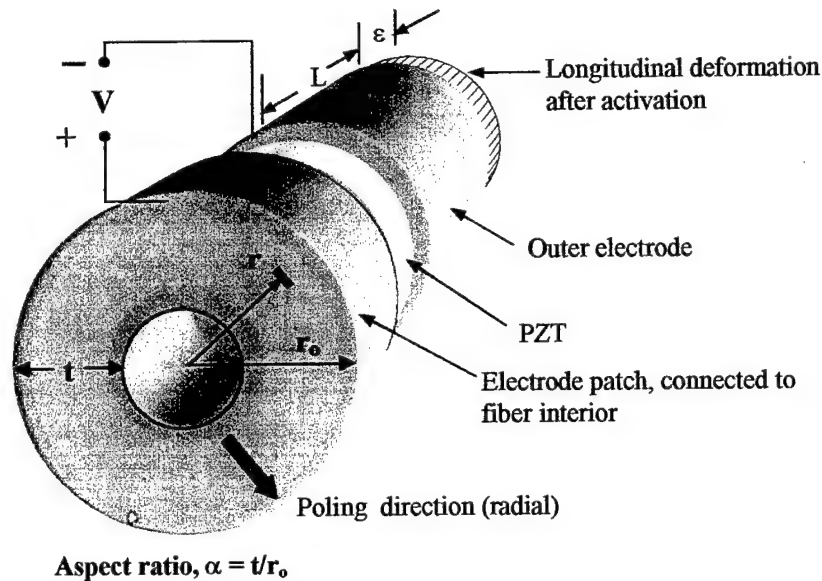
Aspect ratio, $\alpha = t/r_o$

Figure 13: Hollow fiber design

conducted that proved that hollow fiber active composites are within 10% of the reliability of active composites based upon solid fibers. The details of this study and findings are found in references.[26, 27]

4. ACTUATOR PERFORMANCE MODELING

The second task embarked upon was the modeling of the performance the telescopic actuator to provide predictive analysis/synthesis design tools and a foundation to study the architecture behavioral mechanisms and losses. This effort was focused on the derivation of analytical models, quasi-static and dynamic, for a generic configuration in order to gain insight into the sensitivity of the architecture to its various design parameters; however, finite element models were developed to assist in validating and refinement of the analytical models and for stress analyses. All of the analytical models were derived based upon the following assumptions:

- Piezoelectric induced radial strains are neglected in modeling the shells because the useful displacement, force, and work of the actuator is in the axial direction.
- The shells are long, thin, and of constant thickness and cross sectional area.
- The end caps are made from an isotropic, non-piezoelectric material - either metal or unpoled piezoelectric.
- The deformed shape of the end cap is a linear function of the radial direction coordinate.
- Displacements and vibrations in the radial direction (3) are assumed negligible with respect to the axial (1) direction.
- Bonding layer effects were assumed negligible in the dynamic modeling but were taken into account in the refinement of the quasi-static model.

A summary of the derivation methodology and the resulting models are given below, detailed derivations are provided in references.

4.1. QUASI-STATIC ANALYTICAL MODEL DERIVATION

An analytical model to predict the quasi-static performance of a generic telescopic actuator, arbitrary number of shells with a general cross-section, was derived using Castigliano's theorem with the piezoelectric strain taken as an additional forcing term. To simplify the model, the piezoelectric shells of the telescopic actuator and bonding layers were modeled as material under simple compression or tension. The end caps of the telescopic actuator were considered to be compliant; and therefore, were modeled as linear springs connecting the piezoelectric shells as shown in Figure 14. The resulting force-deflection model for a n-tube, m-bonding layer actuator is:

$$F = -P = \frac{\sum_{i=1}^{n}\left((d_{3j})_i(E_3)_i L_i^t\right) - \Delta}{\left(\sum_{i=1}^{n}\left(\frac{L_i^t}{(Y_j^t)_i A_i^t}\right) + \sum_{i=1}^{n-1}\left(\frac{1}{k_i^c}\right) + \sum_{i=1}^{m}\left(\frac{t_i^b}{Y_i^b A_i^b}\right)\right)} \tag{1}$$

where F is the force produced by the actuator which is countered by P the applied load, L_i^t is the ith tube's length, $(Y_j^t)_i$ is its Young's modulus in the j direction, A_i^t is its cross-sectional area, $(d_{3j})_i$ is its piezoelectric coefficient in the j direction, $(E_3)_i$ is the electric field applied to that tube, the stiffness of the ith end cap is denoted by k_i^c, t_i^b is the ith bonding layer's thickness, Y_i^b is its Young's modulus, and A_i^b is its cross-sectional area.

The stiffness of the ith end cap, k_i^c, (Equation 1) was derived from shell bending theory applied to the cylinders bonded to the end cap (Figure 15),

$$k_i^c = \frac{1}{\left(R_i - R_{i+1} - t_i^c\right)Tan\left(\frac{M_i}{D_i^s \lambda_i} - \frac{V_i}{2D_i^s \lambda_i^2}\right)} \tag{2}$$
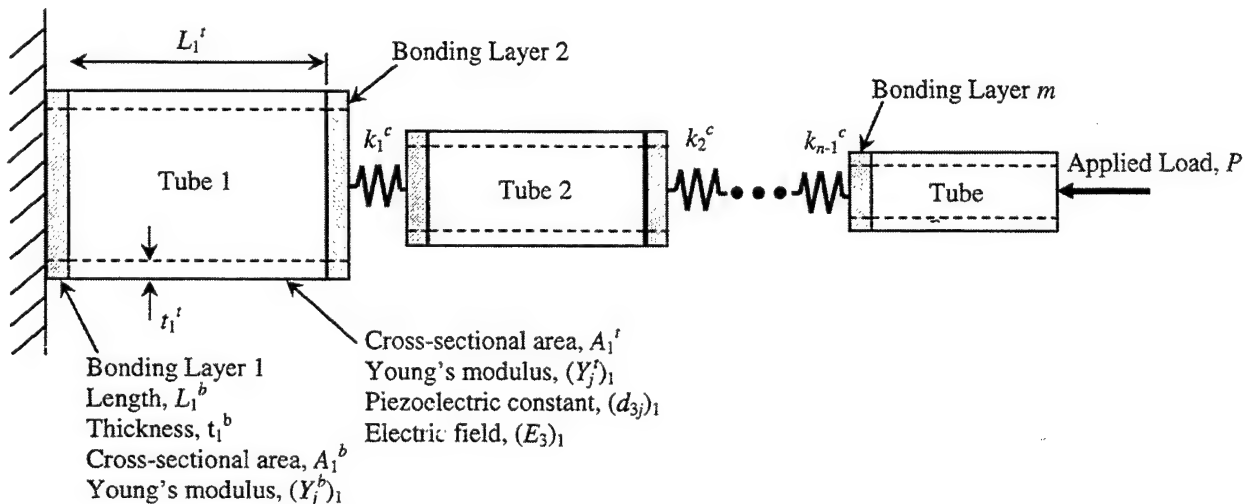

Figure 14: Analytical model of the telescopic architecture

The term t_i^c is the axial thickness of the ith end cap while R denotes a tube's mean radius. M_i and V_i are the moments and shears that an end cap is subjected to during loading, D_i^s is the tube's bending stiffness and λ_i is a geometric term.[30]

The expression for the actuator free deflection, Δ^F, can be found by setting the applied load, P, to zero, resulting in a simplified, rearranged version of Equation 1.

$$\Delta^F = \sum_{i=1}^{n} \left(d_{3j}\right)_i \left(E_3\right)_i L_i^t \tag{3}$$

The free deflection is simply the sum of the strains from each individual shells. It is interesting to note that the bonding layer terms are not present and have no effect on the unloaded displacement. However, the bonding layers do play a significant role in the force generating capabilities as denoted by the actuator blocking force, found by setting the deflection, Δ, in Equation 1 to zero,

$$F^B = \frac{\sum_{i=1}^{n} \left(\left(d_{3j}\right)_i \left(E_3\right)_i L_i^t\right) - \Delta}{\left(\sum_{i=1}^{n}\left(\frac{L_i^t}{\left(Y_j^t\right)_i A_i^t}\right) + \sum_{i=1}^{n-1}\left(\frac{1}{k_i^c}\right) + \sum_{i=1}^{m}\left(\frac{t_i^b}{Y_i^b A_i^b}\right)\right)} = k^o\left(\left(d_{3j}\right)_i \left(E_3\right)_i L_i^t\right) \tag{4}$$

the bonding layer terms will reduce the actuator blocking force, F^B. The force is also decreased by any compliance in the end caps, k^c, whereas the free deflection is completely unaffected. This gives rise to k^o, a term that lumps all the compliances within the telescopic architecture into a single stiffness value. These two factors will be shown to be very significant in the *Performance Analysis and Evaluation* section.
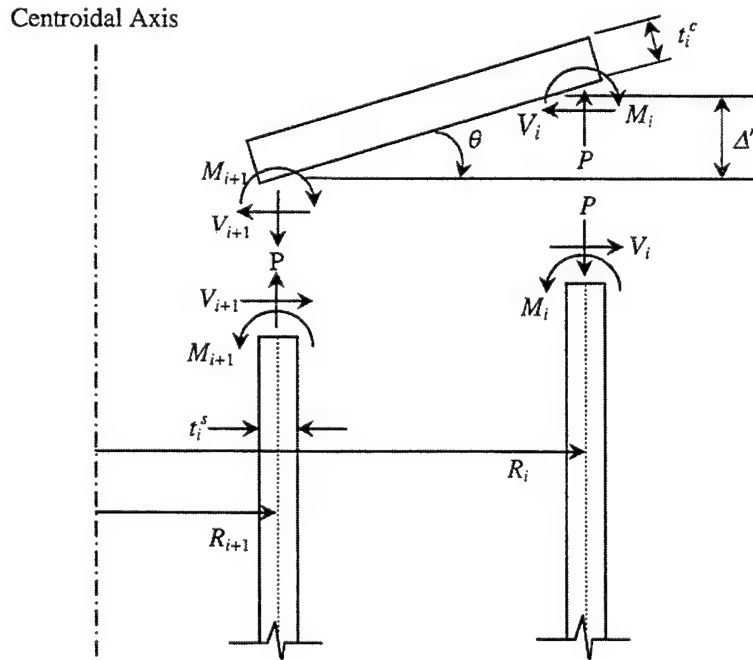

Figure 15: Compliant end cap model

4.2. FINITE ELEMENT MODEL DEVELOPMENT

Each of the three types of telescopic prototypes was numerically modeled in three dimensions including all physical elements: piezoelectric tubes, discrete or piezoceramic end caps, and bonding layers at the end caps and even at the actuator mounts. Because of their symmetry, only one half of an actuator's axial cross-section was constructed and meshed using the Hypermesh program, an example mesh shown in Figure 16. By using the eight noded, bi-quadratic axisymmetric elements (type CAX8 & CAX8E) available in ABAQUS, the full three-dimensional model was obtained that accounts for bending and shearing within the tubes, endcaps, and bonding layers and radial as well as circumferential piezoelectrically induced strains. Two different cases with different end conditions were modeled for each prototype: a free deflection case and a completely blocked case. For both trials, the bonding layer on the bottom edge of the outer tube of the models was restricted from moving in the radial and vertical direction (fully constrained in an axisymmetric model). For the blocked case, the top edge of the inner tube was additionally restricted from moving in the vertical direction. Each prototype was theoretically activated by specifying an electric potential along the electroded actuator surfaces. The ABAQUS files containing the deflection and reaction force values generated from these modeling runs were used to create a numerically predicted deflection-voltage and force-deflection curve for each prototype. These were used to validate and refine the analytical model.

In addition, these models were utilized in a stress study to verify that the monolithic structures would not break or buckle. The telescopic models were blocked and activated and the resulting material stress was calculated. The results of these trials were encouraging, with the maximum calculated Von Mises stress within a five-tube telescopic model reaching 36 Mpa, significantly lower than the 63 MPa tensile strength of the piezoceramic material. The problem points within the actuator, as can be seen in Figure 17, are the corners where the actuator tubes join with the end caps. The sharp corners act as stress concentration sites, but the 57% factor of safety for even these potential failure sites provides assurance that the telescopic architecture should easily withstand use as an actuator.
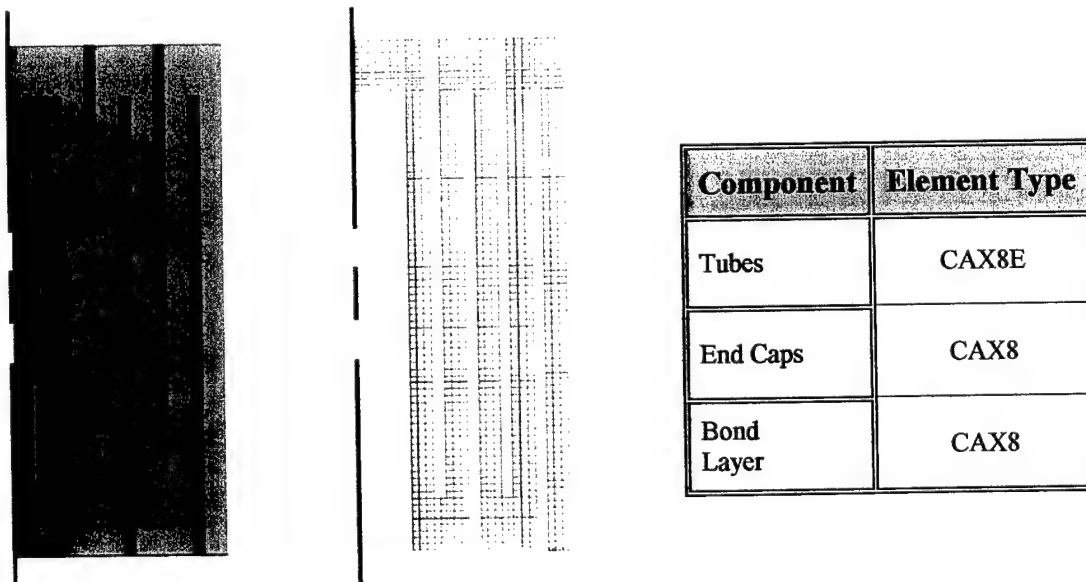

Component	Element Type
Tubes	CAX8E
End Caps	CAX8
Bond Layer	CAX8

Figure 16: Finite element model of the injection molded actuator
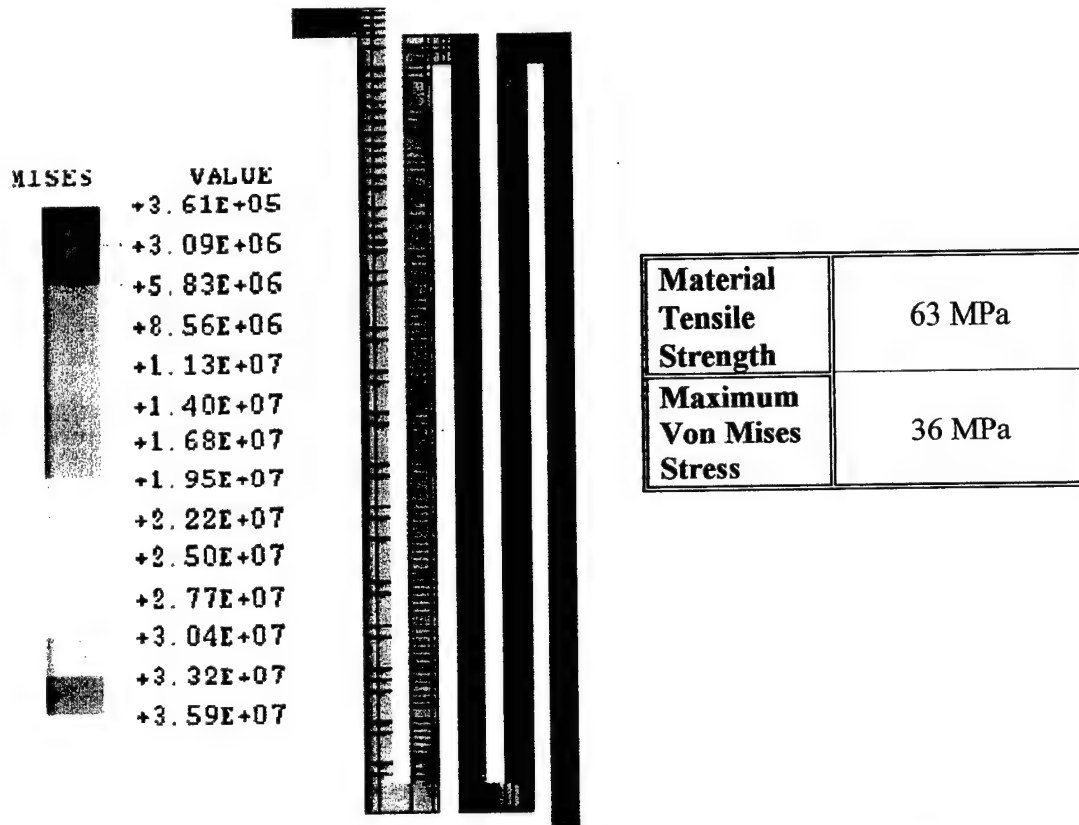
Figure 17: Numerical stress field within a five-tube telescopic actuator

MISES	VALUE
	+3.61E+05
	+3.09E+06
	+5.83E+06
	+8.56E+06
	+1.13E+07
	+1.40E+07
	+1.68E+07
	+1.95E+07
	+2.22E+07
	+2.50E+07
	+2.77E+07
	+3.04E+07
	+3.32E+07
	+3.59E+07

Material Tensile Strength	63 MPa
Maximum Von Mises Stress	36 MPa

4.3. DYNAMIC ANALYTICAL MODEL DERIVATION

The dynamic model was more complicated, thus, the more sophisticated transfer matrix method for inactive structures[31] was modified to account for piezoelectric loading. The telescopic actuator was modeled as a collection of uniform shells in axial vibration. The shells were numbered $\{1,..,k,..n\}$, the first shell being rigidly mounted at $x = 0$. The transfer matrix for the kth shell is:

$$U_k = B_k(l)B_k^{-1}(0) = \begin{bmatrix} \cos\left(\dfrac{\omega l}{c}\right) & \dfrac{c}{A_k Y_k \omega}\sin\left(\dfrac{\omega l}{c}\right) \\ -\dfrac{A_k Y_k \omega}{c}\sin\left(\dfrac{\omega l}{c}\right) & \cos\left(\dfrac{\omega l}{c}\right) \end{bmatrix} \tag{5}$$

where Y_k is the Young's Modulus, A_k is the cross-sectional area, and l is the length.

The end caps were treated as point masses and were numbered $\{1,..,k,..n\}$, the nth mass being at the free end of the actuator. The transfer matrix for the kth point mass is:[31]

$$P_k = \begin{bmatrix} 1 & 0 \\ -m_k\omega^2 & 1 \end{bmatrix} \tag{6}$$

where m_k is the mass of the kth end cap.

Using these transfer matrices, natural frequencies and mode shapes can be determined via the boundary conditions, which can in turn be applied to the equation of motion for a structurally damped continuous system under sinusoidal forcing:[32]

$$\left\{ \sum_{i=1}^{\infty} u_{hi}(x)\frac{d^2\alpha_i(t)}{dt} \right\}_k + \frac{\chi}{\Omega}\omega_i^2 \left\{ \sum_{i=1}^{\infty} u_{hi}(x)\frac{d\alpha_i(t)}{dt} \right\}_k + \omega_i^2 \left\{ \sum_{i=1}^{\infty} u_{hi}(x)\alpha_i(t) \right\}_k = \Omega^2\{U_P(x)\}_{j_k}\sin(\Omega t) \tag{7}$$

where Ω is the forcing frequency, χ is a structural damping coefficient, ω_i is the ith natural frequency, u_{hi} is the ith mode shape, U_p is the static solution, and α_i is a scaling function of time. Using orthogonality of modes, this equation can be simplified into a collection of 1-degree of freedom problems, which can be solved for α_i using conventional methods. According to this procedure, the displacement of the kth shell was found to be:

$$\{u(x,t)\}_k = \{U_P(x)\}_k \sin(\Omega t) + \sum_{i=1}^{\infty} \{u_{hi}(x)\}_k (B_i \cos(\Omega t) + C_i \sin(\Omega t)) \tag{8}$$

where $\{U_P(x)\}_k$ is the static displacement of the kth shell, $\{u_{hi}(x)\}_k$ are the mode shapes of the kth shell, B_i and C_i are constants that depend on the mode shapes and static displacements of all of the shells that make up the actuator, as well as the masses of the end caps. By evaluating Equation 8 with $k = n$ (the last shell) and $x = 1$ (the end of the shell), the amplitude magnitude is

$$\Delta_x = \sqrt{\left[\sum_{i=1}^{\infty} \{u_{hi}(l)\}_n B_i \right]^2 + \left[\{U_P(l)\}_n + \sum_{i=1}^{\infty} \{u_{hi}(l)\}_n C_i \right]^2} \tag{9}$$

and the phase at the free end of the actuator is

$$\phi = tan^{-1}\left(\frac{\sum_{i=1}^{\infty} \{u_{hi}(l)\}_n C_i}{\sum_{i=1}^{\infty} \{u_{hi}(l)\}_n B_i} \right) \tag{10}$$

Typically, the first natural frequency of the actuator is of primary interest. As would be expected, increasing the stiffness of any element, by either decreasing the length or increasing the cross-sectional area, will result in a higher first natural frequency. An increase in the structural damping of the system will result in a decrease in the first natural frequency. Additionally, increasing the mass of the mass of the end caps will result in a lower first natural frequency.

5. EXPERIMENTAL COMPONENT TESTING

The third task undertaken was the experimental characterization of telescopic actuators of various sizes and configurations, given in Table 1 (fabrication was described in the *Manufacturing Development and Process Modeling Section*). Three different types of experiments were conducted: 1) a force-deflection study, that allows for the evaluation of the architecture's performance under loaded conditions, just as it will experience in actual service situations, giving insight into the telescopic actuator stiffness and blocked force capabilities as well a loss mechanisms; 2) a deflection-voltage study, which measures the free deflection of an actuator at a range of electrical driving potentials giving insight into the material properties of the actuators and the hysteresis present within the actuator; and 3) a dynamic study which identified the resonances of the actuator by measuring the amplitude (under no load) and phase as a function of frequency.

Table 1: Material properties used in modeling of prototypes

Actuator Component	Material Type	Density	Young's Modulus	Poisson's Ratio	Piezoelectric Coefficient
Polymerized Prototype					
Tubes	APC PZT 856	7500 kg/m³	62 GPa	0.3	430 pm/V
End Caps	APC PZT 856	7500 kg/m³	62 GPa	0.3	Inactive
Bonding Layers	Insulcast 501 Insulcure 24	1150 kg/m³	1.9 GPa	0.3	N/A
Injection Molded Prototype					
Tubes	MSI-53	7500 kg/m³	62 GPa	0.3	440 pm/V
End Caps	MSI-53	7500 kg/m³	62 GPa	0.3	Inactive
Bonding Layers	Insulcast 501 Insulcure 24	1150 kg/m³	1.9 GPa	0.3	N/A
Conventionally Assembled Prototype					
Tubes	APC PZT 855	7500 kg/m³	62 GPa	0.3	420 pm/V
End Caps	Aluminum	2700 kg/m³	70 GPa	0.3	N/A
Bonding Layers	Insulcast 501 Insulcure 24	1150 kg/m³	1.9 GPa	0.3	N/A

5.1. FORCE-DEFLECTION STUDY

To measure the quasi-static performance of each prototype, the experimental test apparatus in Figure 18 was employed. Because of the high stiffness of each telescopic actuator, close attention was paid to the test set up, insuring a high degree of stiffness in the actuator mount and eliminating any low stiffness components from the chain of deflection measurement. For example, the actuators were mounted to quarter-inch aluminum plates that were secured to a reinforced steel back-plate that was bolted to a one-inch thick aluminum bed; this test bed was in turn bolted to a vibration isolation table. Each actuator was activated by a 100 V potential supplied by a Kepco APH 2000 DC power supply. For this driving voltage, the free displacement of the activated prototype was measured by a Philtec A88NE1 fiber optic probe at various points around the actuator circumference and was averaged. Once the free displacement was measured, force was applied to the actuator by dialing-in a micrometer on a Newport load bearing stage with a Cooper LPM 530 load cell in-line with the prototype. Force was measured in 25 N increments until the blocked force was reached or 100 N. While each actuator was predicted to generate more force than 100 N at large driving potentials, this was set as a conservative upper limit due to the small set of prototypes available for testing. This process was repeated, incrementing the electric driving potential by 100 V each test run, until the maximum driving field for each actuator was reached.

Experimental results for each prototype are displayed in Figure 19. The analytical model predicts the injection molded prototype (Figure 19 top) to exhibit a free deflection of 13.6 μm, a blocked force of 229.3 N, and a stiffness of 16.8 N/μm (values for the utilized analytic end cap stiffnesses are given in Table 2). The error between the analytical model and observed behavior
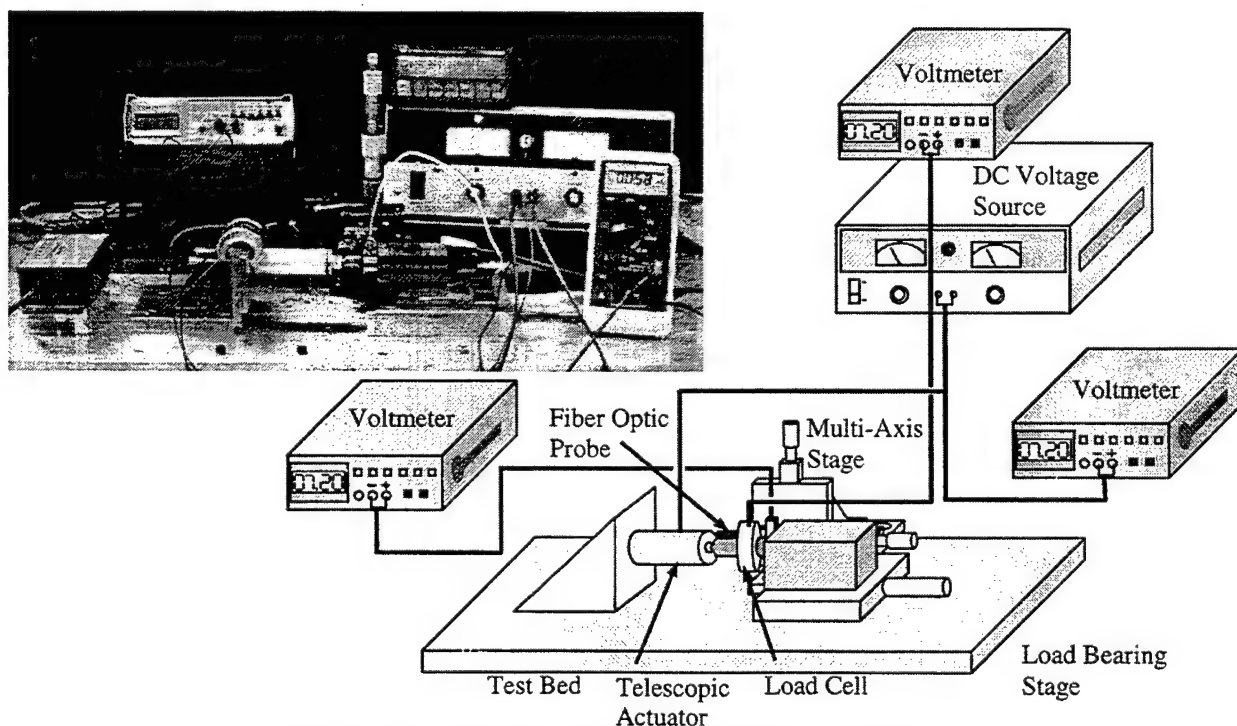

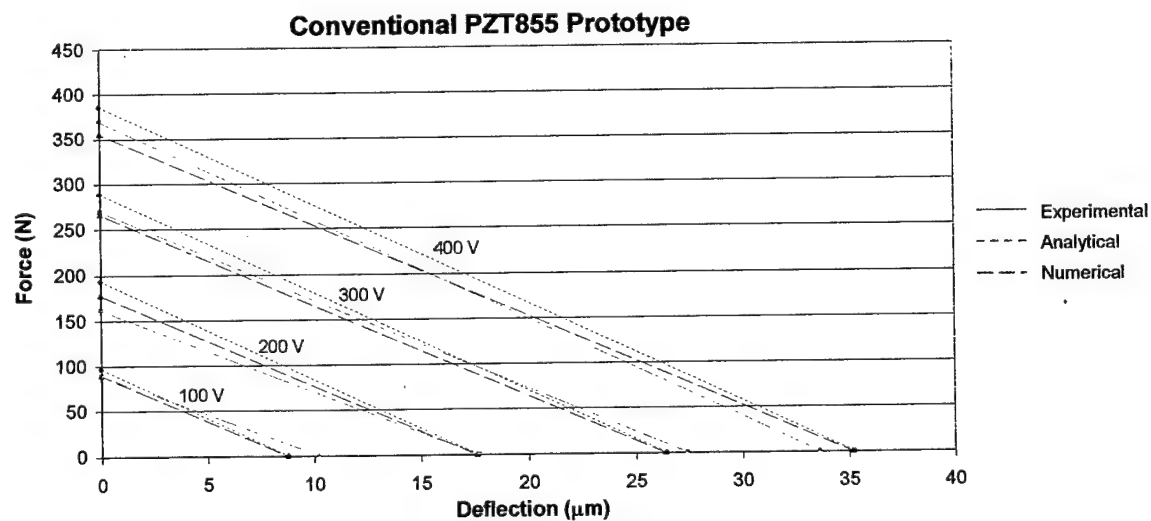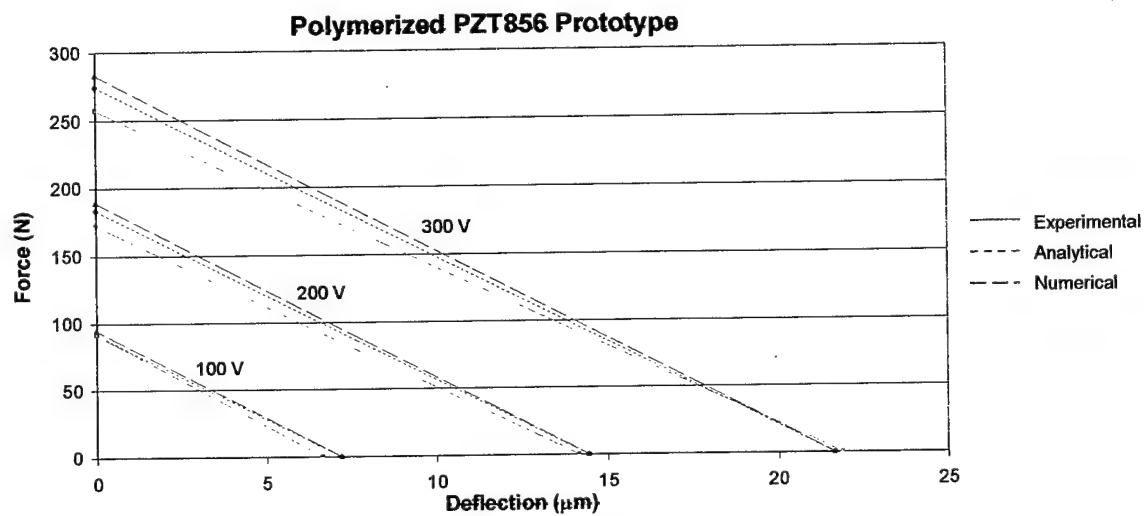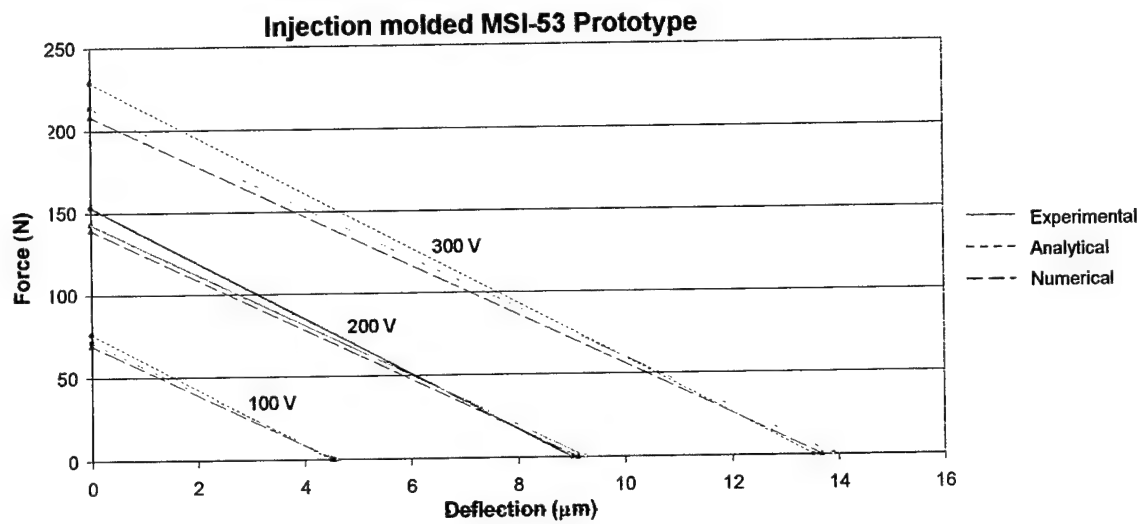**Figure 18: Force-Deflection experimental test apparatus**

Injection molded MSI-53 Prototype

300 V

200 V

100 V

Experimental
Analytical
Numerical

Polymerized PZT856 Prototype

300 V

200 V

100 V

Experimental
Analytical
Numerical

Conventional PZT855 Prototype

400 V

300 V

200 V

100 V

Experimental
Analytical
Numerical

Figure 19: Force-Deflection results

Table 2: Analytical prototype end cap stiffnesses

Prototype	End Cap 1 (outer)	End Cap 2	End Cap 3	End Cap 4 (inner)
Injection Molded	908 N/μm	876 N/μm	840 N/μm	798 N/μm
Acrylate Polymerized	174 N/μm	375 N/μm	N/A	N/A
Conventionally Assembled	182 N/μm	157 N/μm	N/A	N/A

was 2.2% for free deflection, 7.4% for the blocked force, 9.1% for the stiffness and an overall modeling error of 4.8%. The numerical model of the injection molded prototype predicts 13.7 μm of unrestrained motion that could be blocked by a force of 208.4 N, yielding a stiffness 15.2 N/μm at the maximum electric driving potential. This showed a close correlation to the experimental results with errors of 1.5% in predicted deflection, 2.4% for the blocked force, 0.9% for the actuator stiffness, and an overall model error of 1.9%. This prototype was well made with very little variability in dimensions and material properties; thus, it was possible to model it quite accurately.

The acrylate polymerized prototype on the other hand, had variability in dimensions which were difficult to fully measure. The prototype possesses poor geometric tolerances, with varying wall thickness and warping of the tubes in both the radial and axial directions, in addition to a large degree of uncertainty in the extent of the hand painted electrode and its integrity. Despite this, the analytic model of the acrylate polymerized prototype yields a predicted free deflection of 21.7 μm, a blocking force of 275.9 N, and an overall actuator stiffness of 12.7 N/μm, giving errors of 0.9% in the free deflection, 7.4% in the blocked force, 8.4% in the actuator stiffness, and an overall model error of 4.2%. The numerical model of this prototype was less accurate with 1.1% error in the free displacement of 21.7 μm, 10.2% error in the blocked force of 283.1 N, 11.4% error in the overall actuator stiffness of 13.1 N/μm, and 5.9% total model error. In light of all the unknowns in this prototype, this correlation is still very good.

The assembled prototype was between these two prototypes in quality. The material properties and dimensions were well known except for the internal bonding layers which could not be easily measured from the completed prototype due to their inaccessibility. The presence of many bonding layers within this prototype played a pronounced role in the actuator's performance. At the driving potential of 300 V the analytical model for this prototype predicts a free deflection of 26.6 μm with 2.9% error, a blocked force of 289.1 N with 7.2% error, and an actuator stiffness of 10.9 N/μm with 10.4% error, which gives an overall model error of 5.1%. The numerical model of the conventional actuator gives a free deflection of 26.5 μm that can be blocked by a force of 266.3 N, which gives an overall stiffness of 10.1 N/μm. This model had slightly better correlation with the experimental results with 3.2% in the deflection, 1.2% in the forcing capabilities, 10.7% error in the stiffness, and a relatively low 2.2% overall model error. Interestingly, the analytical models do not systematically over-predict their numerically derived counterparts. For example, the numerical model for the polymerized prototype gives higher

predictions for forcing capabilities when compared to both the experimental results and the revised analytical model. But the numerical models for the other two prototypes are much more conservative, always under-predicting the analytical models, and often under-predicting even the experimental results, these trends led to an exploration of the bonding layers and end cap thickness; parameters of the telescopic architecture that could account for these results as well as influence the actual performance.

Though each actuator was made from various materials and has different dimensions, it is possible to compare them at a qualitative level at the 300 V activation level. As would be expected, the longer telescopic actuators produced more deflection, 27.4 μm for the assembled actuator and 21.9 μm for the polymerized prototype, than the shorter injection molded actuator which generated only 13.9 μm of deflection. While length was the major factor in this, it is important to note that if the injection molded actuator had not been composed of five nested tubes, the difference in displacement would have been much greater. Though the dimensions of the polymerized and assembled actuators are similar, because of the material properties and differing end cap thickness, the blocked forces did vary from 269.7 N, giving a stiffness of 9.8 N/μm for the assembled prototype and 256.9 N and 11.7 N/μm for the polymerized prototype. Because the end caps on the polymerized prototype are ceramic and thicker than those of the assembled actuator, the stiffness of the polymerized prototype is slightly higher. The injection molded actuator had the highest stiffness of all prototypes at 15.4 N/μm which resulted in the large blocking force of 213.4 N, despite the smaller cross-sectional areas of the tubes. This higher stiffness is a result of shorter tubes that are closely spaced and stiff end caps.

5.2. DEFLECTION-VOLTAGE STUDY

The free deflection performance of each prototype was experimentally measured utilizing the test setup depicted in Figure 20 to gain insight into the hysteresis losses. Each prototype was mounted to an aluminum plate and secured with a vise. A thin square of aluminum was bonded to the inner most tube of each actuator to serve as a reflective surface to facilitate readings using
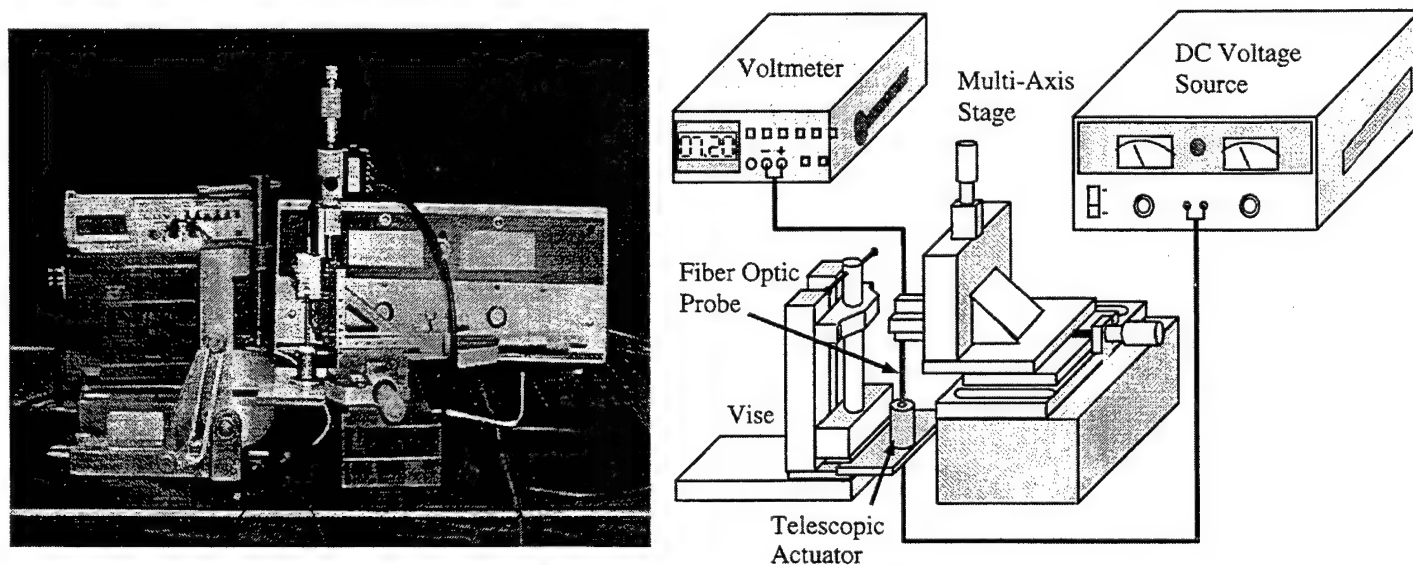

Figure 20: Deflection-Voltage experimental test apparatus

a Philtec fiber optic displacement sensor. The sensor was monitored with a Fluke digital multi-meter. The actuators were activated using a Kepco power supply in 50 volt increments. At each increment the displacement was measured with the fiber optic probe. This process was repeated until the maximum applied voltage was reached, 300 V for the two monolithic actuators and 400 V for the baseline actuator. Once the maximum field was reached, the voltage was stepped down, again in 50 volt increments, until zero volts was reached. At this point the leads from the power supply were reversed and the process was repeated for negative voltages.

The experimental results for each of the three actuators are given in Figure 21, with 14.7 μm deflection for the injection molded actuator (at 300 kV/m), 24.7 μm of deflection for the acrylate polymerized telescopic prototype, (at 230 kV/m), and 33.2 μm of deflection for the conventionally assembled actuator (at 400 kV/m). For the injection molded prototype, an experimentally measured d_{31} value of 440 pm/V was employed in the model, yielding a maximum theoretical deflection of 14.9 μm analytically and 13.7 μm numerically. The average error for this prototype was determined to be 13.4% for the analytic model, and 14.1% for the numeric model, but this is mainly due to hysteresis, which reached a maximum of 6.6 μm. The error at the maximum free deflection, where there is little hysteresis, was only 1.8% for the analytic model and 6.9% for the numeric model. The experimentally determined d_{31} value for the polymerized actuator was 430 pm/V, which gave an analytically predicted maximum deflection of 21.9 μm for 12.6% error and 21.7 μm of numerically predicted deflection giving 12.1% error when compared to the measured maximum deflection. It should be noted that the increased error in this case most likely stems from uncertainty in the electroded length of the polymerized actuator's cylinders. For the polymerized telescopic actuator, the average error in the analytic model was 20.5% with the numeric model giving a similar error of 20.6%; again, mostly due to hysteresis, which peaked at 11.5 μm. For the baseline prototype, the maximum free deflection correlated well with the theoretical values of 31.9 μm for the analytic model and 35.1 μm for the numeric model, to within 3.9% analytically and 5.8% numerically when using the measured d_{31} value of 420 pm/V. The maximum hysteresis was 19.1 μm, and the average error in the analytic model was 18.2% while the numerical model yielded 18.9% overall error. The minor difference in the predictions of the two models for each of the prototypes arises because the numerical model accounts for piezoelectric effects in three dimensions, while the analytical model is only one-dimensional. It is relevant to once again point out that the linear nature of the theoretical models do not attempt to capture the hysteresis that all piezoceramics exhibit; but, as evidenced in Figure 21, when hysteresis is taken into account, the experiments do track both the numerical and analytical model well.

5.3. DYNAMIC STUDY

For the dynamic experimental study, only the conventionally assembled prototype was tested. Dynamic frequency-amplitude tests were conducted to measure the amplitude and phase of the free end of the actuator as a function of the forcing frequency. The prototype was clamped in place and an HP model 35670A dynamic signal analyzer amplified by a Trek model 50/750 amplifier provided a 50 V input sine wave input signal (Figure 22) to the actuator. The frequency of this sine wave was swept from 100 Hz to 20,000 Hz. During this sweep, the peak
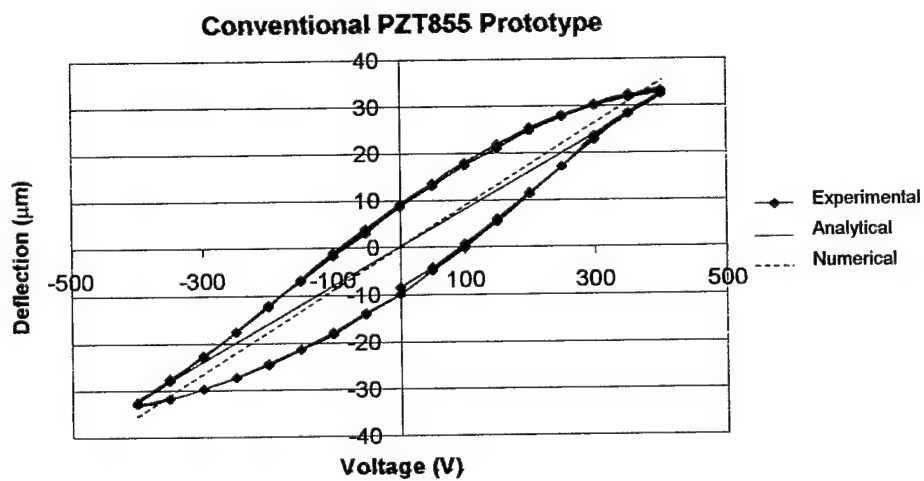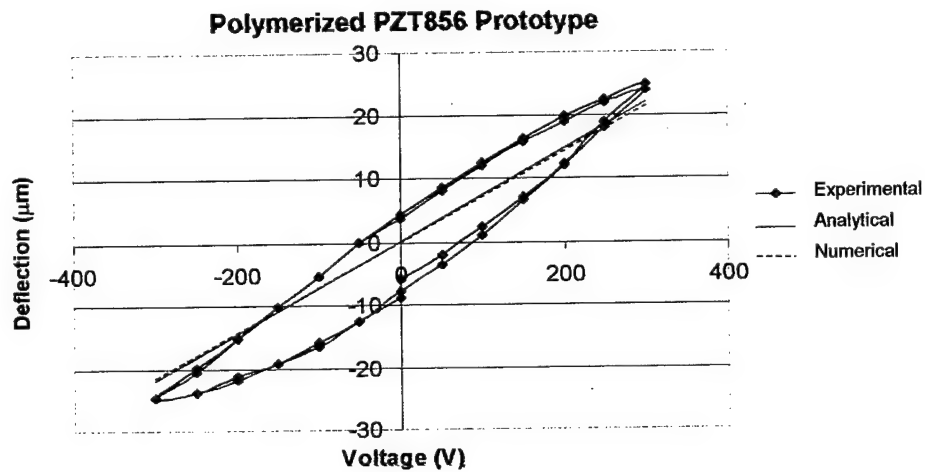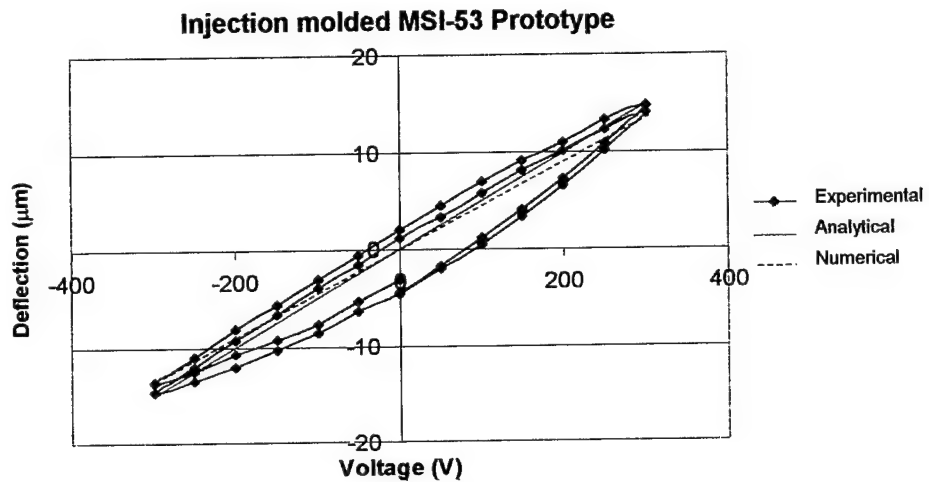
Injection molded MSI-53 Prototype

Polymerized PZT856 Prototype

Conventional PZT855 Prototype

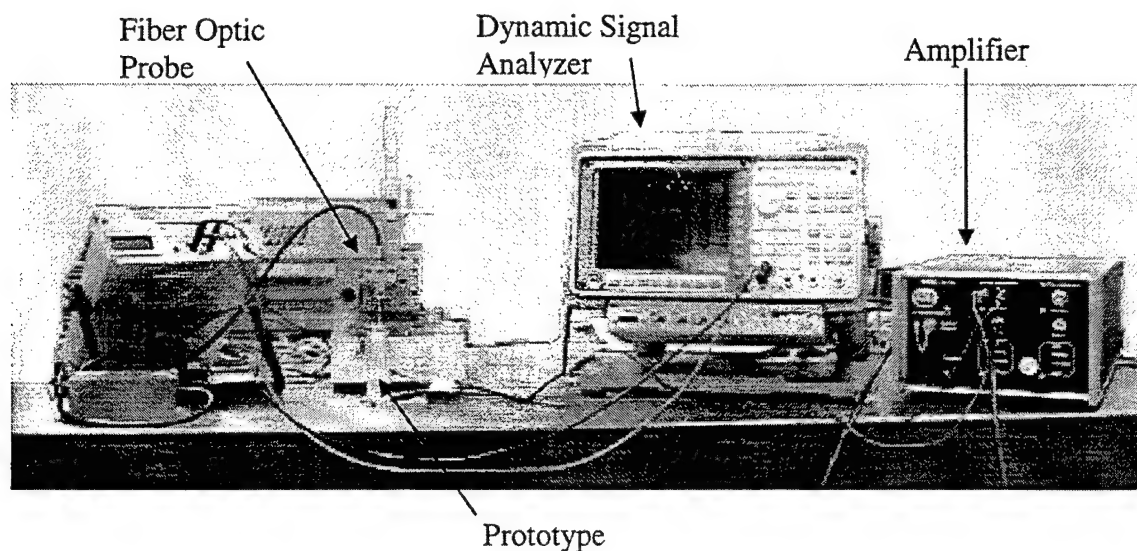**Figure 21: Deflection-Voltage results**

Figure 22: Dynamic performance experimental test apparatus

amplitude and phase of the free end of the actuator was measured using Philtec model A88NE1 fiber optic probe fed back to the dynamic signal analyzer, which processed the deflection data.

Figure 23 contains the experimental and analytical frequency-amplitude and phase response. The model predicts the low frequency behavior accurately with an average error from 100 to 1000 Hz of 1.4% for the amplitude. At these frequencies, the amplitude of the deflection of the free end of the actuator is very close to that of the static solution. The low error is expected because the properties of the material are well known (specifically the d_{31}) and many of the simplifying assumptions will not manifest themselves in the form of error at such low frequencies. As shown in Table 3, the first and second natural frequencies are slightly lower than those predicted analytically, 6.3% and 6.4%, respectively. Additionally, the observed peak amplitude at the natural frequencies is lower than the predicted values, 9.2% lower at the first natural frequency and 3.3% lower at the second natural frequency. Both effects could be the result of neglecting the epoxy layers used to bond the shells to the end caps because it introduces compliance and damping into the stiffer ceramic structure.

In examining the amplitude data, there appears to be a small peak near 10,000 Hz. However, since the phase data does not identify this as a natural frequency, it is most likely due to some

Table 3: Experimental and theoretical natural frequencies

Mode	Experimental Natural Frequency (Hz)	Natural Frequency (Hz)	Percent Error (%)
1	3500	3722	6.3
2	8720	9282	6.4
3	16330	14781	-9.5

Mode	Experimental Peak Value (µm)	Peak Value (µm)	Percent Error (%)
1	17.4	19.0	9.2
2	6.1	6.3	3.3
3	2.1	1.9	-9.5

factor other than resonance in the axial direction; for example, it may be an excited radial mode causing a disturbance in the transducer. Near the third natural frequency, the experimental phase data becomes very noisy, which may be due to a mounting unable to handle such high frequency vibrations without affecting the prototype. However, since the peak attributed to the third natural frequency in the analytical model matched reasonably well with the peak in the experimental data (they differed by 9.5%), it was assumed that this was indeed the third natural frequency.
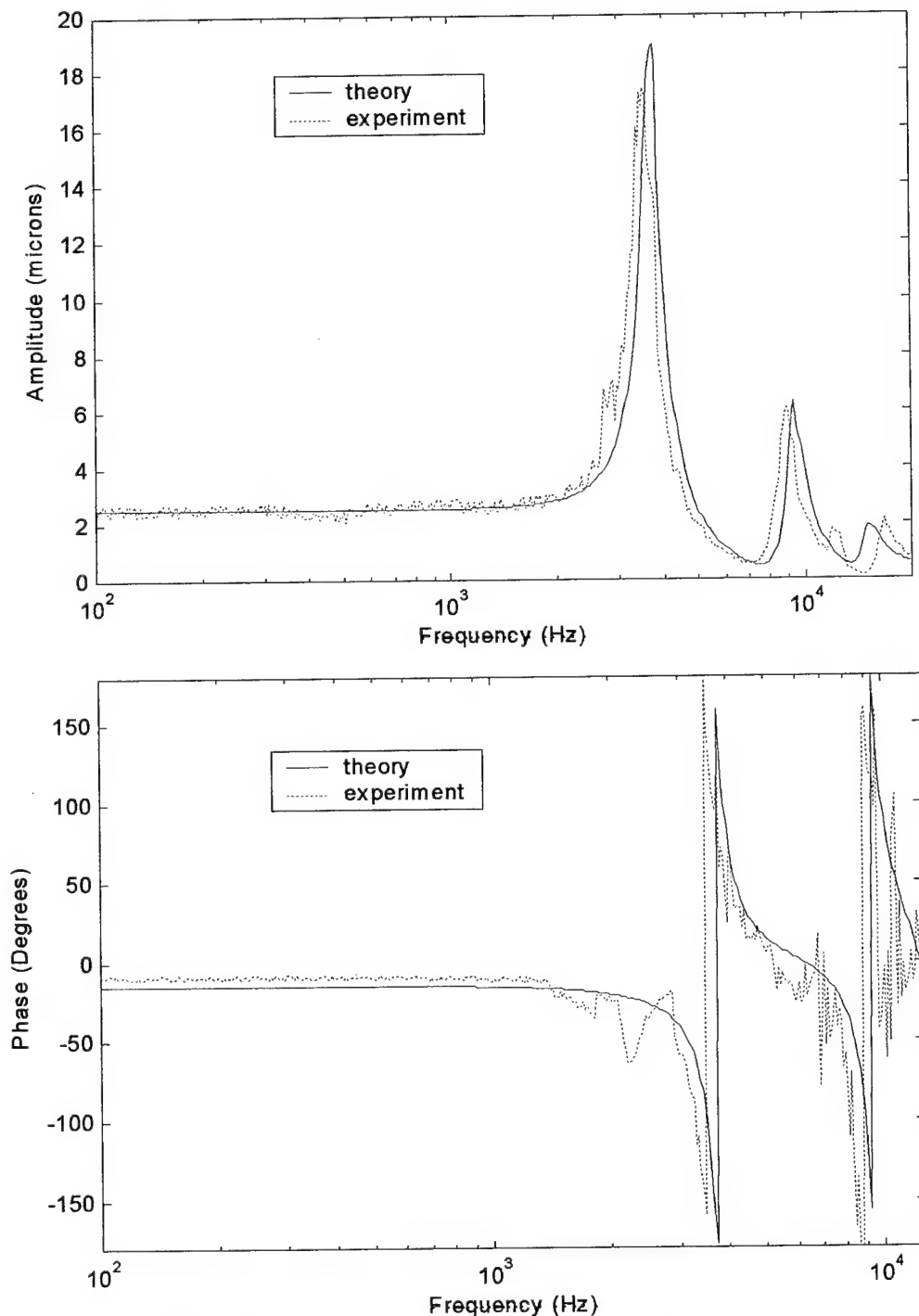
Figure 23: Experimental and theoretical dynamic performance at 50 V

6. PERFORMANCE ANALYSIS AND EVALUATION

The final task built upon the findings from the others to identify and understand the sensitivity of the performance to different architectural design parameters, manufacturing tolerancing, and practical considerations such as bonding layer effects and other parasitic losses not completely captured by the models.

6.1. DESIGN PARAMETER SENSITIVITY ANALYSIS

Loss mechanisms of the telescopic actuator due to architectural, manufacturing tolerance, and material considerations were investigated using the validated analytical models. Architecturally, as the number of shells is increased for a fixed actuator volume, the cross sectional area, and thus the force capabilities are decreased. Also, from a practical manufacturing standpoint, there must be a finite gap between the shells when fabricated. This is potential active actuation volume being sacrificed, which also decreases the force and work output. Material properties come into play in the telescopic design when the mode of actuation of the piezoceramic is considered, d_{33} versus d_{31}. Thus, to evaluate the telescopic actuator architecture, the sensitivity of the deflection, force, and work of the telescopic actuator was studied with respect to the length of the radial gap between the shells and number of shells, as well as similar effects due to activation mode – d_{31} or d_{33}. In addition to the assumptions made for the model derivation, the following assumptions were made:

- The actuator shells are all assumed to be circular cylinders.
- All of the n cylinders in the telescopic actuator have the same length, L^s, and wall thickness, t^s.
- The end caps in the telescopic actuator have the same thickness, t^c, and are assumed to be perfectly rigid.
- The ratio of the piezoelectric strain coefficients d_{31} to d_{33} is 0.44.
- The ratio of the material compliances s_{33} to s_{11} is 1.22.
- The thickness of the end caps accounts for 5% of the total actuator length.
- Bonding layer effects were negligible.

For the purposes of this sensitivity study, the quasi-static performance of the telescopic architecture was normalized with respect to an ideal circular stack actuated in the d_{33} mode and exhibiting no losses that are typically present in actual devices of this nature. Both the telescopic and the baseline actuators are made out of the same piezoelectric material, were driven at the same electric field, E, and were of the same overall length, L, and outer radius, r_o (Figure 24). Comparison ratios were then formulated for the free deflection, Δ^T, blocking force, F^T, and work, W^T, of the telescopic actuator by normalizing these values with respect to the free deflection, Δ^P, blocking force, F^P, and work, W^P, of a baseline actuator. To facilitate the derivation of these performance factors, each is written in terms of the actuator gap parameter, α, which is defined as the percentage of the ideal tube thickness (r_o/n) that is set aside for the inter-tube gap.

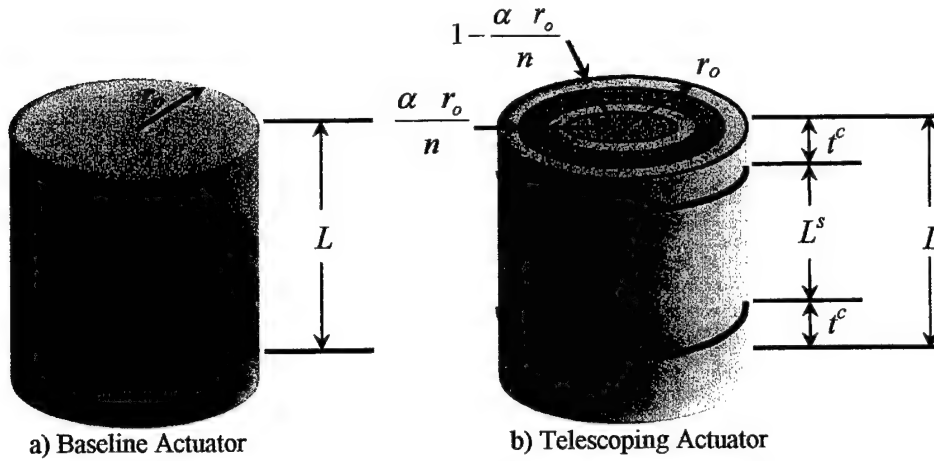a) Baseline Actuator   b) Telescoping Actuator

Figure 24: Sensitivity study parameters

The first of these comparison ratios relates the deflection of the telescopic actuator to that of the baseline actuator. This deflection amplification factor, Ω, is the factor by which the free deflection of an actuator is amplified when compared to that of a comparable idealized stack. For an n-cylinder telescopic architecture, the factor is:

$$\Omega = \frac{\Delta^T}{\Delta^P} = \frac{nd_{3j}\left(L - 2t^c\right)}{d_{33}L} \tag{11}$$

The subscript j in these equations denotes the mode of activation for the telescopic actuator, with 3 corresponding to the d_{33} mode and 1 corresponding to the d_{31} mode.

The amplification of displacement comes at a cost to the actuation force. To quantify these losses, the force reduction factor, Ψ, was derived. For the telescopic actuator, the ratio between its force and that of the idealized stack is:

$$\Psi = \frac{F^T}{F^P} = \frac{d_{3j}s_{33}\left(1 - \alpha\right)}{d_{33}s_{jj}n\displaystyle\sum_{i=1}^{n}\frac{1}{2i - 1 + \alpha}} \tag{12}$$

For ideal actuation architectures, the force reduction and deflection amplification would negate each other, resulting in the same amount of actuator work as the idealized case. In reality, there are transmission and packaging losses inherent to any architecture, reducing actuator work. The work efficiency factor, Φ, is the ratio of the work output of an actuator to that of an equivalent, idealized stack. This equation reduces to the following for the telescopic architecture:

$$\Phi = \Omega\Psi = \frac{W^T}{W^P} = \frac{\Delta^T}{\Delta^P}\frac{F^T}{F^P} = \frac{d_{3j}^2 s_{33}\left(1 - \alpha\right)\left(L - 2t^c\right)}{d_{33}^2 s_{jj}L\displaystyle\sum_{i=1}^{n}\frac{1}{2i - 1 + \alpha}} \tag{13}$$

This can also be viewed in terms of work loss by defining a work loss factor, Θ, for a given architecture as one minus the work efficiency factor. For the telescopic actuator this is:

$$\Theta = 1 - \Phi = 1 - \frac{d_{3j}^2 s_{33}(1-\alpha)(L-2t^c)}{d_{33}^2 s_{jj} L \sum_{i=1}^{n} \frac{1}{2i-1+\alpha}} \tag{14}$$

Assuming a cylindrical actuator, Figure 25 depicts the plots of these comparison factors for a d_{31} architecture in terms of the number of actuation shells, n, and a range of gap parameters, α. As seen in Figure 25a, the deflection amplification factor increases linearly as the number of cylinders, n, increases and is independent of the size of the gap between the shells. The deflection amplification ratio dips below unity because of the inferiority of the d_{31} coefficient compared to the d_{33} coefficient of the ideal stack. Thus, a couple of cylinders are needed to make this architecture viable in the d_{31} mode. The force reduction factor decreases inversely with additional actuator shells. This behavior is due to the fact that, in this comparison, only a set amount of cross-sectional surface area is available and it must be divided equally among all of the actuator shells. Additional shells mean a reduction in individual tube surface area, which is directly related to the force generated, accounting for the drop in actuator blocking force. This is the most substantial loss mechanism. The force also decreases slightly with increasing gap size (Figure 25b), due again to loss in area, but this loss is not as significant as that attributed to the number of actuator cylinders. The work efficiency factor also decreases nonlinearly with increasing actuation tubes, and decreases with increasing gap size as shown in Figure 25c, and the work loss factor behaves in a converse manner, illustrated in Figure 25d.

When comparing the d_{31} telescopic architecture to an ideal stack, the performance is obviously limited by the lower piezoelectric coefficient than that of the d_{33} mode. Because of the telescopic architecture's versatility, an actuator can also be constructed to utilize the d_{33} mode of actuation. Figure 26 displays the derived performance factors (Equations 11-14) for both the d_{31} and d_{33} telescopic actuator versus the number of actuation tubes. The linear deflection amplification factor (Figure 26a) effectively displays the jump in actuator performance because of the change in actuation mode. Note that for the d_{33} mode of actuation, the displacement is either equivalent to the idealized stack ($n = 1$) or is amplified. Assuming a 30% loss in cylinder stiffness due to bonding layers in the d_{33} telescopic actuator, Figure 26b shows the force reduction factor of the telescopic actuators. In addition to the improved material performance and because the d_{33} actuator is activated by generating a field in the axial direction, it is possible to use cylinders with differing wall thickness. Therefore, the actuator can also be constructed so that each cylinder has the same cross-sectional area (and thus the same stiffness) versus the constant thickness requirement of the d_{31} mode. While the constant area versus constant thickness does not have much impact on the displacement of the actuator, the force and work can be significantly improved by the constant area design. As seen in Figures 26c and 26d, the work factors are constant for the d_{33} constant area actuator and are as high as theoretically possible given the assumed loss mechanisms. Naturally, there will still be a reduction in work due to increasing gap size, stemming from the fact that any gap present in the actuator volume is wasted
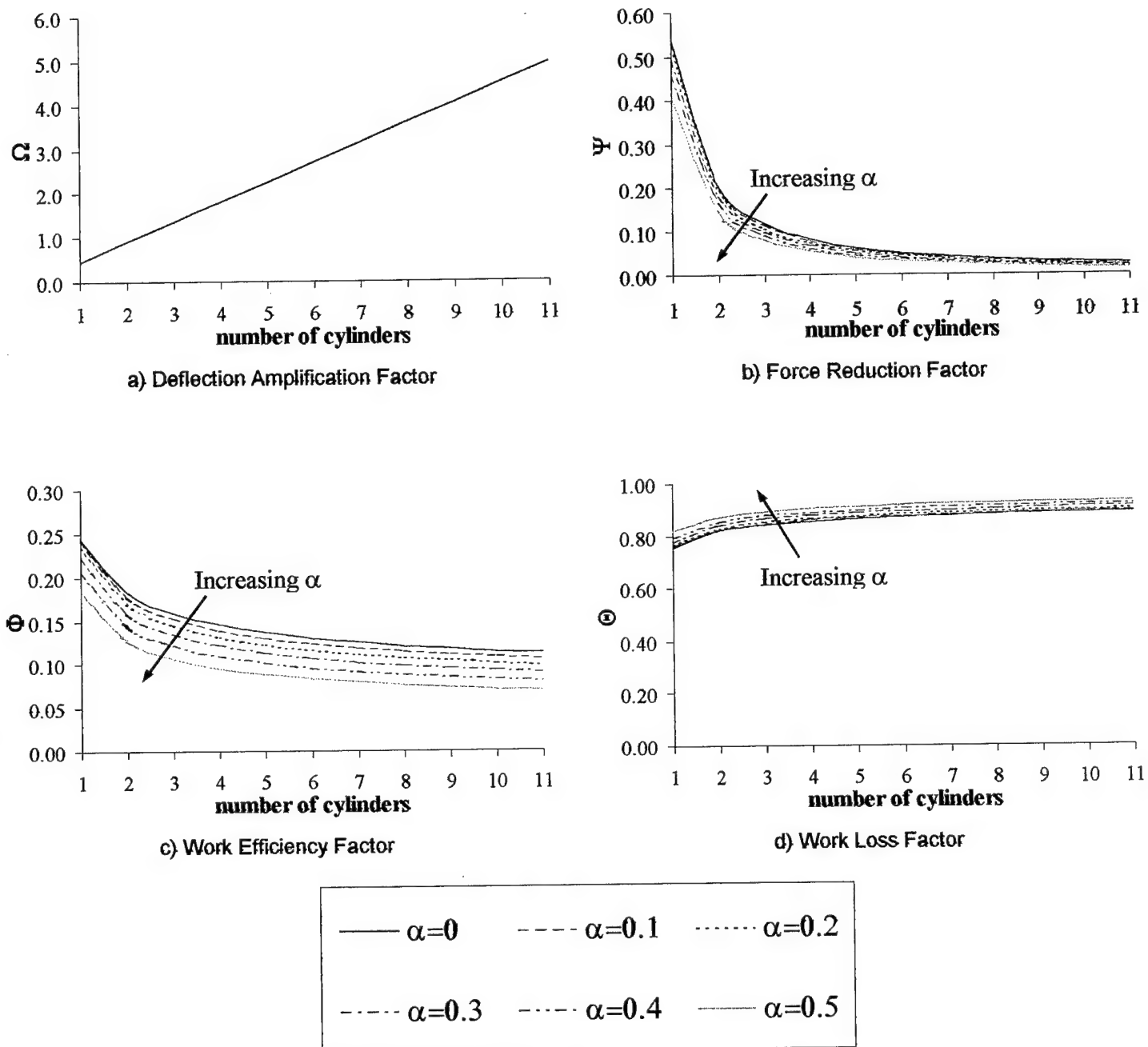
Figure 25: Comparison factors for d_{31} telescopic actuators

when compared to the baseline stack where the entire actuator volume is contributing to the actuator's performance. But this is inherent to the architecture and is present in either a d_{31} or d_{33} mode actuator. Therefore, a d_{33} mode actuator is preferable to a comparable d_{31} actuator. The improved performance of the d_{33} mode actuator can be broken down into two basic facets: the additional strain available in this mode of actuation and the freedom to design actuator tubes of varying and larger cross-sections. It should be noted that the d_{33} mode actuator is more complicated to manufacture, which may lead to increased cost and losses due to bonding layers.

a) Deflection Amplification Factor

b) Force Reduction Factor

c) Work Efficiency Factor

d) Work Loss Factor

——— d31 constant thickness
········· d33 constant thickness
– – – – d33 constant area
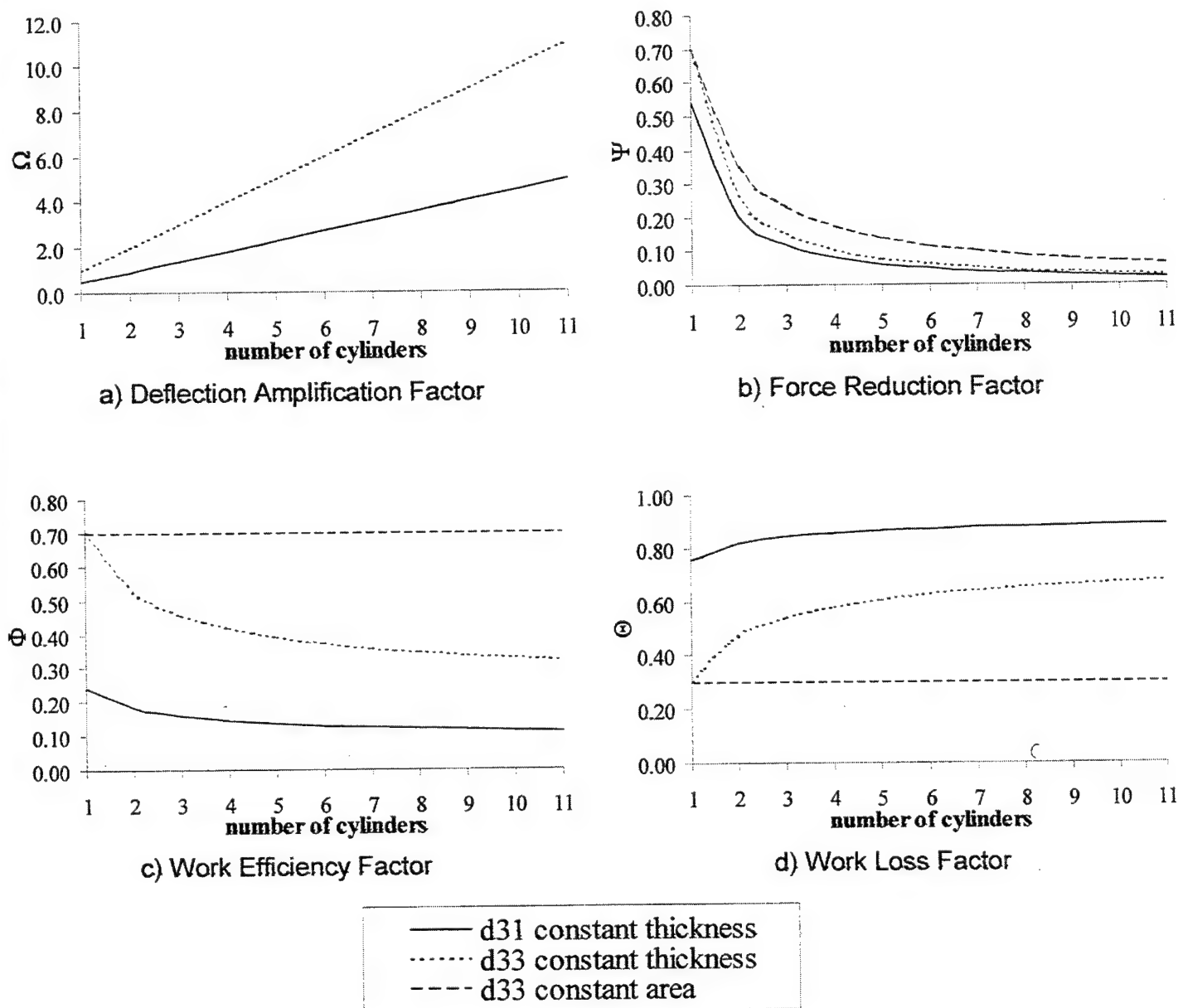
Figure 26: d_{31} versus d_{33} telescopic actuator architectures

If these factors are significant, the d_{31} mode of actuation may be competitive because of its simplicity.

6.2.   END CAP THICKNESS EFFECTS

In the previous study, the governing equations (Equations 11-14), were analyzed with respect to the geometric gap parameter α, the architectural parameter, n and the material parameters – d and s. Of the two remaining parameters, the relationship with L is straight forward with the displacement and work increasing and the end cap effects being reduced. The last parameter, the end cap thickness was assumed to be perfectly rigid; however, from the
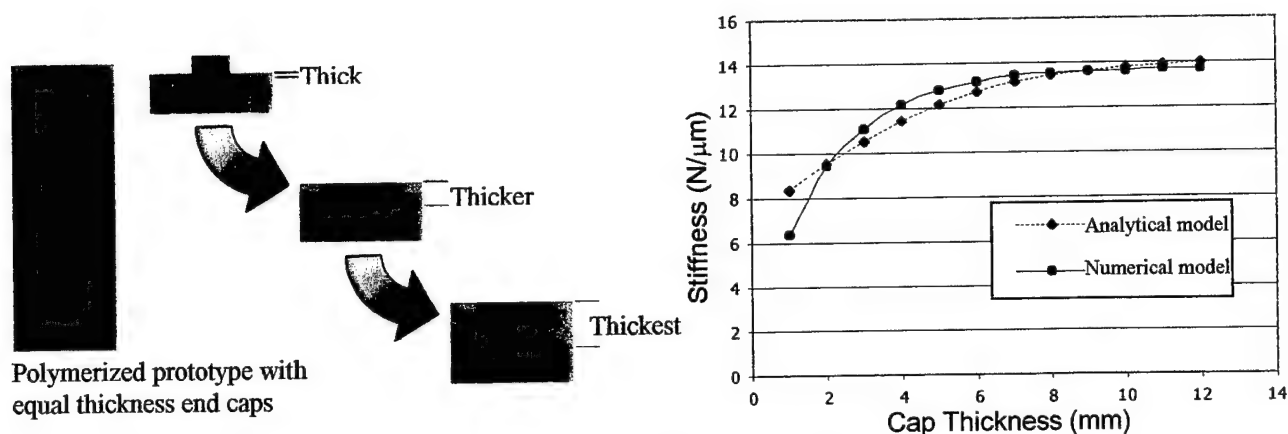
Figure 27: End cap thickness effects on stiffness modeling

experimental results it is know this is not a reasonable assumption. Thus, further investigation was conducted and it was discovered that the thickness of the end caps displays an unexpected effect on actuator stiffness. For example, Figure 27 gives the predicted actuator stiffness of the polymerized prototype while varying end cap thickness. There is a range of end cap thickness where the numerical model gives a higher theoretical stiffness than the revised analytical model, and other thickness ranges where the converse is true, with the two curves crossing each other at the 2 mm and 9 mm end cap thicknesses. This is due to the fundamentally different ways that the end caps are modeled; where the numerical model simply regards them as just another piece of the three-dimensional telescopic structure and the analytical model includes them as spring terms. The polymerized actuator's end caps are moderately thick, thus falling into the middle range where the revised analytical model is most conservative. The other two prototypes, with thinner end caps, come into the range where the numerical model becomes much more conservative, falling into the left most region for their particular geometries. From these results, it is clear that the performance of the actuator is sensitive to the thickness of the end caps and the best model will depend on which region the thickness falls.

6.3. BONDING LAYER EFFECTS

Another parameter that has impact on the performance that was not originally accounted for in the models and sensitivity analysis was the bonding layer. Initial experiments identified and the numerical modeling effort clarified that bonding layers play a key role. There are two places where bonding layers can be introduced – at the end caps or at the base in mounting. A detailed investigation into the mechanics of the bonding layers showed that accounting for three-dimensional shearing, bending, and twisting of these layers within a telescopic actuator effects primarily the predicted actuator stiffness. Figure 28 displays how the stiffness of the conventionally assembled actuator varies as the thickness of the base bonding layer and the internal end cap bonding layers increase in the final analytical and numerical models. There is little difference between the two models where the base bonding layer is concerned, each linearly reducing the actuator stiffness but not to an extreme degree. A much more pronounced effect is exhibited by the internal end cap bonding layer thickness, with actuator stiffness declining more drastically and nonlinearly as it is increased. Because of the numerical model's three-dimensional nature, it captures better the true behavior of the bonding layers as opposed to the revised analytical model which only accounts for axial deformations. These differences can
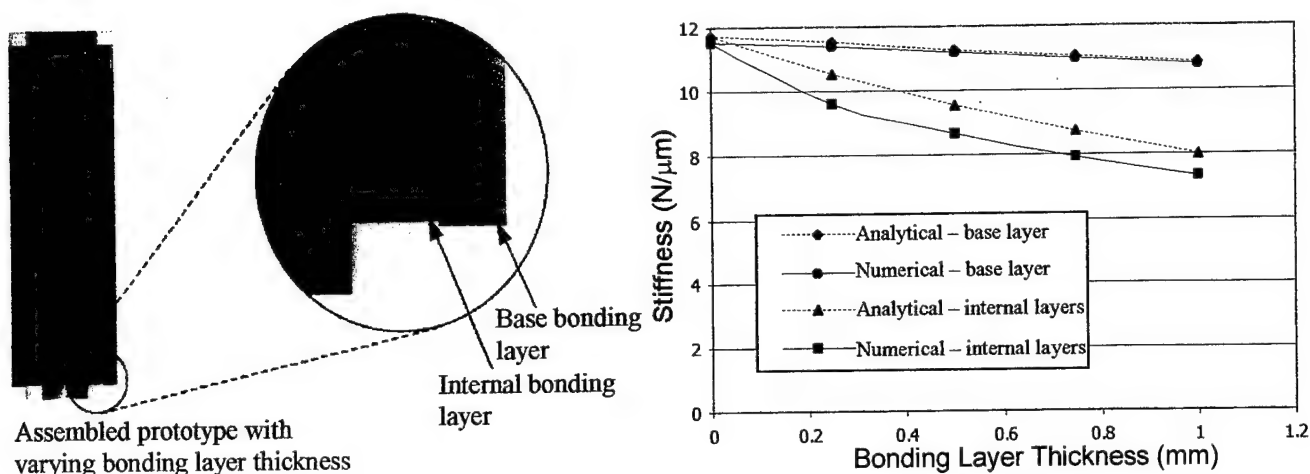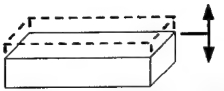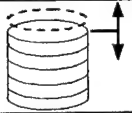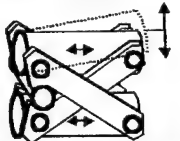
Figure 28: Bonding layer thickness effects on stiffness modeling

amount to a 9.3% change in predicted actuator stiffness due to 1 mm thick internal bonding layers. Thus, the numerical model is more accurate for the modeling of assembled actuators with multiple internal bonding layers, but such factors are not critical to monolithic actuators and either model is good.

6.4. ACTUATOR ARCHITECTURE COMPARISON
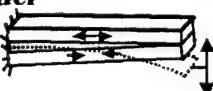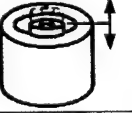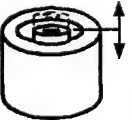
The comparison ratios derived in the sensitivity analysis were also used to compare the telescopic actuator architecture to other piezoelectric actuator architectures.[33] The displacement, force, and/or work for a variety of commonly used piezoelectric actuator architectures were collected from research literature and were normalized as in the previous section by an idealized d_{33} stack of the same material and package volume. The resulting comparison ratios are given in Table 4. This is by no means an exhaustive comparison of all piezoelectric actuation options, but does give insight into what application niche the telescopic architecture falls. The values given for the d_{31} and d_{33} telescopic actuators reflect an assumption of a 15% loss in actuator force due to compliant end caps. As Table 4 shows, the telescopic architecture yields displacement amplification similar to actuators such as leveraged stacks, moonies, and c-blocks. While the displacement maybe slightly lacking, this architecture does excel at its designed purpose, output force. As evidenced by the force reduction factors in Table 4, only the solid plates and stack actuator out perform the telescopic architecture. Both of the work comparison factors calculated for the telescopic exceed or are on par with other actuation architectures; however, none of the other actuation amplification architectures generate the same order of magnitude of force coupled with the deflection amplification. This validates the potential of this design to fill a certain actuation application niche. The niche includes applications that require a similar magnitude of force as a stack provides, and 1 to 20 times the deflection. Examples include active mounts, fuel injectors or active rotor blades.

Table 4: Comparison of actuator architectures

ARCHITECTURE	DISPLACEMENT AMPLIFICATION FACTOR	FORCE REDUCTION FACTOR	WORK EFFICIENCY FACTOR	WORK LOSS FACTOR
d_{33} Plate[34]	1.0	1.0	1.0	0.0
Stack[35]	1.0	0.70	0.70	0.30
Leveraged Stack[35]	2 to 80	1.6e-3 to 6.3e-2	0.126	0.82
IDE Material[36]	0.44	0.54	0.24	0.76
d_{31} Plate[34]	0.44	0.54	0.24	0.76
Moonie/Cymbal[37-39]	4 to 60	1.6e-3 to 2.4 e -2	0.067	0.991
C-Block[40]	4 to 67	2.2e-3 to 3.6e-2	0.15	0.85
Rainbow/ THUNDER[41,42]	7 to 1800	1.7e-5 to 4.4e-3	0.024	0.97
Bimorph Bender[42,43]	33 to 7400	1.8e-5 to 2.6e-3	0.13	0.87
Recurve[33]	33 to 7400	1.8e-5 to 2.6e-3	0.13	0.87
d_{33} Telescopic	1 to 20	2.8e-2 to 0.6	0.40	0.60
d_{31} Telescopic	1 to 20	1.9e-2 to 0.17	0.15	0.85

7. CONCLUSIONS

This research effort successfully demonstrated a family of d_{31} piezoceramic actuators ranging in size from the submillimeter scale, for embedment in composite structures, to discrete actuators up to the centimeter scale, that provide modest stroke amplification (2 to 15 times) in a compact package with minimal force reduction. This research consisted of the four specific tasks: 1) Manufacturing development and process modeling, 2) Actuator performance modeling, 3) Experimental component testing and 4) Performance analysis and evaluation.

In the manufacturing development and process modeling, several different fabrication techniques where investigated: acrylate polymerication, injection molding, conventional assembly, and microfabrication by coextrusion process. All of the techniques developed produced quality piezoceramic parts with high densities and piezoelectric properties. The injection molding was found to be best suited to producing complex structures of moderate height (about a centimeter) in large volumes where cost is a factor. Acrylate polymerization is better for fabricating tall structures (many centimeters) in smaller quantities and, when coupled with SLA molds, is ideal for rapid prototyping of complex ceramics. While telescopic actuators can be assembled from off-the-shelf components, it was found that the bonding layers present a substantial loss mechanism significantly decreasing the performance output in comparison to the monolithic structures. In addition to these mesoscale fabrication techniques, microfabrication via coextrusion was also developed. While it is not possible to fabricate "spaghetti-like" telescopic actuators because of the out of plane end caps, it is possible to fabricate very long hollow fibers. It was demonstrated that these fibers, without any appreciable loss in reliability, can reduce the voltage requirements as much as 10 times with respect to solid fibers in interdigated electroded active fiber composites and they can be embedded within conductive matrices which is not possible with solid fibers.

Models, both analytical and numerical, were developed to predict the quasi-static and dynamic performance of the telescopic architecture. These models were refined to a degree where the predictions correlated to physical actuator performance within 10% for a majority of cases, and often significantly less. Necessary refinements included accounting for the complex deformations of the architecture's end caps and loss mechanisms such as bonding layers. Numerically modeling the stresses within the telescopic architecture further validated the technology, showing that under blocked conditions actuators will experience less than 60% of the material tensile strength, ensuring a low occurrence of device failure in service. These models can be used as telescopic behavioral predictors as well as synthesis tools for efficiently designing telescopic actuators for a wide range of high force-moderate displacement applications.

The experimental analysis of the various telescopic prototypes validated the impetus of their design. The deflection experiments confirmed the prediction by the models that the stroke of the actuator is just the linear summation of the individual shells. Thus, the number of shells utilized can proportionally reduce the overall height of the actuator. While there is a sacrifice in the force when compared to a stack of equivalent size, the forces still remain high, over 350 N for some prototypes. These are very stiff actuators with a high bandwidth, the 1st natural frequencies of 3500 Hz. These results successfully demonstrate that telescopic actuators can provide a

compact actuator that provides 2 to 15 times more stroke than a stack of equivalent volume while maintaining high force and excellent dynamic response.

Through the characterization of this architecture, the primary design parameters, both ideal and pragmatic, have been identified which govern the quality of the telescopic actuator's performance. End cap material and thickness play a definitive role in the actuator's forcing capabilities nonlinearly reducing actuator stiffness by up to 50% for extreme cases, as well as dictate certain modeling criteria for the actuator. Bonding layers were found to be a significant loss mechanism in the architecture, with base bonding layers playing a less significant role than internal bonding layers giving stiffness reductions of up to 8% versus 30% respectively. The actuator tube thickness also affects actuation abilities, calling for uniform shell cross-sectional areas for optimized performance. This can be achieved via a d_{33} versus d_{31} modes of telescopic actuator studied in this investigation. The d_{33} actuators outperform d_{31} designs in deflection, force, and work capabilities, with constant shell cross-section d_{33} actuators approaching the theoretical maximum. No matter which mode is chosen, because of manufacturing considerations there must be a gap between the shells and this gap reduces deflection, force and thus work. Therefore, good manufacturing techniques that can minimize this gap are essential.

Most of the loss mechanisms can be mitigated through careful design and manufacturing utilizing the tools developed in this research. In the evaluation of this architecture with respect to the current state of art, it was found that only solid plates and stack actuators out perform the telescopic architecture from a work perspective. However, solid plates and stacks cannot provide the same level of displacement output with telescopic actuators providing up to 20 times more. Thus, they are better positioned for many applications where stacks and plates fall short – such as active mounts, fuel injectors, precision shape control for optics, etc. Thus, there is a significant niche for this new family of actuators and this research established the necessary foundation – fabrication methods, predictive performance models and experimental procedures.

8. REFERENCES

1. Paine, J.S.N. and Chaudhry, Z., 1996, "The impact of amplification on efficiency and energy density of induced strain actuators", *Proc. of the ASME Aerospace Division*, **52**, pp. 511-516.
2. Bridger, K., Jones, L., Poppe, F., Brown, S.A., and Winzer, S.R., 1996 "High-Force Cofired Multilayer Actuators," *Smart Structures and Materials: Industrial and Commercial Applications of Smart Structures Technologies*, San Diego, CA, pp. 341-352.
3. Haertling, G.H., 1994, "Rainbow Ceramics – A New Type of Ultra-High Displacement Actuator," *American Ceramic Society Bulletin*, **73**, pp. 93-96.
4. Shakeri, C., Bordonaro, C.M., Noori, N.M., and Champagne, R., 1999, "Experimental study of THUNDER: A New Generation of Piezoelectric Actuators," *Proc. of the Smart Structures and Materials Conference*, Newport Beach, CA, pp. 63-71.
5. Wu, C.C.M., Kahn, M., and Moy, W., 1996, "Piezoelectric Ceramics with Functional Gradients: A New Application in Material Design," *Journal of the American Ceramic Society*, **79**, pp. 809-812.
6. Zhu, X., Wang, Q., and Meng, Z., 1995, "Functionally Gradient Piezoelectric Actuator Prepared by Powder Metallurgical Prosess in PNN-PZ-PT System," *Journal of Materials Science Letters*, **14**, pp. 516-518.
7. Panda, R.K., Kholkin, A.L., and Safari, A., 1998, "Design and Fabrication of Volume Fraction Gradient Piezoelectric Composites for Medical Imaging Applications," *Proceeding of the 11th IEEE International Symposium on Applications of Ferroelectrics*, Montreaux, Switz., pp. 265-268.
8. Safari, A. and Danforth, S.C., 1998, "Development of Novel Piezoelectric Ceramics and Composites for Sensors and Sctuators by Solid Freeform Fabrication," *Proc. of the 11th IEEE International Symposium on Applications of Ferroelectrics*, Montreaux, Switz., pp. 229-234.
9. Bowen, L. and French, K., 1992, "Fabrication of Piezoelectric Ceramic/Polymer Composites by Injection Molding," *Proc. of the 8th IEEE International Symposium on Application of Ferroelectrics*, Greenville, SC, pp. 160-164.
10. Crumm, A.T. and Halloran J.W., 1998, "Fabrication of Microconfigured Multicomponent Ceramics," *Journal of the American Ceramic Society*, **81**, pp. 1053-1057.
11. Miao, W. 2000, Fabrication of Lead Zirconate Titanate Actuator by Suspension Polymerization Casting, PhD dissertation, University of Michigan.
12. Reilly, C.J., 2001, Novel Electroactive Ceramic Architectures by Indirect Solid Freeform Fabrication, PhD dissertation, University of Michigan.
13. Gentilman, R.L., Fiore, D.F., Pham, H.T., French, K.W., and Bowen, L.J., 1994, "Fabrication and Properties of 1-3 PZT-polymer composites," *Ceramic Transactions*, **43**, pp. 239-247.
14. Crumm, A.T., 2000, *Microfabrication by Coextrusion*, 2000, PhD dissertation, University of Michigan.
15. Venkataswamy, K., Waack, R., Novich, B.E., and Halloran, J.W., 1990, "Forming Whisker Reinforced Sintered Ceramics with Polymerizable Binder Precursors," U. S. Pat., 4978643.
16. Chu, G.T-M, Brady, G.A., Miao, W., Halloran, J.W., Hollister, S.J., and Brei, D., 1999, "Ceramic SFF by Direct and Indirect Stereolithography," *Solid Freeform and Additive Fabrication*, D. Dimos, S. C. Danforth, and M. J. Cima – Editors, **542**, MRS Symposium Proceedings, pp. 119-123.
17. Omatete, O.O., Janney, M.A., and Strehlow, R.A., 1991, "Gelcasting-A New Ceramic Forming Process," *Ceramics Bulletin*, **70**, pp. 1642-1649.

18. Janney, M.A., Omatete, O.O., Walls, C.A., Nunn, S.D., Ogle, R.J., and Westmoreland, G., 1998, "Development of Low-Toxicity Gelcasting Systems," *Journal of the American Ceramic Society*, **81**, pp. 581-91.

19. Reed, J.S., 1988, "Critical Issues and Future Directions in Powder Forming Processes," *Ceramic Transactions: Ceramic Powder Science IIB*, **1**, pp. 601-610.

20. Bent, A.A., Hagood, N.W., and Rodgers, John P., 1995, "Anisotropic actuation with piezoelectric fiber composites", *Journal of Intelligent Material Systems and Structures*, **6** [3], pp. 338-349.

21. Rodgers, J.P., Hagood, N.W., and Weems, D.B., 1997, "Design and manufacture of an integral twist-actuated rotor blade", *38th AIAA/ ASME/ASCE/AHS/ASC Structures, Structural Dynamics, and Materials Conference*, AIAA Paper No. 97-1264.

22. Wilkie, W.K., Bryant, R. G., High, J. W. Fox, R. L., Hellbaum, R. F., Jalink, A. Jr., Little, B. D., and Mirick, P. H., 2000, "Low-cost piezocomposite actuator for structural control applications", *Proceedings of SPIE - The International Society for Optical Engineering*, **399**, Bellingham, WA, USA, pp. 323-334.

23. Maclean, B.J. and Jacobsen, S.C., 1995-96, "Active Fibers for Development of Adaptive Structures", *ARPA Actuator Issues Workshop*.

24. Fernandez, J.F., Dogan, A., Zhang, Q.M., Tressler, J.F., and Newnham, R.E., 1995, "Hollow piezoelectric composites", *Sensors and Actuators, A: Physical*, **51** [2-3], pp. 183-192.

25. Zhang, Q., Wang, H., and Cross, L.E., 1993, "Piezoelectric tubes and tubular composites for actuator and sensor applications", *Journal of Materials Science*, **28** [14], pp. 3962-3968.

26. Cannon, B.J. and Brei, D., 2001, "Piezoceramic hollow fiber active composites", accepted in the *AIAA Journal*.

27. Cannon, B.J., 2001, *Piezoceramic Hollow Fiber Active Composites*, PhD dissertation, University of Michigan.

28. Brei, D., Berner, N.T., and Alexander, P.W., 2001, "Modeling and study of the quasi-static behavior of piezoceramic telescopic actuation architectures", accepted in the *Journal of Intelligent Materials Systems and Structures*.

29. Alexander, P.W. and Brei, D., 2001, "Experimental characterization and model validation of the quasi-static performance of piezoceramic telescopic actuators", submitted to *Smart Materials and Structures*.

30. Timoshenko, S. and Woinowsky-Krieger, 1959, *Theory of Plates and Shells*, McGraw-Hill, New York, pp. 5,52.

31. Pestel, E. and Leckie, F. A., 1963, *Matrix Methods in Elastomechanics*, McGraw-Hill, New York.

32. Meirovitch, L., 1967, *Analytical Methods in Vibration*, Macmillan, New York.

33. Ervin, J., 1999, Design, Characterization, and Assessment of the Recurve Actuation Architecture, PhD dissertation, University of Michigan.

34. EDO Corporation, 1996, *Piezoelectric Ceramics: Material Specifications, Typical Applications* [brochure], available from EDO Corporation, 2645 South 300 West, Salt Lake City, UT.

35. Prechtl, E.F., and Hall, S. R., 1999, "Design of a high efficiency, large stroke, elecromechanical actuator," *Smart Materials and Structures*, **8**, pp. 13-30.

36. Bent, A. A., and Hagood, N. W., 1997, "Piezoelectric fiber composites with interdigitated electrodes," *Journal of Intelligent Material Systems and Structures*, **8**, pp.903-919.

37. Sugawara, Y., Onitsuka, K., Yoshikawa, S., Xu, Q. C., Newnham, R. E., and Uchino, K., 1992, "Metal-ceramic composite actuators," *Journal of the American Ceramic Society*, **75**, pp. 996-998.

38. Onitsuka, K., Dogan, A., Tressler, J. F., Xu, Q., Yoshikawa, S., and Newnham, R. E., 1995, "Metal-ceramic composite transducer, the 'moonie'," *Journal of Intelligent Material Systems and Structures*, **6**, pp. 447-455.

39. Dogan, A., Uchino, K., and Newnham, R. E., 1997, "Composite piezoelectric transducer with truncated conical endcaps 'cymbal,'" *IEEE Transactions on Ultrasonics, Ferroelectrics, and Frequency Control*, **44**, pp. 597-605.

40. Moskalik, A. J., and Brei, D., 1998, "Parametric investigation of the deflection performance of serial piezoelectric C-block actuators," *Journal of Intelligent Material Systems and Structures*, **9**, pp. 223-231.

41. Wise, S., 1997, "Displacement Properties of RAINBOW and THUNDER Piezoelectric Actuators," *Sensors and Actuators*, **A-69**, pp. 33-38.

42. Kugel, V. D., Chandran, S., and Cross, L. E., 1997, "Comparative analysis of piezoelectric bending-mode actuators," in *Smart Structures and Materials 1997: Smart Materials Technologies*, W. C. Simmons, I. A. Aksay, and D. R. Huston, Eds., Proc SPIE 3040, pp. 70-80.

43. Near, C. D., 1996, "Piezoelectric actuator technology," in *Smart Structures and Materials 1996: Smart Structures and Integrated Systems*, I. Chopra, Ed., Proc. SPIE 2717, pp. 246-258.

44. FACE International Corporation, 1996, "THUNDER, Thin-Layer Composite Unimorph Ferroelectric Driver and Sensor," 427 W. 35th St., Norfolk, VA.

45. Elissalde, C., and Cross, L. E., 1995, "Dynamic Characteristics of Rainbow Ceramics," *Journal of the American Ceramic Society*, **78**, pp. 2233-2236.

APPENDICIES

A. SCIENTIFIC PERSONNEL SUPPORTED

PhD
Kelly Bailo, PhD candidate in Mechanical Engineering
G. Allen Brady, PhD candidate in Materials Science and Engineering
Bryan Cannon, PhD in Mechanical Engineering, 2001
Aaron Crumm, PhD in Materials Science and Engineering, 2000
Weiguo Miao, PhD in Materials Science and Engineering, 2000
Andy Moskalik, PhD in Mechanical Engineering, 1998

Masters
Paul Alexander, MS in Mechanical Engineering, 1998
Neal Berner, MS in Mechanical Engineering, 1998
James Vendlinski, MS in Mechanical Engineering, 2001

Undergraduate
Benjamin Bulat, Undergraduate in Mechanical Engineering
Melissa Coletta, Undergraduate in Mechanical Engineering
Christopher Grimmer, Undergraduate in Mechanical Engineering
Simon Palko, Undergraduate in Mechanical Engineering
Steve Swisher, Undergraduate in Mechanical Engineering

B. Papers Published and Submitted Under DARPA/NRL Sponsorship

Ceramic SFF by Direct and Indirect Stereolithography, 1999, Gabriel T-M Chu, G. Allen Brady, Weiguo Miao, J. W. Halloran, Scott J. Hollister, and Diann Brei, *Solid Freeform and Additive Fabrication* , D. Dimos. S. C. Danforth, and M.J. Cima, Editors, MRS Symposium, Proceedings Vol. 542, pp. 119-123.

Fabrication and experimental characterization of d$_{31}$ telescopic piezoelectric actuators, 2001, Paul W. Alexander, Diann Brei, Weiguo Miao, John.W. Halloran, Richard L. Gentilman, Gerald E. Schmidt, Patrick T. McGuire, and John R. Hollenbeck, *Journal of Materials Science*, Vol. 36 No. 17, pp. 4231-4237.

Feasibility study of microfabrication by coextrusion (MFCX) hollow fibers for active composites, 2001, Brian J. Cannon and Diann Brei, *Journal of Intelligent Material Systems and Structures*, Vol. 11 No. 9, pp. 659-670.

Modeling and study of the quasi-static behavior of piezoceramic telescopic actuation architectures, 2001, Diann Brei, Neal T. Berner, and Paul W. Alexander, *Journal of Intelligent Materials Systems and Structures*, Vol. 12 No. 5, pp. 303-313.

Piezoceramic Hollow Fiber Active Composites, 2001, Brian J. Cannon and Diann Brei, accepted in the *Adaptive Structures – AIAA Conference*, April 2002, (AIAA 2002-1357).

Experimental characterization and model validation of the quasi-static performance of piezoceramic telescopic actuators, 2001, Paul W. Alexander and Diann Brei, to be submitted to *Smart Materials and Structures*, also in *Proceedings of Smart Structures and Materials 2001- Smart Structures and Integrated Systems*, Newport Beach, CA, USA, Vol. 4327, pp. 342-353.

Analytical dynamic performance modeling for telescopic actuators, 2002, James Vendlinski and Diann Brei, to be submitted.

Microfabrication by Coextrusion, 2000, Aaron Crumm, PhD dissertation, University of Michigan.

Fabrication of Lead Zirconate Titanate Actuator by Suspension Polymerization Casting, 2000, Weiguo Miao, PhD dissertation, University of Michigan.

Piezoceramic Hollow Fiber Active Composites, 2001, Bryan J. Cannon, PhD dissertation, University of Michigan.

Novel Electroactive Ceramic Architectures by Indirect Solid Freeform Fabrication, 2001, Christopher J. Reilly, PhD dissertation, University of Michigan.

CERAMIC SFF BY DIRECT AND INDIRECT STEREOLITHOGRAPHY

Gabriel T-M. Chu, G.Allen Brady, Weiguo Miao,John W. Halloran, Department of
Materials Science and Engineering, Scott J. Hollister, Departments of Biomedical
Engineering, Surgery and Mechanical Engineering, Diann Brei, Department of
Mechanical Engineering and Applied Mechanics, University of Michigan, Ann Arbor
USA

Abstract

Direct ceramic stereolithography (SLA) is done using UV-curable suspensions of
powders in acrylates in a conventional SLA machine. Hydroxyapatite prototypes for
bone tissue scaffolds are built from Image-Based Design files, featuring an interior
architecture of void passages. Complex alumina objects are built as digital sculptures.
Piezoelectric ceramic actuators from PZT, which are difficult to photocure, are built
using indirect stereolithography, where SLA-built epoxy molds are used to form a
thermal-cured suspension of PZT powders. We report on the thermal-curing behavior
of the suspensions, and the fundamentals of part building.

Introduction

Stereolithography, and other Solid Freeform Fabrication (SFF) methods, can be
used to directly fabricate ceramic green objects. We briefly outline our activities in
direct ceramic Stereolithography. However, these SFF techniques, including SLA, can
also be used to produce molds or rapid tools for more conventional ceramic fabrication.
We have done this by using SLA molds, which we discuss in this paper as "indirect"
ceramic Stereolithography.

Direct Ceramic Stereolithography

Direct ceramic stereolithography (SLA) is convenient for producing single
component ceramics of any arbitrary complexity (1-4). The ceramic SLA process is the
same as conventional SLA (5), but uses a photocurable ceramic suspension in place of
the resin. A typical ceramic SLA suspension contains 50 vol% ceramic powder
dispersed in a low-viscosity acrylate monomer system, with suitable photoinitiators.
Solutions of aqueous acrylamide monomers can also be used (3). An example of a
direct ceramic SLA object is shown in Figure 1, which is "Anja Test", a digital
sculpture by Michael Rees (6) built in our laboratory from aluminum oxide suspended
in hexane diol diacrylate. The SLA green body, consisting of alumina in cured
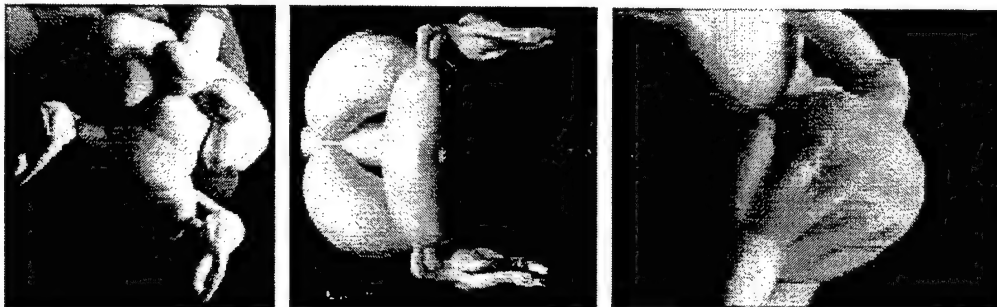polyacrylate binder, was sintered at 1650°C after slowly heating to burn off the binder.

Figure 1. Three views of Anja Test, by Michael Rees. A digital sculpture built on an
SLA 250 in an alumina-acrylate, after sintering. (by permission of the artist)

Direct ceramic SLA has two limitations: it is difficult to build high refractive
index ceramics and it is difficult to achieve features finer than 600 microns. The
former is related to the optical properties of concentrated suspensions. We find (7) that
the depth of cure achieved by the SLA laser is proportional to $1/\Delta n^2$, where Δn is the

difference of the refractive index of the medium (the monomer) and the ceramic particles. The 23 mW He-Cd laser of our SLA-250, we can easily achieve the required depth of cure (100-300 microns) with low-index ceramics such as silica, alumina, and hydroxyapatite. However, the refractive index of lead zirconate titanate (PZT) is too high, so we cannot accomplish direct SLA of PZT objects with our current laser.

Feature size is a second limitation of direct ceramic SLA. The minimum feature size is determined in the z-direction by the layer thickness and in the x-y direction by the width of the cured line. Scanning the SLA laser creates a "string" of cured resin. The SLA object is built from these strings, so the width of the string is a practical limit for feature size. The cured width depends on the spot size of the focused laser beam, and on the spreading of the UV radiation by side-scatter from the ceramic particles. Our SLA 250 has an 200 micron wide beam (Very fine focus lasers are commercially available.)

Indirect Ceramic Stereolithography

To overcome the limitation of refractive index and to build with finer features we use "indirect ceramic SLA". Indirect SLA uses a thermally-cured version of the acrylate suspension, with the photoinitiator system replaced with a thermal initiator system based on benzoyl peroxide. Figure 2 is a process schematic for indirect SLA. The suspension is prepared as with the direct SLA process. The SLA machine is used to fabricate a casting mold, into which the suspension is cast and thermally cured. The cured green ceramic can be removed from the SLA mold for "permanent mold" processing. For "lost mold" processing the SLA mold is thermally removed.

The suspension is cast into a mold defined by an SFF process. These can be multipart rapid molds made from epoxy by conventional SLA. We use these for large-scale PZT telescoping actuators (8). Alternately, silicon rubber soft molds can be made from SLA epoxy masters, into which PZT can be cast. This process faithfully reproduces very fine features in the mold. It has the same limitations as any permanent mold process, i.e., the object must be removable from the mold. Reentrant angles and complex interior architectures cannot be achieved.

For smaller scale objects, especially those with "unmoldable" interior features which cannot be achieved with permanent molds, we use a "lost mold" process. For example, lost molds can be made on the Sanders Model Maker from the red wax support material, into which the ceramic-acrylate can be directly cast (9). Most of our recent work has involved small objects with a complex very fine scale interior architecture, which we make with SLA epoxy lost molds.

Figure 3 shows a bone tissue engineering scaffold built from hydroxyapatite (HAp). It features an array of 420 micron channels, built to study the influence of channel architecture on the bone growth (10), for biomedical Image-Based Design research (11). Figure 3A shows the implant design and Figure 3B is the CAD file describing the internal channel architecture. This is an image of the epoxy lost mold. A 40 vol% suspension of HAp was prepared in a monomer system based on isobornyl acrylate and propoxylated neopentyl glycol acrylate. This suspension is cast into the lost mold and cured at 60°C. The cured HAp object -- with the embedded epoxy mold still inside-- was heated at 10°C/hr to a) pyrolyze the polyacrylate binder, and b) to burn away the epoxy lost mold. Note that epoxies usually make poor ceramic binders and that the pyrolysis of the Cibatool 5100 resin is difficult. However, the lost mold process works well if the epoxy section size is small. We find that 1 mm sections can be easily removed, which is adequate for the 450-750 micron features of these scaffolds.
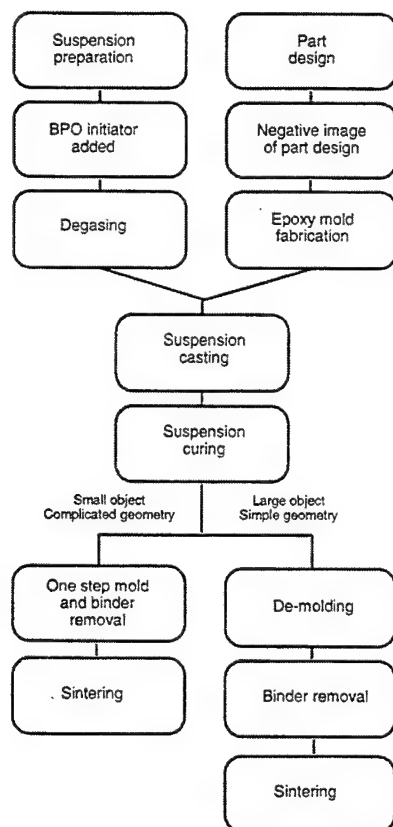
Figure 2 Process schematic for
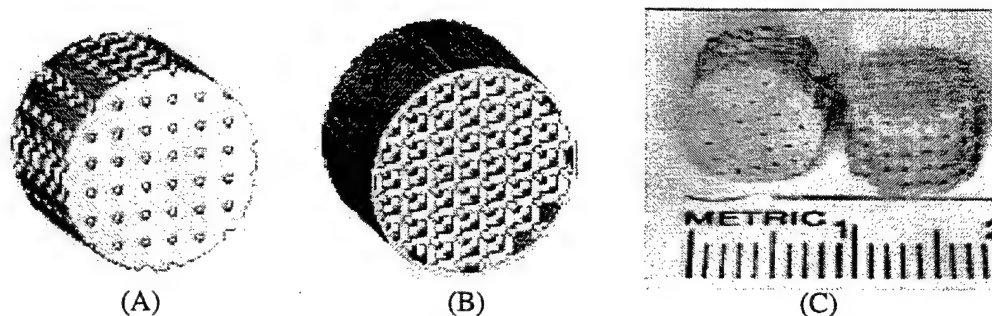Indirect SLA

(A)

(B)

(C)

Figure 3 (A) Design of bioceramic implant. (B) Negative image of mold design,
showing the channel connection pattern. (C) Hydroxyapatite bioceramic bone tissue
scaffold, featuring 400 micron channels for ingrowth of vascularized bone tissue. This
object was fabricated by Indirect Ceramic Stereolithography

The photocuring of the ceramic suspensions has been characterized using photo-
rheology and photo-differential scanning calorimetry (photo-DSC), and is presented
elsewhere (1). Thermal curing can also be characterized by DSC. Figure 4 shows the
fractional conversion of the monomer in a PZT- IBA/PNPDGA suspension and a HAp
-IBA/PNPDGA suspension cured at 80°C. The fraction conversion is calculated from
the DSC heat evolution, using the established heat of reaction of the acrylate monomer.
The thermal curing kinetics of the PZT and the HAp are similar, suggesting that the

presence of a large quantity of ceramic particles and dispersant does not significantly change the kinetics of the peroxide-radical catalyzed polymerization of acrylates.
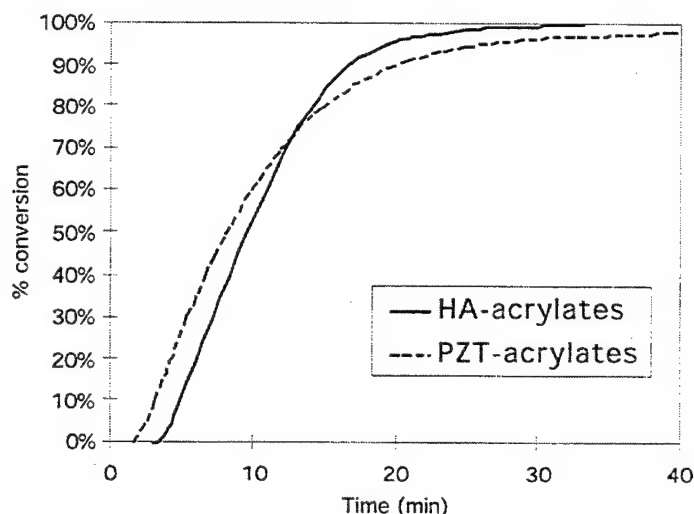

Figure 4. Thermal curing kinetics at 80°C of ceramic acrylate suspensions as fractional conversion of monomer

Conclusions

Complex ceramic objects can be made with direct SLA using UV-curable suspensions of powder in acrylate monomers. The process works best with low refractive index ceramics, for objects with exterior features larger than 700 micron.

Ceramic objects from high refractive index materials, or objects with very fine interior features can be made by indirect ceramic stereolithography, by thermally curing acrylate suspensions in SLA-fabricated molds. Objects with fine interior features can be fabricated by indirect stereolithography using epoxy lost molds. The indirect process can also be used with permanent molds created by stereolithography, or with silicone molds from stereolithography masters.

The thermal curing kinetics are determined by the initiator and the monomer system, and are not strongly affected by the ceramic filler.

Acknowledgment

References

1) G. Allen Brady and John W. Halloran, "Stereolithography of Ceramic Suspensions", Rapid Prototyping Journal, **3**, [2], 61-65 (1997)
2) G. Allen Brady and J.W. Halloran, "Solid FreeForm Fabrication of Ceramics via Stereolithography" to appear in Naval Research Reviews (1998)
3) M.L. Griffith and J. W. Halloran, "Free Form Fabrication of Ceramics via Stereolithography", J. American Ceramic Soc. **79** [10], p. 2601-2608, [1996]
4) T-M Chu and J.W. Halloran, "Hydroxyapatite for Implant Fabrication by Stereolithography", pp. 119-125*Case Studies of Ceramic Product Development, Manufacturing, and Commercialization*, Edited by A. Ghosh, B. Hiremath, and R.Barks, Ceramic Transactions Vol. 75, Am. Ceramic Soc. Westerville, OH (1997)

5) P.F. Jacobs, *Rapid Prototyping and Manufacturing: Fundamentals of Stereolithography*, SME, Dearborn, MI (1992)

6) Michael Rees, "Rapid Prototyping: Realizing Convoluted Form and Nesting in Sculpture", *Prototipazione e Produzione Rapida*, May 1997, (www.sound.net/~zedand00/)

7) M.L. Griffith and J. W. Halloran, "Scattering of Ultraviolet Radiation in Turbid Ceramic Suspensions", J. Applied Physics **81** [10] pp. 2538-46[1997]

8) Diann Brie paper on telescoping?????

9) Owain Hughes, Brian Derby, John Halloran, unpublished research, Oxford University (1997)

10) T-M Gabriel Chu, J.W. Halloran, S.J. Hollister, and S.E Feinberg, "Hydroxyapatite with Controlled Internal Architecture by Acrylic Polymerization", to be submitted to J. Materials Research

11) S.J. Hollister, T.M. Chu, R.E. Guldberg, P.K. Zysset, R.A. Levy, J.W. Halloran, S.E. Feinberg, "Image Based Design and Manufacture Scaffolds for Bone Reconstruction", Martin Bendsøe and Pauli Pedersen, Eds. *Synthesis in Biosolid Mechanics* IUTAM Symposium, Kluwer Press, Lyngby, Denmark, May 24-27 (1998)

Fabrication and experimental characterization of d_{31} telescopic piezoelectric actuators

PAUL W. ALEXANDER*, DIANN BREI*, WEIGUO MIAO†, JOHN W. HALLORAN†
*Departments of *Mechanical Engineering and Applied Mechanics and †Materials Science and Engineering, University of Michigan, Ann Arbor, MI 48109, USA*
E-mail: dibrei@engin.umich.edu

RICHARD L. GENTILMAN, GERALD E. SCHMIDT, PATRICK T. McGUIRE, JOHN R. HOLLENBECK
Materials Systems Inc., Littleton, MA 01460, USA

A popular and useful piezoelectric actuator is the stack. Unfortunately with this type of actuation architecture the long lengths normally required to obtain necessary displacements can pose packaging and buckling problems. To overcome these limitations, a new architecture for piezoelectric actuators has been developed called telescopic. The basic design consists of concentric shells interconnected by end-caps which alternate in placement between the two axial ends of the shells. This leads to a linear displacement amplification at the cost of force; yet the force remains at the same magnitude as a stack and significantly higher than bender type architectures. This paper describes the fabrication and experimental characterization of three different telescopic prototypes. The actuator prototypes discussed in this paper mark a definitive step forward in fabrication techniques for complex piezoceramic structures. Materials Systems, Inc. has adapted injection molding for the fabrication of net shape piezoceramic actuators. Injection molding provides several advantages over conventional fabrication techniques, including: high production rate, uniform part dimensions, uniform piezoelectric properties, and reduced fabrication and assembly costs. Acrylate polymerization, developed at the University of Michigan, is similar to gelcasting, but uses a nonaqueous slurry which facilitates the production of large, tall, complex components such as the telescopic actuator, and is ideal for the rapid manufacture of unique or small batch structures. To demonstrate these fabrication processes a five tube telescopic actuator was injection molded along with a very tall three tube actuator that was cast using the acrylate polymerization method. As a benchmark, a third actuator was built from off-the-shelf tubes that were joined with aluminum end-caps. Each prototype's free deflection behavior was experimentally characterized and the results of the testing are presented within this paper. © *2001 Kluwer Academic Publishers*

1. Introduction

The fabrication of piezoceramic actuators has historically depended on the assembly of simple discrete components to construct actuators capable of amplifying the limited strain produced by the material. For example, stacks are composed of multiple, thin layers of piezoceramic, each individually electroded and then bonded together. Benders are composed of two or more layers of piezoceramic bonded together or bonded to an inactive substrate. Fortunately, piezoceramic processing technology has made great strides in the last few years. For example, stacks can now be co-fired [1]; benders can be made using rainbow [2] or thunder technology [3] or functionally gradient materials [4–6]. Very complex shapes can be fabricated using solid freeform fabrication [7] or injection molding [8]. Even micro actuators with very large aspect ratios can be fabricated using microextrusion [9].

These advances in processing technology open the door for actuation designers since they are no longer restricted to simple geometric shapes. One particular actuation architecture that has benefited is the telescopic actuator developed by the Naval Research Laboratory. This architecture was created to generate forces of the same order of magnitude as stack actuators, while producing 1–20 times the displacement of a similar length stack. This aids in those applications that would require very long stacks because of stroke requirements, which could experience problems such as buckling. A telescopic actuator is composed of multiple nested shells interconnected by end-caps alternating in placement between the two axial ends of the shells (Fig. 1). The shells are activated in an alternating manner, resulting in the expansion (contraction) of one cylinder while the adjacent cylinders contract (expand); thus, the architecture "telescopes" outward
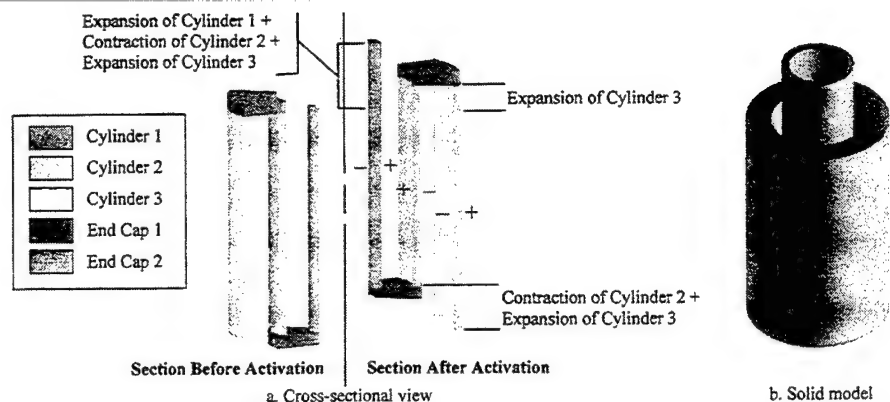
Figure 1 Operation of a telescopic actuator—cylinders alternate in expansion and contraction, thereby telescoping out.

(inward), producing useful amounts of work in the axial direction.

Although it is possible to construct a telescopic actuator by connecting individual tubes with discrete end-caps, current processing technologies make it feasible to construct a monolithic structure. Obviously, there are advantages to utilizing these solid-state processing techniques, such as decreased production time, reduced number of components and elimination of losses in discrete end-caps and bonding layers. Though the advantages of the telescopic architecture can be reaped in both the d_{33} and d_{31} modes of activation, all the actuators discussed in this paper utilize the d_{31} mode of actuation. All of the cylinders are poled in the radial direction and are activated such that each cylinder is driven with a radial potential opposite the potential of the adjacent cylinder. This paper presents two novel fabrication processes well suited to the construction of very complex ceramic structures: injection molding and acrylate polymerization. To demonstrate the capabilities of these manufacturing techniques, monolithic piezoceramic telescopic actuators were created. Experimental results are given for several d_{31} telescopic prototypes built using the new processes along with a baseline actuator built from discrete components and end-caps.

2. Injection molding

Injection molding is widely used in the plastics industry as a means for rapid mass production of complex shapes at low cost. It has been adapted for the fabrication of net shape piezoceramic actuators to provide several advantages over conventional fabrication techniques, including: high production rate, uniform part dimensions, uniform piezoelectric properties, and reduced fabrication and assembly costs. Ceramics injection molding was recently demonstrated as a low cost method for fabricating and simultaneously aligning thousands of identical PZT rods to produce highly repeatable, low-cost 1–3 piezocomposites for medical imaging and Navy undersea applications [10]. It is now being adapted for the fabrication of a telescoping tube actuator that is difficult to produce by conventional techniques, such as isostatic pressing, machining, or slip casting [11].

The basic injection molding process used by Materials Systems Inc. (MSI) for PZT transducer fabrication is shown schematically in Fig. 2 [8]. Materials Systems'

injection molding process utilizes a heated thermoplastic mix of PZT powder and a wax-based binder. The binder in the mixture acts as a carrier during molding, allowing the material to be transferred as a viscous fluid when subjected to heat and pressure. The hot thermoplastic mixture of ceramic powder and organic binder is forced into a cooled mold creating a net shape green part (Fig. 3). The molded part is subsequently heated slowly in air to remove the organic binder. The PZT shape is then sintered at 1250°C for 1 hour, under controlled atmospheric conditions to achieve the desired piezoelectric properties.

Fig. 4 is an example of a telescopic actuator consisting of five nested ceramic tubes with five integrated monolithic end-caps. By designing the mold cavity to achieve the final actuator dimensions (18.5 mm O.D. × 25 mm overall length), no further assembly or machining is required (Fig. 5). Each sintered part is subsequently contact poled in five steps (one tube at a time) using a field of 1.2 kV/mm through the wall thickness to achieve a positive polarity on the inner diameter of each tube. After poling, a permanent nickel electrode is applied to all surfaces of the actuator. The four end-caps that connect adjacent tubes and the one that bridges the inner tube, as seen in Figs 4 and 5, isolate the positively and negatively charged surfaces and allow for the continuous electroding process. However, the electrode layer on the bottom ring of the outer tube must be ground off so that two distinct electrodes are created; to which, wires are attached for the purpose of activation (Fig. 6). This arrangement reverses the electric field that is applied to the second and fourth tubes, causing the structure to "telescope" during actuation.

MSI formulates its own piezoelectric compositions for enhanced piezoelectric performance, and the injection molding and proprietary sintering processes ensures a uniform and defect-free microstructure (Fig. 7). Because the process utilizes a liquid feed stock injected under high pressure, the macroscopic voids often associated with traditional dry powder processing are eliminated. Furthermore, the isostatic nature of the process produces a very uniform green microstructure and green density; therefore, subsequent densification leads to uniform mechanical properties and part dimensions. PZT components routinely exceed a density of 7500 kg/m^3 (approaching the theoretical maximum density). MSI-53HD ceramic's d_{33} piezoelectric

| 1 Compound | 2 Cold Mold | 3 Injection Molding |

| 4 Part Solidified and Ejected | 5 Burn Out Binder (Low Temp.) |

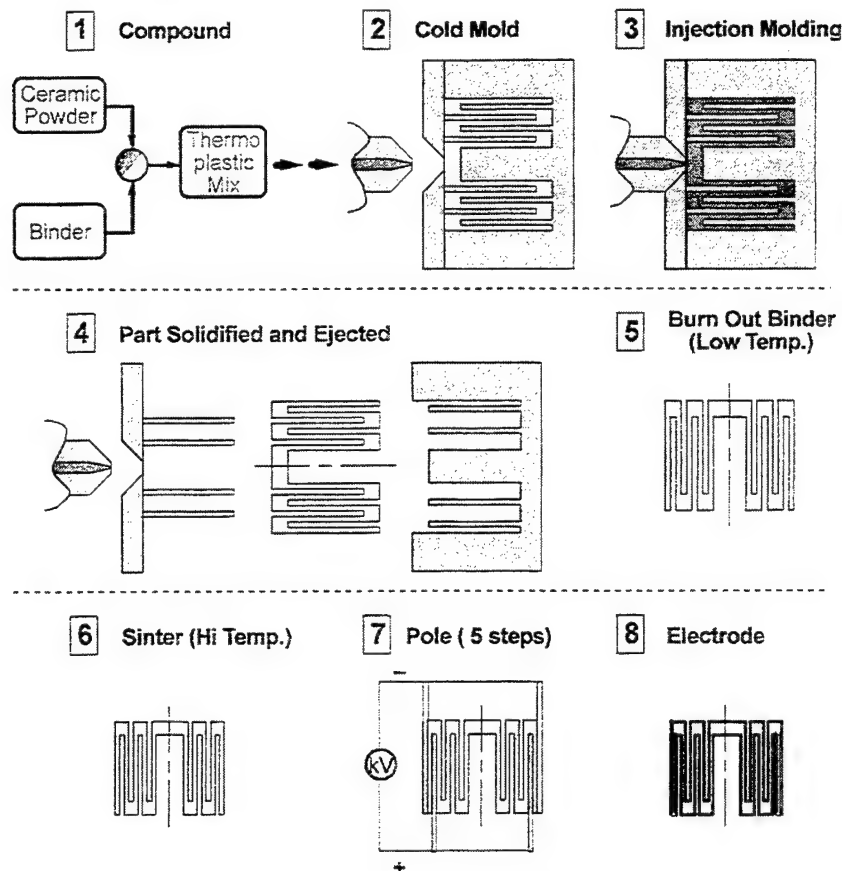| 6 Sinter (Hi Temp.) | 7 Pole (5 steps) | 8 Electrode |

Figure 2 Schematic description of injection molding process—(1) Hot wax-ceramic mixture in nozzle. (2) Injection of mix into mold. (3) Mix cools and forms solid part. (4) Net shape green part is ejected from mold. (5) Green part is heated slowly in air to remove organic binder. (6) PZT shape is sintered in a controlled atmosphere. (7) Sintered PZT shape is contact poled in oil. (8) Permanent electrode is applied.
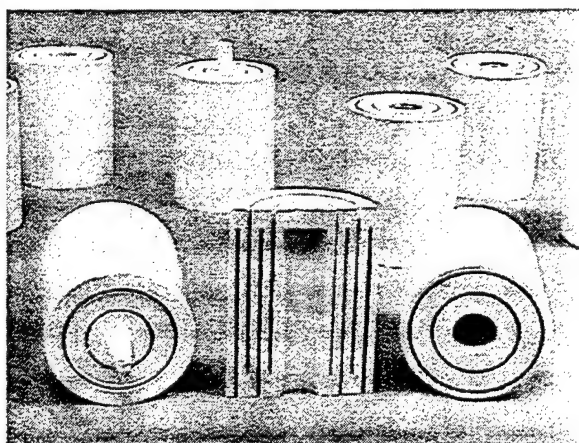

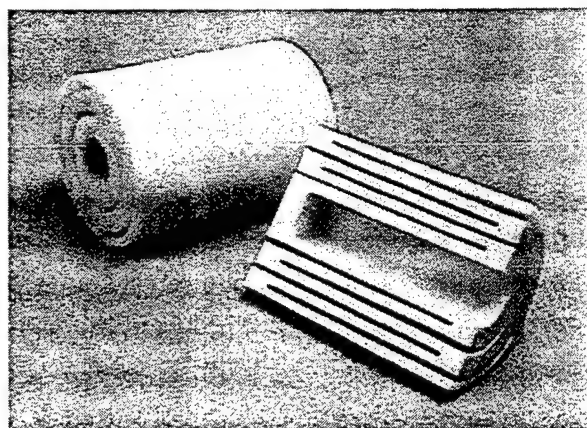*Figure 3* Green parts—net shape injection molded wax-ceramic preforms.

Figure 4 Sintered actuators—net shape ceramic preforms shown after sintering.

coefficient was measured to be 725 pm/V, which is similar to the MSI-53 used to fabricate the telescoping tube actuators.

3. Acrylate polymerization

Polymerization is another novel technique that can be employed for the fabrication of complex ceramic shapes by the molding of, or solid freeform fabrication of a polymerized ceramic slurry [12]. Most of the research into this polymerizing procedure has been focused on aqueous polymerization where the solvent utilized is water [13–15]. Aqueous polymerization produces a green body that is relatively soft and fragile, which leads to problems removing the structure from the mold prior to the drying process. A process which uses a nonaqueous slurry is described here that will produce a green ceramic body that is much more durable, thus facilitating the demolding procedure. This makes it optimal for rapid production of one-of-a-kind, large complex ceramic structures, such as the telescopic actuator prototype.

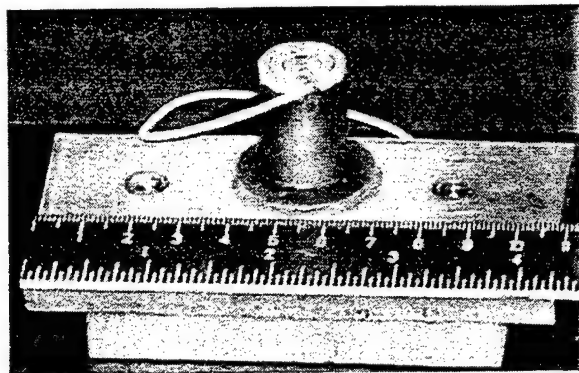The proper slurry composition is crucial to this fabrication process. The slurry's main ingredient is PZT

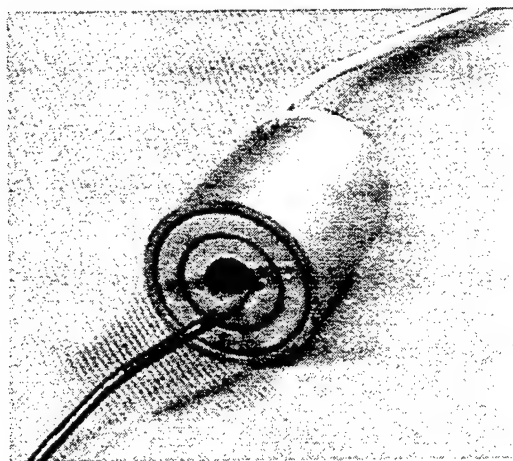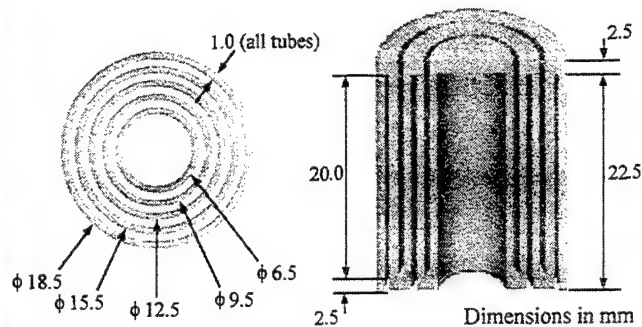Figure 5 Injection molded MSI-53 actuator—photograph and schematic.

Figure 6 Finished actuator—after poling, electroding, and wiring.
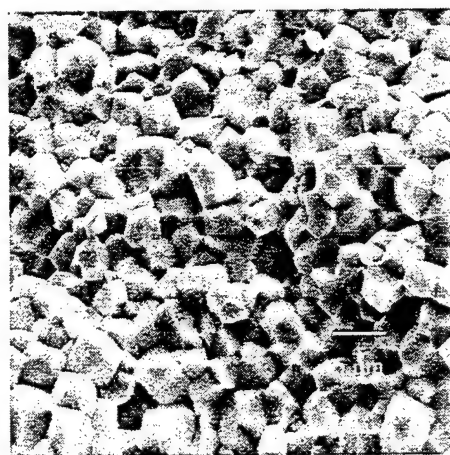

Figure 7 Injection molded fracture surface—MSI-53 ceramic.

586 powder, obtained from American Piezo Ceramics, Inc. (similar to PZT 5A) with a median particle size of 1.1 μm. This powder is mixed with the difunctional monomer propoxylated neopentyl gycol diacrylate (PNPDGA, Sartomer) and the monofunctional monomer 2-(2-ethoxyethoxy) ethyl acrylate esters (EOEOEA, Sartomer). The system solvent, decahydronaphthalene (decalin, Avocado), was also added to the mixture, as was the dispersant, 1 wt% Emcol CC-55 (Witco Corp.), which ensures the PZT powder remains in suspension. The resulting slurry has a high solid load of 51 vol% PZT, but is fluid enough to easily fill a mold. Polymerization of the acrylate

monomers is initiated with 0.1 wt% Benzoyl peroxide (BPO, Aldrich) and 0.025 wt% N,N-dimethyl-p-toluidine (DMPT, Aldrich) is added as a catalyst to lower the curing temperature.

The slurry described above remains workable for approximately ten minutes, during which time the casting process must be completed. In this case, the slurry was simply poured into a mold and allowed to cure at room temperature. The molds used to fabricate the telescopic actuator prototype were made from an epoxy resin utilizing a stereolithography technique. A computer-designed two-piece mold was created, which produced a 75.2 mm tall, three tube, cylindrical telescopic actuator with 1.2 mm wall thickness (Fig. 8). To facilitate demolding, the SLA molds were carefully polished and lubricated prior to use. After the curing process was completed, the green ceramic actuator was carefully removed from the mold. The use of a nonaqueous slurry makes the removal step easier. The resulting telescopic actuator in its green state is shown in Fig. 9. The polyacrylate binder is removed by slowly heating in air. After polymer burnout, the actuator is still relatively fragile and the individual grains of the PZT must be sintered together to impart structural rigidity. The part is heated up to 1275°C where it is sintered for 4 hours in
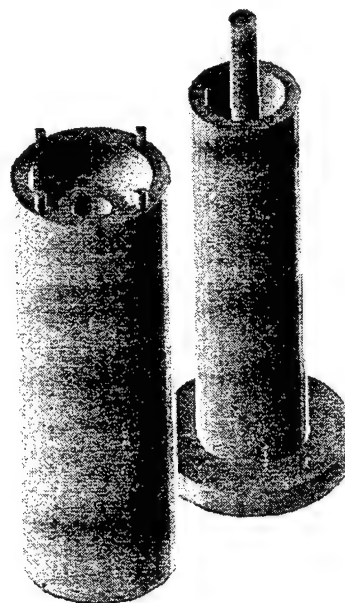

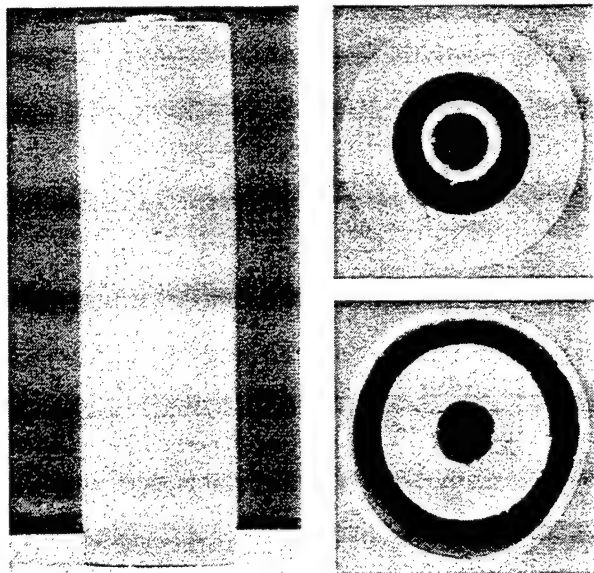Figure 8 SLA mold—two piece, three tube actuator mold.

Figure 9 Green part—polymerized actuator preform.

Figure 11 Polymerized PZT586 micrograph—low porosity piezo-ceramic.

a PbO rich atmosphere. The actuator is finished by applying silver paint for electrodes and poling it at 2000 V (1.67 MV/m) in a 160°C silicone oil bath. The resulting telescopic prototype is shown in Fig. 10.

This fabrication procedure produced PZT of extremely high quality. The material showed a large amount of densification, as illustrated in the micrograph of Fig. 11. The density was greater than 98% of the theoretical. This compares favorably with commercially fabricated PZT, whose densities are around 95–96% of theoretical. The piezoelectric properties were also higher than expected, yielding d_{33} values of 680 pm/V as opposed to the expected value of 590 pm/V for PZT586. Thus, this acrylate polymerization procedure is indeed capable of producing high quality ceramic structures of complex shape.

4. Conventional component assembly

As a baseline, a third telescopic actuator prototype was constructed from off-the-shelf piezoceramic tubes and aluminum 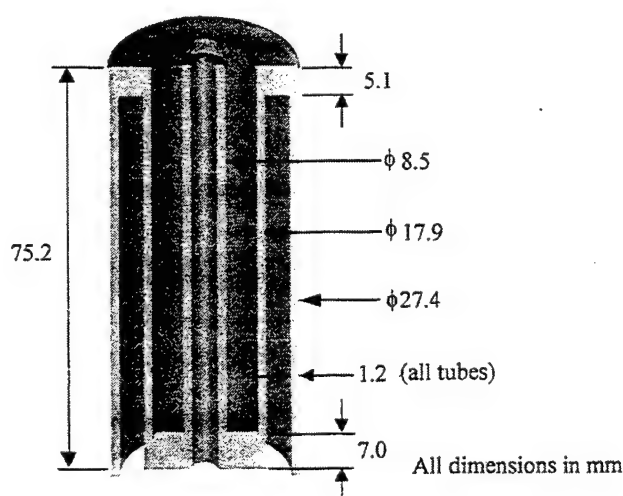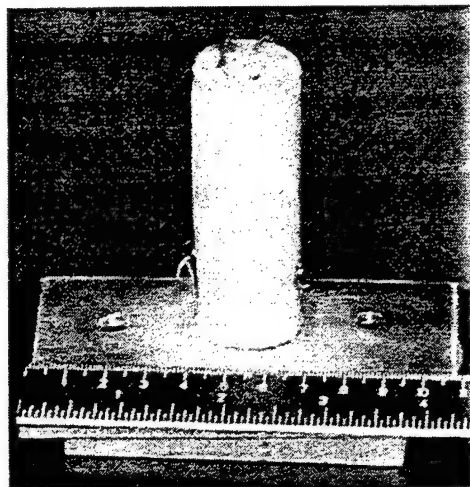washer-like end-caps. The piezoceramic tubes were APC's 855 composition, similar to PZT 5H. The three tubes used to build the actuator were all of a length of 76.0 mm, a thickness of 1 mm, and outer diameters of 25.4 mm, 19.1 mm, and 12.7 mm. The tubes were linked together by two aluminum end-caps, each 3.2 mm thick, as shown in Fig. 12. The components were bonded together using a two part epoxy from Insulcast (Insulcure 24, Insulcast 501). The actuator was completed by wiring adjacent tubes with opposite polarity.

5. Experimental characterization

To assess the different fabrication methods, the free deflection performance of each prototype was experimentally measured utilizing the experimental setup depicted in Fig. 13. Each prototype was mounted on an aluminum plate and secured with a vise. A thin square of aluminum was bonded to the inner most tube of each actuator to serve as a reflective surface to facilitate readings using a Philtec fiber optic displacement sensor. The sensor was monitored with a Fluke digital multimeter. The actuators were activated using a Kepco DC power supply in 50 volt increments. At each increment the displacement was measured with the fiber optic probe. This process was repeated until the maximum applied

Figure 10 Polymerized PZT586 actuator—photograph and schematic.

Figure 12 Conventionally assembled component actuator—photograph and schematic.

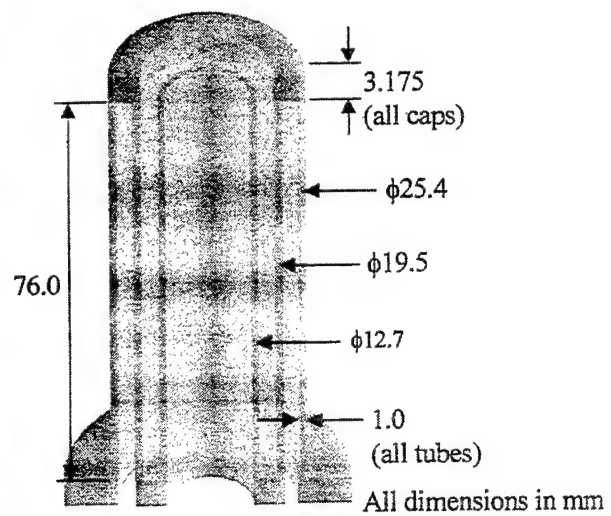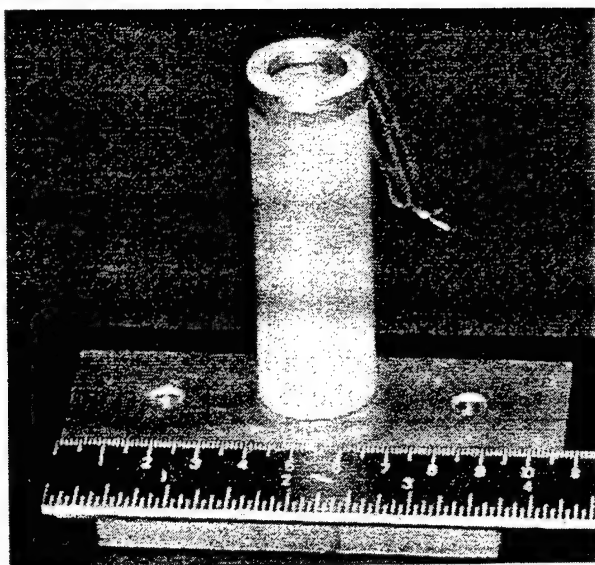3.175 (all caps)

φ25.4

φ19.5

φ12.7

76.0

1.0 (all tubes)

All dimensions in mm

Voltmeter

Fiber Optic Probe

Vise

Multi-Axis Stage

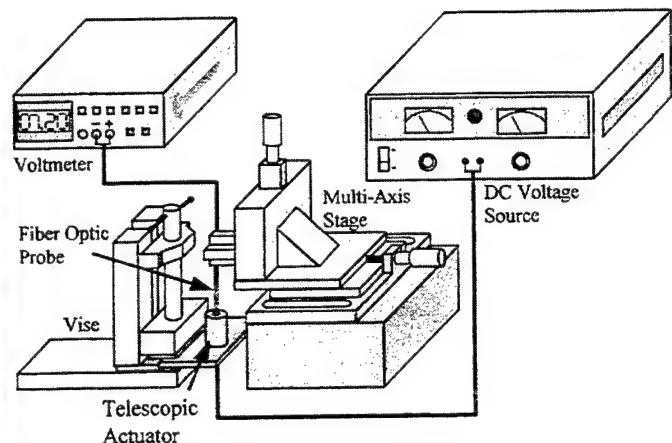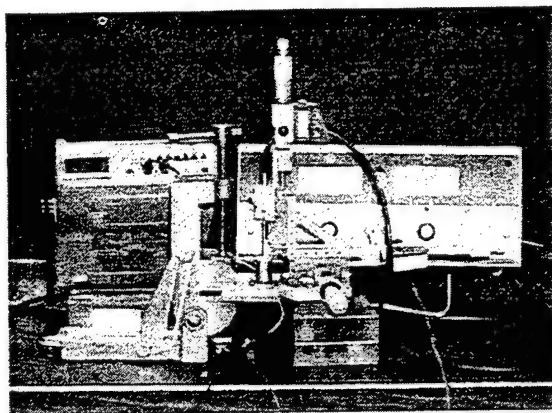DC Voltage Source

Telescopic Actuator

Figure 13 Experimental test apparatus—photograph and schematic.

DC voltage was reached, 300 V for the two monolithic actuators and 400 V for the baseline actuator. Once the maximum field was reached, the voltage was stepped down, again in 50 volt increments, until zero volts was reached. At this point the leads from the power supply were reversed and the process was repeated for negative voltages.

The experimental results for each of the three actuators when driven to their maximum allowable field are given in Fig. 14. The injection molded actuator produced a maximum deflection of 14.72 μm when subjected to an electric field of 300 kV/m. The polymerized telescopic prototype, activated by 250 kV/m, produced 24.69 μm of deflection. And lastly, the conventionally assembled actuator exhibited a maximum deflection of 33.17 μm when placed in a 400 kV/m electric field. The average displacement of each prototype when driven to 250 kV/m is 11.63 μm for the injection molded actuator, 24.69 μm for the polymerized prototype, and 22.53 μm for the conventionally assembled actuator. The corresponding resultant strains (deflection/length of actuator) are 465 $\mu\varepsilon$, 328 $\mu\varepsilon$, and 284 $\mu\varepsilon$ for the injection molded, polymerized, and conventional actuators respectively.

Since the prototypes were manufactured with different material characteristics and physical dimensions to highlight strengths of each fabrication process, it is not reasonable to compare the prototypes to one another. However, they can be compared individually to the theoretically predicted performance [16]. Using linear piezoelectric theory, the free deflection of a telescopic actuator is simply the sum of the individual displacements from each cylinder, given by:

$$\Delta = \sum_{i=1}^{n} d_{31_i} \frac{V}{t_i} L_i \qquad (1)$$

Where Δ is the deflection, n is the number of tubes in the actuator, d_{31_i} is the ith tube's piezoelectric coefficient, V is the applied voltage, t_i is the ith tube's thickness, and L_i is the ith tube's length. For the injection molded prototype, an experimentally measured d_{31} value of 440 pm/V was employed in the model, yielding a maximum theoretical deflection of 14.99 μm. The average error for this prototype was determined to be 13.4%, but this is mainly due to hysteresis, which reached a maximum of 6.56 μm. The error at the maximum free deflection (14.72 μm), where there is little hysteresis, was only 1.8%.

The experimentally determined d_{31} value for the polymerized actuator was 430 pm/V, which gave a predicted maximum deflection of 21.93 μm, resulting in

Injection molded MSI-53 Prototype
(length – 25 mm, wall thickness – 1 mm)

Polymerized PZT586 Prototype
(length – 75.2 mm, wall thickness – 1.2 mm)

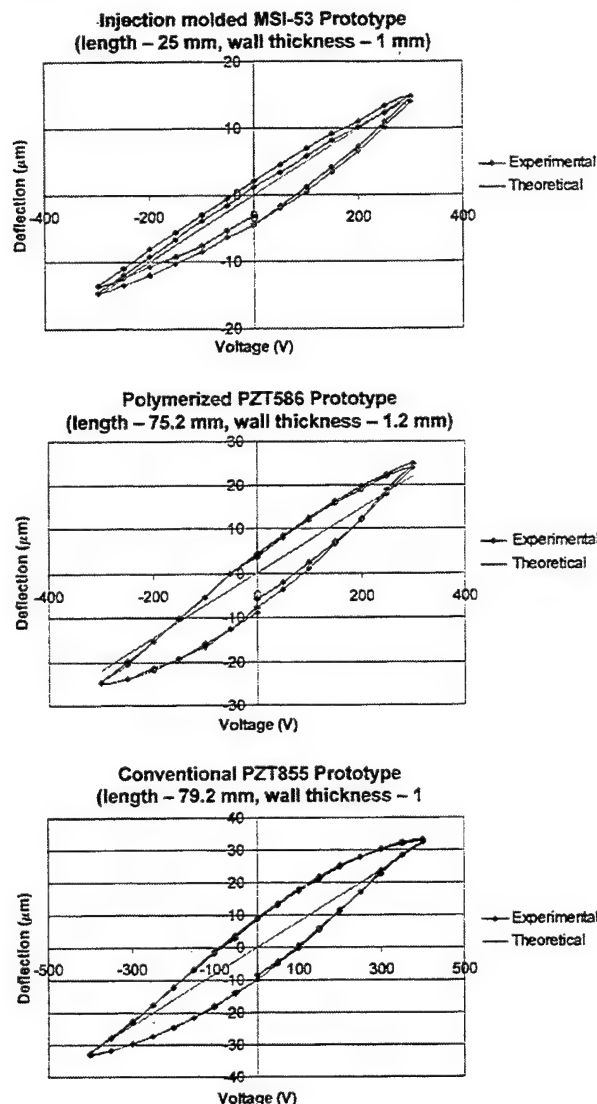**Conventional PZT855 Prototype**
(length – 79.2 mm, wall thickness – 1

Figure 14 Deflection-Voltage experimental results.

12.6% error when compared to the measured maximum deflection of 24.69 μm. It should be noted that the increased error in this case most likely stems from uncertainty in the electroded length of the polymerized actuator's cylinders. For the polymerized telescopic actuator, the average error in the model was 20.5%; again, mostly due to hysteresis, which peaked at 11.47 μm.

For the baseline prototype, the maximum free deflection, 33.17 μm, correlated well with the theoretical value of 31.92 μm, to within 3.9% when using the measured d_{31} value of 420 pm/V. The maximum hysteresis was 19.07 μm, and the average error in the model was 18.2%. It is relevant to once again point out that the linear nature of the theoretical model does not attempt to capture the hysteresis that all piezoceramics exhibit; but, as evidenced in Fig. 14, when hysteresis is taken into account, the experiments do track the model well.

6. Conclusions

This paper describes two novel manufacturing techniques, injection molding and acrylate polymerization, each of which were used to fabricate a monolithic telescopic actuator. Such an actuator is complex and would be very difficult to construct using conventional techniques such as isostatic pressing or slip casting. Both of these techniques produced quality piezoceramic parts with high densities and piezoelectric properties. Injection molding is best suited to producing complex structures of moderate height in large volumes where cost is a definite factor. Acrylate polymerization is better suited to fabricating tall or large structures in smaller quantities, and is ideal for the rapid prototyping of complex ceramics. The analytically derived linear model correlates well with the deflection-voltage behavior of all three telescopic prototypes, regardless of the actuator geometry, fabrication process employed, or construction materials. This paper demonstrated the viability of fabricating large monolithic telescopic actuators.

References

1. K. BRIDGER, L. JONES, F. POPPE, S. A. BROWN and S. R. WINZER, Smart Structures and Materials: Industrial and Commercial Applications of Smart Structures Technologies, San Diego, CA, 1996, p. 341.
2. G. H. HAERTLING, *American Ceramic Society Bulletin* **73** (1994) 93.
3. C. SHAKERI, C. M. BORDONARO, M. N. NOORI and R. CHAMPAGNE, Proceedings of the Smart Structures and Materials Conference, Newport Beach, CA, 1999, p. 63.
4. C. C. M. WU, M. KAHN and W. MOY, *J. Amer. Ceram. Soc.* **79** (1996) 809.
5. X. ZHU, Q. WANG and Z. MENG, *J. Mater. Sci. Lett.* **14** (1995) 516.
6. R. K. PANDA, A. L. KHOLKIN and A. SAFARI, in Proceeding of the 11th IEEE International Symposium on Applications of Ferroelectrics, Montreaux, Switz., 1998, p. 265.
7. A. SAFARI and S. C. DANFORTH, in Proceeding of the 11th IEEE International Symposium on Applications of Ferroelectrics, Montreaux, Switz., 1998, p. 229.
8. L. BOWEN and K. FRENCH, in Proceedings of the 8th IEEE International Symposium on Application of Ferroelectrics, Greenville, SC, 1992, p. 160.
9. A. T. CRUMM and J. W. HALLORAN, *J. Amer. Ceram. Soc.* **81** (1998) 1053.
10. R. L. GENTILMAN, D. F. FIORE, H. T. PHAM, K. W. FRENCH and L. J. BOWEN, *Ceramic Transactions* **43** (1994) 239.
11. J. S. REED, *Ceramic Transactions: Ceramic Powder Science IIB* **1** (1988) 601.
12. K. VENKATASWAMY, R. WAACK, B. E. NOVICH and J. W. HALLORAN, US Patent no. 4978643 (1990).
13. G. T.-M. CHU, G. A. BRADY, W. MIAO, J. W. HALLORAN, S. J. HOLLISTER and D. BREI, "Solid Freeform and Additive Fabrication," edited by D. Dimos, S. C. Danforth and M. J. Cima, MRS Symposium Proceedings, Vol. 542, 1999, p. 119.
14. O. O. OMATETE, M. A. JANNEY and R. A. STREHLOW, *Ceramics Bulletin* **70** (1991) 1642.
15. M. A. JANNEY, O. O. OMATETE, C. A. WALLS, S. D. NUNN, R. J. OGLE and G. WESTMORELAND, *J. Amer. Ceram. Soc.* **81** (1998) 581.
16. D. BREI and N. T. BERNER, in Proceedings of the ASME International Mechanical Engineering Congress and Exposition—Adaptive Structures and Material Systems, Nashville, TN, 1999, p. 189.

Feasibility Study of Microfabrication by Coextrusion (MFCX) Hollow Fibers for Active Composites

Bryan J. Cannon and Diann Brei*

Department of Mechanical Engineering and Applied Mechanics, The University of Michigan, Ann Arbor, MI 48109-2125

ABSTRACT: Active composites based on a hollow fiber topology have advantages over solid piezoelectric fiber composites in that they require lower voltages for activation and are not limited to electrically non-conductive matrix materials. One critical issue for hollow fiber composites is the fiber aspect ratio (ratio of wall thickness to fiber radius). In this paper analytical and finite element models, which include electric field variations, were developed to determine the "effective d_{31}" of an individual piezoelectric hollow fiber. The effective fiber properties were used to derive a single-row lamina strain/electric field model from classical composite theory. The models were validated with a series of deflection/voltage experiments conducted with hollow piezoelectric fibers fabricated utilizing microfabrication by coextrusion (MFCX) techniques. To determine the feasibility of MFCX hollow fiber composites, the models and experimental results were employed to study the effect of the fiber aspect ratio on a variety of fiber/composite design issues: fiber/lamina performance, fiber strength, matrix material, and electric field effects (incomplete poling and field concentrations).

INTRODUCTION

ACTIVE composites, a composite consisting of one or more phases of a smart material, have received attention lately as a means to address actuation needs in smart structure design (Herold-Schmidt et al., 1997; Schetky and Wu; Jang, 1993; Chen and Chopra, 1996; Agrawal, Tong, and Nagaraja, 1994). Composites with embedded active fibers have the advantage of being more resistant to damage and less obtrusive in active flow control systems than common externally mounted actuators (Rodgers, Bent, and Hagood, 1996). Active composites can essentially be formed from two types of piezoelectric fibers: short and long. Due to the small size of the active elements, short-fiber composites have very high frequency response and force characteristics (Safari, 1994), but generally produce low displacements. Because of their length, short fiber composites can generally not be configured to produce bending and twisting motion. For these reasons, this type of composite is suited for ultrasonic applications (Safari, 1994; Gururaja et al., 1981) and high-frequency vibration suppression and isolation (Krishna-Murty, Anjanappa, and Wu, 1996; Safari et al., 1996). On the other hand, long fibers can be used to create large sheets, or lamina, which in turn can be laid up in composites to produce extensional, bending, and twisting motion of the entire composite. Thus, long fiber composites are often implemented in shape (Hagood and Bent, 1993) and flow control (Bent and Hagood, 1997) applications. The low frequency response of long fibers also makes them suitable for low- and mid-frequency vibration and acoustic control applications (Zhang et al., 1993).

In contrast to the beneficial characteristics and versatility of long piezoelectric fiber composites, there are some current problems being faced in their implementation. First, most existing long fiber composite designs require high voltage levels for actuation. For example, innovative techniques such as interdigitated electroding (Bent and Hagood, 1997) are popular because they exploit the d_{33} mode of the fiber, but they require the electrode to be placed outside the matrix. To generate an electric field on the order of the piezoelectric working field, high voltage levels must be applied (as high as several kilovolts). This external electrode placement causes a substantial portion of the field to be lost in the matrix. Second, by generating the electric field through the matrix, only electrically non-conductive materials can be used as the composite matrix. A conductive matrix would simply "short" the poles of the applied field, rendering the composite inactive. Third, long fiber composites are susceptible to reliability problems such as fiber pullout and breakage in much the same way as conventional (inactive) fibrous composites (Sottos et al., 1996).

Hollow fibers that are individually electroded, as depicted in Figure 1, address many of these issues. By individually electroding each fiber, the voltage requirements of the composite drop drastically since the electric field only needs to be applied across the thin fiber wall (Maclean and Jacobsen, 1995). Similarly, the placement of electrodes directly on the fiber walls eliminates field losses in the matrix, raising composite efficiency. The hollow nature of the fiber allows one of the electrodes (inner) to be completely isolated from the matrix, allowing the fiber to be embedded in electrically conductive matrices (Maclean and Jacobsen, 1995; Fernandez et al., 1995, 1996).

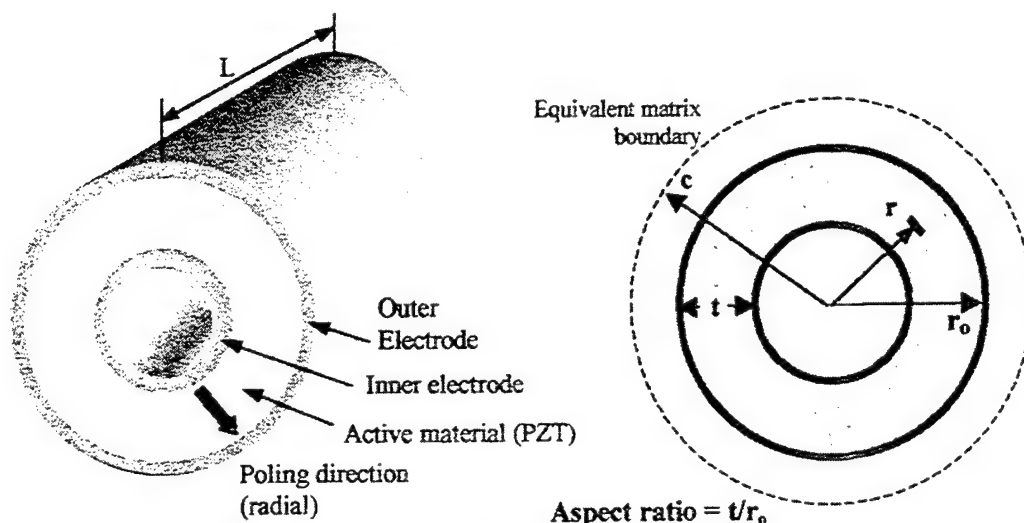Yet, even though the hollow concept has inherent advan-

Figure 1. *Hollow fiber design. The basic fiber design consists of a hollow cylinder of active material, electroded on both the inside and outside surfaces. In the case of piezoelectric material (PZT), the poling direction is radial; therefore the d_{31} response of the fiber is used to create longitudinal motion.*

tages, there are apparent drawbacks. For example, fiber breakage can be an issue, unlike interdigitated electrode composites which function even when individual fibers are fractured. Also, because of the topology of a hollow fiber, the electric field is not uniform across its cross-section. This electric field variation affects the poling of the fiber, maximum allowable voltages during activation, and can possibly decrease the performance of the fiber as the wall thickness increases. Finally, because hollow fibers are naturally weaker than solid fibers, it is not clear in exactly what matrix materials they will survive the embedment process.

Before a hollow fiber design can be implemented, each of these issues must be addressed and fully understood. This type of fiber has been successfully modeled and used in short form for hydrophone applications (Zhang et al., 1993b; Wang et al., 1995), but to date research on long hollow fibers is limited. The issues posed are directly related to the aspect ratio, defined as the ratio of the fiber wall thickness to the outside radius. For example, the electric field varies across the walls of the fiber as a function of the aspect ratio; thereby, rendering the piezoelectric effect non-homogenous. This paper analyzes how the aspect ratio affects individual fiber and composite characteristics as a means to investigate the feasibility of the hollow fiber concept as a whole. A strain/electric field model for an individual fiber based upon aspect ratio was derived to develop an effective d_{31} value. Using the effective d_{31}, classical composite theory was employed to model the strain performance of a lamina, or single layer composite. These models were validated with finite element simulations and experiments in which fiber and lamina prototypes were fabricated using a novel piezoceramic processing technique called Microfabrication by Coextrusion (MFCX). These experiments confirmed that it is possible to fabricate and activate composites containing hollow fibers, demonstrating the feasibility of the concept. The aspect ratio

also affects the strength of the fiber, such as the stresses present during embedment in a matrix. To examine this, stresses during embedment were modeled, and various matrix materials were evaluated for compatibility with hollow fibers. These efforts were employed to examine the effect of the aspect ratio on individual fiber and associated composite characteristics as a means to assess the feasibility of the hollow fiber concept.

INDIVIDUAL FIBER MODEL

To investigate the effect of fiber aspect ratio on composite characteristics, it was first necessary to model an individual hollow piezoelectric fiber. The overriding goal of this effort was to produce a relationship between the electric field applied across the fiber wall and the resulting longitudinal fiber strain. The ratio of strain to electric field (or slope of a strain/field plot) can be thought of as an "effective fiber d_{31}" which can then be used directly to construct lamina and full composite models. The following sections describe the individual fiber modeling and the validation of these models, including fabrication and performance testing of several fiber prototypes.

Electric Field Model

In smart structures, it is common to model the electric field applied across a curved surface by the thin-wall approximation, E_{tw}, given by

$$E_{tw} = \frac{V}{t} \tag{1}$$

where V is the applied voltage, and t is the thickness of the structure. However, in general the electric field within the

wall of the hollow piezoelectric fibers being investigated is not constant. Therefore, these fibers cannot be considered "thin-walled" fibers, and simple piezoelectric deflection/voltage relationships do not apply. Thus, to understand exactly how the fibers will perform, it was necessary to first examine the nature of the non-constant electric field. From Gauss's Law, the expression for the electric field, E, at a distance, r, from the geometric center of a hollow circular fiber is (Halliday and Resnick, 1988).

$$E(r) = \frac{-V}{r \ln(1 - t/r_o)} \tag{2}$$

where t is the wall thickness of the fiber, and r_o is the outside radius (Figure 1). It can be seen that the maximum electric field occurs at the inside edge of the fiber, whereas the minimum field is located at the outside edge. Normalizing the electric field throughout the fiber by the thin-wall electric field approximation. E_{tw}, leads to the maximum and minimum field values in terms of the aspect ratio t/r_o,

$$\text{maximum:} \quad \frac{E_{max}}{E_{tw}} = \frac{-1}{\left(\dfrac{r_o}{t} - 1\right)\ln\left(1 - \dfrac{t}{r_o}\right)} \tag{3}$$

$$\text{minimum:} \quad \frac{E_{min}}{E_{tw}} = \frac{-1}{\left(\dfrac{r_o}{t}\right)\ln\left(1 - \dfrac{t}{r_o}\right)} \tag{4}$$

It is apparent that the aspect ratio alone governs the behavior of the normalized electric field in the wall of a circular hollow fiber for a given applied field.

Figure 2 summarizes this behavior with the minimum and maximum electric field values plotted as a function of aspect ratio [Figure 2(a)], while the electric field is plotted as a function of normalized position within the wall in Figure 2(b). Even before considering how the electric field affects the performance of the fiber, there are several points that can be made about the choice of aspect ratio when designing a hollow fiber. For example, consider a fiber of aspect ratio 0.52. According to Figure 2(b), the electric field on the inside edge is more than double the field at the outer edge (1.5 vs. 0.7). Therefore, when poling this fiber, to produce an adequate field at the outer edge of the fiber, extremely high field levels exist at the inner edge of the fiber. These field levels could easily be high enough to damage the piezoelectric material in the fiber. This mismatch between the electric field at the inner and outer edges increases with the fiber's aspect ratio. Therefore, if it is determined that a thick-walled fiber is needed for strength or other mechanical reasons, it must also be decided whether to risk damaging the material near the inside edge, or leave the outside regions un-poled and inactive. Similarly, when activating a hollow fiber it is not possible to achieve the maximum working electric field at the outer edge
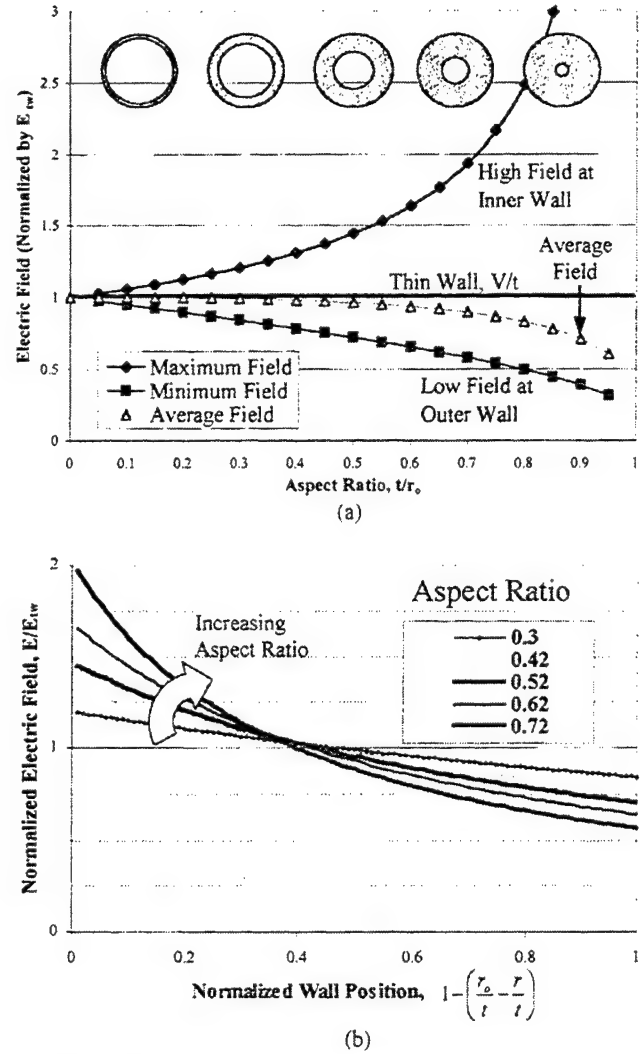
Figure 2. *Electric field in thick wall fibers. As the aspect ratio of a hollow fiber increases, the difference between the maximum and minimum electric fields increases. The highest field occurs at the inside wall; the lower field at the outside wall. (a) Normalized field vs. apect ration and (b) field vs. normalized wall position.*

because this voltage would overdrive the inside of the fiber. resulting in de-poling or even material damage. Thus, it is clear that the choice of aspect ratio has a significant effect on the ability to pole hollow fibers, voltage levels needed for poling, and voltage levels allowable during fiber activation.

Effective d_{31} Fiber Model

Since the electric field is the key driver for piezoelectric actuation, the aspect ratio of a hollow fiber naturally affects the longitudinal strain of the active fiber. To model this behavior, the ratio between longitudinal strain and applied electric field was derived. This ratio can be considered the effective piezoelectric constant, or effective d_{31}. The subscript "31" was chosen because, under the thin wall approximation in which the electric field does not vary, this effective constant simply reduces to the d_{31} of the piezoelectric material.

In deriving the effective piezoelectric constant, it was as-

sumed that end effects were negligible. a valid assumption considering the long, narrow nature of the fibers. Thus, the longitudinal free strain is constant across the cross-section of the fiber. However, the electric field is not constant, and therefore the one-dimensional longitudinal piezoelectric stress, σ, within a differential element varies as a function of radius, given by

$$\sigma(r) = Yd_{31}E(r) \tag{5}$$

where Y is the Young's modulus of the material. The overall piezoelectric forcing, F_{tot}, can be found by integrating the stress over the cross-section of the fiber.

$$F_{tot} = \int_0^{2\pi} \int_{r_i}^{r_o} Yd_{31}E(r)dA \tag{6}$$

The free strain resulting from the piezoelectric forcing can be derived by assuming the stress is simply the total force divided by the area and using a one-dimensional Hooke's Law.

$$\varepsilon = \frac{F_{tot}}{AY} = \frac{\int_o^{2\pi} \int_{r_i}^{r_o} Yd_{31}E(r)dA}{YA} \tag{7}$$

where A is the cross-sectional area of the fiber. Completing the integration gives the free strain in terms of the effective properties,

$$\varepsilon = \frac{-2E_{tw}d_{31}}{\ln\left(1 - \frac{t}{r_o}\right)\left(\frac{2r_o}{t} - 1\right)} = E_{avg}d_{31} = E_{tw}d_{31,eff} \tag{8}$$

Note that the free strain of the fiber can be expressed as the product of the true material d_{31} and the area average of the electric field. E_{avg},

$$E_{avg} = \frac{-2E_{tw}}{\ln\left(1 - \frac{t}{r_o}\right)\left(\frac{2r_o}{t} - 1\right)} \tag{9}$$

or the free strain can be expressed as the product of the thin-wall electric field. E_{tw}. and the effective d_{31} of the fiber, $d_{31,eff}$. given by

$$d_{31,eff} = \frac{-2d_{31}}{\ln\left(1 - \frac{t}{r_o}\right)\left(\frac{2r_o}{t} - 1\right)} \tag{10}$$

When developing models for a lamina consisting of multiple hollow fibers, it is useful to utilize the effective d_{31} model for strain because it allows classical composite theories to be applied directly. Note that the effective d_{31} is only a function of the aspect ratio of the fiber and the material d_{31}. The effective d_{31} decreases with increasing aspect ratio: therefore, as would be expected for a given applied electric field E_{tw}. fibers with low aspect ratio (thin wall) produce the highest strain.

Fabrication of Fibers

To validate the effective d_{31} fiber model. individual fibers of increasing aspect ratio (Table 1) were fabricated and experimentally tested. The micro-fine features of these fibers called for a new manufacturing process—Microfabrication by Coextrusion (MFCX). This straightforward process was chosen because it is currently one of the only available methods capable of producing quickly and inexpensively long fibers of arbitrary cross-section (including hollow) at such small scales (Crumm and Halloran, 1998). The MFCX process is comprised of three main steps as depicted in Figure 3: feed rod formation, extrusion, and burnout/sintering.

FEED ROD FORMATION

The goal of the feed rod formation step is to transform piezoelectric powder into a state capable of being formed and extruded. To do this, piezoelectric powder was mixed with thermoplastic polymers (ethyl acrylates) and polyethylene glycol (PEG 1000) in a Brabender shear mixer. The powder used was ball-milled EDO EC-76 (industry standard PZT-5H), a piezoelectric ceramic with relatively low stiffness and high d_{31}. In a similar fashion and composition, a mixture of the same thermoplastic polymers and carbon black powder was created. This carbon black mixture enables the feed rod to maintain its shape during extrusion and was burned out during step 3 of fabrication. The composition of the carbon black was monitored and adjusted so that the viscosity of the two mixtures is approximately the same. Viscosity matching is crucial because it allows the two mixtures to be simultaneously extruded without cross-section deformation. The resulting piezoelectric and carbon black mixtures resembled soft. formable plastics that were then warm pressed. The PZT mixture was warm pressed into a cylinder and a hole was lathed through the center of it. A portion of the carbon black mixture was formed into a smaller cylinder to precisely fit in the hole in the PZT cylinder. The remainder of the carbon black was pressed into a square cross-section to

Table 1. *Geometric properties of hollow fiber prototypes.*

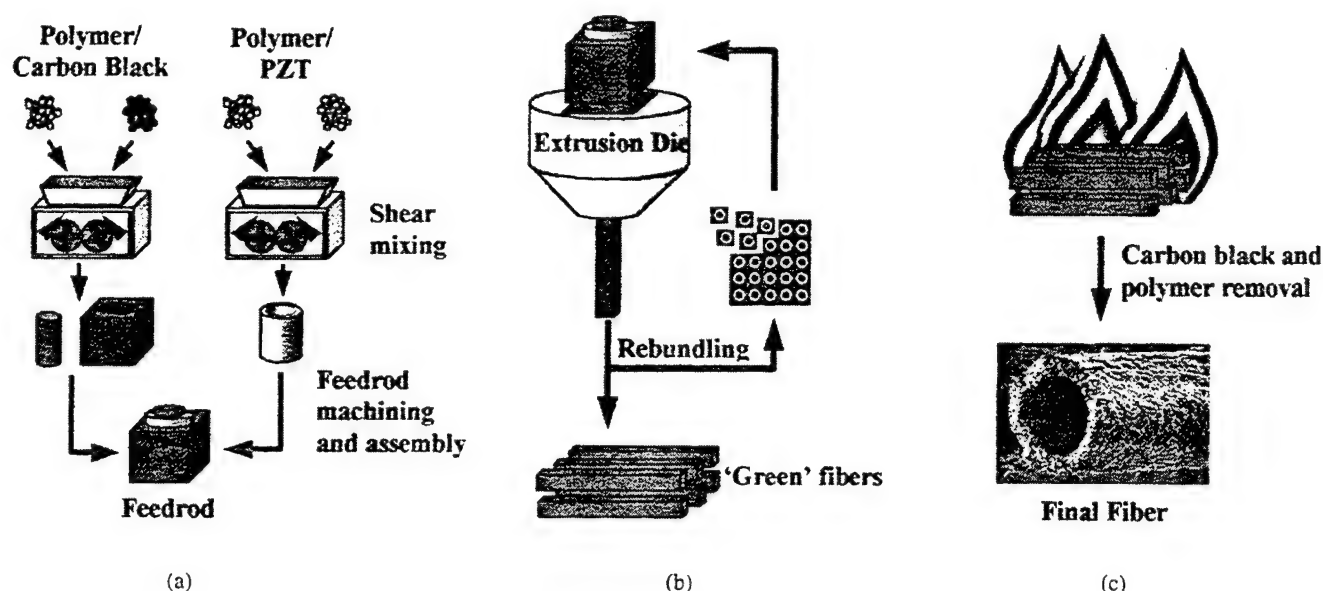| Prototype	Length (mm)	Outside Radius, r_o (μm)	Wall Thickness, t (μm)	Aspect Ratio, t/r_o
A	35	300	90	0.3
B	43	450	190	0.42
C	45	450	235	0.52
D	45	450	280	0.63

Figure 3. *MFCX overview. Piezoelectric and carbon black powders are mixed with thermoplastic polymers to form initial feed rod. The feed rod is extruded (and re-extruded) until desired fiber size is produced. Polymers and carbon black are removed during burnout and piezoelectrics are sintered to produce the final fiber. (a) Step 1: feed rod formation, (b) step 2: extrusion and (c) step 3: burnout/sintering.*

match the inlet of the extrusion die. A hole was drilled into this square block so that the PZT and carbon black cylinders could be assembled as shown in Figure 3(a). The resulting feed rod was 25 mm × 25 mm with cylinders ranging from 22.5 to 24 mm in diameter and 3.6 to 7 mm wall thickness.

EXTRUSION

Once the feed rod was formed, it was heated (160°C) and extruded through a die (25 mm square inlet), reducing the overall cross-sectional area. The reduction in area was either a factor of 25 or a factor of 40, depending on the desired fiber size. If smaller ceramic elements are required, the extrudate can be cut, bundled, and passed through the extrusion die again. This process can be repeated until the desired reduction in cross-sectional area is achieved. For the fibers fabricated under this effort, however, only a single extrusion pass was necessary.

BURNOUT AND SINTERING

The final step in the coextrusion of hollow PZT fibers was the burnout and sintering phase. During this phase, the extruded fibers were heated to 1300°C for 48 hours. During this time, the fugitive material (carbon black) burns off, resulting in a void in the center of the fiber, producing the desired hollow cylinder. The thermoplastics were removed from the PZT mixture, densifying the ceramic. Typically, an additional 30% reduction in cross-section occurs during this phase of fabrication. An end-view of a typical fiber at this phase of fabrication is shown in Figure 4.

POST PROCESSING

To be able to pole and activate the fibers, they were individually electroded using silver paint. In order to access both the positive and negative electrode as the fiber decreases in size, the electrode pattern shown in Figure 5 was utilized. This pattern allows for multiple fibers to be connected electrically using a bus versus many separate wires. This pattern was accomplished by masking with wax a small band around the circumference of the fiber at each end. The exterior electrode was painted on over this mask and the interior electrode was applied using a hypodermic needle. With the electrodes in place, the fibers were poled radially at approximately 1200 V/mm (or three times the maximum working voltage for PZT-5H) for approximately one hour. The un-electroded bands were made large enough so that poling could be done in air without arcing and at room temperature to avoid thermally induced stresses.

HOLLOW FIBER EXPERIMENTAL VALIDATION

To determine the success of the fabrication and post processing efforts, as well as validate the effective d_{31} model, the free deflection behavior of the fibers were experimen-
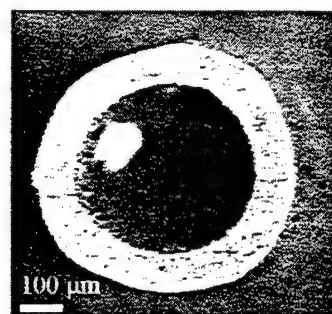

Figure 4. *Hollow fiber prototype. Cross-section of coextruded fiber following the burnout/sintering process. Outside radius = 300 μm; thickness = 90 μm.*
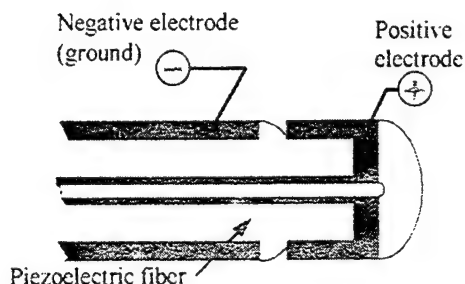
Figure 5. Electrode pattern. Wrapping the electrode around the end of each fiber allows both poles of the fiber to be accessed externally and for multiple fibers to share an external electrode bus.

tally measured as a function of applied voltage. Each fiber was placed in the test setup shown in Figure 6. A Kepco DC voltage source was used to supply the electric field to the fiber, which was glued to a glass slide and mounted in a vise. A fiber optic displacement probe (Philtec) and voltmeter were used to measure the deflection of the end of the fiber. To enable the gain on the probe to be lowered and to increase the precision of the measurements for the very small deflections, a small piece of aluminum shim was attached to the end of the fiber. The applied voltage was varied from zero to 80 percent of the maximum electric field (400 V/mm for PZT-5H).

As additional validation for the analytical models, a finite element model was constructed. A single fiber was modeled using the pre-processor Hypermesh, and analyzed using the numerical solver ABAQUS. It was found that modeling the fiber with axi-symmetric elements did not produce an accurate electric field gradient, and therefore the fiber was modeled using full three-dimensional piezoelectric elements (20-noded quadratic brick, type C3D20E). A typical mesh and the resulting displaced mesh are shown in Figure 7.

The deflection for one fiber prototype (0.42 aspect ratio) was converted to strain, and plotted against the applied electric field, E_{tw} [Figure 8(a)]. The maximum measured deflec-

tion for the four prototypes ranged from 2.9 to 3.6 microns for voltages from 29 to 90 volts, resulting in strains of 0.0062% to 0.0080%. Because these strains are plotted against the applied field, the slope of the experimental curve is the measured d_{31} of the fiber. The experimentally measured effective d_{31} for each of the four fiber types is plotted in Figure 8(b) along with the fiber d_{31} values determined by the effective d_{31} model, the thin wall approximation, and the finite element simulation. In each of the four cases, the error between theoretical and experimental displacement values ranged from three percent to nine percent, with an average of approximately six percent. The displaced mesh in Figure 7(b) shows that although the end of the fiber does not displace uniformly, this effect dies out almost immediately (less than one fiber diameter from the end). Therefore, the assumption that end effects are negligible in the model is certainly valid. In fact, the error between theory and the finite element simulation was nearly zero for all fibers, indicating that existing errors are experimental in nature. One source for this error could be that the actual d_{31} of the material deviated from typical PZT-5H, which was used in the modeling. In addition, the fact that the error tends to increase with aspect ratio suggests it may be due to incomplete poling caused by the high electric field gradient. Nevertheless, this experimental effort agrees well with the effective d_{31} model, demonstrating the nonlinear decrease in free strain performance as aspect ratio is increased.

LAMINA MODEL

With the behavior of the single fiber known, it is no longer necessary to keep track of the micromechanics and electrical effects occurring within the fiber wall. Instead, the fiber is treated only as a simple piezoelectric element with an effective piezoelectric constant, allowing classical composite theory based on solid fibers to be directly applied.
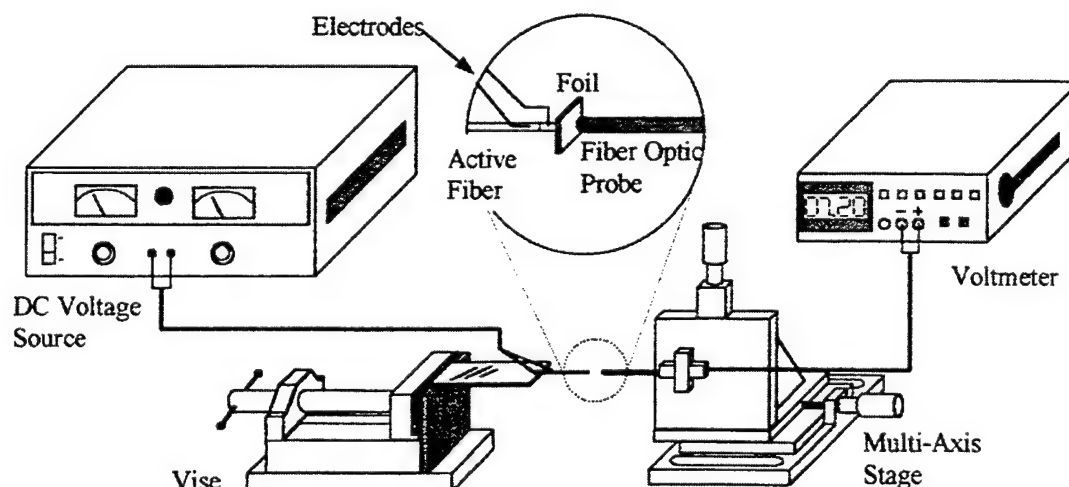
Figure 6. Active fiber free deflection test setup. To test the voltage/deflection response of a single fiber, the deflection was measured with a fiber optic displacement probe. Voltages were incremented from 0 to approximately 80 percent of the maximum working voltage for the fiber.

Figure 7. *Single fiber finite element model. The deflection of a single fiber was modeled using ABAQUS as a solver and Hypermesh as a pre- and post-processor. (a)Hypermesh model and (b) ABAQUS results.*

(a)

(b)
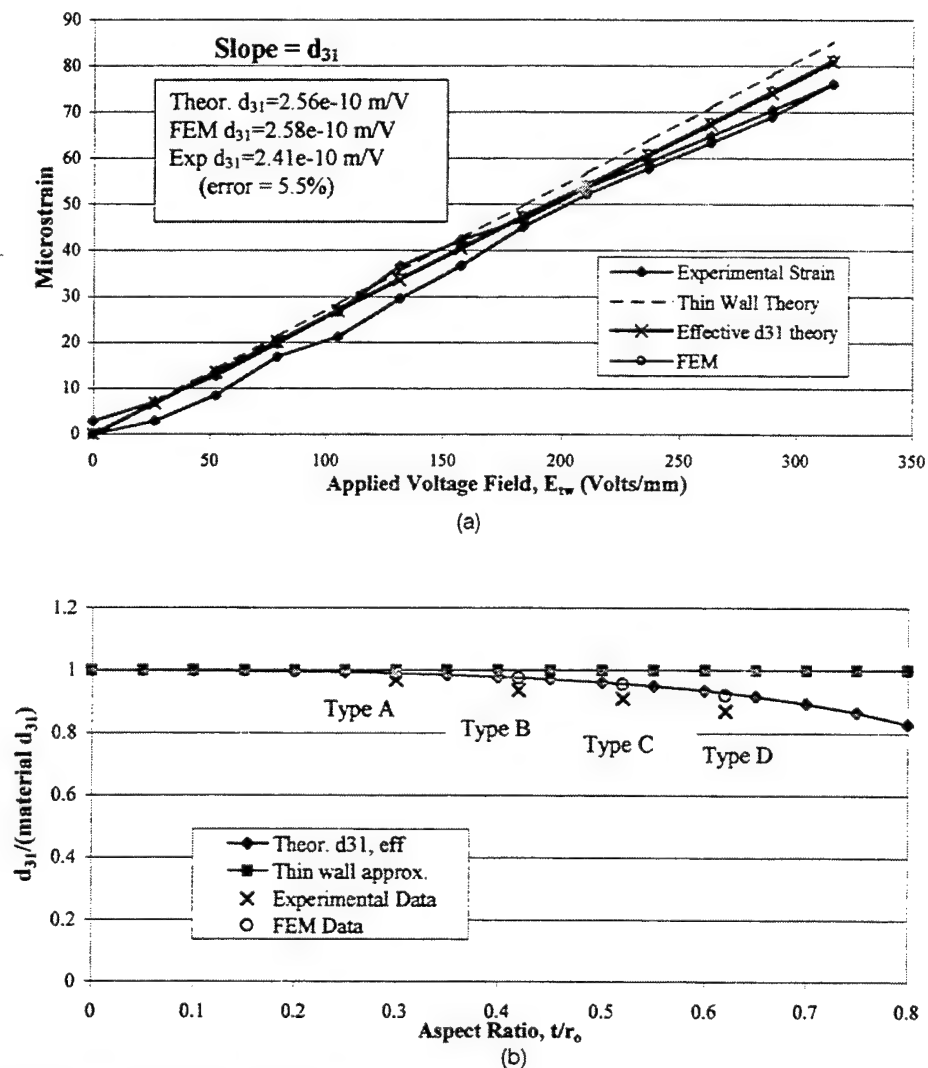
Figure 8. *Single fiber prototype free strain. The slope of the strain/field curve yields the effective d_{31}: (a) shows the strain of a single prototype (aspect ratio = 0.42) and (b) plots the effective d_{31} as a function of aspect ratio. The error between theory and measured values of effective d_{31} ranged from approximately 3 to 9 percent. FEM models match theory within one percent.*

Modeling

Following the same philosophy as the single fiber modeling. the equivalent stiffness and piezoelectric behavior of a thin lamina containing a row of hollow fibers is derived. To do this. the concentric cylinders fibrous composites model (Hashin and Rosen. 1964) was employed. This method was chosen because it has been shown (for inactive composites) to produce very accurate results for lamina properties in the axial direction. transverse direction. and in shear (Hyer, 1998). For the work presented here, however. only longitudinal properties were examined in detail. To apply this model. it was assumed that the all of the fibers were of equal size and aspect ratio. equally spaced. and arranged parallel within the lamina. It was also assumed that the Poisson's ratio of the fibers and the matrix were very close in value. in which case the longitudinal (fiber-direction) modulus of the lamina. Y_{lam}. is simply given by (Hyer. 1998)

$$Y_{lam} = Y_f v_f + Y_m(1 - v_f) \qquad (11)$$

where the subscripts f and m refer to the properties of the piezoelectric fiber and the matrix, respectively.

In a similar manner. because only the fibers strain internally. this "rule of mixtures" can be applied to determine the overall piezoelectric response of the lamina. By recognizing that the piezoelectric strain in the fiber direction is analogous to thermal strains in a conventional composite. the equivalent piezoelectric constant can be given by (Hyer, 1998).

$$d_{31,lam} = \frac{d_{31,eff} Y_f v_f}{Y_{lam}} \qquad (12)$$

Note that this only applies in the longitudinal direction on which this analysis is focused because. unlike thermal strains. piezoelectric materials strain orthotropically. The resulting free strain of the lamina is given by

$$\varepsilon_{lam} = d_{31,lam} E_{tw} \qquad (13)$$

Lamina Fabrication

A single layer composite was fabricated as a lamina prototype. Eight MFCX fibers with an aspect ratio of 0.42 (type B in Table 1) were embedded in epoxy using the process depicted in Figure 9. A small layer of Insulcast epoxy (Insulcure 24/Insulcast 501) was poured into a wax mold. The fibers were spaced equally across this epoxy layer so that the banded end protruded from one end of the lamina. This allowed all the fibers to be connected into an electrical bus. The remainder of the mold was filled with epoxy and allowed to cure. Once cured. the wax was melted and removed from the lamina and fibers. and copper wire was connected to the positive and negative electrodes to form the electrode bus. The resulting prototype (shown in Figure 9) measured 26 mm wide by 77 mm long with a thickness of approximately 2.8 mm. The lamina had a fiber volume fraction of approximately 4.6%, a very dilute composite.

Hollow Fiber Lamina Experimental Validation

The free strain of the lamina [Equation (13)] was validated using the same experimental setup and procedure as the single fiber. In addition, a finite element model was constructed using full 3D piezoelectric elements (ABAQUS type C3D20E) (Figure 10), with the matrix modeled as a concentric cylinder surrounding the individual fiber. The lamina was activated with voltages raised to 80 percent of the maximum working voltage of the fibers. The overall displacement of the lamina was measured at several points across its width

Figure 9. Lamina fabrication. A lamina prototype was fabricated using hollow piezoelectric fibers (aspect ratio 0.42) in an epoxy matrix. The banded ends of each fiber protruded from the lamina, allowing all fibers to be connected using a single pair of copper leads.
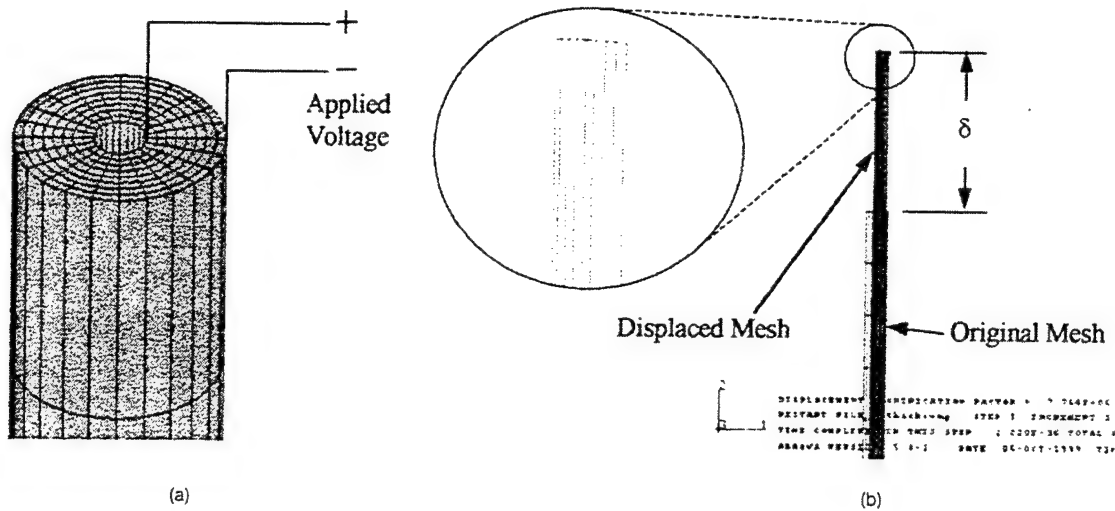
(a)   (b)

Figure 10. *Lamina finite element model. The deflection of a single fiber was modeled using ABAQUS as a solver and Hypermesh as a pre- and post-processor. (a) Hypermesh model and (b) ABAQUS results.*
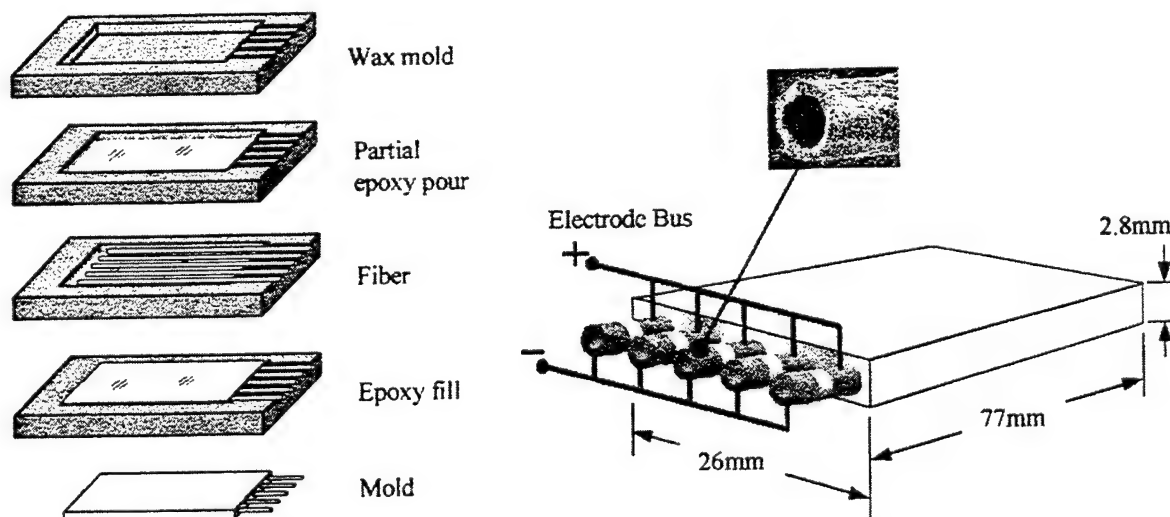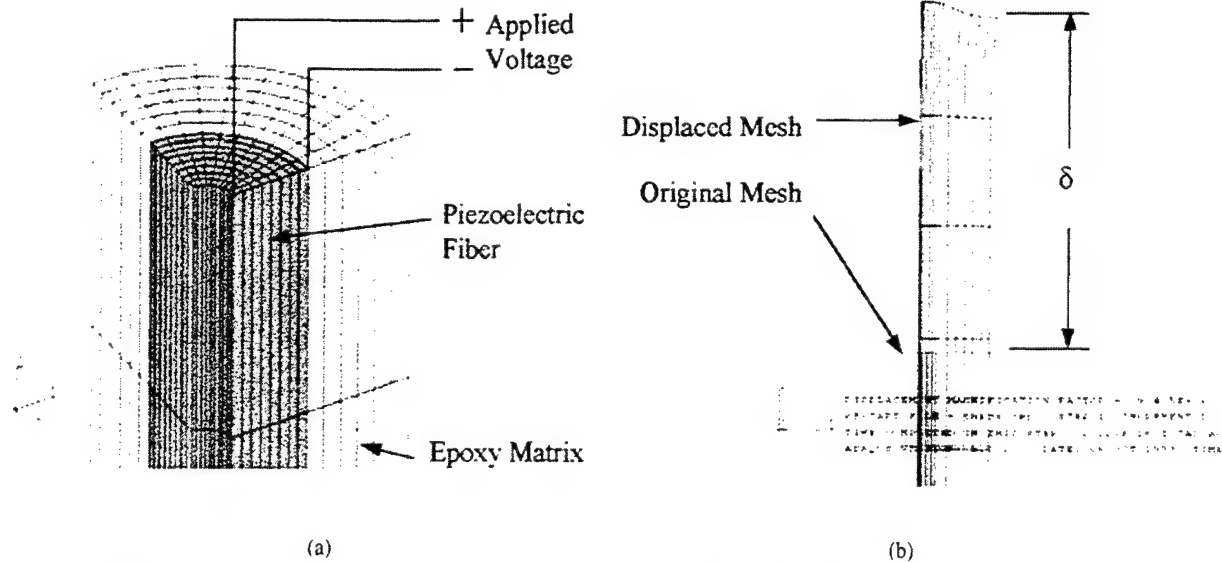
with the fiber optic displacement probe. The maximum lamina deflection measured was 3.7 microns at 60 volts. Figure 11 shows these results converted to strain and averaged across the width of the lamina. The error between theoretically predicted and experimentally measured lamina d_{31} values (slope of the strain/field curve) was approximately 6.5 percent. As with the single fiber testing, the finite element results agree very closely (within one percent) with the theory, suggesting experimental errors such as inaccurate material d_{31} values or incomplete poling. Yet the experimental results do correlate well with the lamina deflection model. They also demonstrate the feasibility of embedding and activating hollow fibers in active composites. Note that only 60 volts were needed to achieve 80% of full performance, showing the ability of hollow fibers to drastically reduce the voltage requirements of active composites.
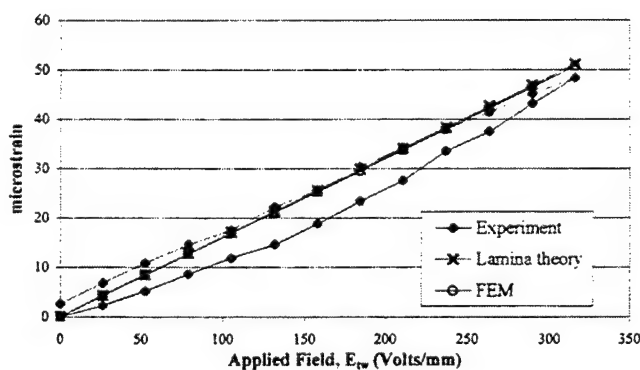

Figure 11. *Lamina prototype free strain. The slope of the strain/field curve yields the lamina equivalent piezoelectric constant. The error between theory and measured equivalent d_{31} was approximately 6.5 percent; the error between theory and FEM was less than 0.5 percent.*

Embedding Stress Model

The final portion of this feasibility study was a modeling effort in which the stresses on a hollow fiber during the embedding process were assessed. These stresses arise from the relative difference in strain between the matrix and the fiber as it is embedded. This strain differential can be caused by thermal effects during a casting process (thermal expansion coefficient mismatch), or strain induced during curing, as with epoxy. To determine these stresses, the fiber was first modeled as a cylindrical pressure vessel with an internal pressure equal to atmospheric. Using the expressions for radial and circumferential (hoop) stress in the vessel wall, the maximum Von Mises stress occurs at the interior wall (Young, 1989), and the only non-zero stresses at this location are hoop and axial (longitudinal) stresses. Therefore, for the remainder of the stress analysis, only the inside radius will be considered to maintain a worst-case failure condition. The value of the hoop stress, σ_θ, at this location, given zero internal pressure and outside pressure, p_o, can be expressed as

$$\sigma_\theta = \frac{-2p_o\beta^2}{\beta^2 - 1} \quad (14)$$

where β is a function of the aspect ratio (Figure 1).

$$\beta = \left(1 - \frac{t}{r_o}\right)^{-1} \quad (15)$$

The contraction of the matrix around the fiber results in an equivalent shrink fit interference, $\delta_m - \delta_f$, with the pressure between the fiber and matrix given by, (Shigley and Mischke, 1989):

$$p_o = \frac{(\delta_m - \delta_f)}{\frac{1}{Y_m}\left(\frac{1+v_f}{1-v_f}+\mu\right)+\frac{1}{Y_f}\left(\frac{\beta^2+1}{\beta^2-1}-\mu\right)} \qquad (16)$$

In this expression, v_f represents the quantity r_o^2/c^2 (Figure 1) and is essentially the overall volume fraction of the active material in the composite. This simplification is consistent with the assumptions of the concentric cylinders model used to model laminate properties (Hyer, 1998). Substituting the pressure [Equation (16)] into the hoop stress [Equation (14)], and non-dimensionalizing the stress by the Young's modulus of the fiber results in

$$\frac{\sigma_\theta}{Y_f(\delta_m-\delta_f)} = \frac{-2\beta^2}{(\beta^2-1)\left[\frac{Y_f}{Y_m}\left(\frac{1+v_f}{1-v_f}+\mu\right)+\left(\frac{\beta^2+1}{\beta^2-1}\right)-\mu\right]} \qquad (17)$$

This hoop stress is a function of the relative stiffness of the fiber and matrix, the fiber volume fraction, Poisson's ratio (μ), and of course the geometry of the fiber.

The longitudinal stress in each of the fibers was modeled in a similar way under the assumption that the bond between fiber and matrix was perfect. In this case, the rule of mixtures is applied to result in the following expression for longitudinal stress on the inside wall of the fiber, again in non-dimensional form,

$$\frac{\sigma_l}{Y_f(\delta_m-\delta_f)} = \frac{-1}{1+\left(\frac{Y_f}{Y_m}\right)(v_f)} \qquad (18)$$

Note that in the dilute composite case, this expression is conservative because it does not account for shear lag in the matrix. Finally, the non-dimensional Von Mises stress,

$$\sigma_{vm}^* = \frac{\sigma_{vm}}{Y_f(\delta_m-\delta_f)} = \frac{[\sigma_\theta^2+\sigma_l^2-\sigma_\theta\sigma_l]^{1/2}}{Y_f(\delta_m-\delta_f)} \qquad (19)$$

at the inner wall was calculated from the hoop and longitudinal stresses. The dimensionless Von Mises stress is plotted in Figure 12 as a function of the aspect ratio of the fibers and the modulus ratio of the composite for a mid-range volume fraction (35%). The feasibility plane shown on the graphs denotes the maximum allowable value of the non-dimensional stress (stress values above this plane exceed the maximum stress for typical piezoceramics). It can be seen that matrices much stiffer than the fiber, such as steel, will result in stresses above the failure limit of the piezoelectric ceramic regardless of the fiber aspect ratio. For softer metals and stiff carbon-fiber matrices, which have approximately the same modulus as piezoelectric ceramics, it was found that aspect ratios of at least 0.55 were needed to prevent fiber failure. These materials were examined because, unlike traditional active composites, the nature of hollow fibers allows them to be embedded in electrically conductive matrices. Finally, for low values of matrix stiffness and strain differential (epoxy, soft carbon-fiber matrices), stresses were well below the failure limit for all piezoelectric fibers with an aspect ratio exceeding only 0.09 (very thin wall). Therefore, although some metals such as steel are not suitable for use with hollow fibers, it is feasible to embed hollow fibers into epoxies, carbon fiber matrices of various hardness, and even soft metals such as aluminum and copper, provided the aspect ratio chosen is high enough.

CONCLUSIONS

This paper presents an investigation of the feasibility of hollow fibers for active composites. This study was based upon variations in the aspect ratio of the hollow fiber. An effective d_{31} model for an individual fiber was derived and used to develop a lamina model based upon classical com-
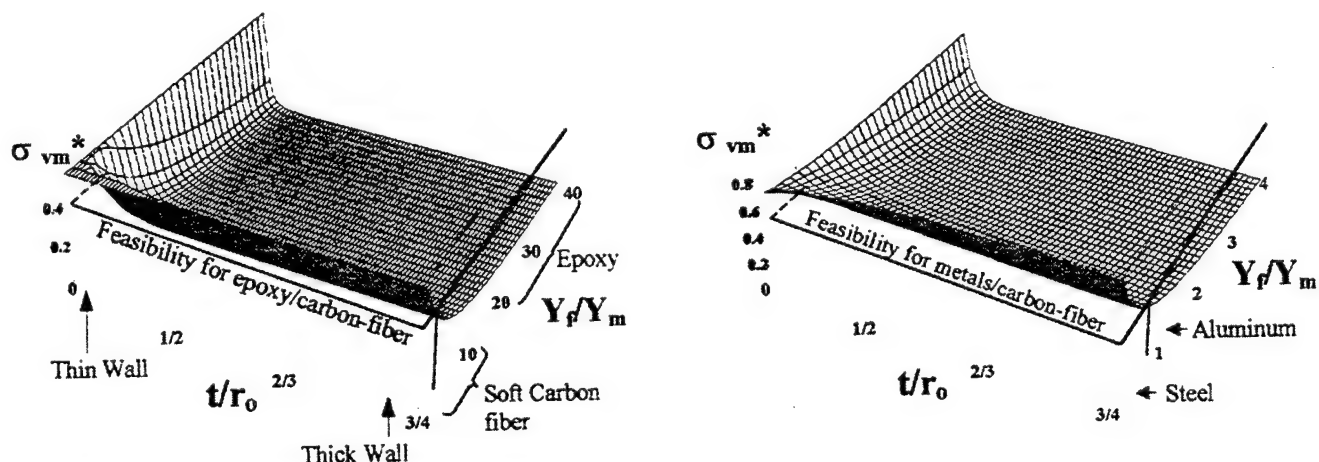

Figure 12. Non-dimensional fiber stress vs. aspect ratio and modulus ratio. The dimensionless Von Mises stress present during the embedding process was plotted as a function of the aspect ratio and the ratio of material moduli. The feasibility plane represents the maximum allowable stress in typical PZT fibers.

posite theory. From these models, it was shown that the electric field variation inherent in circular hollow fibers increased the potential for incomplete poling and even material damage as the aspect ratio (or wall thickness) of the fiber increased. The models also indicate that high aspect ratio fibers, although stronger, show decreased longitudinal strain when compared to thin wall fibers, highlighting critical design tradeoffs and the importance of aspect ratio on hollow fiber design.

To validate the fiber effective d_{31} model, four piezoelectric fiber prototypes with different aspect ratios were fabricated using a new manufacturing technique, Microfabrication by Coextrusion. The free strain of each prototype was measured in a series of experiments, with results correlating to within nine percent of the analytical model. Perhaps more importantly, these experiments demonstrated that it is feasible to manufacture, electrode, pole, and actuate hollow piezoelectric fibers at the microscale. Similarly, a successful validation of the lamina model was accomplished by deflection experiments conducted on a lamina prototype, consisting of eight similar hollow fibers embedded in epoxy. These tests showed that hollow fibers can be embedded in a matrix, and that many fibers can be activated through an electrode bus once incorporated into the composite, thereby decreasing wiring. The lamina model incorporating the effective d_{31} correlated to within six percent of the experimental values.

Hollow fibers lead to lower voltage requirements and allow embedment in electrically conductive matrices. This motivated the derivation of an embedding stress model to determine the overall feasibility of the fibers to be incorporated into a wide range of matrix materials. It was concluded that it is feasible to embed very thin wall PZT fibers in epoxy and soft carbon fiber matrices. Fibers with aspect ratios greater than 0.55 can be embedded into soft metals at a midrange fiber density, but hollow fibers are not viable with harder metals, such as steel.

In summary, even though hollow fibers can be susceptible to large electric field gradients and high stresses during the embedding process, if properly designed, they are feasible. This work clearly demonstrated that the hollow fiber concept can be implemented successfully. Hollow fibers have the advantages of lowering composite voltage requirements and being compatible with conductive matrix materials; thus, they have the potential to improve the state of the art of active composites.

NOMENCLATURE

A = Fiber cross-sectional area
c = Radius of equivalent matrix boundary
d_{31} = Piezoelectric material constant
$d_{31,eff}$ = Effective fiber d_{31}
$d_{31,lam}$ = Equivalent lamina d_{31}
E = Electric field
E_{avg} = Average electric field in fiber cross-section
E_{max} = Maximum electric field
E_{min} = Minimum electric field
E_{tw} = Thin wall electric field approximation, $E_{tw} = V/t$
F_{tot} = Piezoelectric force
p_o = External pressure
r = Radial position
r_o = Fiber outside radius
t = Fiber wall thickness
t/r_o = Fiber aspect ratio
V = Applied voltage
Y = Young's modulus
Y_{lam} = Equivalent lamina Young's modulus
Y_m = Matrix modulus
Y_f = Piezoelectric fiber modulus
β = Non-dimensional intermediate variable,
$\quad \beta = (1 - t/r_o)^{-1}$
δ_m = Matrix curing strain
δ_f = Fiber curing strain
ε = Piezoelectric free strain
μ = Poisson's ratio
v_f = Fiber volume fraction
σ_l = Longitudinal stress
σ_θ = Circumferential (hoop) stress
σ_{vm} = Von Mises stress
σ_{vm}^* = Non-dimensional Von Mises stress,

$$\sigma_{vm}^* = \frac{\sigma_{vm}}{Y_f(\delta_m - \delta_f)}$$

ACKNOWLEDGEMENTS

REFERENCES

Agrawal, S. K., Tong, D. and Nagaraja, K., 1994, "Modeling and shape control of piezoelectric actuator embedded elastic plates," *Journal of Intelligent Material Systems and Structures*, v5 n4, pp. 514–521.

Bent, A. A. and Hagood, N. W., 1997, "Piezoelectric fibrous composites with interdigitated electrodes," *Journal of Intelligent Material Systems and Structures*, v8.

Chen, P. C. and Chopra, I., 1996, "Induced strain actuation of composite beams and rotor blades with embedded piezoceramic elements," *Smart Materials and Structures*, v5 n1, pp. 35–48.

Crumm, A. T. and Halloran, J. W., 1998, "Microfabrication of Multicomponent Ceramics," *Journal of The American Ceramic Society*, v81, pp. 1053–1057.

Fernandez, J. F., Dogan, A., Zhang, Q. M., Tressler, J. F., and Newnham, R. E., 1995–1996, "Hollow piezoelectric composites," *Sensors and Actuators*, v51 n2, pp. 183–192.

Gururaja, T. R., Schulze, W. A., Shrout, T. R., Safari, A., Webster, L., and Cross, L. E., 1981, "High frequency applications of PZT/polymer composite materials," *Ferroelectrics*, v39 n 1–4 Pt 5, pp. 1245–1248.

Hagood, N. W. and Bent, A. A., 1993, "Development of piezoelectric fiber composites for structural actuation," *Collection of Technical Papers—AIAA/ASME Structures, Structural Dynamics and Materials Conference*, pt 6, p 3625–3638.

Halliday, D. and Resnick, R., 1988, *Fundamentals of Physics*. John Wiley & Sons, Inc., New York.

Hashin, Z. and Rosen, B. W., 1964, "The Elastic Moduli of Fiber-Reinforced Materials," *Transactions of the ASME, Journal of Applied Mechanics*. v31, pp. 223–232.

Herold-Schmidt, U., Floeth, E., Last, B., Schaefer, W. and Zaglauer, H. W., 1997, "Qualification of smart composites for use in aerospace applications," *Proceedings of SPIE—The International Society for Optical Engineering*. v3044, pp. 168–175.

Hyer, M. W., 1998, *Stress Analysis of Fiber-Reinforced Composite Materials*. The McGraw-Hill Companies, Inc., New York.

Jang, B. Z., 1993, "Intelligent composites and structures—a review," *Proceedings of the International Conference on Advanced Composite Materials*, p 661–667.

Krishna-Murty, A. V., Anjanappa, M. A. and Wu, Y., 1996, "Vibration control of magnetostrictive composite beams," *Proceedings of SPIE—The International Society of Optical Engineering*. v2717, pp. 482–491.

Maclean, B. J. and Jacobsen, S. C., 1995, "Active Fibers for Development of Adaptive Structures," *ARPA Actuator Issues Workshop*.

Rodgers, J. P., Bent, A. A. and Hagood, N. W., 1996, "Characterization of interdigitated electrode piezoelectric fiber composites under high electrical and mechanical loading," *Proceedings of SPIE—The International Society for Optical Engineering*. v2717 pp. 642–659.

Safari, A., 1994, "Development of piezoelectric composites for transducers," *Journal De Physique III*. v4 n7, pp. 1129–1149.

Safari, A., Janas, V., Jadidian, B., French, J., Weitz, G., Luke, J. and Cass, B., 1996, "Incorporation of piezoelectric $Pb(Zr,Ti)O_3$ fibers into ceramic/polymer composites," *Proceedings of SPIE—The International Society for Optical Engineering*. v2721, pp. 240–250.

Schetky, L. McD. and Wu, M. H., "Properties and processing of shape memory alloys for use as actuators in intelligent composite materials," *Smart Structures and Materials American Society of Mechanical Engineers, Aerospace Division (Publication)*, v24, pp. 65–71.

Shigley, J. E. and Mischke, C. R., 1989, *Mechanical Engineering Design*, The McGraw-Hill Companies, Inc., New York.

Sottos, N. R., Kline, G. E., Qidwai, M. A. and Lagoudas, D. C., 1996, "Analysis of phase transformation fronts in SMA composites," *Proceedings of SPIE*. v2715.

Wang, H., Zhang, Q. M., Cross, L. E. and Trottier, C. M., 1995, "Tailoring material properties by structure design—radially poled piezoelectric cylindrical tube," *Ferroelectrics*. v173, pp. 181–189.

Young, W. C., 1989, *Roark's Formulas for Stress and Strain*. The McGraw-Hill Companies, Inc., New York.

Zhang, Q. M., Cao, W., Wang, H. and Cross, L. E., 1993a, "Characterization of the performance of 1-3 type piezocomposites for low-frequency application," *Journal of Applied Physics*. v73 n3.

Zhang, Q. M., Wang, H. and Cross, L. E., 1993b, "Piezoelectric tubes and 1-3 tubular composites as tunable actuators and sensors," *Proceedings of SPIE—The International Society for Optical Engineering*. v1916, pp. 244–254.

Modeling and Study of the Quasi-Static Behavior of Piezoceramic Telescopic Actuation Architectures

DIANN BREI,* NEAL T. BERNER AND PAUL W. ALEXANDER

The University of Michigan, Department of Mechanical Engineering and Applied Mechanics, 2250 G. G. Brown Building, 2350 Hayward St., Ann Arbor, Michigan, 48109-2125, USA

ABSTRACT: Piezoelectric stacks are often used in smart structures applications that demand large forces. However, there are numerous applications that require slightly more displacement than is available from stacks, and the performance requirements allow room for some force to be sacrificed to obtain this displacement. A new type of piezoelectric actuation architecture, referred to as telescopic, was designed to meet the need for moderate displacement amplification (up to 20 times) while still producing large forces. This architecture internally leverages the piezoelectric strain by a series of cascading shells uniquely connected by end caps such that the shells "telescope" out when activated. This paper presents an analytical model to predict the force-deflection behavior of this actuator with compliant end caps. To aid in evaluating this new architecture, the losses due to architectural features such as end caps, gap size, number of shells, and constant thickness/area are presented along with a comparison to the current state of the art.

INTRODUCTION

EVEN though piezoelectric materials have high energy density, they are notorious for supplying low strains and overall displacements. Thus, actuation architectures commonly employ either external or internal amplification schemes. Internal amplification schemes such as benders (Kugel et al., 1997; Near, 1996; Koratkar and Chopra, 1997; Hall and Prechtl, 1996), rainbows and Thunders (Wise, 1997; Kugel et al., 1997; Elissalde and Cross, 1995; Heartling and Robinson, 1994; FACE Int'l, 1996), C-blocks (Moskalik and Brei, 1996), and Recurves (Ervin, 1999) can produce significant amplifications, but do so at the expense of force generation. There are numerous applications, such as heavy machinery isolation mounts (Martinez et al., 1996; Sumali and Cudney, 1994), active rotor blade flaps (Barrett and Brozoski, 1996; Hall and Prechtl, 1996; Samak and Chopra, 1996), and fuel injectors (Martin, 1995) that require much higher forces than these internal amplification schemes can supply. Even though most of these applications do not require the full force available from a stack, these applications generally do require more deflection (1 to 20 times more) than a stack. One solution for these types of applications are externally leveraged actuators (Samak and Chopra, 1996; Bamford et al., 1995), including such architectures as the X-frame (Prechtl and Hall, 1997) and the moonie or cymbal

(Sugawara et al., 1996; Onitsuka et al., 1995). However, many of these actuation architectures have significant transmission losses and packaging issues (Paine and Chaudhry, 1996).

This paper introduces a new piezoelectric actuation architecture called telescopic that exploits a unique internal amplification scheme to generate forces comparable to stacks with potential displacement amplifications in the range of 1 to 20 times that of a stack. The design and operation of this new family of actuators is described and a simple force-deflection model is derived for a fundamental actuator with compliant end caps. These models were validated with a variety of finite element models and the stress levels were confirmed to be below the strength of commonly used piezoceramic materials. The basic telescopic architecture was studied to identify the sensitivity of the quasi-static performance to design parameters such as gap size and number of shells. The paper concludes by evaluating the telescopic actuator with respect to the current state of the art.

TELESCOPIC ACTUATOR ARCHITECTURE

Conceptually, the telescopic leveraging scheme has concentric embedded piezoelectric shells that are connected at altering ends to effect a telescoping motion in a densely packed volume, as shown in Figure 1. The shells can have any cross section, but it is assumed that the cross section remains constant throughout the actuator's length, is of a shape that can be embedded within the

*Author to whom correspondence should be addressed.
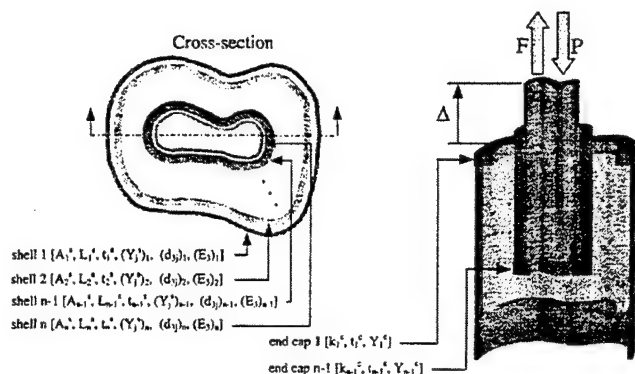E-mail: dibrei@engin.umich.edu

Figure 1. *General Telescopic Actuator Architecture: A depiction of a general telescopic actuator composed of n shells and n − 1 end caps.*

previous shell, and has a constant wall thickness. The telescopic actuator can be built in a monolithic configuration, or individual shells can be connected with discrete end caps. The number, length, and cross-sectional area of the cascaded shells can be varied to meet the force and deflection requirements for a given application. The telescopic actuator internal leveraging scheme can be applied to a d_{31} actuator or a d_{33} actuator.

The d_{31} telescopic actuator is a series of concentric, radially poled piezoceramic shells connected on alternating ends. The useful force and deflection of the actuator is in the axial direction of the shells. The actuator is electroded such that each shell is driven with a radial potential opposite to the radial potential of its neighboring shells. This electroding pattern causes each shell to expand (contract) while its neighboring shells contract (expand), and the activated actuator "telescopes" out. The total deflection of the actuator becomes the sum of the deflections of the individual shells. The operation of a three circular cylinder d_{31} telescopic actuator is shown in Figure 2.

The d_{33} telescopic actuator operates in the exact same manner as the d_{31} actuator except that the shells are ring stacks axially poled and activated through their length. This allows the shells in the d_{33} actuator to expand and contract in the d_{33} piezoelectric mode of actuation, where successive shells are activated oppositely, similar to the d_{31} actuator, generating the telescopic leveraging effect. Note though, that the d_{33} mode of actuation produces approximately 2.2 times the deflection of the d_{31} mode because of the higher piezoelectric coefficient in the poling direction.

ANALYTICAL MODELING

An analytical model to predict the quasi-static performance of a generic telescopic actuator was derived using Castigliano's theorem. To simplify the model, the
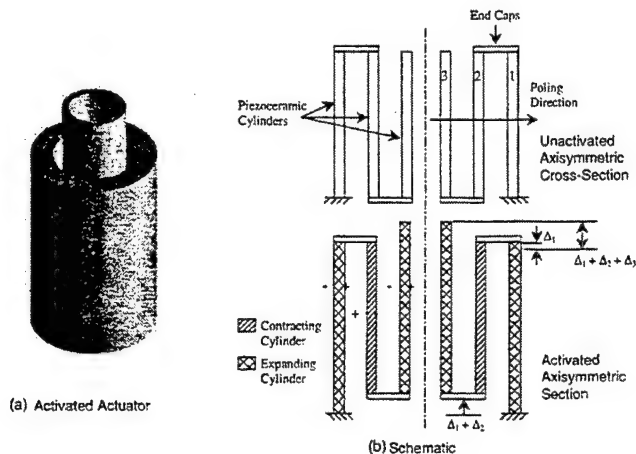

(a) Activated Actuator   (b) Schematic

Figure 2. *Telescopic Operation: Depicted is a three cylinder d_{31} actuator poled radially and alternatingly activated through the thickness resulting in expansion, contraction, and expansion of the respected tubes. The result is a net displacement equal to the sum of the individual displacements.*
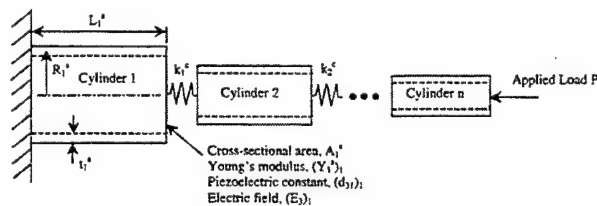
Figure 3. *Telescopic Analytical Model: The telescopic actuator is modeled as discrete cylinders connected by end caps modeled as springs.*

piezoelectric shells of the telescopic actuator were modeled as material under simple compression. The end caps of the telescopic actuator were considered to be compliant; and therefore, were modeled as linear springs connecting the piezoelectric shells as shown in Figure 3. The following assumptions were made:

- Piezoelectric induced radial strains are neglected in modeling the shells because the useful displacement, force, and work of the actuator is in the axial direction.
- All bonding layers are assumed to be ideal, with negligible thickness.
- The shells are long, thin, and of constant thickness.
- The end caps are made from an isotropic material.
- The deformed shape of the end cap is a linear function of the radial direction coordinate.

The goal of the derived analytical model was to develop a simple equation for the force-deflection behavior of a telescopic actuator with an arbitrary number of shells. This model could then be used for designing a telescopic actuator to meet the needs of a specific application. The derivation of this model is detailed below.

Strain Energy

Based on the simple one-dimensional linear piezo-electric constitutive equation, the stress due to the applied electrical and mechanical loads, σ_j^s, in the axial direction of a piezoelectric shell is given by:

$$\sigma_j^s = \frac{P}{A^s} - Y_j^s d_{3j} E_3 \qquad (1)$$

where P is the applied mechanical load, Y_j^s is the axial Young's modulus of the shell, and A^s is the cross sectional area of the shell. The piezoelectric constant, d_{3j}, relates the strain in the axial direction of the shell to the applied electric field, E_3. The j subscript in the above equation denotes the mode of actuation for the shell. The strain energy due to bending of the shells was assumed to be much less than the strain energy due to the axial loading. The strain energy, U^T, in an actuator consisting of n shells is given by:

$$U^T = \left(\sum_{i=1}^{n} \int_0^{L_i^s} \frac{(\sigma_j^s)_i^2 A_i^s}{2(Y_j^s)_i} dx \right) + \left(\sum_{i=1}^{n-1} \frac{P^2}{2k_i^c} \right) \qquad (2)$$

where k_i^c is the stiffness of the ith end cap, and L_i^s is the length of the ith shell. Substituting the stress given in Equation (1) into Equation (2), the resulting strain energy in the telescopic actuator is:

$$U^T = \left(\sum_{i=1}^{n} \int_0^{L_i^s} \frac{\left((P/A_i^s) - (Y_j^s)_i (d_{3j})_i (E_3)_i \right)^2 A_i^s}{2(Y_j^s)_i} dx \right)$$
$$+ \left(\sum_{i=1}^{n-1} \frac{P^2}{2k_i^c} \right) \qquad (3)$$

Force-Deflection Model

The strain energy of the actuator (Equation (3)) is used in Castigliano's second theorem to derive the force-deflection model for a telescopic actuator. The deflection of the entire actuator, Δ, is found by taking the partial derivative of the strain energy with respect to the applied load, P,

$$-\Delta = \frac{\partial U^T}{\partial P} = \left(\sum_{i=1}^{n} \frac{PL_i^s}{(Y_j^s)_i A_i^s} \right) + \left(\sum_{i=1}^{n-1} \frac{P}{k_i^c} \right) - \left(\sum_{i=1}^{n} (d_{3j})_i (E_3)_i L_i^s \right) \qquad (4)$$

Noting that the force, F, generated by the actuator balances the applied load, P, in the quasi-static case,

the general force-deflection model can be written as:

$$|F| = |P| = \frac{\sum_{i=1}^{n} \left((d_{3j})_i (E_3)_i L_i^s \right) - \Delta}{\left(\sum_{i=1}^{n} \left(L_i^s/(Y_i^s)_i A_i^s \right) + \sum_{i=1}^{n-1} (1/k_i^c) \right)} \qquad (5)$$

The stiffness of the actuator, k^T, is given by the slope of the force deflection relation,

$$k^T = \frac{1}{\left(\sum_{i=1}^{n} \left(L_i^s/(Y_j^s)_i A_i^s \right) + \sum_{i=1}^{n-1} (1/k_i^c) \right)} \qquad (6)$$

The free deflection of the actuator, Δ^T, is found when there is no applied load:

$$\Delta^T = \sum_{i=1}^{n} (d_{3j})_i (E_3)_i L_i^s \qquad (7)$$

which is simply the sum of the deflections of each individual shell. The blocked force, F^T, is found when the actuator deflection is completely negated:

$$F^T = \frac{\sum_{i=1}^{n} \left((d_{3j})_i (E_3)_i L_i^s \right)}{\left(\sum_{i=1}^{n} \left(L_i^s/(Y_j^s)_i A_i^s \right) + \sum_{i=1}^{n-1} (1/k_i^c) \right)} \qquad (8)$$

It is important to note the effect of the compliance in the end caps in the force-deflection model. The free deflection of the actuator (Equation (7)) is unaffected by the end caps. However, the force and stiffness of the actuator (Equations (5) and (6)) are affected by the stiffness of the end caps. If the end caps were assumed to be perfectly rigid, then from Equation (6), the stiffness of the actuator, k^T_r, would become:

$$k_r^T = \frac{1}{\left(\sum_{i=1}^{n} \left(L_i^s/(Y_j^s)_i A_i^s \right) \right)} \qquad (9)$$

End Cap Stiffness

The end cap stiffness is critical in predicting the telescopic architecture's performance when loaded. To derive the end cap stiffness terms used in the above calculations, the actuator was assumed to be cylindrical in nature, yielding round, washer-like end caps. Stiffness terms for other end cap geometries could be derived, but as the shape increases in complexity, so does the derivation of the stiffness value. The stiffness of the ith end cap, k_i^c, (in Equation (3)) was derived from shell bending theory applied to the cylinders bonded to the end cap. A free body diagram of a deformed end cap and its associated cylinders is shown in Figure 4 where P is the applied load. The shears and moments shown are
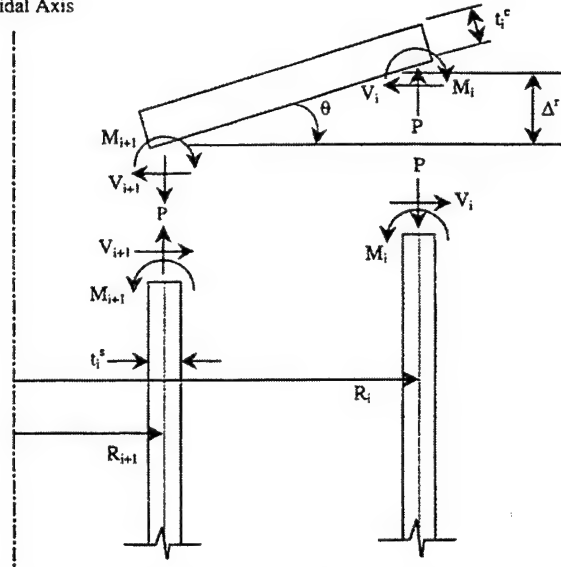
Figure 4. *Compliant End Cap Model: Shown is a compliant end cap connection between two piezoelectric cylinders and the resulting forces and moments.*

per unit circumferential length. From the conditions that the radial displacements, u, and the slopes, θ, at the ends of cylinders i and $i+1$ are equal, the following two equations arise (Young, 1989):

$$u = \frac{M_i}{2D_i^s\lambda_i^2} - \frac{V_i}{2D_i^s\lambda_i^3} = \frac{M_{i+1}}{2D_{i+1}^s\lambda_{i+1}^2} - \frac{V_{i+1}}{2D_{i+1}^s\lambda_{i+1}^3} \quad (10)$$

$$\theta = \frac{M_i}{D_i^s\lambda_i} - \frac{V_i}{2D_i^s\lambda_i^2} = \frac{M_{i+1}}{D_{i+1}^s\lambda_{i+1}} - \frac{V_{i+1}}{2D_{i+1}^s\lambda_{i+1}^2} \quad (11)$$

where M and V are the moment and shear, respectively, and D_i^s and λ_i are shell bending stiffness and geometric terms, respectively, given by (Young, 1989):

$$D_i^s = \frac{(Y_j^s)_i(t_i^s)^3}{12(1-(\nu_i^s)^2)} \quad (12)$$

$$\lambda_i = \left(\frac{3(1-(\nu_i^r)^2)}{R_i^2(t_i^s)^2}\right)^{1/4} \quad (13)$$

Y_j^s is the Young's modulus of the ith cylinder, t_i^s is the wall thickness of the ith cylinder, ν_i^s is the Poisson's ratio of the ith cylinder, and R_i is the mean radius of the cylinder as shown in Figure 4. Using Hooke's Law, the shear terms combine to cause a radial displacement in the end cap equal to the radial displacement of the two cylinders, giving:

$$V_iR_i + V_{i+1}R_{i+1} = \frac{Y_i^c t_i^c(R_i - R_{i+1} + t_i^c)}{(R_i + R_{i+1})}$$
$$\times \left(\frac{M_i}{D_i^s\lambda_i^2} - \frac{V_i}{D_i^s\lambda_i^3} + t_i^c\left(\frac{M_i}{D_i^s\lambda_i} - \frac{V_i}{D_i^s\lambda_i^2}\right)\right)$$

where Y_i^c is the Young's modulus of the ith end cap, and t_i^c is the thickness of the ith end cap. Summing the moments on the end cap yields:

$$(R_i - R_{i+1}) = 2\pi M_i R_i + 2\pi M_{i+1} R_{i+1}$$
$$+ 2\pi \nu_i^c D_i^c\left(\frac{M_i}{D_i^s\lambda_i} - \frac{V_i}{2D_i^s\lambda_i^2}\right) \quad (15)$$

where it is assumed that a unit mechanical load is applied to the actuator. The bending rigidity of the ith end cap, D_i^c, is defined as (Timoshenko and Woinowsky-Krieger, 1959):

$$D_i^c = \frac{Y_i^c(t_i^c)^3}{12(1-(\nu_i^c)^2)} \quad (16)$$

where ν_i^c is the Poisson's ratio of the end cap.

By solving the linear system defined by Equations (10), (11), (14), and (15), the moments M_i and M_{i+1}, and the shears V_i and V_{i+1} can be determined, from which the slope of the deformed end cap can be calculated (Equation (11)). This slope is then employed to determine the relative axial deflection between the two cylinders, Δ^r in Figure 4, which can be calculated from this slope. The stiffness of the ith end cap, k_i^c, is the mechanical load, P, divided by the relative axial deflection, Δ^r,

$$k_i^c = \frac{P}{\Delta^r} = \frac{1}{(R_i - R_{i+1} - t_i^c)\tan(M_i/D_i^s\lambda_i - V_i/2D_i^s\lambda_i^2)} \quad (17)$$

where it is assumed that a unit mechanical load is applied to the actuator.

The effects of end cap compliance are shown in Figure 5 by the difference in the force-deflection performance of a telescopic actuator with perfectly rigid end caps and an actuator with compliant end caps made of various materials. As seen in Figure 5, the slope (stiffness) for the aluminum end cap case is 15% less than the rigid end cap case. The blocked force (force at zero deflection) is also 15% less for the aluminum end cap case compared to the rigid end cap case. Losses for the steel and brass end caps were 9% and 12%, respectively. Thus, losses in the end caps can be significant and conscientious design, especially in material selection, is necessary.

FINITE ELEMENT MODEL AND RESULTS

To evaluate the validity of the analytical model, finite element models were created for a variety of cases and analyzed using ABAQUS software. The numerical
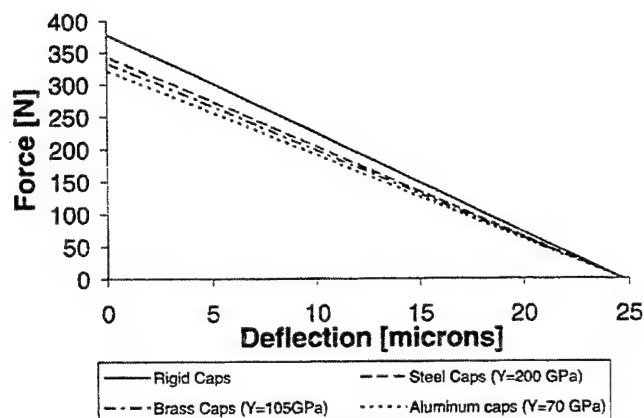
Figure 5. End Cap Material Comparison: Given is the force-deflection analytical results for a three tube PZT 5H actuator with 25.4 mm, 19.5 mm, and 12.7 mm dia. tubes 76 mm long each driven at 400 V. This shows the degradation in performance due to compliant end caps.

Figure 6. Force-Deflection Model Predictions: Shown is the force-deflection behavior predicted by the analytical and numerical model for a three tube PZT 5H actuator with 25.4 mm, 19.5 mm, and 12.7 mm outer dia. tubes 76 mm long each driven at 400 V. The correlation is to within 1.2%.

results from ABAQUS were then compared to the predictions made by the analytical model (Equation (5)). Telescopic actuators, using the d_{31} mode of activation, were modeled using 8-noded, biquadratic, piezoelectric, axisymmetric CAX8E elements. Use of these elements greatly decreases the amount of elements and nodes needed because only a two dimensional slice of the actuator has to be modeled for an axisymmetric analysis. To achieve a fixed end condition, the displacements of the finite element model were constrained in the radial and axial directions at the end of the outer cylinder. The mechanical load was applied to the model by applying a constant pressure to the faces of the elements at the free end of the inner cylinder. This pressure is related to actuator force, F, in the analytical model (Equation (5)) through the cross sectional area of the inner cylinder. An electric potential of 400 V was applied across the wall thickness of each cylinder. The assumption of constant thickness, thin-walled cylinders yields an easy calculation of the driving electrical field, E_3 (in Equation (5)), this is simply the potential, V, divided by the shell wall thickness, t^s.

The correlation between all models was very good. Force-deflection numerical and analytical results for an example telescopic actuator are shown in Figure 6. The actuator consisted of three PZT 5H cylinders 76 mm long with a wall thickness of 1 mm and outer diameters of 25.4 mm, 19.5 mm, and 12.7 mm. The aluminum end caps had a thickness of 3.175 mm. The error for the stiffness and blocked force of the analytical model with respect to the ABAQUS model was approximately 1.2%. The maximum stresses within the actuator were also numerically calculated. As would be expected, the highest stresses occur at end cap-shell junctions. However, stresses in all the simulations conducted (actuators composed of 20 or fewer shells) were found to be beneath the ceramic's tensile strength.
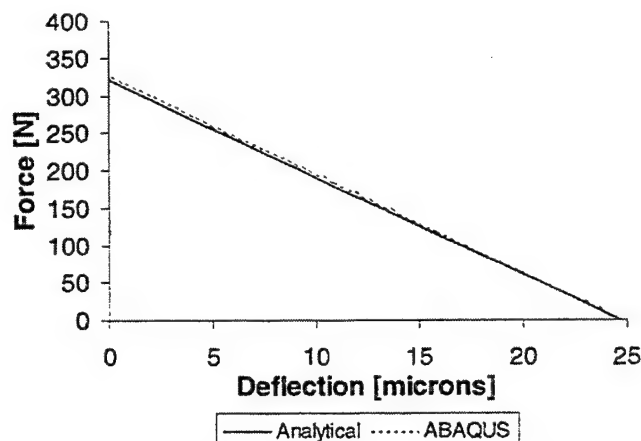
TELESCOPIC PERFORMANCE SENSITIVITY STUDY

As discussed in the modeling section, there can be substantial losses in performance due to improper end cap design. In addition to this, there are two main areas where work is lost due to this architecture design. First, as the number of shells is increased for a fixed actuator volume, the cross sectional area, and thus the force is decreased. Second, from a practical standpoint, there must be a gap between the shells when fabricated. This is potential active actuation volume being sacrificed, which also decreases the force and work output. Thus, to evaluate the telescopic actuator architecture, the sensitivity of the deflection, force, and work of the telescopic actuator was studied with respect to the length of the radial gap between the shells and number of shells. For this study, the following assumptions were made:

- The actuator shells are all assumed to be circular cylinders.
- All of the n cylinders in the telescopic actuator have the same length, L^s, and wall thickness, t^s.
- The end caps in the telescopic actuator have the same thickness, t^c, and are assumed to be perfectly rigid.
- The ratio of the piezoelectric strain coefficients d_{31} to d_{33} is 0.44.
- The ratio of the material compliances s_{33} to s_{11} is 1.22.
- The thickness of the end caps accounts for 5% of the total actuator length.

For the purposes of this sensitivity study, the quasi-static performance of the telescopic architecture was normalized with respect to an ideal circular stack actuated in the d_{33} mode and exhibiting no losses that are typically present in actual devices of this nature. Both the telescopic and the baseline actuators were

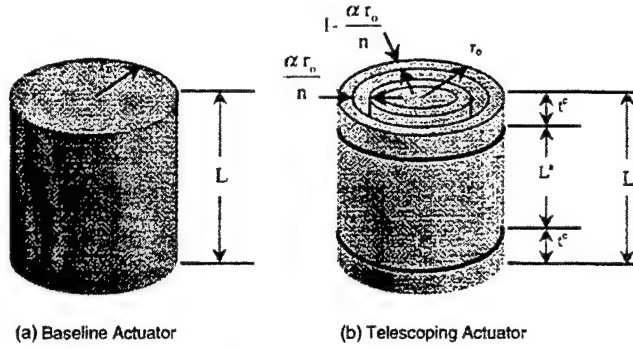(a) Baseline Actuator   (b) Telescoping Actuator

Figure 7. Sensitivity Study Parameters: The telescopic actuator is normalized with respect to an equivalent size idealized baseline stack made from the same material driven in the d_{33} mode with no losses.

made out of the same piezoelectric material, were driven at the same electric field, E, and were of the same overall length, L, and outer radius, r_o (see Figure 7). Comparison ratios were then formulated for the free deflection, Δ^T, blocking force, F^T, and work, W^T, of the telescopic actuator by normalizing these values with respect to the free deflection, Δ^P, blocking force, F^P, and work, W^P, of a baseline actuator. To facilitate the derivation of these performance factors, each is written in terms of the actuator gap parameter, α, which is defined as the percentage of the ideal tube thickness (r_o/n) that is set aside for the inter-tube gap.

The first of these comparison ratios relates the deflection of the telescopic actuator to that of the baseline actuator. This deflection amplification factor, Ω, is the factor by which the free deflection of an actuator is amplified when compared to that of a comparable idealized stack. For an n-cylinder telescopic architecture, the factor is:

$$\Omega = \frac{\Delta^T}{\Delta^P} = \frac{nd_{3j}(L - 2t^c)}{d_{33}L} \qquad (18)$$

The subscript j is these equations denotes the mode of activation for the telescopic actuator, with 3 corresponding to the d_{33} mode and 1 corresponding to the d_{31} mode.

The amplification of displacement comes at a cost to the actuation force. To quantify these losses, the force reduction factor, Ψ, was derived. For the telescopic actuator, the ratio between its force and that of the idealized stack is:

$$\Psi = \frac{F^T}{F^P} = \frac{d_{3j}S_{33}(1 - \alpha)}{d_{33}s_{jj}n \sum_{i=1}^{n} 1/(2i - 1 + \alpha)} \qquad (19)$$

For an ideal actuation architecture, the force reduction and deflection amplification would negate each other, resulting in the same amount of actuator work as the idealized case. In reality, there are transmission and

packaging losses inherent to any architecture, reducing actuator work. The work efficiency factor, Φ, is the ratio of the work output of an actuator to that of an equivalent, idealized stack. This equation reduces to the following for the telescopic architecture:

$$\Phi = \Omega\Psi = \frac{W^T}{W^P} = \frac{\Delta^T}{\Delta^P}\frac{F^T}{F^P} = \frac{d_{3j}^2 s_{33}(1 - \alpha)(L - 2t^c)}{d_{33}^2 s_{jj}L \sum_{i=1}^{n} 1/(2i - 1 + \alpha)} \qquad (20)$$

This can also be viewed in terms of work loss by defining a work loss factor, Θ, for a given architecture as one minus the work efficiency factor. For the telescopic actuator this is:

$$\Theta = 1 - \Phi = 1 - \frac{d_{3j}^2 s_{33}(1 - \alpha)(L - 2t^c)}{d_{33}^2 s_{33}L \sum_{i=1}^{n} 1/(2i - 1 + \alpha)} \qquad (21)$$

Assuming a cylindrical actuator, Figure 8 depicts the plots of these comparison factors for a d_{31} architecture in terms of the number of actuation shells, n, and a range of gap parameters, α. As seen in Figure 8a, the deflection amplification factor increases linearly as the number of cylinders, n, increases and is independent of the size of the gap between the shells. The deflection amplification ratio dips below unity because of the inferiority of the d_{31} coefficient compared to the d_{33} coefficient of the ideal stack. Thus, a couple of cylinders are needed to make this architecture viable in the d_{31} mode. The force reduction factor decreases inversely with additional actuator shells. This behavior is due to the fact that, in this comparison, only a set amount of cross-sectional surface area is available and it must be divided equally among all of the actuator shells. Additional shells mean a reduction in individual tube surface area, which is directly related to the force generated, accounting for the drop in actuator blocking force. This is the most substantial loss mechanism. The force also decreases slightly with increasing gap size (Figure 8b), due again to loss in area, but this loss is not as significant as that attributed to the number of actuator cylinders. The work efficiency factor also decreases nonlinearly with increasing actuation tubes, and decreases with increasing gap size as shown in Figure 8c, and the work loss factor behaves in a converse manner, illustrated in Figure 8d.

When comparing the d_{31} telescopic architecture to an ideal stack, the performance is obviously limited by the lower piezoelectric coefficient than that of the d_{33} mode. Because of the telescopic architecture's versatility, an actuator can also be constructed to utilize the d_{33} mode of actuation. Figure 9 displays the derived performance factors (Equations (18)–(21)) for both the d_{31} and d_{33} telescopic actuator versus the number of actuation tubes. The linear deflection amplification factor
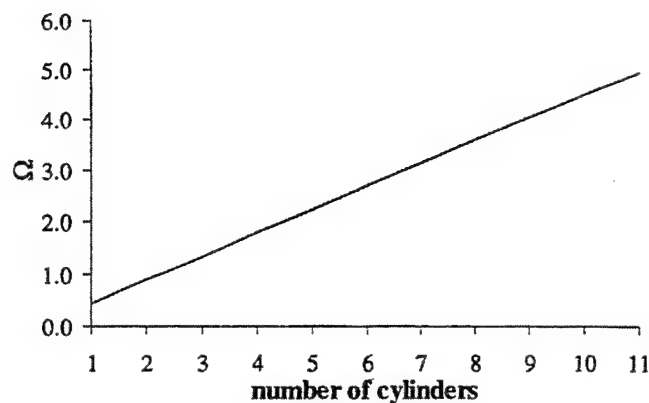
(a) Deflection Amplification Factor
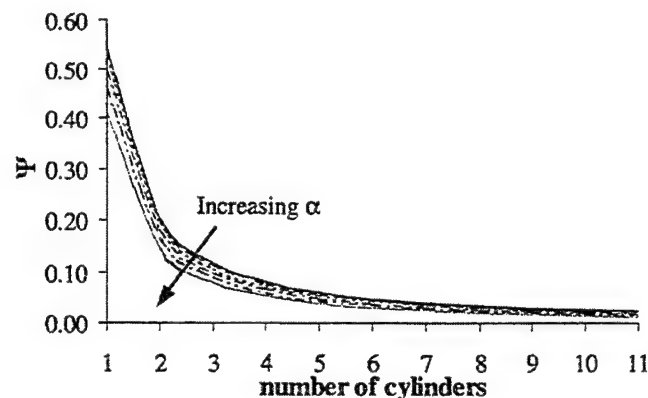
(b) Force Reduction Factor
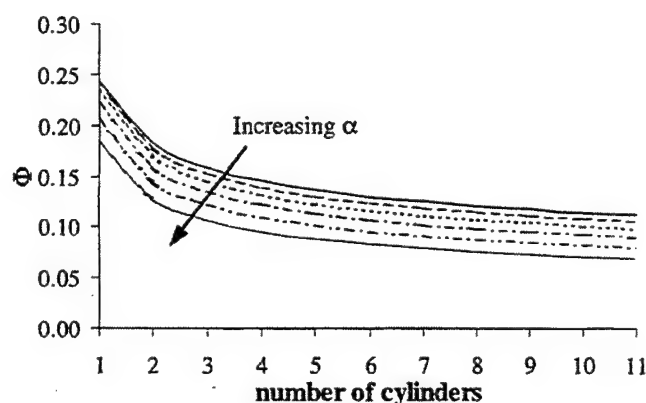
(c) Work Efficiency Factor
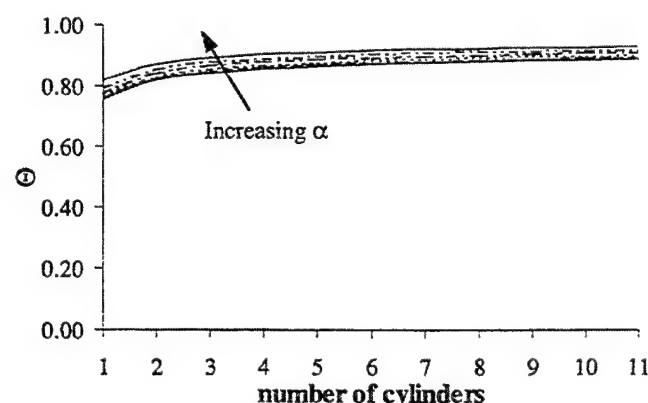
(d) Work Loss Factor
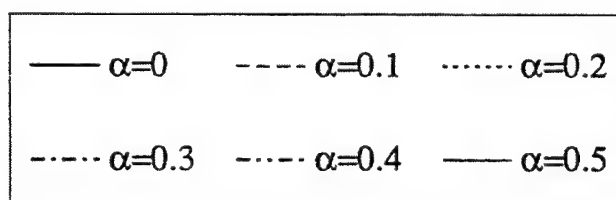
Figure 8. *Comparison factors for d_{31} Telescopic Actuators: A d_{31} constant thickness actuator is plotted relative to increasing number of cylinders and gap size, given a fixed actuation volume.*

(Figure 9a) effectively displays the jump in actuator performance because of the change in actuation mode. Note that for the d_{33} mode of actuation, the displacement is either equivalent to the idealized stack ($n = 1$) or is amplified. Assuming a 30% loss in cylinder stiffness due to bonding layers in the d_{33} telescopic actuator, Figure 9b shows the force reduction factor of the telescopic actuators. In addition to the improved material performance and because the d_{33} actuator is activated by generating a field in the *axial* direction, it is possible to use cylinders with differing wall thickness. Therefore, the actuator can also be constructed so that each cylinder has the same cross-sectional area (and thus the same stiffness) versus the constant thickness

requirement of the d_{31} mode. While the constant area versus constant thickness does not have much impact on the displacement of the actuator, the force and work can be significantly improved by the constant area design. As seen in Figures 9c and 9d, the work factors are constant for the d_{33} constant area actuator and are as high as theoretically possible given the assumed loss mechanisms. Naturally, there will still be a reduction in work due to increasing gap size, stemming from the fact that any gap present in the actuator volume is wasted when compared to the baseline stack where the entire actuator volume is contributing to the actuator's performance. But this is inherent to the architecture and is present in either a d_{31} or d_{33} mode actuator.
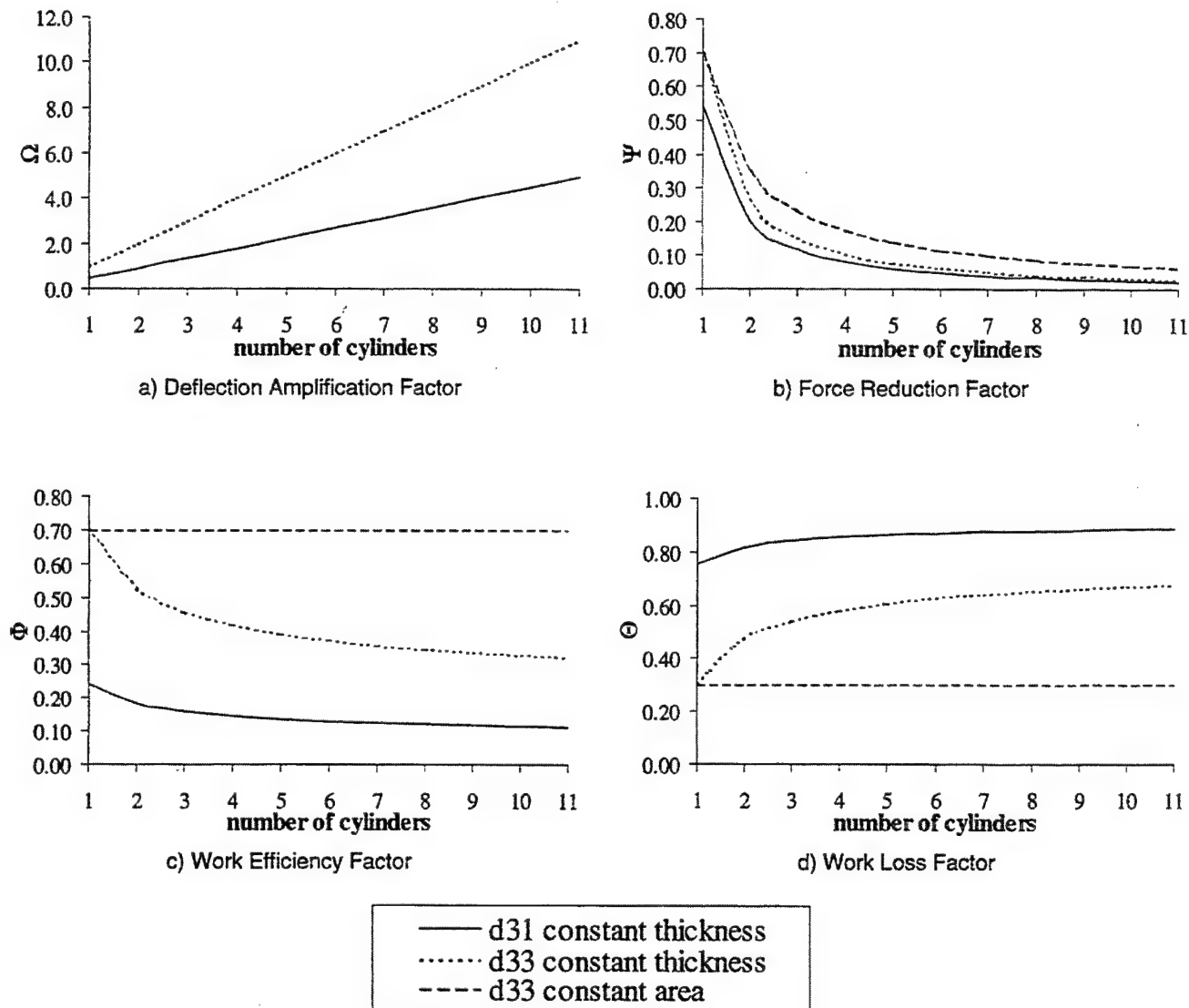
Figure 9. d_{31} *versus* d_{33} *Telescopic Actuator Architectures: The* d_{31} *constant thickness actuator is compared to the* d_{33} *constant thickness and constant area architectures.*
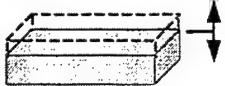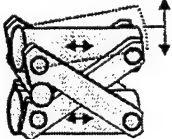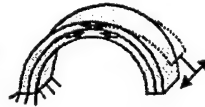
Therefore, a d_{33} mode actuator is preferable to a comparable d_{31} actuator. The improved performance of the d_{33} mode actuator can be broken down into two basic facets: the additional strain available in this mode of actuation and the freedom to design actuator tubes of varying and larger cross-sections. It should be noted that the d_{33} mode actuator is more complicated to manufacture, which may lead to increased cost and losses due to bonding layers. If these factors are significant, the d_{31} mode of actuation may be competitive because of its simplicity.

ACTUATOR ARCHITECTURE COMPARISON

The comparison ratios were also used to compare the telescopic actuator architecture to other piezoelectric

actuator architectures (Ervin,1999). The displacement, force, and/or work for a variety of commonly used piezoelectric actuator architectures were collected from research literature and were normalized as in the previous section by an idealized d_{33} stack of the same material and package volume. The resulting comparison ratios are given in Table 1. This is by no means an exhaustive comparison of all piezoelectric actuation options, but does give insight into what application niche the telescopic architecture falls. The values given for the d_{31} and d_{33} telescopic actuators reflect an assumption of a 15% loss in actuator force due to compliant end caps. As Table 1 shows, the telescopic architecture yields displacement amplification similar to actuators such as leveraged stacks, moonies, and c-blocks. While the displacement maybe slightly lacking, this architecture does excel at its designed purpose,

Table 1. **Comparison of Actuator Architectures.**

Architecture	Displacement Amplification Factor	Force Reduction Factor	Work Efficiency Factor	Work Loss Factor
d_{33} Plate (EDO, 1996)	1.0	1.0	1.0	0.0
Stack (Prechtl and Hall, 1997)	1.0	0.70	0.70	0.30
Leveraged Stack (Prechtl and Hall, 1997)	2–80	2.0e-5–3.2e-2	0.18	0.82
d_{31} Plate (EDO, 1996)	0.44	0.54	0.24	0.76
Moonie (Sugawara et al., 1992) (Onitsuka et al., 1995)	4–15	6.5e-4–1.8e-3	0.009	0.991
C-Block (Moskalik and Brei, 1996)	4–67	2.3e-3–3.3e-2	0.15	0.85
Rainbow (Wise, 1997) (Kugel et al., 1997)	7–1800	2.0e-5–4.1e-3	0.03	0.97
Bimorph Bender (Near, 1996) (Kugel et al., 1997)	33–7400	1.7e-5–2.6e-3	0.13	0.87
Recurve (Ervin, 1999)	33–7400	1.7e-5–2.6e-3	0.13	0.87
d_{33} Telescopic	1–20	2.8e-2–0.6	0.40	0.60
d_{31} Telescopic	1–20	1.9e-2–0.17	0.15	0.85

output force. As evidenced by the force reduction factors in Table 1, only the solid plates and stack actuator out perform the telescopic architecture. Both of the work comparison factors calculated for the telescopic exceed or are on par with other actuation architectures; however, none of the other actuation amplification architectures generate the same order of magnitude of force coupled with the deflection amplification. This validates the potential of this design to fill a certain actuation application niche. The niche includes applications that require a similar magnitude of force as a stack provides, and 1 to 20 times the deflection. Examples include active mounts, fuel injectors or active rotor blades.

CONCLUSION

A new type of internally leveraged actuation archi-
tecture called the telescopic actuator has been proposed
for smart structures applications approximately requir-
ing up to 20 times more deflection than a stack, and
forces on the same order of magnitude as a stack. To
evaluate this architecture, an analytical model for the
force-deflection behavior of the telescopic actuator was
derived using Castigliano's second theorem. Results
from the analytical model were also compared with an
ABAQUS finite element model for verification. A study
of the deflection, force, and work of the telescopic
actuator normalized with respect to the same metrics for
an idealized d_{33} plate was performed using the analytical
model. The comparison ratios were studied with respect
to the number of cylinders, gap size, material mode of
actuation, and constant area versus constant thickness
designs. These ratios were also utilized to compare the
telescopic actuator architecture to other commonly used
piezoelectric actuator architectures. From this, the
following conclusions can be drawn.

The force-deflection analytical model agreed very well
with the results from the finite element model. Both
models predicted linear behavior, and the error between
the stiffness calculated from the analytical model and
the stiffness of the finite element model was approxi-
mately 1.2%. This agreement verifies that the analytical
model is a useful tool for designing a telescopic actuator
for a specific application.

The sensitivity study provided many useful insights
into the behavior and losses of the telescopic architec-
ture. The deflection amplification of any telescopic
actuator architecture increases linearly with increa-
sing number of shells, and is independent of the gap
between the shells and end cap effects. Unfortunately,
improper end cap design can contribute up to 15%
losses in force generation. In addition, the force of
constant thickness telescopic actuator architectures
decreases dramatically and nonlinearly with increasing
number of shells, and shows a relatively small reduction
with increasing gap length. This causes the work
efficiency of the telescopic actuator to also decrease
nonlinearly with increasing number of shells, with a
reduction in work output with increasing gap length.
These effects can be mitigated by using constant area
telescopic architectures that yield a proportional loss in
force with increased deflection, resulting in available
work that is independent of the number of actuator
cylinders. However, constant area is only convenient
with d_{33} mode actuators.

Despite these drawbacks, the telescopic actuator has
potential to produce a similar amount of normalized
work per volume as other currently used actuators. In
particular, the telescopic actuator has the potential to
produce more work per volume than a leveraged stack,

which is currently used in applications requiring
relatively low displacements and high forces.

The telescopic actuator is capable of deflection
amplification on par with such actuation technologies
as leveraged stacks, moonies, and c-blocks, while
excelling in forcing characteristics that can only be
rivaled by solid plate and stack actuators. With work
capabilities similar to other actuation architectures, the
telescopic architecture can indeed be useful for many
smart material and structure applications.

REFERENCES

Bamford, R., Kuo, C. P., Glaser, R. and Wada, B. K. (1995). Long
Stroke Precision PZT Actuator. *AIAA/ASME/ASCE/HAS/ASC
Structures, Structural Dynamics, and Materials Conference –
Collection of Technical Papers*. New York: AIAA. pp. 3278–3284.

Barret, R. and Brozoski, F. (1996). Adaptive flight control surfaces,
wings, rotors, and active aerodynamics. In: Chopra, I. (Ed.), *Smart
Structures and Materials 1996: Smart Structures and Integrated
Systems*. Proc. SPIE 2717, pp. 178–198.

EDO Corporation. (no date). *Piezoelectric Ceramics: Material
Specifications, Typical Applications*. 2645 South 300 West, Salt
Lake City, UT.

Elissalde, C. and Cross, L. E. (1995). Dynamic Characteristics of
Rainbow Ceramics. *Journal of the American Ceramic Society*, **78**:
2233–2236.

Ervin, J. (1999). Design, Characterization, and Assessment of the
Recurve Actuation Architecture. Doctoral Dissertation, University
of Michigan, USA.

FACE International Corporation (1996). THUNDER, Thin-Layer
Composite Unimorph Ferroelectric Driver and Sensor. 427 W.
35th St., Norfolk, VA.

Giurgiutiu, V., Rogers, C. A. and Chaudhry, Z. (1996). Energy-based
Comparison of Solid-state Induced-strain Actuators. *Journal of
Intelligent Material Systems and Structures*, **7**: 4–14.

Haertling, G. H. and Robinson, G. C. (1994). Compositional Study of
PLZT Rainbow Ceramics for Piezo Actuators. In: Pandey, R.K.,
Liu, M. and Safari, A. (Eds.), *Proceedings of the 9th IEEE
International Symposium on Applications of Ferroelectrics*, IEEE,
pp. 313–318.

Kugel, V. D., Chandran, S. and Cross, L. E. (1997). Comparative
Analysis of Piezoelectric Bending-mode Actuators. In: Simmons,
W. C., Aksay, I. A. and Huston, D. R. (Eds.), *Smart Structures and
Materials 1997: Smart Materials Technologies*. Proc SPIE 3040.
pp. 70–80.

Martin, R. (1995). Ein neues elektronisches Hochdruck-Einspritz-
system fuer Disselmotoren. *MTZ Motortechnische Zeitschrift*, **56**:
142–148.

Martinez, D. R., Hinnerichs, T. D. and Redmond, J. M. (1996).
Vibration control for precision manufacturing using piezoelectric
actuators. *Journal of Intelligent Material Systems and Structures*, **7**:
182–191.

Moskalik, A. and Brei, D. (1996). Force-Deflection Behavior of
Individual Piezoceramic C-Block Actuators. *Proceedings of the
ASME 1996 International Mechanical Engineering Congress and
Exposition*.

Near, C. D. (1996). Piezoelectric Actuator Technology. In: Chopra, I.
(Ed.), *Smart Structures and Materials 1996: Smart Structures and
Integrated Systems*. Proc. SPIE 2717, pp. 246–258.

Onitsuka, K., Dogan, A., Tressler, J. F., Xu, Q., Yoshikawa, S. and
Newnham, R.E. (1995). Metal-ceramic composite transducer, the
'moonie'. *Journal of Intelligent Material Systems and Structures*, **6**:
447–455.

Paine, J. S. N. and Chaudhry, Z. (1996). The Impact of Amplification
on Efficiency and Energy Density of Induced Strain Actuators.

In: Chang, J.C.I., Coulter, J., Brei, D. Martinez, D., Ng, W. and Friedman, P.P. (Eds.), *Proceedings of the ASME Aerospace Division*, AD-Vol. 52, ASME, New York. pp. 511–516.

Prechtl, E.F. and Hall, S.R. (1997). Design of a High Efficiency Discrete Servo-flap Actuator for Helicopter Rotor Control. In: Regelbrugge, M.E. (Ed.), *Smart Structures and Materials 1997: Smart Structures and Integrated Systems*. Proc. SPIE 3041, pp. 158–182.

Samak, D.K. and Chopra, I. (1996). Design of High Force, High Displacement Actuators for Helicopter Rotors. *Smart Materials and Structures*, **5**: 58–87.

Sugawara, Y., Onitsuka, K., Yoshikawa, S., Xu, Q., Newnham, R.E. and Uchino, K. (1992). Metal-ceramic Composite Actuators. *Journal of the American Ceramic Society*, **75**: 996–998.

Sumali, H. and Cudney, H. (1994). An active engine mount with a piezoelectric stacked actuator. *Proceedings of the 35th SDM Conference*, New York: AIAA. pp. 1233–1241.

Timoshenko, S. and Woinowsky-Krieger (1959). *Theory of Plates and Shells*. New York: McGraw-Hill. pp. 5, 52.

Tzou, H.S. (1989). Development of a Light-weight Robot End-effector Using Polymeric Piezoelectric Bimorph. *Proceedings of the 1989 International Conference on Robotics and Automation*, Vol. 3, Washington D.C.: IEEE Computer Society. pp. 1704–1709.

Wise, S. (1997). Displacement Properties of RAINBOW and THUNDER Piezoelectric Actuators. *Sensors and Actuators*, **A-69**: 33–38.

Young, W. (1989). *Roarks's Formulas for Stress and Strain*. New York: McGraw-Hill. pp. 530–534.

PIEZOCERAMIC HOLLOW FIBER ACTIVE COMPOSITES

Bryan J. Cannon, Diann Brei

Department of Mechanical Engineering and Applied Mechanics,
The University of Michigan, Ann Arbor, MI 48109

ABSTRACT

While active fiber composites (AFC) based upon solid cross-section piezoelectric fibers are very useful for anisotropic activation of composites, they require high voltages and are constrained to non-conductive matrix materials. AFC's based upon hollow cross-section piezoelectric fibers have shown promise to lower operating voltages and broaden the choice of possible matrix materials. This paper presents an investigation of the key design parameters for hollow piezoelectric fibers (matrix/fiber Young's moduli, aspect ratio of the individual fibers, and the overall active composite volume fraction) and their effect on the performance, manufacturing · and reliability of active fiber composites. Because the ultimate objective in utilizing active composites centers on their ability to deform, an analysis was conducted on existing fiber and lamina strain/electric field models to identify optimal parameter values and determine limitations via an embedment stress model. Fabrication of the fibers has a clear impact on these factors. To assess this, standard machinery inspection criteria was used to evaluate fibers, manufactured through microfabrication by coextrusion (MFCX), with respect to their geometric (cross-sectional ovality, eccentricity, straightness) and material (density, porosity, piezoelectric properties, Young's modulus) properties. These studies indicated that there are circumstances under which low aspect ratio (thin walled) fibers will be optimal, but clearly, reliability issues will arise. Unfortunately, little data exists on reliability of either hollow or solid piezoelectric fibers. To identify the primary failure mechanism, ultimate strength, strain-to-failure and interfacial shear strength were examined using three types of experimental tests: 1) tensile strain-to-failure, 2) single fiber fragmentation, and 3) single fiber indentation. From this work, it is clear there will always be design trade-offs present and it is important to consider performance, fabrication, and reliability

issues simultaneously in the design of hollow piezoelectric fiber active composites.

Keywords: Active composites, piezoelectric, piezoelectric fibers, hollow fiber, smart structures, active fiber composites, PZT.

INTRODUCTION

Active Fiber Composites (AFC), ones in which smart materials are embedded directly into the composite matrix, have received a great deal of attention[1-5] because they possess desirable characteristics for a wide range of smart structure applications such as vibration, shape, and flow control.[6-11] One major advantage to AFC's is the ability to create anisotropic laminate layers, making them particularly useful in applications requiring off-axis or twisting motions.[1,2] In addition, embedded fibers are damage tolerant and do not negatively affect the composite's interface with the environment. A common form of AFC that can generate high levels of strain (as high as 1700 microstrain) is based on embedded solid piezoelectric fibers activated by an external interdigitated electrode pattern.[2] This type of AFC has been employed in a twist configuration for control of a rotorcraft blade, where twist angles of several degrees have been achieved.[10] The major drawback to this approach is the requirement of the electric field to pass through the composite matrix. Due to the placement of the electrode on the matrix surface, electric field losses are significant requiring high voltages (on the order of 1 kV) for actuation.[12] Furthermore, this approach limits the matrix to electrically nonconductive materials, which is particularly a problem in large structure and air vehicle applications where metals and carbon fiber composites are almost exclusively utilized in construction.

An alternative approach to solid fiber AFC's is based upon hollow piezoelectric fibers (Figure 1). These fibers, individually electroded on both the inside and outside surfaces, are activated by an electric field
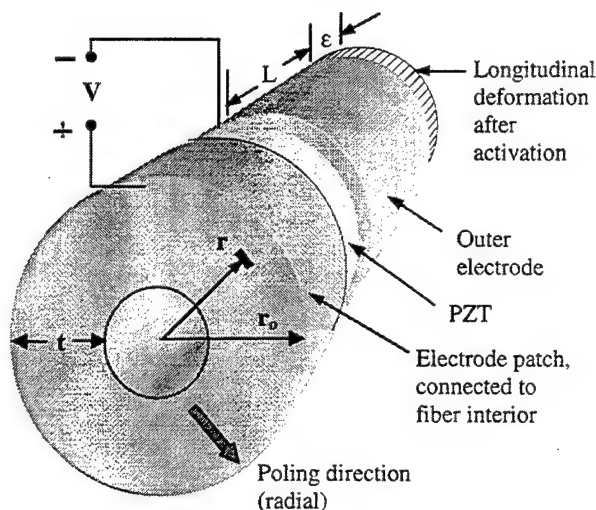
Aspect ratio, $\alpha = t/r_o$

Figure 1. Hollow Fiber Design. The basic fiber design consists of a hollow cylinder of active material, electroded on both the inside and outside surfaces. For piezoelectric materials (PZT), the poling direction is radial; therefore the d_{31} response of the fiber is used to create longitudinal motion.

applied directly across the walls of the fiber, generating longitudinal strain due to the piezoelectric d_{31} mode. Even though the longitudinal strain is decreased by approximately half by using d_{31} versus the d_{33} mode used in solid fiber AFCs, the required voltage can be decreased by a factor of ten or more since the electric field is applied only across the wall of the fiber instead of through the matrix, thereby eliminating field losses. An additional benefit to the hollow topology is the isolation of the inner electrode from the matrix, enabling the fiber to be embedded in electrically conductive matrices.[3-5]

Several processes, based on molding or extrusion techniques, are available for fabricating piezoelectric fibers - each with their own pros and cons. Molding techniques[13-15] are capable of producing highly detailed cross-sections with wall thickness on the order of a grain size, although the fiber length is limited to 10 mm or less. Traditional extrusion or drawing methods[16,17] can produce extremely long fibers (thousands of feet[17,18]), but are difficult and expensive to apply to hollow fiber fabrication. Microfabrication by Coextrusion (MFCX) is capable of inexpensively producing long ceramic forms (>100 mm long) with complex cross-sections having small feature sizes (as small as a grain size); however, this method is still at the research stage and further characterization is required.[19]

While the feasibility of producing piezoelectric hollow fibers has been established [3,18,20], there has been limited research in modeling and characterization of this new type of AFC. Most of the modeling efforts for hollow piezoelectric fibers has focused on the radial strain of short fibers used in hydrophone applications.[4,5] Unfortunately, this research doesn't extend to longitudinal strain in long fibers. However, Maclean and Jacobsen[3] have numerically modeled the nonlinear electric field behavior across the fiber walls. The authors have built on Maclean and Jacobsen's earlier work to derive basic analytical models capturing the strain behavior as a function of the nonlinear applied field in individual fibers and lamina.[20]

The research that has been conducted to date on hollow fiber composites has successfully demonstrated the basic feasibility of the concept. However, for engineers to use hollow fibers effectively in active composite design, they must be aware of the key design issues impacting performance, fabrication, and reliability of these fibers. For example, while basic performance models do exist for these hollow fibers, the relationship between the primary design parameters has not been fully studied. These parameters represent the range of choices available to the engineer when designing a composite, and include the fiber and matrix Young's moduli, aspect ratio of the individual fibers, and the overall active composite volume fraction.

All of these parameters are governed by the quality of the fabrication technique. For instance, traditional extrusion and drawing methods often suffer from poor ovality or eccentricity (out-of-roundness) due to handling of hollow green fibers during the fabrication process, which can ultimately result in electric field stress concentrations in the fiber wall. The MFCX process alleviates many of these issues by including a solid carbon black core in the green fiber; however, as with any ceramic processing technique the high temperatures experienced during the sintering phase have a tendency to shrink and warp the fibers. This warping can clearly affect the fiber layup and the achievable volume fraction, affecting the overall composite design. Thus, it is important to know exactly how the individual design parameters, particularly aspect ratio, influence the quality of the manufactured fiber.

Finally, very little research has been conducted on the reliability of active fiber composites, whether hollow or solid. It is known that long-fiber active composites are susceptible to reliability problems such as fiber pullout and breakage in much the same way as conventional (inactive) fibrous composites.[7] Hollow fibers introduce another level of complexity due to the potentially

fragile nature of the fiber walls. Therefore, it is critical when designing a hollow fiber active composite to know the primary failure mechanism and have a sense of the strain-to-failure and ultimate strength of the individual fibers in addition to the entire composite. This paper presents an in-depth study addressing these performance, fabrication and reliability issues for hollow piezoelectric fibers with concentration on the design tradeoffs presented by the primary design parameters: fiber aspect ratio, matrix/fiber modulus ratio, and composite volume fraction.

HOLLOW FIBER COMPOSITE PERFORMANCE STUDY

To gain insight into the sensitivity of the AFC performance to the primary design parameters (aspect ratio, fiber/matrix material, and volume fraction), individual fiber and AFC lamina models derived in previous work[20] were analyzed with respect to each of the design parameters. For continuity, a brief summary of the fiber and lamina analytical models is presented before the analysis. For a more detailed derivation the reader is referred to previous literature.[20,21]

Hollow Fiber Performance Modeling Summary

Simple analytical models to predict the strain in AFC lamina were built up from the fiber level by establishing effective piezoelectric constant, $d_{31,eff}$, for both the individual fiber and a lamina ply. This enables classical laminate composite methods to be applied when incorporating multiple hollow fiber laminas into complex composite architectures. At both the individual fiber and lamina level, these performance models were validated through experimentation and finite element models with correlation within 6.5%.[20]

Individual Fiber Model. In smart structures, it is common and convenient to model the electric field applied across a curved piezoelectric structure by the thin-wall approximation - the applied voltage divided by the wall thickness ($E_{tw} = V/t$). However, in general the electric field through the thickness of a curved structure is not constant, with the approximation breaking down quickly as the thickness increases. Therefore, it is critical in the individual fiber model to account for the nonlinear electric field effects. From Gauss' Law, the expression for the electric field, E, at a distance, r, from the geometric center of a hollow circular fiber is[22]:

$$E(r) = \frac{-V}{r \ln(1-\alpha)}, \qquad (1)$$
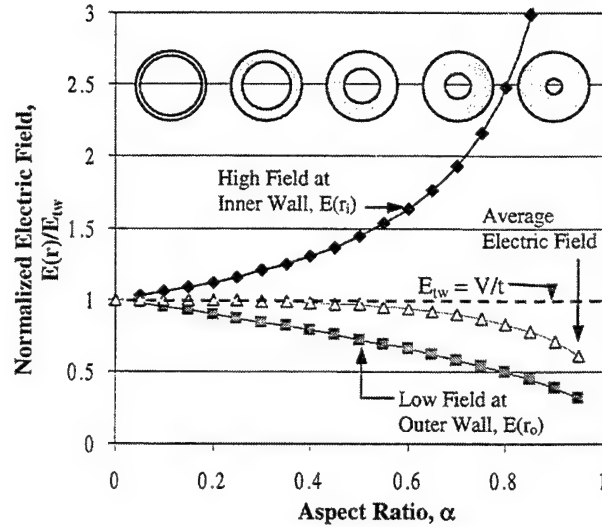
Figure 2. Electric Field vs. Aspect Ratio. As the aspect ratio of a hollow fiber increases, the difference between the maximum and minimum electric fields increases. The highest field occurs at the inside wall; the lowest field is located at the outside wall.

where α is the fiber aspect ratio, t/r_o, and V is the voltage applied across the fiber wall. The field is maximum at the inner diameter (Figure 2) and decreases with increasing radius to a minimum at the outer diameter. The variation between maximum and minimum field increases with the fiber aspect ratio, α. A significant variation in field can lead to severe problems. To produce an adequate poling field at the outer edge of a high aspect ratio fiber (thick wall), the electric field at the inner edge of the fiber must be so large that the induced stress may damage the fiber. Likewise, when activating a hollow fiber it is not possible to achieve the maximum working electric field at the outer edge because this voltage would overdrive the inside of the fiber resulting in de-poling. Thus, it is clear that the choice of aspect ratio has a significant effect on voltage levels needed for poling and fiber activation, with low aspect ratios being a preferred choice.

By integrating the internal piezoelectric forcing created by the local electric field (Equation 1) over the cross-section of the fiber, the longitudinal free strain, ε, is

$$\varepsilon = \left(\frac{-d_{31}}{\ln(1-\alpha)\left(\frac{1}{\alpha}-0.5\right)} \right) E_{tw} = d_{31,eff}{}^F E_{tw}. \qquad (2)$$

The effective d_{31} of the fiber, $d_{31,eff}{}^F$, (in parentheses) incorporates the nonlinear electric field effects, thus enabling the thin wall electric field approximation, E_{tw},
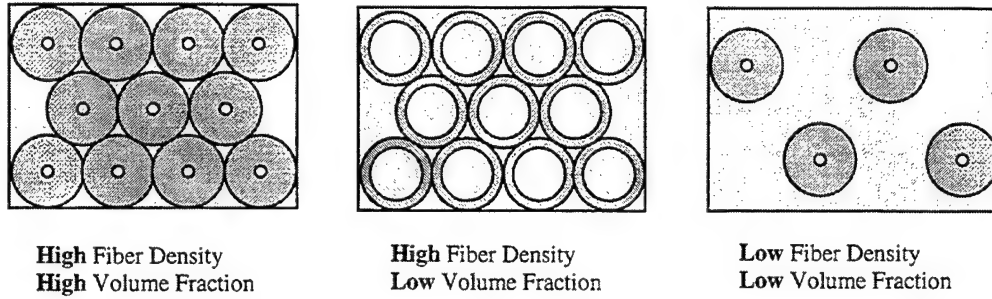
Figure 3. Volume Fraction vs. Fiber Density. The volume fraction refers to the overall volume of the composite taken up by fiber material. The fiber density refers to the *number* of fibers in a given volume divided by the maximum number of fibers that can be embedded into the same volume.

to be used to simplify the lamina composite models. Note that the effective fiber d_{31} is only a function of the aspect ratio of the fiber and the piezoelectric material d_{31}. The effective fiber d_{31} increases with decreasing aspect ratio; therefore, as would be expected, fibers with low aspect ratio (thin wall) produce the highest strain for a given applied electric field.

***Lamina Model.*** A classical composite theory, the concentric cylinders model[23], was used to derive the expression for the equivalent lamina longitudinal Young's modulus, $Y_{lam} = Y_f v_f + Y_m(1-v_f)$, where Y_f and Y_m refer to the Young's modulus of the fiber and matrix, and v_f is the fiber volume fraction (percentage of active material). In this model, it is assumed that each fiber is back-filled with matrix material in the determination of volume fraction. Dividing the equivalent Young's modulus by the modulus of the fiber yields, in dimensionless form,

$$Y_{lam}^{\ N} = \frac{Y_{lam}}{Y_f} = v_f + \frac{Y_m}{Y_f}(1 - v_f), \qquad (3)$$

Recognizing that the piezoelectric strain in the fiber direction is analogous to thermal strains in a conventional composite, the strain of a hollow fiber lamina can be expressed as a product of the effective lamina d_{31}, $d_{31,eff}^{\ L}$ (given in the parentheses) and the thin wall approximation of the applied field E_{tw},

$$\varepsilon_{lamina} = \frac{1}{Y_{lam}}\left(\frac{-d_{31}}{\ln(1-\alpha)\left(\frac{1}{\alpha} - 0.5\right)}\right)E_{tw}$$

$$= \left(\frac{-d_{31,eff}^{\ F}}{Y_{lam}}\right)E_{tw} = d_{31,eff}^{\ L}E_{tw}. \qquad (4)$$

With the use of these effective piezoelectric parameters, models for any AFC layup architecture can be derived utilizing traditional laminate composite theory methods built upon this single lamina model. [23]

Effective Lamina d_{31} Model Analysis

From the above models, the primary design parameters are: aspect ratio, Young's modulus ratio (Y_m/Y_f) and fiber volume fraction. These models can also be written in terms of fiber density, Δ_f, instead of fiber volume. It is important to draw a distinction between volume fraction and fiber density. The volume fraction, v_f, used in the model derivation, is the percentage of the composite taken up by fiber *material* irrespective of how that material is arranged in the matrix. Fiber density, on the other hand, refers to the *number* of fibers in a given volume divided by the maximum number of fibers that can be embedded into the same volume. This is dependent only on the geometric arrangement of the fibers, not how much piezoelectric material is present. For solid fiber composites, volume fraction and fiber density are essentially interchangeable because the percentage of fibers uniquely determines the percentage of fiber material. For hollow fibers, however, the volume fraction is also determined by the aspect ratio of the fibers – two composites with an equal number of fibers (thus, equal fiber density) can have very different values of volume fraction depending on aspect ratio, as shown in Figure 3. Fiber density and volume fraction are related by the relationship,

$$v_f = \left(\frac{\pi}{2\sqrt{3}}\Delta_f\right)(2 - \alpha)\alpha. \qquad (5)$$

Insight into the fiber strain behavior can be gained by studying the effective lamina d_{31} assuming the applied electric field is constant. Figure 4 shows the effective lamina d_{31}, normalized with respect to the d_{31} of the
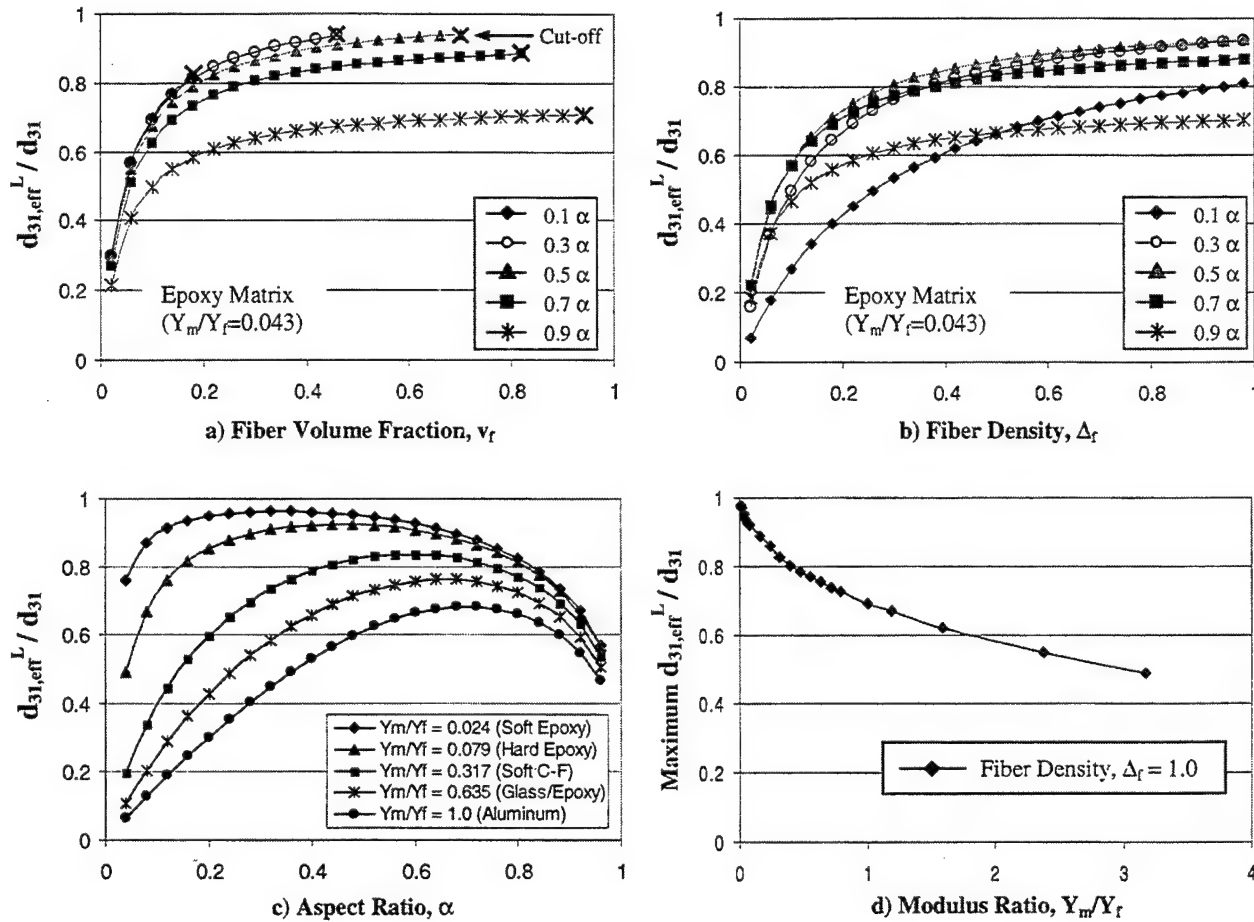
Figure 4. PZT / Epoxy Effective Lamina d_{31}. a) The effective lamina d_{31} normalized by material d_{31} ($d_{31,eff}^L/d_{31}$) was plotted as a function of volume fraction for several aspect ratios. b) The normalized effective lamina d_{31} was plotted as a function of fiber density. The largest lamina d_{31} was 94% of the material d_{31}, corresponding to 254 pm/V for PZT-5H, for fiber aspect ratios from approximately 0.3 to 0.5. c) The normalized effective lamina d_{31} (calculated at maximum fiber density) was plotted as a function of aspect ratio for several modulus ratios. d) The maximum value of the normalized effective lamina d_{31} was plotted versus the modulus ratio and varied from 0.96 for very soft epoxy to 0.48 for steel.

piezoelectric material composing the individual fiber, plotted as a function of volume fraction (Figure 4a) and fiber density (Figure 4b). These plots are based on the assumption of typical epoxy for the matrix and PZT-5H for the fiber (Young's modulus ratio $Y_m/Y_f = 0.043$). Figure 4(a) indicates that for a given volume fraction, the greatest effective lamina d_{31} is achieved by the lowest aspect ratio fiber. However, the hollow topology of the fibers places an upper limit on volume fraction achievable (Equation 5), dependent on aspect ratio, resulting in the 'cut-off' of each curve. Thus, while the highest individual fiber strain is achieved with the thinnest walled fibers resulting in less electric field losses, overall, a higher lamina strain may be achieved

by a thicker walled fiber because they enable a higher potential fiber volume fraction.

Figure 4(b) presents the effective lamina d_{31} in a slightly more intuitive manner because each value of fiber density corresponds to an equal number and arrangement of fibers within the matrix, regardless of their individual aspect ratio. As expected, the maximum effective lamina d_{31} occurs at maximum fiber density (254 pm/V - 93.9% of the piezoelectric material d_{31}). It is interesting to note, however, that this maximum lamina d_{31} is achieved near the mid-range aspect ratio values of 0.3 and 0.5. This highlights one of the trade-offs that must be considered when choosing an aspect ratio for active composite applications. The

Table 1. Optimum Aspect Ratio vs. Matrix Material. As the Young's modulus ratio is increased, the optimum aspect ratio (producing the maximum effective lamina d_{31} increases) while the value of this effective d_{31} decreases.

Matrix Material	Modulus Ratio (Y_m/Y_f)	Optimum Aspect Ratio	Maximum Effective Lamina d_{31}/Mat. d_{31}
Soft Epoxy	0.024	0.36	**96%** [260 pm/V]
Hard Epoxy	0.079	0.46	**92%** [248 pm/V]
Soft C-F Matrix	0.317	0.60	**84%** [227 pm/V]
Glass/Epoxy	0.635	0.64	**76%** [205 pm/V]
Aluminum	1.0	0.70	**68%** [184 pm/V]
Steel	3.1	0.77	**49%** [132 pm/V]

thin-walled fiber exhibits the highest effective fiber d_{31}, but cannot effectively activate the composite due to limitations on the achievable volume fraction of these fibers. The thick-walled fiber, although more able to activate the composite because of its higher cross-sectional area, has the lowest effective fiber d_{31} (Equation 2). Thus, the maximum *lamina* d_{31} is achieved by balancing the high effective d_{31} of the thin wall fibers with the high volume fraction of the thick wall fibers. Figure 4(c) is a plot of the effective lamina d_{31} versus aspect ratio for a variety of material modulus ratios (Y_m/Y_f), and Figure 4(d) plots the *maximum* normalized effective lamina d_{31} (achieved using the optimum aspect ratio) against modulus ratio, with the results summarized in Table 1. The optimum aspect ratio ranged from 0.36 for the softest matrix to 0.77 for steel, and generally followed an upward trend with matrix modulus. The ratio of the effective lamina d_{31} to material d_{31}, however, decreased with matrix stiffness, ranging from 96% for soft epoxy to 48% for steel (Figure 4d). Essentially, for maximum performance as the stiffness of the matrix is increased, the fiber aspect ratio must also be increased to match the stiffness of the matrix (through increased volume fraction). Unfortunately at the same time, inefficiencies due to the electric field gradient also increase with aspect ratio; thus, these two effects must be balanced to arrive at an optimal aspect ratio.

Embedding Stress Modeling

The maximum Young's modulus ratio is limited by the embedment stresses that an individual fiber can withstand. These stresses arise from the relative difference in strain between the matrix and the fiber caused by thermal effects during a casting process (thermal expansion coefficient mismatch), or strain induced during curing, as with epoxy. A detailed derivation of these stresses is presented in Cannon and Brei[20] and summarized here for completeness. The fiber was modeled as a cylindrical pressure vessel with an internal pressure equal to atmospheric. Using the expressions for radial and circumferential (hoop) stress in the vessel wall, the maximum Von Mises stress occurs at the interior wall, and the only non-zero stresses at this location are hoop and axial (longitudinal) stresses. The hoop stress was derived by recognizing that the contraction of the matrix around the fiber results in an equivalent shrink fit interference.[24] Assuming the bond between fiber and matrix is ideal, the rule of mixtures was applied to derive the longitudinal stress on the inside wall of the fiber. The longitudinal and hoop stresses, σ_l and σ_θ, were combined to yield the non-dimensional Von Mises stress, σ^*_{vm}, at the inner wall of the fiber,

$$\sigma^*_{vm} = \frac{\sigma_{vm}}{Y_f(\delta_m - \delta_f)} = \frac{\left[\sigma_\theta^2 + \sigma_l^2 - \sigma_\theta \sigma_l\right]^{1/2}}{Y_f(\delta_m - \delta_f)}, \quad (6)$$

where σ_l is given by

$$\frac{\sigma_l}{Y_f(\delta_m - \delta_f)} = \frac{-1}{1 + \left(\dfrac{Y_f}{Y_m}\right)(v_f)}, \quad (7)$$

and σ_θ is given by

$$\frac{\sigma_\theta}{Y_f(\delta_m - \delta_f)} = \frac{-2\beta^2}{(\beta^2 - 1)\left[\dfrac{Y_f}{Y_m}\left(\dfrac{1 + v_f}{1 - v_f} + \mu\right) + \left(\dfrac{\beta^2 + 1}{\beta^2 - 1} - \mu\right)\right]}. \quad (8)$$

In these expressions, the quantity $(\delta_m - \delta_f)$ is simply the strain differential between the matrix and fiber during curing, and β is a non-dimensional intermediate variable equal to $(1-\alpha)^{-1}$. Thus, all three design

6
American Institute of Aeronautics and Astronautics
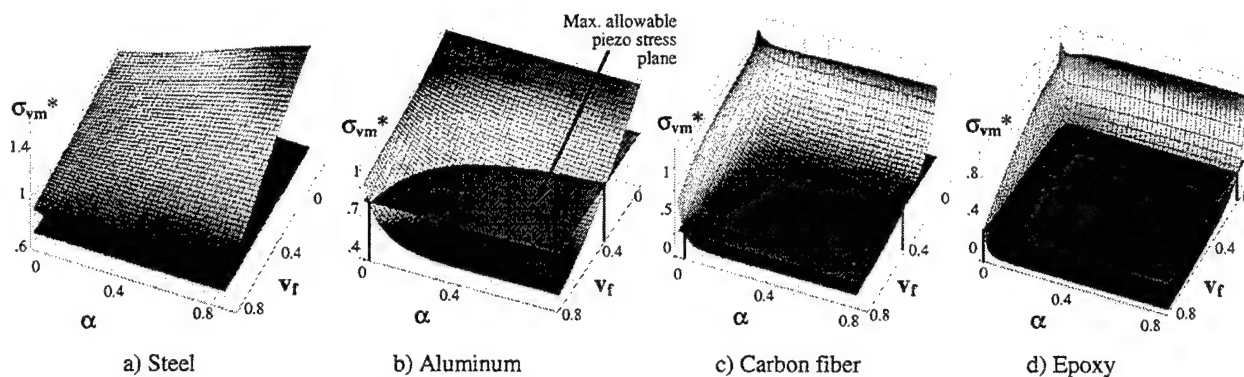
a) Steel b) Aluminum c) Carbon fiber d) Epoxy

Figure 5. Embedding Stresses. The non-dimensional Von Mises stress at the inner wall of a fiber is plotted as a function of fiber aspect ratio (α) and volume fraction, v_f. The red horizontal plane represents the allowable upper limit for the Von Mises stress during embedment. a) For steel matrices, the embedding process results in stresses above the failure limit for all conditions. b) For aluminum matrices, however, the stresses are below the limit for volume fractions above 0.35 and aspect ratios higher than 0.1. c) For carbon fiber matrices, stresses are below the allowable limits for volume fractions above 0.45 and all aspect ratios higher than 0.35. d) For epoxy matrices, stresses are below the limits for nearly all aspect ratios and volume fractions.

variables, aspect ratio, volume fraction, and modulus ratio, play an important role in the stresses on a fiber during embedding.

Embedment Stress Analysis

The non-dimensional Von Mises stress is plotted in Figure 5 as a function of fiber aspect ratio and the volume fraction of the composite for various matrix materials. For the aluminum and steel matrices, the strain differential was taken to be the difference in thermal expansion coefficients multiplied by the temperature drop during cooling of the matrix (solidus temperature minus room temperature). For most metal alloys, this value is approximately one percent. For epoxy and carbon fiber/epoxy matrices, the strain differential used was the cure shrinkage of a typical epoxy, or 2%.[25] The metals were examined because, unlike traditional active composites, the nature of hollow fibers allows them to be embedded in electrically conductive matrices. The horizontal stress plane shown in red on the graphs denotes the maximum allowable value of the non-dimensional stress (stress values above this plane exceed the maximum compressive stress for typical piezoceramics). A steel matrix (Figure 5a), which is three times stiffer than the fiber, results in stresses above the failure limit of the piezoelectric ceramic regardless of the fiber aspect ratio or volume fraction. It is possible, however, to embed fibers in softer metals, such as aluminum (Figure 5b) that have approximately the same modulus as piezoelectric ceramics, depending on the aspect ratio and volume fraction. For an aspect ratio of 0.8, a minimum volume fraction of approximately 0.35 is

necessary to prevent failure. However, as the volume fraction is increased, the necessary aspect ratio of the fibers drops. For example, for a mid-range volume fraction of 0.45, fibers with an aspect ratio above 0.3 will survive the embedding process in aluminum. When using extremely high volume fractions (>0.8), an aspect ratio as low as 0.1 is sufficient to prevent failure. For typical carbon fiber matrices (Figure 5c), stresses are below the allowable limits for volume fractions above 0.45 and all aspect ratios higher than 0.35. Similar to aluminum, the aspect ratio can be as low as 0.09, provided extremely high volume fractions are used (>0.8). For epoxy matrices much softer than PZT (Figure 5d), stresses are below the limit for all volume fractions and aspect ratios (stress levels appearing above the plane at the edges of the plot are an artifact due to shear lag effects not included in the model). Therefore, although some metals with greater stiffness than PZT ($Y_m/Y_f >1$), such as steel, are not suitable for use with hollow fibers, it is feasible to embed hollow fibers into epoxies, carbon fiber matrices of various hardness, and even metals with Young's modulus on the order of PZT, provided the aspect ratio and volume fraction are sufficiently high.

HOLLOW FIBER FABRICATION AND EVALUATION

The performance study indicates that the geometric (aspect ratio) and the material (Young's modulus and d_{31}) properties govern the strain behavior of the AFC and embedment stresses constrain the potential matrix material. Clearly, fabrication method selected for the fibers will have a direct impact on all of these
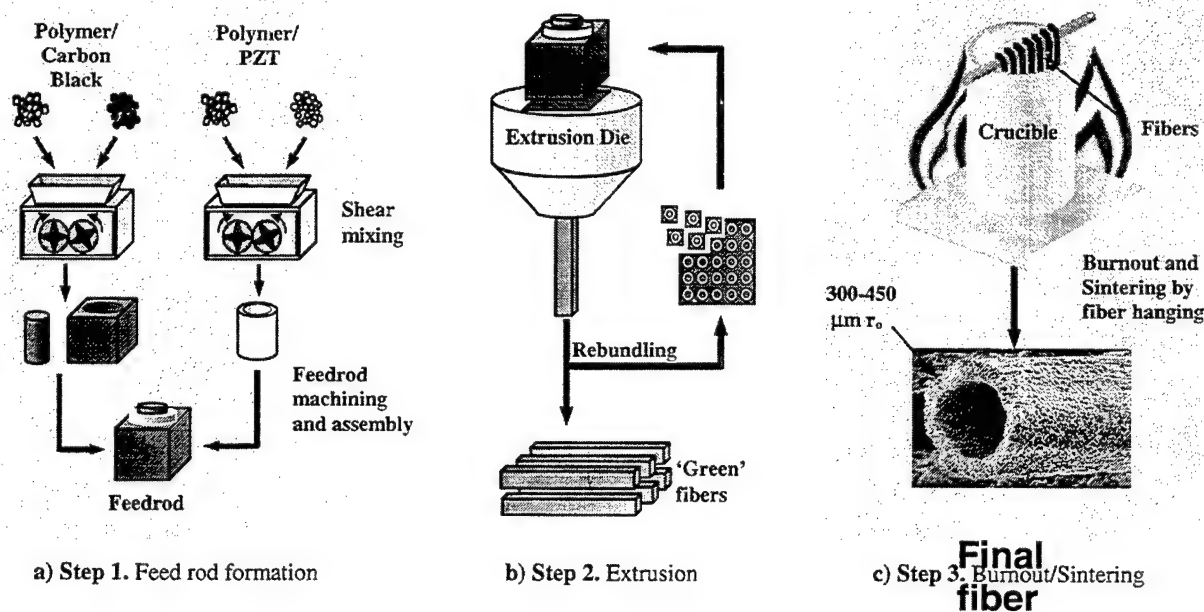
Polymer/ Carbon Black   **Polymer/ PZT**

Shear mixing

Feedrod machining and assembly

Feedrod

Extrusion Die

Rebundling

'Green' fibers

Crucible   **Fibers**

Burnout and Sintering by fiber hanging

300-450 $\mu m\ r_o$

Final fiber

a) **Step 1.** Feed rod formation   b) **Step 2.** Extrusion   c) **Step 3.** Burnout/Sintering

Figure 6. MFCX Overview. Piezoelectric and carbon black powders are mixed with thermoplastic polymers to form an initial feedrod. The feedrod is extruded (and re-extruded) until desired fiber size is produced. Polymers and carbon black are removed during burnout to produce the final fiber.

parameters. Unfortunately, the methods available for fabricating these types of fibers, drawing, extrusion, and coextrusion, are relatively new and the variability in the key fiber parameters has not been documented. This section describes an evaluation of fibers fabricated using the Microfabrication by Coextrusion (MFCX) process, chosen because it has been highly successful in producing forms of arbitrary cross-section on a small scale (on the order of grain size) out of a variety of ceramic materials.[19] Furthermore, the ability to apply this method both efficiently and inexpensively to hollow circular PZT fibers has previously been demonstrated.[20] Fibers fabricated by this method were evaluated for their geometric properties (ovality, eccentricity, straightness) and material properties (density, porosity, d_{31} and Young's modulus). A brief overview of the MFCX process is provided; for more detail the reader is referred to earlier research.[19,20]

Microfabrication by Coextrusion (MFCX) Overview

The MFCX process can be described as a multi-phase, or multi-material extrusion process, as depicted in Figure 6. Carbon black powder and PZT-5H (APC PZT-856) powder were each combined with thermoplastic polymers in a shear mixer (Model PL2100, CW Brabender Instruments, Inc.) at approximately 160°C at a speed of 30 rpm until the mixtures were of equal viscosity. Viscosity matching is critical because it allows the two materials to be simultaneously extruded without cross-sectional deformation. Each of the mixtures was hardened by cooling to room temperature, warm-pressed into a solid block of material, and then machined to create a feedrod (Figure 6a). The cross-sectional dimensions of the feedrod were chosen so that the aspect ratio matched the desired fiber aspect ratio. During the extrusion step, the feedrod was forced through a reduction die at approximately 1200 kg on a Bradley University Research Extruder, reducing its diameter by a factor of 25, but maintaining the aspect ratio of the original feedrod. By re-bundling the extrudate and making multiple extrusion passes (Figure 6b), diameter reductions up to three orders of magnitude are possible. To create the hollow fiber cross-section, the carbon black core and the thermoplastic polymers were removed during the burnout cycle by slowly heating the fibers over 18 hours to a temperature of 600°C (HIPAN Series furnace, Micropyretics Heaters International). Finally, the fibers were sintered by heating at a rate of 180°C per hour to a two-hour dwell at 1285°C to strengthen and densify the ceramic. To prevent fiber warping, a common problem in ceramics processing, it was necessary to burnout and sinter the fibers vertically, hanging under their own weight (Figure 6c). During the post-processing phase of fiber electroding and poling, gaining access to the fiber interior was problematic due to the hollow fiber topology and the extremely small hole in the fiber center. To address this problem, a unique electrode pattern was introduced

during this step, where the inside electrode was extended around the end of the fiber to an external patch, enabling access to both the inside and outside electrodes from the exterior of the fiber. Silver paint was used to electrode the fibers (DuPont Conductor Composition #7421), creating a large enough electrode patch so that multiple fibers could be connected through a single electrical bus, as shown in Figure 7. A gap (approximately 2mm) separated the inner and outer electrodes, allowing the fibers to be poled in air without arcing. Each of the fibers was poled by applying an electric field of 1200 V/mm at room temperature for approximately 30 minutes. For the evaluation effort, approximately 200 PZT-5H fibers of varying outside radius (300-450 µm) and aspect ratio (0.3 – 0.52) were fabricated; examples are shown in Figure 8.

Geometric Property Evaluation

During the coextrusion process the cross-section of the feedrod can be deformed, which can lead to variations in wall thickness in a single fiber, ultimately resulting in electric field variations. The optimum fabrication process would minimize the cross-sectional deformation. It is also important that the process be repeatable so that there is minimal variation in diameter and wall thickness (and thus electric field) *between* fibers as well. The nominal diameter measurements made during the cross-sectional analysis were utilized to assess the repeatability of the MFCX process. The largest deviation from the nominal diameter was 4.8% for the lowest aspect ratio fibers (0.3), whereas the larger aspect ratio fibers (0.42, 0.52) had a maximum deviation of 1.8%, much less than the common ceramics processing tolerance of ± 5%. To measure the geometric quality of the MFCX fiber fabricated, two cross-sectional properties commonly used in machinery shaft inspection were applied to the hollow fibers: ovality and eccentricity.[26] Ovality is a measure of the out-of-roundness, or 'lobing' of the cross-section, and is defined as the maximum diametrical deviation from a nominal diameter. Eccentricity, as it applies to hollow fibers, is simply a measure of the distance that the hole
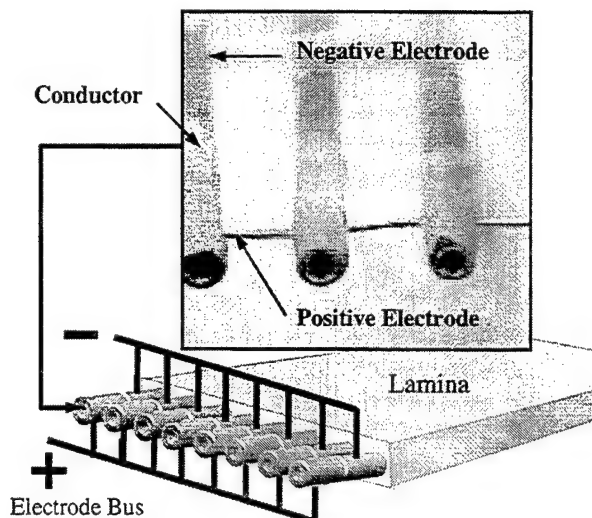
Figure 7. **Wrapped electrode pattern.** By wrapping the inner electrode to the outside of the fiber, multiple fibers could be connected through a single electrode bus.

is off-center with respect to the outside diameter of the fiber. These two cross-sectional properties are important to the design of a hollow PZT fiber because both ovality and eccentricity cause wall thickness variations, leading directly to electric field variations within the fiber wall. To measure these quantities, the diameter and wall thickness of approximately 40 fibers were measured using calipers at 12 points around the fiber's circumference (Table 2). The average ovality measured resulted in minimal electric field gradients ranging from 1.9% for the largest aspect ratio evaluated (0.52) to 4.1% for the smallest aspect ratio (0.3). However, more significant electric field variations arose due to the eccentricity of the fibers, which ranged from 2.1% to 3.2%. Although these values may appear insignificant, a center hole which is slightly off-center can drastically impact the wall thickness, in this case resulting in field variations as high as 21% for the 0.3 aspect ratio fibers. For aspect ratios of 0.42 and 0.52,

| Aspect Ratio = 0.3 | Aspect Ratio = 0.42 | Aspect Ratio = 0.52 |

Figure 8. **Hollow Fiber Prototype Cross-sections.** Each of the hollow PZT fibers was examined for variations in diameter and wall thickness. In each case, the largest deviations occurred in the 0.3 (lowest) aspect ratio fibers.

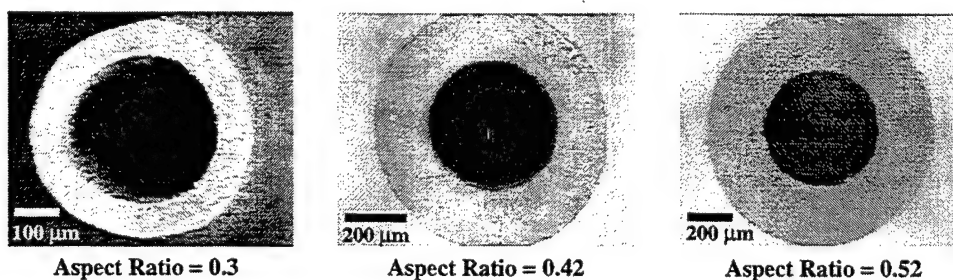**Table 2. Hollow Fiber Cross-sectional Analysis.** In general, ovality and eccentricity increased as aspect ratio decreased. Ovality ranged from 1.9% to 4.1% and eccentricity ranged from 2.1% to 3.2%.

	Aspect Ratio = 0.3		Aspect Ratio = 0.42		Aspect Ratio = 0.52	
	Ovality (%)	Eccentricity (%)	Ovality (%)	Eccentricity (%)	Ovality (%)	Eccentricity (%)
Average	4.1 %	3.2 %	2.1 %	2.1 %	1.9 %	2.1 %
Std. Dev.	2.21 %	1.34 %	1.44 %	0.99 %	0.40 %	0.27 %

the electric field variation due to eccentricity dropped to 9.9% and 8.1%. Overall, the largest levels of eccentricity and ovality occurred in fibers with the thinnest wall, indicating that the ability of the fiber to maintain its shape throughout the process diminishes with decreased aspect ratio. When incorporated into an active composite, the electric field variations brought about by eccentricity and ovality will result in field levels both above and below the nominal voltage applied; thus, potential material damage or decreased performance must be taken into account in the active composite design, especially when using fibers with extremely low aspect ratio.

Similar to the cross-sectional property analysis, the straightness of the fibers was determined using two machinery inspection criteria: curvature (commonly used for shaft characterization) and waviness (commonly used for surface characterization).[26] The curvature of the fiber is essentially the maximum deviation from a nominal centerline, normalized by the length of the fiber. However, because this characterization only measures the single worst point along the length of the fiber, a waviness measurement was also made to capture the 'meandering' nature sometimes found in the fibers. Each of these quantities was measured by enlarging photographs of several fibers and using calipers to measure the deviation of the fiber axis from its nominal centerline at approximately 20 points along the length. Both measurements were normalized by the diameter of the fibers, with the curvature taken to be the maximum deviation and the waviness taken to be the root-mean-square of all measurements taken. Similar to the cross-sectional analysis, the lowest aspect ratio fibers exhibited the highest level of variation along the fiber length. However, even the fibers with the worst measured curvature and waviness (8.1 microns/mm length and 3.3 microns/mm length, respectively) can be incorporated into lamina less than 50% thicker than the fiber diameter without exposing the fiber, allowing the fabrication of very thin, high volume fraction composites. The key manufacturing step that enabled the fabrication of these straight fibers was burnout and

sintering. During this phase, the basic MFCX process was modified by hanging the fibers vertically versus laying them down, drastically reducing warping and improving their straightness. Furthermore, fibers as long as 75 mm were fabricated in this manner, on the order of active fibers currently being used[2], without signs of necking or failure.

Material Property Evaluation

In addition to the large-scale geometric properties of the fiber, a material analysis was conducted to assess the fiber quality based on porosity, density, d_{31}, and Young's Modulus. The density of the hollow fiber PZT was determined using a standard Archimedes density test and was 97.5% theoretical density, corresponding to a porosity of 2.5%. This porosity compares quite well to commercially available piezoceramics, which have porosity ranging from 2.6% to 9%.[27] To verify that the high quality of the fiber microstructure would lead to good mechanical properties, the Young's modulus and d_{31} of the fabricated hollow fibers were experimentally determined. The Young's modulus was measured through a simple Instron stress/strain experiment on a solid PZT fiber, with measurements ranging from 54.2 to 61.0 GPa, very close to the standard book value of 63 GPa given by the supplier for PZT-5H. To measure the d_{31} of the ceramic, a small disk approximately 1 mm thick was cut from the end of a solid PZT feedrod. The disk was post-processed in the same manner as the hollow fibers, using the same burnout and sintering schedules, electrode composition, and poling field (1200 V/mm). A strain/electric field experiment was performed on the sample, yielding a measured d_{31} of 290 pm/V. This value is approximately 7.5% higher than the d_{31} value of 270 pm/V for industry standard PZT-5H, indicating high quality piezoelectric properties.

RELIABILITY INVESTIGATION

The hollow fiber performance study concluded that maximum lamina strain is achieved using individual fibers with an optimum aspect ratio determined by the choice of matrix material. This optimum aspect ratio

can range from relatively thick-walled fibers (0.6 to 0.7 aspect ratio) for stiff matrix materials (above 50 GPa) to thin-walled fibers (0.3 to 0.4 aspect ratio) for softer epoxy matrices (below 5 GPa). However, the need to utilize thin-walled hollow fibers will have a negative impact on the strength of the fibers, along with the overall composite reliability. Obviously, when designing an active composite, it is critical to be able to predict the ultimate strength and strain-to-failure of the composite so that loading conditions resulting in composite failure can be avoided. Unfortunately, this data is not available for piezoelectric fibers – solid or hollow. Typically, to *fully* characterize the ultimate stress and strain-to-failure of fibrous composites under multiple loading conditions, a large battery of standardized tests is required such as 0° tension, 90° tension, 0° compression, 90° compression, ±45° tension, three-point flexural tests, shear testing, short beam shear testing, and end-notched flexure, among others.[23,26] Without knowing the primary failure mechanism, however, this is an overwhelming task.

To initiate the general study of reliability in piezoelectric fibers, an experimental investigation was launched to identify the primary failure mechanism and measure the interfacial shear strength to gain insight into the strain-to-failure and ultimate normal and shear strengths in the transverse and longitudinal direction. Single fiber tests were chosen because they are capable of determining with fewer fiber coupons a) the failure mechanism of the composite near fiber breaks, b) the interfacial shear strength between the matrix and the fiber, and c) the strain-to-failure of an individual fiber. Although these tests *cannot* predict the exact values of ultimate strength and strain-to-failure in a composite, research has shown that there *is* a strong qualitative correlation between the interfacial shear strength (or failure mechanism) in a composite and its transverse normal ultimate strength and ultimate shear strength.[28,29] There are three main types of single fiber tests: single fiber pullout, single fiber indentation, and single fiber fragmentation. Although all three of these methods give the interfacial shear strength of a composite, the fiber pullout test is difficult to conduct on a brittle fiber such as PZT. Thus, the single fiber fragmentation test was conducted to determine the primary failure mechanism, and a simple indentation test was conducted to determine the interfacial shear strength. While interfacial shear strength and failure mechanism can give information about the ultimate strength and strain-to-failure under loading conditions resulting in shear and transverse normal stresses, researchers have found that the correlation between single fiber test results and the *longitudinal* ultimate strength and strain-to-failure is weak.[23,29] Therefore, the fragmentation and indentation tests were augmented

with a standard 0° tensile strain-to-failure test that directly determined the composite longitudinal strain-to-failure and ultimate strength.[26]

Tensile Strain-to-Failure Testing

To directly measure the longitudinal strain-to-failure and ultimate strength of the PZT/Epoxy samples, a tensile strain-to-failure test was conducted using a standard Instron tensile test procedure. Each test coupon was mounted and secured between two wedge action tensile grips in an Instron Satec Model 1137 load frame. The cross sectional area and length were input to LabView 5.0 data acquisition software (National Instruments), which monitored the crosshead displacement and the tensile load on the coupon, both output by the Instron. From this data, the strain-to-failure (crosshead displacement / gauge length) and ultimate strength (crosshead load / cross-sectional area) of the sample were calculated.

The strain-to-failure test procedure was applied to four different types of coupons: epoxy blanks containing no fibers, low aspect ratio hollow fibers ($\alpha = 0.42$), high aspect ratio hollow fibers ($\alpha = 0.52$), and solid fibers. The baseline epoxy blanks were tested because the strain-to-failure of the epoxy was not provided by the manufacturer and is dependent on curing parameters such as atmosphere and temperature. Two different aspect ratio hollow fibers were chosen to determine the effect of aspect ratio on the strain-to-failure of the composite. Similarly, the solid fiber coupons were tested to provide a comparison between the hollow fiber design and existing solid fiber active composites. For all of the fibrous coupons, the strain-to-failure was compared to the blank epoxy specimens to determine the overall effect of the embedded fiber on the tensile strain-to-failure of the composite.

Sample Preparation. In all, thirty-two strain-to-failure coupons were fabricated using MFCX– eight for each type of sample. Both the solid and hollow fibers were fabricated with APC-856 (Young's Modulus of 63 GPa and a d_{31} of 270 pm/V (APC, 1998)) with an outside radius of 450 microns. The coupons, shown in Figure 9, were fabricated using a five-part Delrin™ mold. A thin layer of Struers' Epofix™ epoxy (1.2 GPa Young's Modulus) was poured into the mold and allowed to partially cure until viscous enough to support the weight of a PZT fiber. A single fiber was then placed into the center of the mold, and a second epoxy layer of equal thickness was poured to center the fiber in the coupon. The epoxy was cured for six hours at approximately 40°C, the temperature at which air bubbles would escape for a nominal epoxy thickness of 4 mm. Once fully cured (approximately 12 hours), the
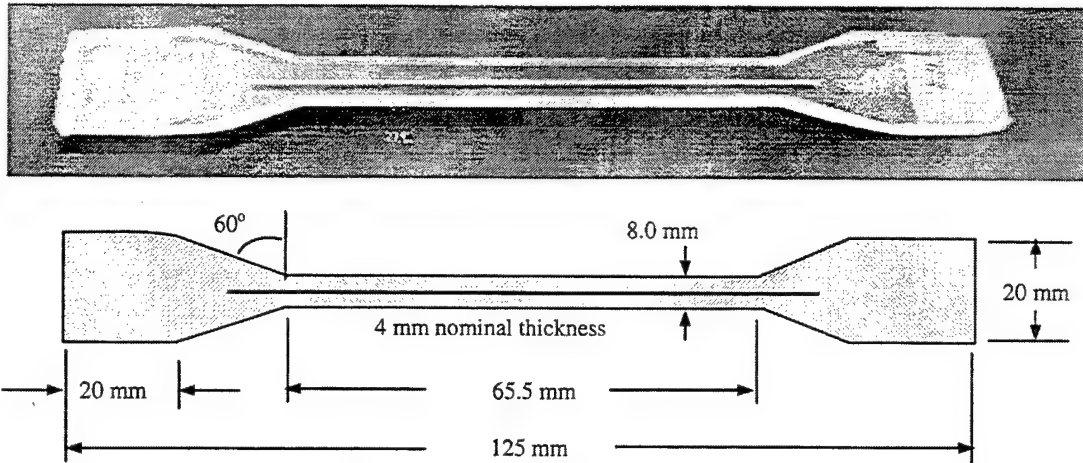
Figure 9. Strain-to-Failure and Single Fiber Fragmentation Test Coupon. Test coupons were fabricated from epoxy and a single PZT fiber. Both hollow and solid test specimens were fabricated. To allow fiber observation during testing, the epoxy was cured at 40°C (to remove air bubbles) and the coupons were ground and polished until transparent.

samples were ground and polished, resulting in a transparent single fiber lamina. The resulting coupons measured 125 mm by 20 mm with thickness ranging from 3.8 to 4.3 mm.

Results. The averages and standard deviations for the ultimate stress and strain-to-failure of each sample type are given in Table 3. In general, the variance in the data was relatively low for all sample types with the largest variations occurring in the pure epoxy samples (0.16%). The measured strain-to-failure of all of the ceramic fiber test specimens compare well to conventional composite types, falling within the range of values for carbon-reinforced epoxy composites (0.6-1.0%), and slightly below glass-reinforced composites (1.4-1.8%).[30] The same is not true, however, for the ultimate strength of the composites, which approach two orders of magnitude below typical glass- and carbon-fiber composites. This was expected. The role

of the fibers in a traditional composite are to reinforce the matrix, and the fibers are therefore chosen based on their high stiffness and strength. Active fibers, on the other hand, are designed solely around the fiber's ability to actuate the composite. Thus, the overall strength of the composite will naturally be lower than conventional composites due to this fundamental difference in design philosophy.

What is more interesting is the comparison of ultimate strength and strain-to-failure between the four sample types tested: epoxy blanks, low aspect ratio, high aspect ratio, and solid fiber coupons.

- **_Fiber Samples vs. Blank Samples._** The largest difference in strain-to-failure occurred between the blank coupons and those with embedded fibers. On average, the fiber samples failed at 0.91% strain, compared to 1.79% strain for the blank

Table 3. Composite Strain-to-Failure Test Results. The largest difference in strain-to-failure and ultimate strength occurred between the epoxy blank samples and those with embedded fibers, with solid and hollow fiber samples behaving very similarly.

		Sample Type			
		Epoxy Blank	**Solid Fiber**	**0.52 Aspect Ratio Fiber**	**0.42 Aspect Ratio Fiber**
Strain-to-Failure	Average	1.79 %	0.92 %	0.89 %	0.91 %
	Std. Dev.	0.16 %	0.10 %	0.08 %	0.12 %
Ultimate Strength	Average	21.6 MPa	12.5 MPa	12.0 MPa	11.9 MPa
	Std. Dev.	1.2 MPa	1.2 MPa	0.8 MPa	0.5 MPa

samples, a decrease in strain-to-failure of 51%. Most likely this decrease was due to residual tensile stresses in the matrix due to the curing process, or the cumulative effects of small cracks at fiber fracture locations resulting in stress concentrations.[29] Furthermore, this reduction in strain-to-failure is similar to conventional composites such as carbon/epoxy and glass/epoxy, where fiber introduction typically lowers composite strain-to-failures by 40 to 60%.[29,30]

- *Hollow samples vs. solid samples.* On average, the strain-to-failure of the hollow fiber coupons was 3.0% lower than the solid fiber coupons; thus, the hollow nature of the fiber when compared to solid fibers does not significantly affect the composite's failure in tension due to induced strain. The same, however, is not true for the composite's ultimate *strength*. The ultimate strength for the solid fiber samples was approximately 12.5 MPa, 8% higher than the two hollow fiber sample types, which had strengths of 11.9 and 12.0 MPa. This trend was expected because of the increased cross-sectional area (and thus stiffness) of solid fibers. Although 8% is a relatively low difference in ultimate strength, this difference is expected to grow as the volume fraction of the composite is increased. For very high volume fractions, for example, the difference in ultimate strength will approach the ratio of cross-sectional area between the solid and hollow fibers. In this limit, very low aspect ratio fibers would have only a fraction of the ultimate strength of solid fibers (<10%), whereas high aspect ratio fibers would have an ultimate strength nearly equal to that of solid fibers.

- *Low aspect ratio vs. high aspect ratio.* Comparing the low and high aspect ratio hollow fibers yielded similar results to the comparison to solid fibers. The difference between the strain-to-failure of the two hollow fiber types was less than 2%, indicating that composite strain-to-failure is not significantly affected by the choice of aspect ratio. There was also little difference in the ultimate strength of the two hollow fiber samples (12.0 MPa for high aspect ratio vs. 11.9 MPa for low aspect ratio). However, this small difference is due to the low difference between the aspect ratios tested, as well as the low volume fraction of the tested composites. Similar to the comparison between hollow and solid fiber prototypes, the increased ultimate strength of high aspect ratio fibers, a function of the fiber cross-sectional area, is expected to be more apparent at higher volume fractions.

It is interesting to note that even though the introduction of the PZT fibers into the epoxy matrix caused a reduction in the strain-to-failure of the AFC, the level of strain at which the *coupon* failed is still a factor of nine above the maximum published value of strain-to-failure of the PZT *fiber*, approximately 0.075% (EDO). Thus, there are two possibilities for what is occurring at high strain levels: 1) the fiber maintains its bond with the matrix resulting in tensile fiber fracture, or 2) the fiber debonds from the matrix, resulting in fiber pullout. During testing, audible 'clicking' sounds were heard, suggesting that the fiber was fracturing within the matrix. It was these individual fiber fracture points that were of interest in the single fiber fragmentation testing.

Single Fiber Fragmentation Testing – Composite Failure Mechanism

To experimentally determine the primary failure mechanism of the composite, a single fiber fragmentation test was conducted. The failure mechanism of the composite was identified by observing the photoelastic stress pattern surrounding a fiber fracture. For any single fiber test, exact correlation between failure mechanism and the ultimate strength and strain-to-failure is complex and analytical models are not in place for a general matrix and fiber material.[31,32] Normally empirical or finite element simulations are used to derive the general relationships, or "trends" between interfacial shear strength and overall composite properties such as ultimate strength and strain-to-failure under shear and transverse normal loading. Because the direct data for piezoceramic fibers was not available in this research, the failure mechanism of hollow fiber and solid fiber PZT composites were compared to the trends found in conventional composites to draw qualitative conclusions about their strength.

Experimental Procedure. Ten single fiber coupons were fabricated in the same manner as the strain-to-failure testing, using PZT fibers of 0.52 aspect ratio. These coupons were mounted in the Instron and tested at a very low rate (approximately 5 microns/sec.). The strain-to-failure test setup was modified by placing a large polarized light behind the sample and a small polarized lens in front of it (Figure 10). As the light passed through the sample, variations in stress levels in the matrix could be detected through the polarized lens as colored bands, or a photoelastic stress pattern, which helped to locate the fiber breaks.[33] As the strain on the coupon was increased, the location of each fiber break was photographed at approximately 30-second intervals until the level of strain approached the maximum value of 0.9% (determined from the composite strain-to-
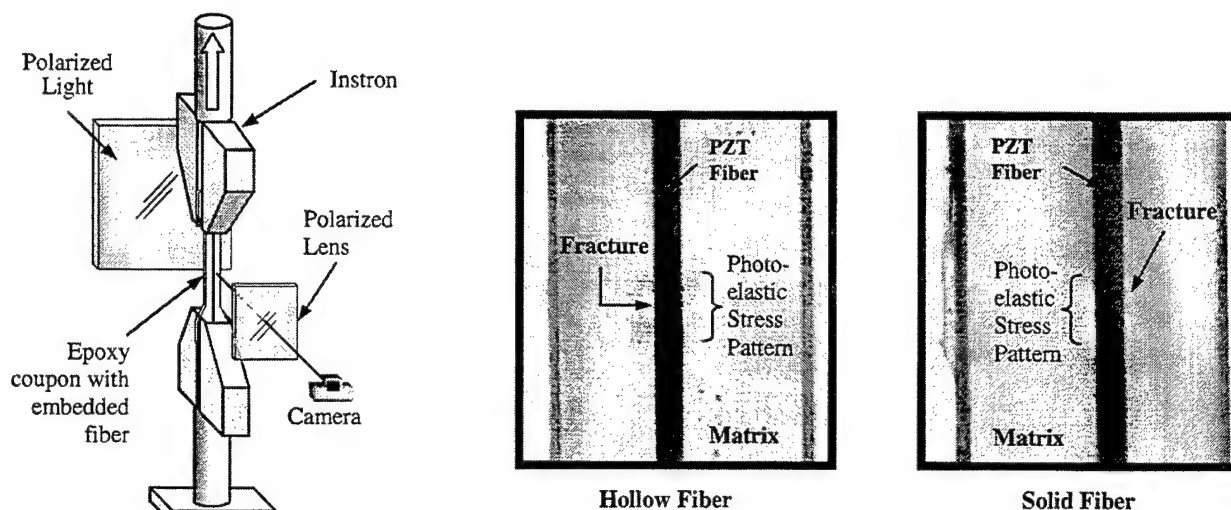
Figure 10. Single Fiber Fragmentation Experimental Setup. A single fiber test coupon was observed during tensile testing using transmitted polarized light photography, which allowed the fiber fracture points to be observed directly. For both hollow and solid PZT fibers, the photoelastic stress pattern observed was characteristic of interfacial crack growth.

failure test). At this point, the strain rate was decreased to 2 microns/second to photograph as many instances of fracture as possible before the coupon ultimately failed.

Results. There are three main types of failure mechanisms in fibrous composites[29]:

- *Frictional debonding.* Frictional debonding occurs when there is a low level of adhesion between the fiber and the matrix. Under this condition, when the fiber fails, it separates from the matrix and ceases to strain with the matrix. The photoelastic stress pattern typical of this type of failure does not radiate from the fiber because the fiber no longer interacts with the matrix at the point of failure.

- *Interfacial crack growth.* Interfacial crack growth occurs when there is a moderate level of interfacial adhesion. When the fiber fails under this condition, it does not completely debond from the matrix, and the stress pattern lines appear a small distance from the fiber, surrounding the fracture point, and running parallel to the fiber axis.

- *Matrix crack growth.* Matrix crack growth occurs when there is an extremely high level of interfacial adhesion. When the fiber fails, it does not separate from the matrix, causing a crack (and thus the photoelastic stress pattern) to extend perpendicular to the fiber, far into the matrix. This results in a very brittle situation, often causing the immediate failure of the entire composite.

For the active composite application, it is important to have a level of interfacial adhesion which results in interfacial crack growth, even more so than in conventional composites. For example, if the bond between the fiber and matrix is too low (resulting in frictional debonding), the fiber cannot transmit shear stresses to the matrix. This would render the entire composite inactive, which is contradictory to the main function of a piezoelectric active composite. On the other hand, a bond that is too strong will result in matrix crack growth, and a composite exhibiting brittle behavior, often failing at low stress levels due to notch-sensitive behavior. Therefore, there is an 'optimum level' of adhesion, characterized by interfacial crack growth, resulting in the greatest strain-to-failure of the composite under any loading condition.[29]

The photoelastic stress patterns for the hollow and solid fiber coupons, examples shown in Figure 10, indicates the failure *is* characteristic of interfacial crack growth. The stress lines are clearly visible surrounding the fracture point, running parallel to the fiber. Therefore, qualitative analysis of the stress patterns in the test coupons show that the level of fiber/matrix adhesion is optimum for the PZT and epoxy that were used for both hollow and solid fiber samples.

Single Fiber Indentation Test – Interfacial Shear Strength

Since the primary failure mechanism is interfacial crack growth, a single fiber indentation test was conducted to directly measure the value of the interfacial shear

14
American Institute of Aeronautics and Astronautics

strength at the fiber/matrix bond. For this test, a test coupon was sectioned into several pieces perpendicular to the fiber length, approximately 0.5 mm in length. A small steel pin, 600 microns in diameter, was placed directly in series with a force transducer (100 lb max; Sensotec, Columbus, OH), and placed against the end of the fiber. A vise was used to slowly increase the force on the fiber until eventually the fiber broke free from the matrix, at which point the maximum force, P, was recorded. From this force, the interfacial shear strength, τ, was calculated by simply dividing the force by the area of the fiber in contact with the matrix:

$$\tau = \frac{P}{\pi d l}, \qquad (9)$$

where l and d are the length and diameter of the embedded fiber.

Results. Ten samples were tested, yielding average interfacial shear strength of 59.2 MPa with a standard deviation of 9.0 MPa. While this value is approximately 13% lower than the optimum interfacial shear strength (68 MPa) reported for carbon fiber/epoxy composites and 50% higher than values reported for the carbon fiber frictional debonding case, it is well within the range of the interfacial crack growth failure mechanism.[29] It is important to note that the outcomes obtained for interfacial shear strength and failure mechanism are a function of the exact interaction between the PZT-5H material and the Struer's Epofix epoxy used in this test. Because the empirical results for the single fiber testing available in the literature focus solely on non-active composites, it is not possible to directly predict the numerical values for the ultimate strength of piezoceramic composites under loading conditions. However, conclusions may be drawn for piezoelectric AFC assuming similar correlations between the failure mechanism, interfacial shear strength, and ultimate strength observed in carbon fiber composites. For example, in transverse tension, the ultimate strength of a *carbon* fiber composite with interfacial crack growth failure mechanism was a factor of 2.1 greater than a similar composite that failed because of frictional debonding. Similarly, for carbon fiber in transverse flexural testing, ultimate strengths of are increased by a factor of 2.8 by changing the failure mechanism from frictional debonding to interfacial crack growth. The influence of the failure mechanism on longitudinal properties such as axial tension and flexure is minimal for carbon fiber, resulting in an increase of only 0.5% over frictional debonding.[30] In fact, higher levels of bonding characterized by matrix crack growth resulted in a *decrease* in longitudinal strain-to-failure, pointing out the importance of

avoiding this brittle failure mechanism.[29] If these same trends hold for piezoelectric fibers, then it can be concluded for the PZT and the epoxy matrix used, the observed failure mechanism and interfacial shear strength result in the best possible properties.

HOLLOW VERSUS SOLID FIBER COMPARISON

Throughout this work, the design trade-offs introduced by the key design parameters have been heavily focused on. Underlying this analysis, however, is perhaps an even more fundamental design trade-off: the advantages and disadvantages of using hollow fibers versus the current state of the art, solid fibers. To highlight the differences, the effective lamina d_{31} of hollow fiber composites was compared directly to the interdigitated active fiber (solid) composites researched by Bent and Hagood.[2] This body of work was chosen because it is regarded as one of the largest and most successful applications of long-fiber piezoelectric composites to date, and a substantial amount of modeling and test results are available. To make an accurate comparison, the effective lamina d_{31} of each design was compared at equal fiber volume fraction and material properties. In comparing the performance of hollow fibers to solid fiber active composites, the greatest difference was the maximum potential strain and activation voltage levels. At a volume fraction of 4.5%, the hollow fiber lamina prototype had a measured effective lamina d_{31} of 153 pm/V, whereas the solid fiber AFC measured 295 pm/V, a factor of 1.93 higher than the hollow design. This is not surprising because the solid fiber AFC design exploits the d_{33} mode of the fibers and thus has higher strain potential. In fact, it was expected that this ratio would be approximately 2.25, the ratio of d_{33} to d_{31} in PZT-5H. The lower ratio suggests that a portion of the electric field in a solid fiber AFC is lost in the matrix and does not reach the fiber. For a high volume fraction of 63%, the hollow fiber design has an effective lamina d_{31} of 92% of material d_{31}, or 248 pm/V (Figure 4a, 0.5 aspect ratio). The measured value for a 63% volume fraction AFC was 460.2 pm/V, a factor of 1.86 higher than the hollow fiber composite. Therefore, due to the d_{33} mode of actuation used, interdigitated solid fiber AFCs do have higher effective lamina d_{31}, and thus maximum strain potential, than equivalent hollow fiber composite at both low and high volume fractions.

Although the effective lamina d_{31} of hollow fiber composites is lower than that of solid fiber composites (approximately 50% less due to the d_{31} mode of activation), solid fiber AFCs require extreme voltages (kilovolts) because the distance between electrodes must be kept on the order of 1mm or larger to allow the

field to penetrate the matrix and reach the fiber, and to prevent dielectric breakdown of the air between electrodes. In general, fabricating smaller fibers and thinner lamina does not alleviate this fundamental problem. Therefore, to generate the maximum recommended working field of 400 V/mm, a minimum of 400 volts must be applied. It should be pointed out that solid fiber AFCs can be driven well above the coercive field, as high as 1600 V/mm, resulting in fiber breakage and re-poling with each actuation cycle.[34] However, driving the composite at these high field levels results in highly non-linear behavior, and the effect of fiber failure in hollow fiber composites is currently unknown. Therefore, to accurately compare the solid and hollow fibers, only the linear region below the maximum recommended field was considered. In hollow fibers, the electric field is generated across the fiber wall, and in this case the voltage requirement *does* drop with fiber size. For the lamina prototype tested, 400 V/mm was achieved by applying 75 volts. Scaling the hollow fibers tested down to the diameter of the solid AFC fibers (130 µm) reduces the voltage required to 10.8 volts, a reduction in voltage of 97% compared to solid fiber composites. Using lower aspect ratio fibers further reduces the needed voltage. Therefore, the use of hollow fibers does have the potential to drastically reduce the overall voltage needed for composite activation, which is one of the key issues currently impeding the use of the interdigitated AFC design.

One of the obvious drawbacks of the hollow fiber design is that it is potentially weaker than a solid fiber; however, the previous section demonstrated that hollow fibers do not introduce any significant decrease in reliability. Both hollow and solid fibers when embedded in epoxy, exhibit interfacial crack growth indicating a high level of fiber/matrix adhesion necessary for active composites. The interfacial shear strength of the composite samples was 59.2 MPa, on the same order as carbon fiber composites. A longitudinal strain-to-failure test was used to provide quantitative information about the strength of the composite in the fiber direction. This testing indicated that the strain-to-failure of the composite was not sensitive to the type of embedded fiber. Both hollow fiber samples failed at approximately the same strain as the solid fiber samples (0.93% vs. 0.97%), as well as at similar strains to carbon fiber composites, which ranged from 0.8% to 1.6%.[29] In addition to providing information about *composite* failure, the single fiber fragmentation test also enabled the strain-to-failure of the *individual fiber* to be observed. On average, the strain-to-failure of hollow fibers was equal to that of solid fibers, approximately 0.067%, which is more than an order of magnitude below the strain-to-failure of the

composite. Therefore, overall the reliability of solid and hollow fibers is comparable. However, the presence of fiber failure within the matrix raises one major difference between the reliability of solid and hollow piezoelectric fiber designs. Solid fiber active composites use an electrode that is external to the matrix, and therefore function regardless of the integrity of the fibers *inside* the matrix. Hollow fibers, on the other hand, rely on an electrode directly on the surface of the fiber. If this electrode breaks, and loses electrical connectivity, the fiber becomes inactive. Under this failure mode, solid fibers have an advantage over hollow fibers due to the external placement of the electrode. For the hollow design to match the reliability of solid fibers, steps must be taken to ensure that both the inner and outer electrodes remain intact in the event of the piezoelectric material in the fiber failing.

CONCLUSIONS

It was shown throughout this paper that the three primary design variables play critical roles in the performance, fabrication and reliability of hollow fibers with interesting design tradeoffs arising. Of the three design parameters, aspect ratio had the greatest overall effect, with impact on all areas of hollow fiber design. From a performance standpoint, low aspect ratio fibers have the lowest operating voltage, lowest electric field gradient, and highest effective d_{31} due to the thin fiber wall. When incorporated into a lamina, however, there exists an optimum aspect ratio, depending on the ratio of matrix to fiber Young moduli, which yields the highest effective lamina d_{31}. This optimum aspect ratio ranges from approximately 0.4 for soft epoxy matrices to 0.7 for stiff matrix materials such as aluminum. When fabricating hollow fibers using the MFCX process, the aspect ratio did not affect the waviness, curviness, or material properties of the fibers. However, cross-sectional properties generally improved (low ovality and eccentricity) as aspect ratio was increased. Naturally, the fiber aspect ratio also had a strong impact on the reliability of hollow fibers. Due to the high volume fractions achievable by high aspect ratio fibers, they have a higher ultimate strength and can be embedded into much stiffer materials than low aspect ratio fibers. This trend in increased ultimate strength continued as the aspect ratio approached the limit of 1.0, equivalent to a solid fiber.

While aspect ratio has the broadest impact, other design parameters still have a strong influence. For example, the Young's modulus ratio governs the choice of feasible materials. When embedding fibers into the matrix, the lowest stresses within the fiber wall occur for low values of the modulus ratio. In fact, through an embedding stress model, it was shown that the modulus

ratio must be below 1.0 for fiber embedment, even for the highest aspect ratio fibers (including solid fibers) and volume fractions. Thus, only matrix materials softer than piezoceramic may be utilized. The choice of modulus ratio actually determines the fiber aspect ratio that yields this maximum effective d_{31} value that occurs at the lower ratios.

In general, high volume fractions produce the greatest lamina performance or maximum effective lamina d_{31} – this is simply because the composite consists of more active material. Because the piezoelectric material has to be stiffer than the matrix ($Y_m/Y_f < 1$) to survive embedment, high volume fractions are required to achieve high ultimate strength. Piezoelectric materials are brittle; thus, composites that are matrix dominated (*low* volume fraction) tend to have the highest strain-to-failure values.

It is clear from this summary that there is no single value of aspect ratio, volume fraction, or modulus ratio, that is optimal in all configurations; thus, design trade-offs will *always* be present when designing a hollow fiber active composite. For example, the choice of fiber and matrix material will dictate a minimum aspect ratio based on the embedding stress model, which must be carefully chosen to achieve the maximum lamina d_{31} and avoid high electric field gradients and lower the operating voltages. Conversely, for low-voltage composites a low aspect ratio must be used which will decrease the geometric quality of the fibers, and severely limit the choice of matrix materials due to reliability issues. Therefore, due to the broad impact of the design parameters introduced in this paper, it is important to consider performance, fabrication, and reliability issues simultaneously in the design of hollow piezoelectric fiber active composites.

ACKNOWLEDGEMENTS

REFERENCES

1. Li, L. and Sottos, N.R., 1994, "Consideration of electro-mechanical coupling in the prediction of 1-3 piezocomposite properties", *Proceedings of the 1994 International Mechanical Engineering Congress*, AMD, Vol. 193, p 23-32.
2. Bent, A.A., Hagood, N.W., and Rodgers, John P., 1995, "Anisotropic actuation with piezoelectric fiber composites", *Journal of Intelligent Material Systems and Structures*, Vol. 6, No. 3, May 1995, p 338-349.
3. Maclean, B.J. and Jacobsen, S.C., 1995-96, "Active Fibers for Development of Adaptive Structures", *ARPA Actuator Issues Workshop*.
4. Fernandez, J.F., Dogan, A., Zhang, Q.M., Tressler, J.F., Newnham, R.E., 1995, "Hollow piezoelectric composites", *Sensors and Actuators, A: Physical*, Vol. 51 No. 2-3, p 183-192.
5. Zhang, Q., Wang, H., Cross, L.E., 1993, "Piezoelectric tubes and tubular composites for actuator and sensor applications", *Journal of Materials Science*, Vol. 28, No. 14, p 3962-3968.
6. Krishna-Murty, A.V., Anjanappa, M. A., and Wu, Y., 1996, "Vibration control of magnetostrictive composite beams", *Proceedings of SPIE - The International Society of Optical Engineering*, Vol. 2717, p 482-491.
7. Sottos, N.R., Kline, G.E., Qidwai, M.A., and Lagoudas, D.C., 1996 "Analysis of phase transformation fronts in SMA composites", *Proceedings of SPIE - The International Society for Optical Engineering*, Vol. 2715, p 427-438.
8. Guigou, C. and Fuller, C.R., 1997, "Foam-PVDF smart skin for aircraft interior sound control", *Proceedings of SPIE - The International Society for Optical Engineering*, Vol. 3044, p 68-78.
9. Herold-Schmidt, U., Schaefer, W., Zaglauer, H.W., 1996, "Piezoceramics/CFRP composites for active vibration control and shape control of aerospace structures", *Proceedings of SPIE - The International Society for Optical Engineering*, Vol. 2779, p 718-723.
10. Rodgers, J.P., Hagood, N.W., and Weems, D.B., 1997, "Design and manufacture of an integral twist-actuated rotor blade", *38th AIAA/ASME/ASCE/AHS/ASC Structures, Structural Dynamics, and Materials Conference*, AIAA Paper No. 97-1264.
11. Thomas, M.M. and Trottier, C. M., 1995, "Industrial fabrication of smart structures for vibration control", *Proceedings of the 1995 ASME International Mechanical Engineering Congress & Exposition*, No. 95-WA/NCA-1, New York.
12. Wilkie, W.K., Bryant, R. G., High, J. W. Fox, R. L., Hellbaum, R. F., Jalink, A. Jr., Little, B. D., and Mirick, P. H., 2000, "Low-cost piezocomposite actuator for structural control applications", *Proceedings of SPIE - The International Society for Optical Engineering* Vol. 399, Bellingham, WA, USA. p 323-334.
13. Safari, A., Janas, V., and Panda, R., 1996, "Fabrication of fine-scale 1-3 Pb(Zrx,Ti1-x)O3/ceramic/polymer composites using a modified lost mold method", *Proceedings of*

SPIE - The International Society for Optical Engineering, Vol. 2721, p 251-262.

14. Bowen, L.J., Gentilman, R.L., Pham, H.T., Fiore, D.F., French, K.W., 1993, "Injection molded fine-scale piezoelectric composite transducers", *Proceedings of the IEEE Ultrasonics Symposium*, Vol. 1, No. 93CH3301-9, p 499-503.

15. Lubitz, K., Wolff, A., and Preu, 1993, "Microstructuring Technology", *Proceedings of the IEEE Ultrasonics Symposium*, Vol. 1, No. 93CH3301-9, p 515-524.

16. Klicker, K.A., Biggers, J.V., and Newnham, R.E., 1981, "Composites of PZT and epoxy for hydrostatic transducer applications", *Journal of The American Ceramic Society*, Vol. 64, No. 1, p 5-9.

17. French, J.D., Weitz, G.E., Luke, J.E., Cass, R.B., Jadidian, B., Bhargava, P., and Safari, A., 1997, "Production of continuous piezoelectric ceramic fibers for smart materials and active control devices", *Proceedings of SPIE - The International Society for Optical Engineering*, Vol. 3044, p 406-412.

18. Strock, H.B., Pascucci, M.R., Parish, M.V., Bent, A.A., and Shrout, T.R., 1999, "Active PZT fibers, a commercial production process", *Proceedings of SPIE - The International Society for Optical Engineering*, Vol. 3675, p 22-31.

19. Crumm, A.T. and Halloran, J.W., 1998, "Microfabrication of Multicomponent Ceramics", *Journal of The American Ceramic Society*, Vol. 81, No. 4, p 1053-57.

20. Cannon, B.J. and Brei, D., 2001, "Feasibility study of microfabrication by coextrusion (MFCX) hollow fibers for active composites", *Journal of Intelligent Material Systems and Structures*, Vol. 11 n 9, p 659-670.

21. Cannon, B.J., 2001, "Piezoceramic hollow fiber active composites", Ph.D. Thesis, The University of Michigan.

22. Halliday, D. and Resnick, R., 1988, *Fundamentals of Physics*, John Wiley & Sons, Inc., New York.

23. Hyer, M.W., 1998, *Stress Analysis of Fiber-Reinforced Composite Materials*, McGraw-Hill Companies, New York.

24. Shigley and Mischke, 1989, *Mechanical Engineering Design*, McGraw Hill, Inc., New York.

25. Mallick, P.K., 1993, *Fiber-reinforced Composites: Materials, Manufacturing, and Design*, M. Dekker, New York.

26. ASM, International, 1998, *"Engineered Materials Handbook: Composites"*, Vol.1, ASM International, Metals Park, OH.

27. Crumm, A.T., 2000, "MicroFabarication by CoeXtrusion", Ph.D. Thesis, The University of Michigan.

28. Deng, S., and Ye, L., 1999, "Influence of fiber-matrix adhesion on mechanical properties of graphite/epoxy composites: I. Tensile, flexure, and fatigue properties", *Journal of Reinforced Plastics and Composites*, Vol. 18, No. 11, p 1021-1040.

29. Drzal, L.T. and Madhukar, M., 1993, "Fibre-matrix adhesion and its relationship to composite mechanical properties", *Journal of Materials Science*, Vol. 28, p 569-610.

30. Hertzberg, R.W., 1996, *Deformation and Fracture Mechanics of Engineering Materials*, John Wiley and Sons, Inc., New York.

31. Curtin, W.A. and Takeda, N., 1998, "Tensile strength of fiber-reinforced composites: II. Application to polymer matrix composites", *Journal of Composite Materials*, Vol. 32, No. 22, p 2060-2081.

32. Tripathi D., and Jones, F.R., 1998, "Single fibre fragmentation test for assessing adhesion in fibre reinforced composites", *Journal of Materials Science*, Vol. 33, No. 1, p1-16.

33. Durelli, A.J., 1958, *Introduction to the Theoretical and Experimental Analysis of Stress and Strain*, McGraw-Hill Companies, New York.

34. Hagood, N.W. and Pizzochero, A., 1997, "Residual Stiffness and Actuation Properties of Piezoelectric Composites: Theory and Experiment", *Journal of Intelligent Material Systems and Structures*, Vol. 8, p 724-737.

Experimental characterization and model validation of the quasi-static performance of piezoceramic telescopic actuators

Paul W. Alexander*, Diann Brei**
Department of Mechanical Engineering, The University of Michigan

ABSTRACT

The piezoelectric telescopic actuation architecture capitalizes upon an internally leveraged amplification technique to produce large actuation forces with amplified displacements. This building-block type actuator consists of interconnected concentric, cascaded cylinders with end cap joints that allow for a telescopic type motion. The internal amplification scheme and building-block nature of the telescopic design allow for efficient, densely packed actuators that yield a high work output for a given volume. This paper presents an experimental investigation of the quasi-static force-deflection performance of three unique telescopic prototypes, each manufactured by different means, from various materials, and in distinct geometries. To accurately predict the observed behavior of this architecture, a full three dimensional numeric model was constructed for each prototype and was used to revise a previously derived analytic model. These models were designed to include extra compliance factors to account for observed actuation losses, focusing primarily on the bonding layer effects. The revised models more accurately captured the complex actuator behavior observed in the experiments and better characterized the loss mechanisms in the telescopic architecture.

Keywords: actuator, piezoelectric, piezoceramic, telescopic

1. INTRODUCTION

Piezoelectric actuators are hampered by their inability to generate large strokes due to the limited strain available from the activated material. This is especially a problem for stack actuators, often resulting in infeasible actuator lengths for a given application. Fortunately, because of their large forcing capabilities, it is possible to employ various amplification techniques that sacrifice some of this forcing potential to amplify the actuator's stroke. Several researchers have been successful in employing external leveraging mechanisms coupled with piezoelectric stacks to amplify actuator displacement[1,2,3] for a variety of applications such as heavy machinery isolation mounts[4,5], active rotor blade flaps[6,7,8], and fuel injectors[9]. While these externally amplified actuators posses a high power efficiency for a given actuator mass, the additional components necessary for this amplification greatly reduce the actuator's volumetric power efficiency. This can be a critical design issue for applications that dictate a highly constrained actuator volume, such as fuel injectors and active munitions.

The telescopic architecture[10,11,12] is a high work per volume architecture, which achieves internal amplification through the nesting of piezoelectric shells. These shells are connected through alternating endcaps to achieve a telescopic motion when activated. This is depicted in Figure 1 for a three-tube actuator. Even though theoretically the shell can be any cross sectional shape, the most common is a cylindrical tube. The shells can be activated in a d_{33} or d_{31} mode causing the tube to either expand or contract, with the direction of strain alternating between adjacent shells; thus, resulting in a total stroke that is the summation of the individual shell deflections. Though actuation force is decreased as the overall cross-sectional shell area drops, the magnitude is still on the same order as a stack of comparable length. Therefore, this internally-leveraged building-block design allows for numerous piezoelectric shells to be packed tightly into constrained volumes, thereby efficiently filling the entire available space with active material.

Previous modeling research on this architecture estimated displacement amplitudes up to 20 times that of a stack, with competitive work efficiencies when compared to the current state of the art[11]. The architecture performance is directly dependant on the number of tubes composing a given actuator, with displacement amplifications equal to this number. However, there is a limit to the amplification that can be achieved because, as the number of tubes increases, the force decreases by as much as 85% for a high number of active tubes. A large portion of this loss can be attributed to the end caps and quality of connections between the tubes. As the gap between the tubes increases, the work capabilities decrease by as much as 28% for excessively large tube spacing. If soft, compliant materials are employed as end caps, losses as high as 15% were predicted for the force generated. This paper describes an experimental study of three prototype telescopic
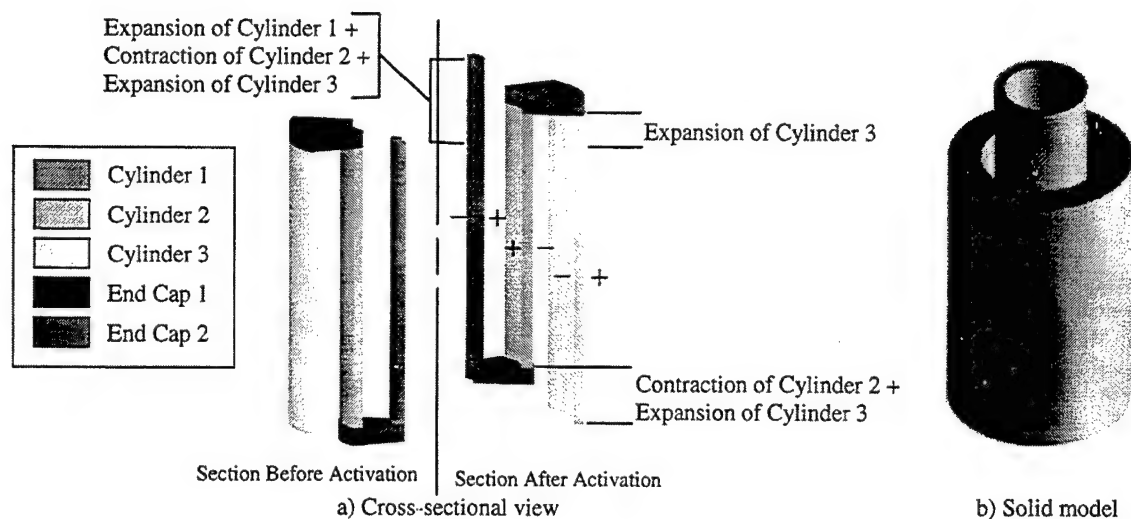
Figure 1: Activation of a three-tube telescopic actuator

actuators, which confirms these previous findings and identified other key loss mechanisms that were neglected in past modeling efforts. The quasi-static analytical and numerical models were updated to include these factors and were analyze with respect to each other and the experimental results.

2. QUASI-STATIC EXPERIMENTAL STUDY

All of the previous work was based on analytical and finite element modeling. With any physical prototype there are always other loss mechanism, such as bonding layers and connections, in addition to inherit architectural losses that limit the performance of the actuator. Many times the losses from the practical implementation of the architecture are the most significant and define the actual performance for a given device. To identify and assess these losses a quasi-static behavior experimental study was conducted with a variety of prototypes ranging from monolithic to assembled with different material and geometric characteristics.

2.1 Telescopic Prototypes

Three different methods were used to fabricate the various prototypes for the experimental study: injection molding, an acrylate polymerization process, and conventional component assembly. A detailed description of each fabrication method is given in a previous paper[12], and is summarized here.

2.1.1 Injection Molded Prototype

An ideal piezoelectric actuator would be one where active material occupies the entire actuation space, maximizing the potential work output. In an effort to reach this vision, a small, high tolerance telescopic actuator was fabricated utilizing the injection molding capabilities of Materials Systems Inc. (MSI) in Littleton, MA[13]. MSI's injection molding process uses a heated thermoplastic mix of PZT powder and a wax-based binder that is forced into a cooled mold where it solidifies and a green part is created. Once the preform is removed from the mold, the binder is burnt out and the remaining ceramic is sintered at 1250° C for 1 hour, under controlled atmospheric conditions to achieve a fully densified ceramic actuator. Each tube is then contact poled in the radial direction, one at a time, by a 1.2 kV/mm electric field. Afterwards, the entire actuator is coated entirely with a nickel electrode. Grinding the end of the final tube to remove unnecessary plating creates two distinct electrodes. This process was used to fabricate a five-tube, monolithic prototype whose dimensions are given in Figure 2, with the relevant material properties listed in Table 1.
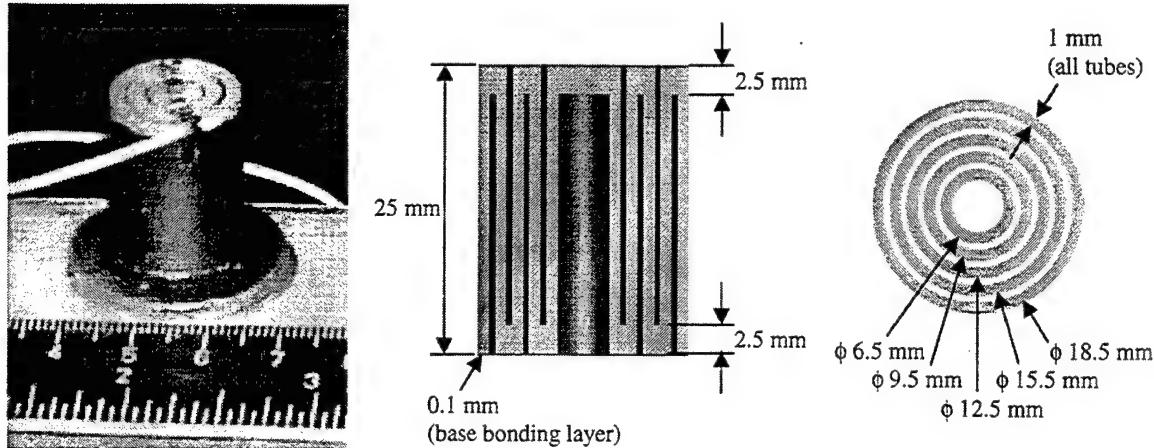
Figure 2: Injection molded prototype – photograph and drawing

2.1.2   Acrylate Polymerized Prototype

While the injection molding technique results in high quality parts, currently it can only produce components having small aspect ratios. To fully explore the behavior of this architecture, a taller actuator was desired. Thus, the new method of acrylate polymerization was developed at the University of Michigan by Prof. John Halloran to fabricate large and complex monolithic piezoelectric structures. The acrylate polymerization processes uses a nonaqueous slurry of American Piezo Ceramic's (APC's) piezoceramic powder, monomers, a catalyst, and a dispersant which is poured into a polished, lubricated mold fabricated utilizing a stereolithography technique. The newly cast perform undergoes a burnout process and is subsequently sintered at $1275°$ C for 4 hours. The densified prototype is painted with a baked-on silver electrode and poled at 2000 V (1.67 MV/m) in a $160°$ C silicone oil bath. The actuator is completed by soldering individual leads onto each side of the actuation tubes. For this experimental study, the resulting three-tube polymerized prototype is depicted with dimensions in Figure 3, while Table 2 lists the relevant material properties.

2.1.3   Conventionally Assembled Prototype

Since both of the other prototypes were fabricated using new methods, the third prototype was assembled from three off-the-shelf, pre-poled electroded piezoceramic cylinders with known material properties purchased from APC. This prototype is unique from the previous monolithic prototypes because it has discrete machined aluminum end caps affixed with Insulcast epoxy, which has the potential to be a loss mechanism. The alternating activation polarity was achieved by soldering wires between the electrodes on the outer wall of the largest tube to the inner wall of the medium tube, then to the outer wall of the small tube. Likewise, the electrodes on the inner wall of the large tube, the outer wall of the medium tube, and the inner wall of the small tube were electrically connected. This enables two electrical leads, one from the outer wall of the large tube and one from the inner wall of the small tube, to fully activate adjacent tubes with opposing polarity. The result is a three-tube telescopic actuator shown in Figure 4 with the material specifications listed in Table 3.

Table 1: Material properties for the injection molded prototype

Actuator Component	Material Type	Density	Young's Modulus	Poisson's Ratio	Piezoelectric Coefficient
Tubes	MSI-53	7500 kg/m³	62 GPa	0.3	440 pm/V
End Caps	MSI-53	7500 kg/m³	62 GPa	0.3	Inactive
Bonding Layers	Insulcast 501 Insulcure 24	1150 kg/m³	1.9 GPa	0.3	N/A

2.2   Experimental Procedure

To measure the quasi-static performance of each prototype, the apparatus in Figure 5 was employed. Because of the high stiffness of each telescopic actuator, close attention was paid to the test set up, insuring a high degree of stiffness in the actuator mount and eliminating any low stiffness components from the chain of deflection measurement. For example, the actuators were mounted to quarter-inch aluminum plates that were secured to a
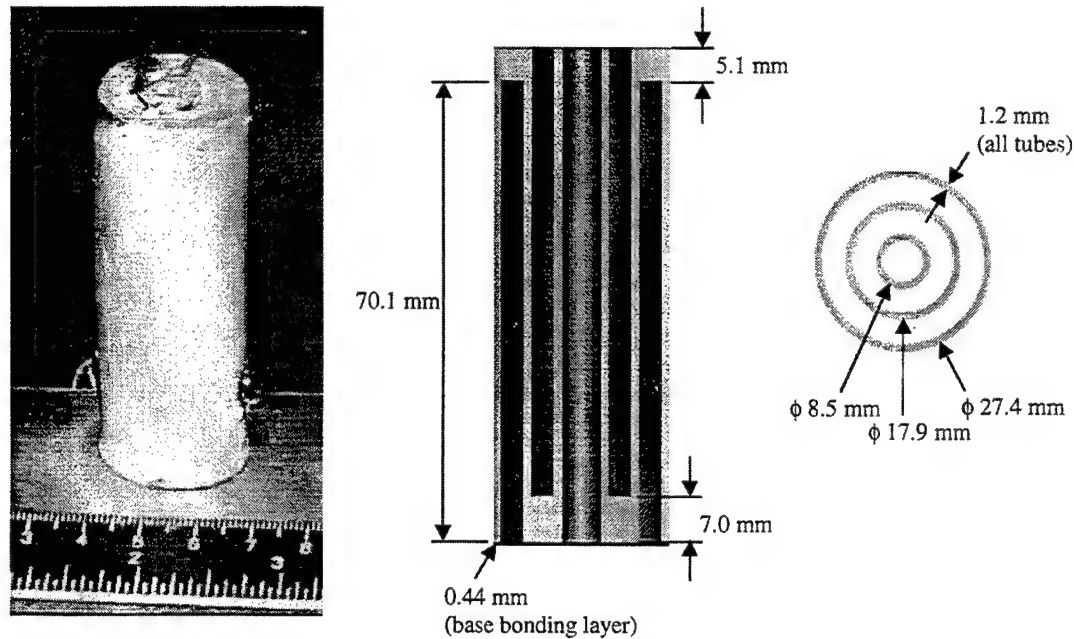
Figure 3: Acrylate polymerized prototype – photograph and drawing

reinforced steel back-plate that was bolted to a one-inch thick aluminum bed; this test bed was in turn bolted to a vibration isolation table. Each actuator was activated by a 100 V potential supplied by Kepco APH 2000 DC power supply. For this driving voltage, the free displacement of the activated prototype was measured by a Philtec A88NE1 fiber optic probe at various points around the actuator circumference and was averaged. Once the free displacement was measured, force was applied to the actuator by dialing-in a micrometer on a Newport load bearing stage with a Cooper LPM 530 load cell in-line with the prototype. Force was measured in 25 N increments until the blocked force was reached or 100 N. While each actuator was predicted to generate more force than 100 N at certain driving potentials, this was set as a conservative upper limit due to the lack of functional prototypes. This process was repeated, incrementing the driving potential by 100 V each test run, until the maximum driving field for each actuator was reached.

2.3   Experimental Results

The experimental results for each prototype are given in Figure 6. As would be expected, the actuator with the longest total tube length produced the most deflection for a similar driving field (300 V/mm for the injection molded and conventionally assembled prototypes, and 250 V/mm for the polymerized prototype), with the assembled actuator generating a free deflection of 27.4 µm, a 269.7 N blocked force, and a 9.8 N/µm actuator stiffness. The blocked force of the assembled and polymerized actuators were quite similar, with the polymerized prototype generating a blocked force of 256.9 N, a free deflection of 21.9 µm, and an overall actuator stiffness of 11.4 N/µm. Because the length of these actuators is much greater than the injection molded prototype, their free deflections are much higher, so the necessary force to negate this deflection also rises. The stiffness of these actuators takes both the free deflection and the blocked force into account, which shows that the injection molded actuator is the stiffest of all prototypes at 15.4 N/µm, with a the low free deflection of 13.9 µm and blocked force of 213.4 N. This is a curious result, because this prototype has more end caps (4) than the other two prototypes (2), which are a known source of compliance in the telescopic architecture. However, the tubes of the injection molded prototype are much shorter, and thus stiffer, but they are

Table 2: Material properties for the acrylate polymerized prototype

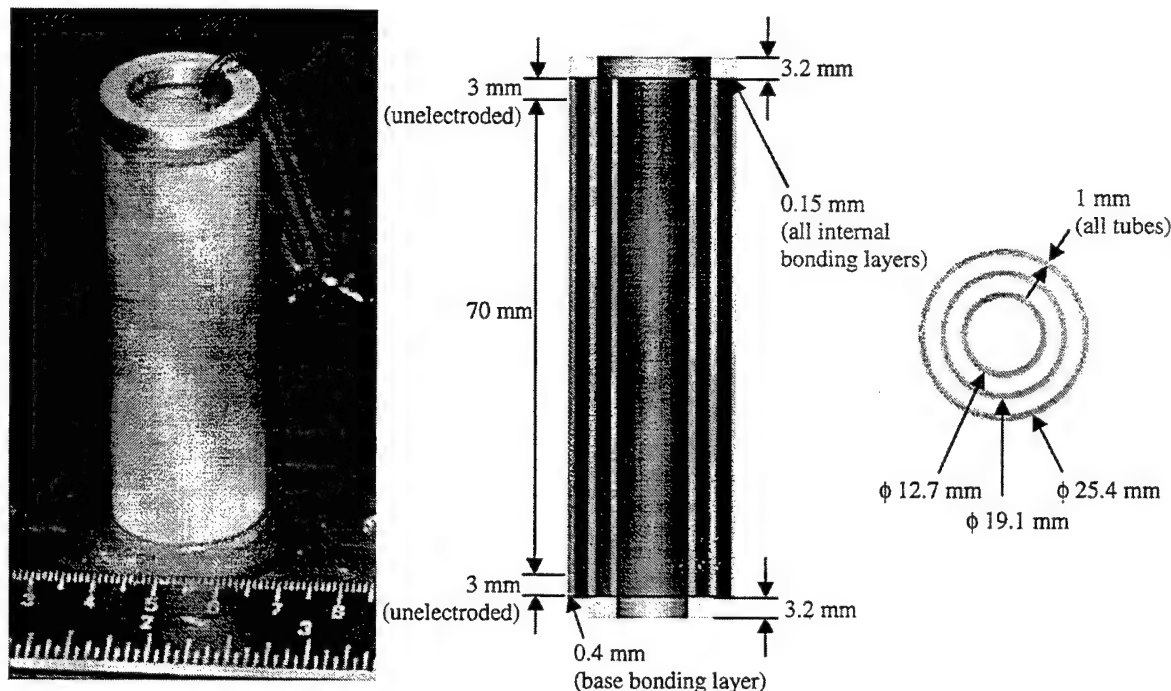| Actuator Component	Material Type	Density	Young's Modulus	Poisson's Ratio	Piezoelectric Coefficient
Tubes	APC PZT 586	7500 kg/m³	62 GPa	0.3	430 pm/V
End Caps	APC PZT 586	7500 kg/m³	62 GPa	0.3	Inactive
Bonding Layers	Insulcast 501 Insulcure 24	1150 kg/m³	1.9 GPa	0.3	N/A

Figure 4: Conventionally assembled prototype – photograph and drawing

also much closer together, resulting in radially thin, ceramic end caps that are quite stiff. The polymerized and assembled actuators are very similar in size, but have long and widely spaced tubes which gives much thicker end caps in the radial direction, and together these factors give a lower overall actuator stiffness. Furthermore, the end caps of the polymerized actuator are ceramic and axially thick, as opposed to the thinner aluminum end caps of the assembled actuator, so it is stiffer than the assembled actuator. Overall the telescopic architecture did produce the type of deflection amplification it was designed to generate with very respectable forcing capabilities for an internally leveraged, building block type piezoelectric actuator.

From Figure 6, the analytical models predict the free deflection to as low as 2.7% for the injection molded prototype, 1.1% for the polymerized prototype, and 0.2% for the assembled actuator. As suspected, the previous developed analytical models[11] do not capture the full actuator performance under loading. Figure 6 shows that the analytical models over estimate the actuator forcing capabilities and stiffness for all cases. The original model predictions of the blocking force were off by as little as 3.6% for the 100 V polymerized prototype trial, but grow to as much as 32.7% for the case of the 200 V assembled prototype. The error in predicted actuator stiffness varied from 4.9% to 28.6%, with the highest error in the 100 V conventionally assembled case and the lowest error attributed to the 100 V acrylate polymerized model. These results strongly suggested a systematic error in the model and not experimental errors.

3. REFINED QUASI-STATIC MODELS

Table 3: Material properties for the conventionally assembled prototype

Actuator Component	Material Type	Density	Young's Modulus	Poisson's Ratio	Piezoelectric Coefficient
Tubes	APC PZT 855	7500 kg/m³	62 GPa	0.3	420 pm/V
End Caps	Aluminum	2700 kg/m³	70 GPa	0.3	N/A
Bonding Layers	Insulcast 501 Insulcure 24	1150 kg/m³	1.9 GPa	0.3	N/A

Comparison between the experimental results and the model predictions demonstrated that the original analytic model derived for this architecture was not accounting for all the necessary components of the telescopic prototype, and was in need of enhancement. Full three-dimensional numerical models were developed to provide insights to the missing elements in the analytical models. Once these were identified, the analytical models were updated to account for these in a simplistic
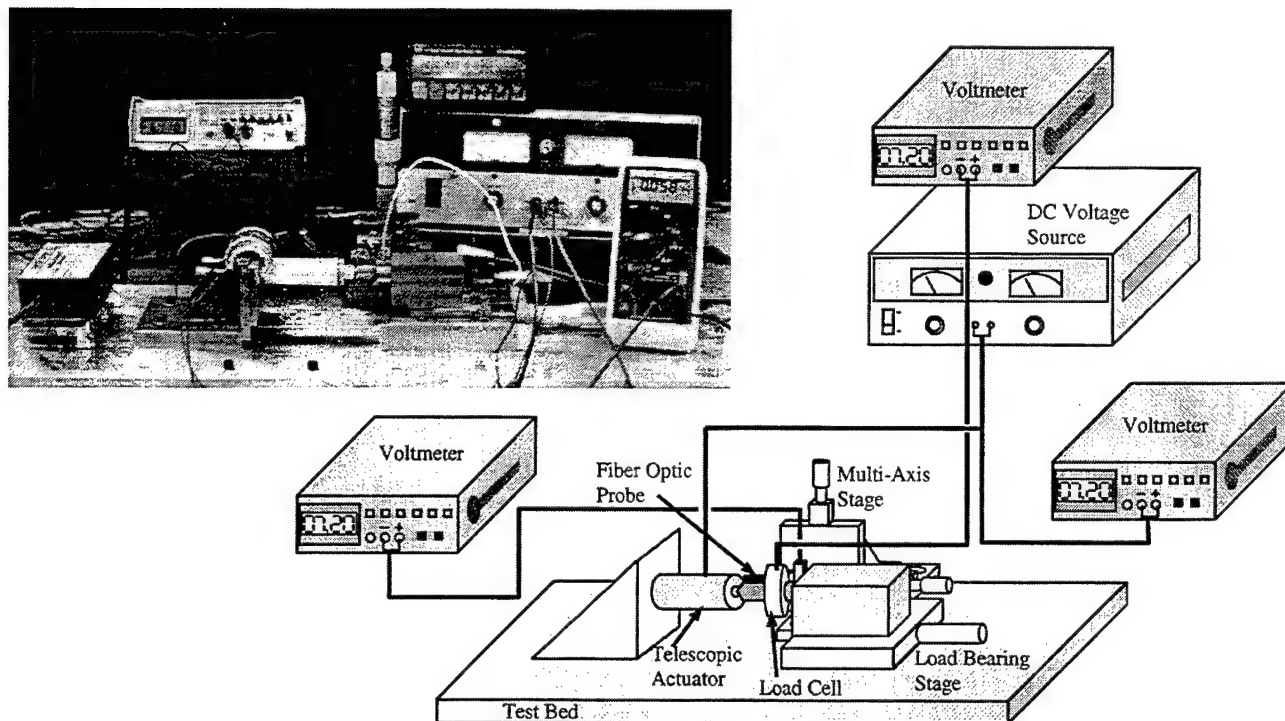
Figure 5: Experimental test apparatus – photograph and schematic

manner. Both models were compared to each other and evaluated against the experimental results.

3.1   Numerical Modeling

Each of the three telescopic prototypes was numerically modeled in three dimensions and included all physical elements: piezoelectric tubes, discrete or piezoelectric endcaps, bonding layers even at mounts. Because of their symmetry, only one half of an actuator's axial cross-section was constructed and meshed using the Hypermesh program. By using the eight nodded, bi-quadratic axisymmetric elements (type CAX8 & CAX8E) available in ABAQUS, the fully three-dimensional model was obtained that accounts for bending and shearing within the tubes, endcaps, and bonding layers and radial and circumferential piezoelectrically induced strains. Two different cases with different end conditions were modeled for each prototype, a free deflection case and a completely blocked case. For both trials, the bonding layer on the bottom edge of the outer tube of the model was restricted from moving in the radial and vertical direction (fully constrained in an axisymmetric

model). For the blocked case, the top of edge of the inner tube was also restricted from moving in the vertical direction. Each prototype was theoretically activated by specifying an electric potential along the electroded actuator surfaces. The ABAQUS files containing the deflection and reaction force values generated from these modeling runs were used to create a numerically predicted force-deflection curve for the each prototype.

Figure 6 displays the results of the numeric modeling compared to experimental data. The numeric model of the injection molded prototype (Figure 6a) predicts 13.7 μm of movement that could be blocked by a theoretic 208.4 N force, yielding a stiffness 15.2 N/μm at the maximum driving potential. This showed a close correlation to the experimental results with errors of 1.5% in predicted deflection, 2.4% for the blocked force, 0.9% for the actuator stiffness, and an overall model error of 1.9%. This prototype was well made with very little variability in dimensions and material properties; thus, it was possible to model it accurately. The polymerized prototype on the other hand had extremes in variability. The prototype possesses poor geometric tolerances, with varying wall thickness and warping of the tubes in both the radial and axial directions, in addition to a large degree of uncertainty in the extent of the hand painted electrode and its integrity. Despite this variability, the model was fairly robust. The numerical model of the polymerized prototype (Figure 6b), at the maximum driving field, gives a predicted deflection of 21.7 μm, a blocked force of 283.1 N, and a stiffness of 13.1 N/μm. This results in 1.1% error
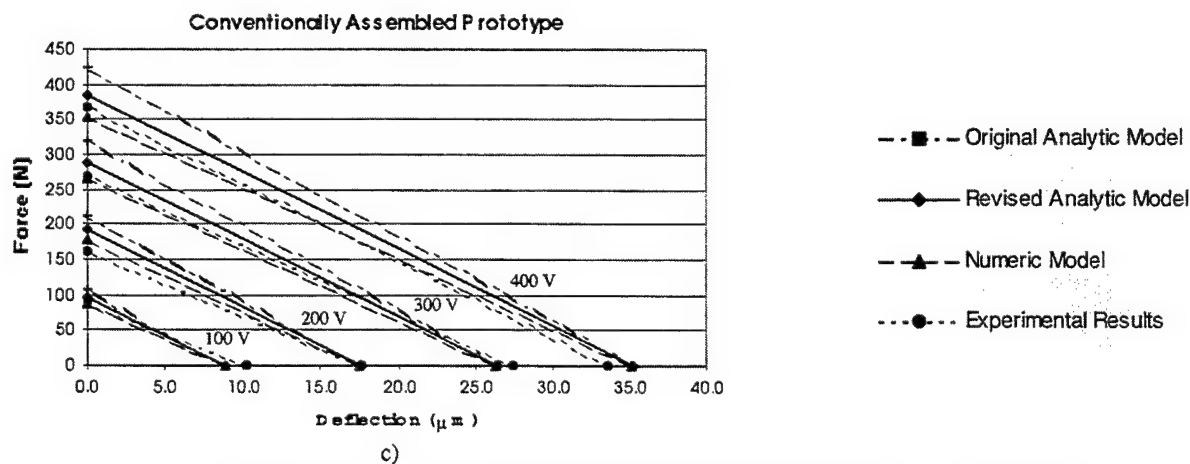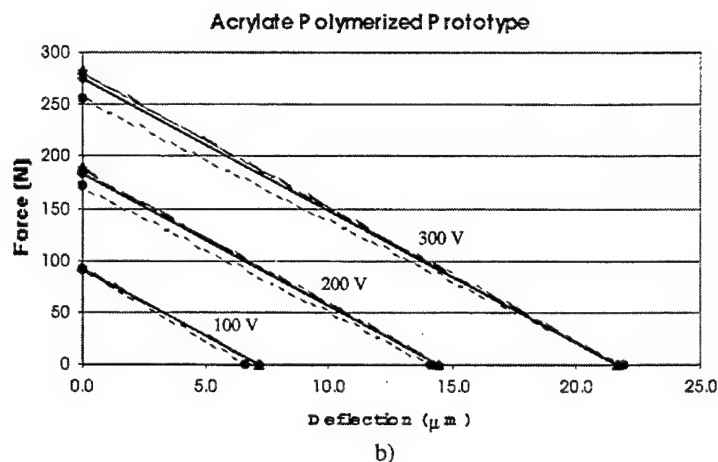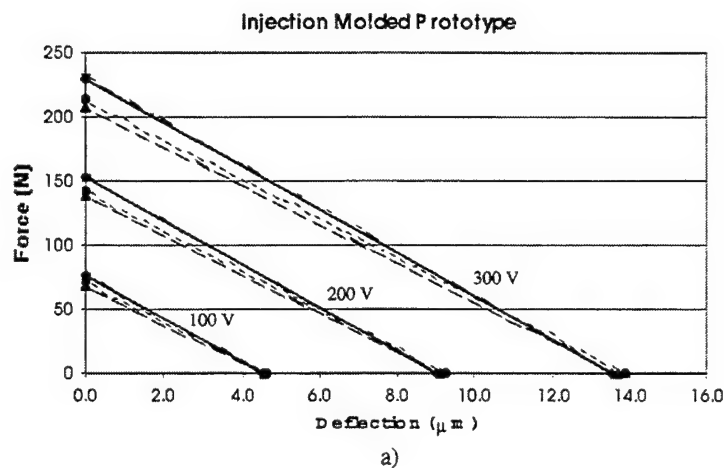
Figure 6: Modeled and experimental results for the quasi-static performance of each prototype

in the displacement, 10.2% error in the blocked force, 11.4% error in the overall actuator stiffness, and 5.9% total model error. In light of all the unknowns in this prototype, this correlation is quite good. The assembled prototype was between these two prototypes in quality. The material properties were well known except the dimensions of the internal bonding layers, which could not be easily measured from the completed prototype due to their inaccessibility. The numerical model of the assembled prototype displayed a good degree of accuracy for its maximum driving potential of 400 V, resulting in 4.4% error in the predicted free deflection of 35.1 μm, 3.7% error in the predicted blocked force of 355.0 N, 8.4% error in the 10.1 N/μm predicted stiffness, with 3.9% in the overall model. The differences between the analytical and numeric models include the modeling of the bonding layers and the fact that the numerical model is three dimensional, so that non-axial
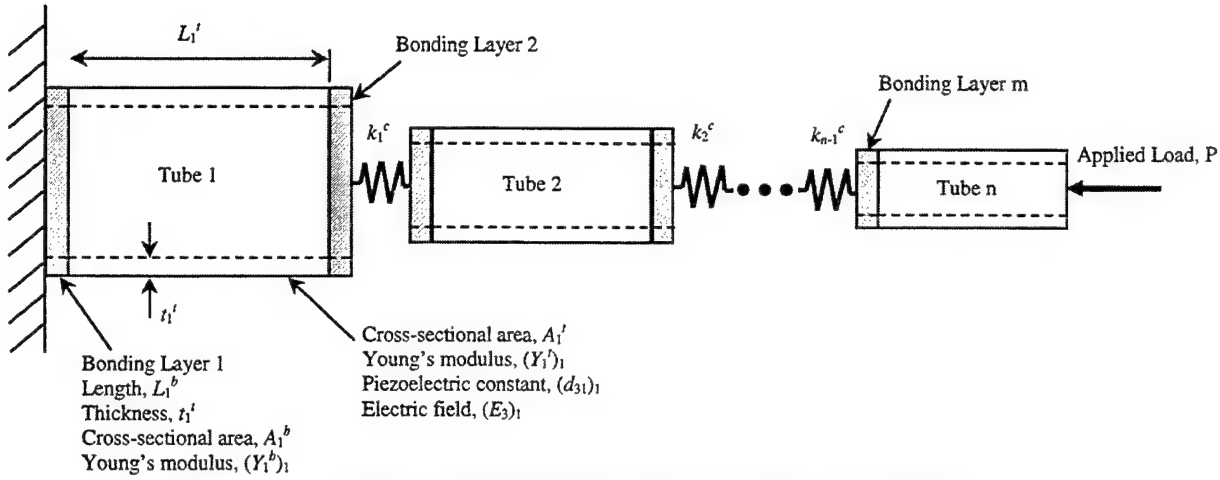
Figure 7: Revised analytical model of the telescopic architecture

deformations, including bending, twisting and shearing, and piezoelectric effects are taken into account, plus the end caps are modeled as they truly are, and not as derived spring coefficients. However, the greatest single factor affecting the predictions appears to be bonding layers, especially when the actuator contains many layers, as is the case with the conventionally assembled prototype.

3.2 Analytical Modeling

To increase the accuracy, the previous analytic model was augmented to account for the presence of bonding layers. The original analytical model was developed using Castigliano's theorem and a strain energy approach, and is extensively outlined in Berner and Brei's paper[11]. The telescopic actuator was modeled as discrete piezoelectric cylinders connect by springs. The linear springs represented the compliance in the end caps. To capture the compliance introduced by the bonding layers, they were incorporated into the original model as an additional term:

$$\frac{P t_i^b}{Y_i^b A_i^b} \tag{1}$$

in the positions depicted in Figure 7. Where P is the applied load and the new terms for the ith bonding layer's thickness - t_i^b, Young's modulus - Y_i^b, and cross-sectional area - A_i^b. This yields the free deflection, Δ^F, of an n-tube, m-bonding layer actuator as:

$$\Delta^F = \sum_{i=1}^{n} (d_{31})_i (E_3)_i L_i^t \tag{2}$$

Where L_i^t is the ith tube's length, $(d_{31})_i$ is its piezoelectric coefficient, and $(E_3)_i$ is the electric field applied to that tube. The predicted blocked force for the revised model, F^B, is:

$$F^B = \frac{\sum_{i=1}^{n} \left((d_{31})_i (E_3)_i L_i^t \right)}{\left(\sum_{i=1}^{n} \left(\frac{L_i^t}{Y_i^t A_i^t} \right) + \sum_{i=1}^{n-1} \left(\frac{1}{k_i^c} \right) + \sum_{i=1}^{m} \left(\frac{t_i^b}{Y_i^b A_i^b} \right) \right)} \tag{3}$$

Where Y_i^t is the ith tube's Young's modulus in the 1 direction and A_i^t is its cross-sectional area. The stiffness of the ith end cap is denoted by k_i^c (Analytical end cap stiffness terms for each prototype are given in Table 4.). By examining the free deflection equation, the additional bonding layer terms play no role in determining the displacement of a telescopic actuator. However, these terms do factor into the predicted blocking force and, as a result of this, they also play a role in defining the actuator's overall stiffness k^o.

$$k^o = \frac{1}{\left(\sum_{i=1}^{n} \left(\frac{L_i^t}{Y_i^t A_i^t} \right) + \sum_{i=1}^{n-1} \left(\frac{1}{k_i^c} \right) + \sum_{i=1}^{m} \left(\frac{t_i^b}{Y_i^b A_i^b} \right) \right)} \qquad (4)$$

The newly added bonding terms will increase the compliance of the modeled structure and therefore will result in more conservative predictions of the blocking force and the actuator stiffness when compared to the previously defined model without impacting the free deflection.

Comparing the revised analytical model to the original model (Figure 6), the effect of the bonding layers on the blocked force and stiffness become readily apparent. For the injection molded prototype at the maximum driving potential (Figure 6a), the original model predicts a blocked force of 233.1 N and a stiffness of 17.2 N/μm while the revised model generates 229.3 N of blocking force and a stiffness of 17.0 N/μm. Giving decrease of 1.7% in the blocked force and 1.2% in the actuator stiffness. Similarly, the injection molded prototype models (Figure 6b) yield blocking forces of 283.4 N for the original model and 275.9 N after the revisions, with the original predicted stiffness of 13.1 N/μm as opposed to 12.7 N/μm for the revised analytic model. The change in the predicted blocking fore for the two models is 2.7% and 3.1% for the actuator's stiffness. The discrepancies for both of these prototypes arise from the inclusion of the single bonding layer present at the base of the actuators, a much greater dependence on the bonding terms is observed for the conventionally assembled actuator, where bonding layers are present between the tubes and endcaps (Figure 6c). The predicted blocking force varies drastically from the original model's 425.9 N to the revised model's 385.4 N, a loss of 10.5%. The predicted stiffness of this actuator also varies to a higher degree than that of the monolithic actuators, with the original model giving 12.1 N/μm as opposed to the revised model's prediction of 10.9 N/μm, a variation of 11.0%.

As would be expected from these results, the revised analytical model better captures the behavior of the actual prototypes compared to the original model. For the 300 V, maximum driving potential of the injection molded actuator (Figure 6a), the revised model predicted a free deflection of 13.5 μm, a blocked force of 229.3 N, and a stiffness of 17.0 N/μm. This yields an error between the revised model and experimental observations of 2.6% for the free displacement, 7.4% for the blocked force, 10.4% for the stiffness, with an overall model error of 5.1%. This is a significant improvement over the original model, but still a slight over-prediction when compared to the numerical model. As expected, the revised model for the conventionally assembled actuator exhibited a much larger improvement compared to the original analytic model because of the many bonding layers within the actuator. The 400 V case results of the revised analytic model are given in Figure 6c, with a free deflection of 35.3 μm that can be negated by a blocking force of 385.4 N, yielding a theoretic stiffness of 10.9 N/μm. The resulting errors in this modeling case are 4.8% for the free deflection, 4.6% for the blocking force, a 0.3% error in stiffness, and an overall error of 4.8%. Again, this model is quite accurate, but not as accurate as the numerical model's predictions for this prototype. The results of the revised analytical model of the polymerized prototype are a free deflection of 21.7 μm, a blocking force of 274.9 N, and a theoretic actuator stiffness of 12.7 N/μm. This results in errors of 5.9% for the free deflection, 7.0% for the blocked force, 8.2% for the prototype stiffness, and 4.1% error in the overall revised analytic model when compared to the experimental findings. Interestingly, for this actuator, the modified analytical model correlates better to the observed behavior than both the numerical model and the original analytical model, which are virtually identical. It is the only prototype where the numerical model predicts

Table 4: Analytically derived end cap stiffness terms for each prototype

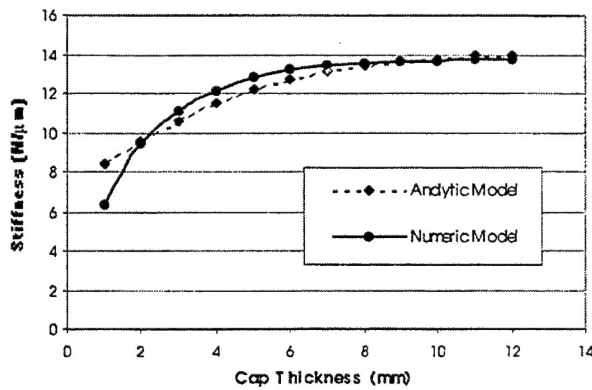| Prototype	End Cap 1 (outer)	End Cap 2	End Cap 3	End Cap 4 (inner)
Injection Molded	908 N/μm	876 N/μm	840 N/μm	798 N/μm
Acrylate Polymerized	174 N/μm	375 N/μm	N/A	N/A
Conventionally Assembled	182 N/μm	157 N/μm	N/A	N/A

Figure 8: Results of modeling a telescopic actuator with varying end cap thickness
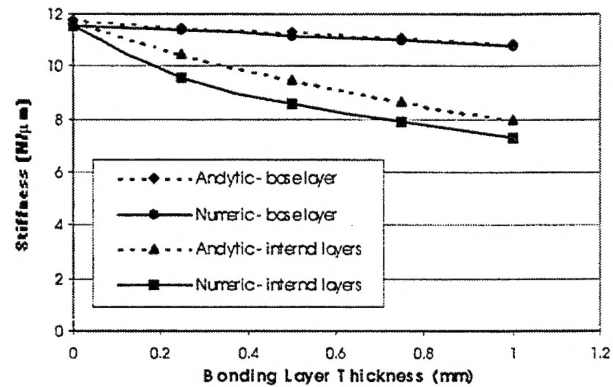

Figure 9: Results of modeling a telescopic actuator with varying base and internal bonding layer thickness

both higher blocking forces and stiffnesses than the new analytic model.

3.3 Model Analysis

After some scrutiny, no experimental errors were identified that could account for the inconsistent trends in behavioral predictions of numeric and revised analytic models, such as the numeric model over-predicting the polymerized actuator's performance, when it consistently under-predicted the quasi-static performance of the injection molded and conventionally assembled prototypes. A more intensive study into telescopic design parameters was performed using both the numeric and revised analytic models. From this parameter study it was discovered that the thickness of the end caps displays an unexpected effect on actuator stiffness. Using the polymerized models and varying end cap thickness, it can be seen in Figure 8 that there is a range of end cap thickness where the numerical model gives a higher theoretic stiffness than the revised analytical model, and other thickness ranges where the converse is true, with the two curves crossing each other at the 2mm and 9mm end cap thicknesses. This is due to the drastically different ways that the end caps are modeled, where the numeric model simply regards them as just another piece of the telescopic structure and the revised analytic model includes them as spring terms. For the other two prototypes, with thinner end caps, the numeric model becomes much more conservative, falling into the left most region for their particular geometries. From these results, it is clear that the thickness of the end caps within an actuator could determine which model is more conservative and thus, proper for use in modeling a specific actuator.

Further investigation into the mechanics of the bonding layers proves that accounting for three-dimensional shearing, bending, and twisting of these layers within a telescopic actuator can seriously affect predicted actuator stiffness. Figure 9 displays how the stiffness of the conventionally assembled actuator varies as the thickness of the base bonding layer and the internal bonding layers increase in each of the developed models. There is little difference between the two models where the base bonding layer is concerned, each linearly reducing the actuator stiffness but not to an extreme degree. A much more pronounced effect is exhibited by the internal bonding layer thickness, with actuator stiffness declining more drastically and nonlinearly as it is increased. Because of the numeric model's three dimensional nature, it captures much more bonding layer compliance than the revised analytical model, which only accounts for axial deformations, where a 9.3% change in actuator stiffness can result because of 1 mm thick internal bonding layers. Thus, the numerical model would be a much more prudent choice for the modeling of assembled actuators with multiple internal bonding layers.

4. CONCLUSIONS

This paper presents a quasi-static experimental study of the performance of three telescopic actuator prototypes: one manufactured by injection molding, one fabricated using acrylate polymerization, and one assembled from off-the-shelf components. It was found that the telescopic actuator does perform as expected, producing moderate amplifications while generating relatively large actuation forces. As was expected, longer actuators produced more free deflection, but short tubes that are closely spaced yield a much stiffer actuator. It was also found that the original analytic model captured the actuator

displacement well, to within an average of 5.6% error, but was off by as much as 32.7% when predicting an actuator's blocked force.

To reduce the extent of this modeling error, a full, three dimensional numerical model was constructed using finite elements. These modeled included every component of the telescopic architecture, including the actuator tubes, the end caps, and the bonding layers. It was found that modeling deformations in three dimensions and the inclusion of bonding layers in the model did affect the predicted behavior, with the bonding layers playing the most dramatic role. For this reason, the analytic model was revised to include bonding layer compliance in one dimension. This had a noticeable impact on the accuracy of analytic model's load bearing characteristics, reducing the error in the blocking force from a high of 32.7% to a range of 7.4% to 4.6%. Similar improvements were also seen in the actuator's predicted stiffness, lowering the maximum error of 28.6% down to a range of 10.4% to 0.3%.

Interestingly, there was not a modeling method that always predicted actuator performance with the highest level of accuracy. Further study identified two factors which could affect which model best suits a given actuator, end cap thickness and the number or thickness of bonding layers within the actuator. As end cap thickness was varied, neither the numeric model nor the analytic model was consistently conservative. Instead, it was found that the numeric model is more conservative for thin and relatively thick end caps, but there is a middle range of end cap thickness where the opposite is true, and the revised analytic model is slightly more conservative. Bonding layer thickness was also found to generate significant discrepancies between model predictions, with the numeric model always generating the more conservative estimate of actuator load bearing capabilities than that of the revised analytic model, especially in there are numerous internal bonding layers within the actuator. Thus, the telescopic actuator type and geometry play a definitive role the selection of the proper modeling technique that should be employed.

ACKNOWLEDGMENTS

REFERENCES

1. E. F. Prechtl, and S. R. Hall, "Design of a High Efficiency Discrete Servo-flap Actuator for Helicopter Rotor Control," *Smart Structures and Materials 1997: Smart Structures and Integrated Systems*, M. E. Regelbrugge, Ed., **3041**, pp. 158-182, 1997.
2. Y. Sugawara, K. Onitsuka, S. Yoshikawa, Q. Xu, R. E. Newnham, and K. Uchino, "Metal-ceramic Composite Actuators," *Journal of the American Ceramic Society*, **75**, pp. 996-998, 1992.
3. K. Onitsuka, A. Dogan, J. F. Tressler, Q. Xu, S. Yoshikawa, and R. E. Newnham, "Metal-ceramic composite transducer, the 'moonie'," *Journal of Intelligent Material Systems and Structures*, **6**, pp.447-455, 1995.
4. D. R. Martinez, T. D. Hinnerichs, and J. M. Redmond, "Vibration control for precision manufacturing using piezoelectric actuators," *Journal of Intelligent Material Systems and Structures*, **7**, pp. 182-191, 1996.
5. H. Sumali and H. Cudney, "An active engine mount with a piezoelectric stacked actuator," *Proceedings of the 35th SDM Conference*, AIAA, pp. 1233-1241, New York, NY, USA, 1994.
6. R. Barret and F. Brozoski, "Adaptive flight control surfaces, wings, rotors, and active aerodynamics," *Smart Structures and Materials 1996: Smart Structures and Integrated Systems*, I. Chopra, Ed., **2717**, pp. 178-198, 1996.
7. S. R. Hall and E. F. Prechtl, "Development of a piezoelectric servoflap for helicopter rotor control," *Smart Materials and Structures*, **5**, pp. 26-34, 1996.
8. D. K. Samak and I. Chopra, "Design of High Force, High Displacement Actuators for Helicopter Rotors," *Smart Materials and Structures*, **5**, pp. 58-87, 1996.
9. R. Martin, "Ein neues elektronisches Hochdruck-Einspritzsystem fuer Disselmotoren," *MTZ Motortechnische Zeitschrift*, **56**, pp. 142-148, 1995.
10. C. C. M. Wu, D. Lewis, M. Kahn, and M. Chase, "High authority, telescoping actuators", *Smart Structures and Materials 1999: Smart Structures and Integrated Systems*, **3674**, pp. 212-216, New Port Beach, CA, USA, 1999.
11. N. T. Berner and D. E. Brei, "Modeling and study of the quasi-static behavior of piezoceramic telescopic actuation architectures", *Adaptive Structures and Material Systems – 1999, The ASME International Mechanical Engineering Congress and Exposition*, **59**, pp.189-197, Nashville, TN, USA, 1999.

12. P. W. Alexander, D. E. Brei, W. Miao, J. W. Halloran, R. L. Gentilman, G. E. Schmidt, P.T. McGuire, and J.R. Hollenbeck, "Fabrication and experimental characterization of d_{31} telescopic piezoelectric actuators", *Smart Structures and Materials 2000: Smart Structures and Integrated Systems*, **3985**, pp. 207-216, New Port Beach, CA, USA, 2000.

13. R. L. Gentilman, R. L., D. F. Fiore, H. T. Pham, K. W. French, and L. J. Bowen, "Fabrication and properties of 1-3 PZT-polymer composites," *Ceramic Transactions*, **43,** pp. 239-247, 1994.

*pwa@engin.umich.edu; phone: (734) 764-9156; http://www.engin.umich.edu/dept/meam/; Smart Materials and Structures Design Laboratory, 2203 G. G. Brown Bldg., 2350 Hayward St., Ann Arbor, MI, USA 48104

**dibrei@engin.umich.edu; phone: (734) 763-6617; fax: (734) 647-3170
http://www.engin.umich.edu/dept/meam/faculty/brei.html; Smart Materials and Structures Design Laboratory, 2250 G. G. Brown Bldg., 2350 Hayward St., Ann Arbor, MI, USA 48104